TUM School of Engineering and Design
Technische Universität München

Multi-Hole Probes for Unsteady Aerodynamics Analysis

Florian Marco Heckmeier

Vollständiger Abdruck der von der TUM School of Engineering and Design der Technischen Universität München zur Erlangung des akademischen Grades eines

Doktors der Ingenieurwissenschaften

genehmigten Dissertation.

Vorsitzende:
Prof. Dr. Sophie Armanini

Prüfende der Dissertation:
1. apl. Prof. Dr. Christian W. M. Breitsamter
2. Prof. Dr. Carlo L. Bottasso

Die Dissertation wurde am 27.09.2021 bei der Technischen Universität München eingereicht und durch die TUM School of Engineering and Design am 16.04.2022 angenommen.

Typesetting: LaTeX

Acknowledgements

Throughout my work on the present doctoral dissertation, I have received support and assistance from many persons whom I want to thank explicitly, here.

I am deeply grateful to my doctoral advisor Prof. Dr.-Ing. Christian Breitsamter for the great supervision during this work. His organizational support and detailed scientific guidance contributed to the success of the present dissertation, for which I am very thankful.

Then, I would like to thank Prof. Dr. Carlo Bottasso to examine this thesis and Prof. Dr. Sophie Armanini for being the chair of the examining committee.

In the course of my work, I could rely on the support of collaboration partners and people who provided me with expertise, material and equipment. Hereby, I want to express my gratitude to: Daniel Iglesias and Christian Haigermoser (Vectoflow GmbH) for the close collaboration and numerous discussions concerning the development of the fast-response probe; Sascha Kienitz (fos4X GmbH / Polytech) for his helpful support with the development of the fiber-optic pressure sensor; Franz Mühle and Prof. Dr.-Ing. Carlo Bottasso for their support in the wind turbine testing campaigns; the mechanic and electric workshop at TUM-AER – Wolfgang Lützenburg, Martin Banzer, Hans-Jürgen Zirngibl, Detlef Mänz, Luigi Findanno and Hans-Gerhard (HG) Frimberger – for their extremely supportive efforts during my time at the chair helping my project to become a success; and Dr.-Ing. Josef Mallog for his advice and guidance as an external mentor.

I would also like to thank my students that I could supervise during my time as a PhD candidate: Jonas Bauer, Emir Boughanmi, Alejandro Garcia-Risco, Stefan Hayböck, Korbinian Meusel, Andreas Molz, Niklas Mooshofer, Matias Mrvelj, Pablo Nieto Muro, Johanna Prummer, Pablo Varillas Iglesias (in alphabetical order).

Further, I am deeply indebted to Prof. Dr.-Ing. Christian Breitsamter, Andreas Kümmel, Patrick Pölzlbauer, Jonathan Pflüger, Julius Stegmüller, Franz Mühle, Florian Hartl, Andreas Rücker and my brother Dr. Philipp J. Heckmeier for revising sections of this thesis. At last, I want to express my appreciation to my colleagues at the Chair of Aerodynamics and Fluid Mechanics for the pleasant work environment.

München, May 2022 Florian M. Heckmeier

Abstract

In the aerodynamic examination of objects in wind tunnels, engineers can choose from a wide range of different measurement tools for quantifying the flow. The choice of the appropriate measurement methodology is made based on the characteristics of the possible tools. Hence, subject of the present work is the development and testing of a multi-hole probe for the measurement of unsteady aerodynamic phenomena, which tries to combine properties of the different measurement systems and is also called fast-response aerodynamic probe (FRAP). For this purpose, the characteristics of the probe and the incorporated pressure sensors are determined and unresolved concerns with respect to the associated metrological possibilities and limitations are addressed. Using miniaturized sensors in the pressure probe body, a competitive measurement solution is to be found.

Therefore, the working principles of multi-hole probes and pressure sensors are briefly discussed. Special focus lies on newly developed fiber-optic pressure sensors. Various methods for the spatial calibration of the probe are presented. Furthermore, the machine learning approach, Gaussian process regression, is applied to reduce the calibration time. Additionally, a temporal calibration characterizes the acoustic system inside the probe. Various tests that determine the sensitivity of the pressure sensor with respect to external effects are explained and the sensor performance is evaluated. The multi-hole probe behavior is further analyzed in numerical investigations of the flow around the probe and of the line-cavity system inside the probe.

In addition, multiple measurement campaigns are carried out in the low-speed wind tunnel facilities at the Chair of Aerodynamics and Fluid Mechanics of the Technical University of Munich (TUM-AER). The determination of the spatial and temporal resolution of the probe in grid-generated turbulence is of special interest and aspects concerning uncertainty quantification of the probe measurements are given. To demonstrate the capabilities of the fully characterized probe, the quantification of unsteady flow phenomena in different measurement scenarios are discussed, a) in the wake of a circular cylinder and b) in the wake of a dynamically actuated wind turbine. By additionally acquiring a synchronization signal, independent FRAP measurements in the wind turbine wake are synchronized in the phase-locking postprocessing procedure. The FRAP investigations unveil that the actuated cases show an earlier mixing and entrainment of high energetic fluid already near the rotor plane. Consequently, the actuated control strategy is a promising approach that can contribute to a synergistic interaction of multiple wind turbines, as found in wind farms.

Measurements with the FRAP show a very robust and easy to use handling with a fast and cost-efficient setup. The incorporation of advanced (post-) processing routines, allows time-averaged, phase-locked and transient analyses of the flow field patterns.

Zusammenfassung

Bei der aerodynamischen Untersuchung von Objekten in Windkanälen können Ingenieure auf eine Vielzahl unterschiedlicher Messinstrumente zurückgreifen. Die Wahl der geeigneten Messmethodik richtet sich nach den Eigenschaften der jeweiligen Messgeräte. Gegenstand der vorliegenden Arbeit ist die Entwicklung und Erprobung einer Mehrlochsonde zur Messung instationärer aerodynamischer Phänomene, welche die Eigenschaften verschiedener Messsysteme kombiniert und als Fast-Response Aerodynamic Probe (FRAP) bezeichnet wird. Dabei werden die Eigenschaften der Sonde und der eingebauten Drucksensoren bestimmt und Fragestellungen im Hinblick auf ihre messtechnischen Möglichkeiten und Grenzen behandelt. Mittels miniaturisierter Sensoren im Sondenkörper soll eine konkurrenzfähige Messmethode entwickelt werden. Die Funktionsweise von Mehrlochsonden und Drucksensoren wird zunächst in ihren Grundzügen dargestellt. Ein besonderer Schwerpunkt liegt dabei auf dem Einsatz neu entwickelter faseroptischer Drucksensoren. Verschiedene Methoden zur räumlichen Kalibrierung der Sonde werden vorgestellt. Darüber hinaus wird der Machine-Learning-Ansatz, die Gaußprozess Regression, zur Reduzierung der Kalibrierzeit untersucht. Eine zusätzliche zeitliche Kalibrierung ermöglicht eine Charakterisierung des akustischen Systems innerhalb der Sonde. Verschiedene Tests zur Bestimmung der Empfindlichkeit des Drucksensors gegenüber äußeren Einflüssen werden diskutiert und die Leistungsfähigkeit des Sensors wird bewertet. In numerischen Simulationen wird das Verhalten der Sonde bei Umströmung und das akustische System innerhalb der Sonde analysiert. Im Rahmen der Arbeit werden zudem mehrere Messkampagnen in den Windkanälen am Lehrstuhl für Aerodynamik und Strömungsmechanik der Technischen Universität München (TUM-AER) durchgeführt. Die Bestimmung der räumlichen und zeitlichen Auflösung der Drucksonde in gittergenerierter Turbulenz ist von besonderem Interesse und Aspekte der Quantifizierung von Messunsicherheiten werden dargestellt. Um die Leistungsfähigkeit der vollständig charakterisierten Mehrlochsonde zu demonstrieren, werden instationärer Strömungsphänomene in verschiedenen Messszenarien untersucht, a) im Nachlauf eines Kreiszylinders und b) im Nachlauf einer dynamisch geregelten Windkraftanlage. Durch die Erfassung eines Synchronisierungssignals werden die unabhängigen FRAP-Messungen im Nachlauf der Windturbine phasengemittelt synchronisiert. Die Untersuchungen zeigen in den angeregten Fällen bereits eine frühere Durchmischung und Aufnahme von hochenergetischem Fluid. Somit ist die untersuchte Regelung ein vielversprechender Ansatz, der zu einer synergetischen Interaktion mehrerer Windturbinen beitragen kann. Die Messungen mit der FRAP belegen eine sehr robuste und einfach zu bedienende Handhabung in Verbindung mit einem schnellen und kosteneffizienten Messaufbau. Die Berücksichtigung umfangreicher Verfahren zur Datenverarbeitung ermöglicht die Analyse von zeitlich gemittelten, phasengemittelten und instationären Strömungsfeldern.

Contents

List of Figures

List of Tables

Nomenclature

Roman Symbols	Denotation
A	cross-sectional area
A	coefficient for decay of TKE law
A_s, A_t	non-dimensional pressure coefficients
a_i, b_i	system identification unknown polynomial parameters
b	node bias value
b	wind tunnel width
b_α, b_β	non-dimensional angle coefficient
b_θ, b_ϕ	non-dimensional angle coefficient
$1/C$	system elastic constant
C_p	pressure coefficient
c	speed of sound
c_i	sensitivity coefficients
D, d	channel diameter
DA	degree of anisotropy
D	cylinder diameter
d_{tip}, d_{shaft}	probe tip and shaft diameter
d	delay between input and output
d	grid/mesh diameter
d_w	wire diameter
E	Young's modulus
E	voltage
E_{LSB}	minimal detectable voltage
E_{kin}	kinetic energy
E_θ	output voltage for azimuthal position
F	coefficient of finesse
F	time saving factor
f	frequency
$\mathbf{f}$, $\mathbf{f}_*$	Gaussian process training/test function values
f_e	excitation frequency

Roman Symbols	**Denotation**
f_e	additional excitation frequency for blade pitch
f_H	Helmholtz resonance frequency
f_{lp}	low-pass filter frequency
f_N	Nyquist(-Shannon) frequency
f_n	natural frequency
f_r	rotational frequency of the rotor
f_s	sampling frequency
f_{vs}	vortex shedding frequency
f_β	excitation frequency for blade pitch
G	voltage gain
$\mathcal{GP}$	Gaussian process
H	transfer function
h	wind tunnel height
h_m	membrane thickness
I	light spectrum
I_R	reflecting light spectrum
I_0	incoming light spectrum
J_i	Bessel function of ith order
K	bending stiffness
K	turbulent kinetic energy (TKE)
k	Gaussian process covariance function
k	coverage factor
k	wave number
k_M	Mach number coefficient
k_p	pressure sensitivity
k_s, k_t	non-dimensional pressure coefficients
k_T	temperature sensitivity
k_α, k_β	non-dimensional angle coefficient
k_1, k_2	non-dimensional angle coefficient
$\mathcal{L}$	log likelihood function
L	channel length
L'	effective channel/tubing length
L_c	cavity length
ΔL	deflection of membrane
l_w	wire length

Roman Symbols	**Denotation**
$l_{w,equi.}$	equivalent wire length
M	Mach number
M	mismatch of reflectance
M	grid/mesh size
M_{calib}	calibrated Mach number
$M_{estimate}$	estimated Mach number
m	Gaussian process mean function
m	mass of the system
m	number of points for sparse approximation
m, n	polynomial order
N	integer multiple
N	number of neurons
n	refractive index of medium
n	number of points
n	King's law exponent
n	exponent for decay of TKE law
O	voltage offset
o	node output
P	point
P	pressures in the frequency domain
P, P^*	extracted/baseline power
$P(E)$	marginal likelihood
$P(E\|H)$	likelihood
$P(H)$	prior probability
$P(H\|E)$	posterior
Pr	Prandtl number
p	pressure
p	exponent for turbulence cascade
p_{LSB}	minimal detectable pressure
p_s	static pressure
p_t	stagnation or total pressure
$p_1, \ldots, p_5$	measured pressures at probe
Δp	applied pressure on membrane
p^+, p^-	pressure in clockwise and counter-clockwise direction
q	dynamic pressure

Roman Symbols	**Denotation**
$\bar{q}$	pseudo dynamic pressure
R	resistance
R	mirror reflection coefficient
R	radius
R	specific gas constant
R	viscous damping coefficient
R	quantity for uncertainty quantification
R^2	coefficient of determination
R_a	acoustic resistance of system
Re	Reynolds number
Re_D	Reynolds number based on the cylinder diameter D
Re_M	Reynolds number based on the mesh size M
Re_λ	turbulence Reynolds number
r	channel radius
r_m	membrane radius
S	sensor sensitivity
St	Strouhal number
s	standard deviation of measurements
$scale$	scaling factor for spatial calibration
T	transmission spectrum
T	temperature
T_r	rotational period
T_w	wire temperature
Tu	turbulence intensity
t	time
Δt	time step
t_s	sampling time
U	absolute velocity
U	Z-transformed of reference sensor data
U	expanded uncertainty
$U_{hw0.06}$	reference velocity measured with a miniature hot-wire probe
U_∞	free-stream velocity
u, v, w	velocity components
u_1, u_2, u_3	velocity components
u, $\mathbf{u}$	inducing point location/vector

Roman Symbols	**Denotation**
u_c	combined uncertainty
u_η	Kolmogorov velocity
V	velocity on the surface of a sphere
V	cavity volume
V_{in}, V_{out}	input/output voltage
w	barycentric coordinate weight
w	node weight
X	node input
X	measured value, input of measurement model
X^*	true value
X, X_*	Gaussian process training/test point
x, y, z	Cartesian coordinates
x, $\mathbf{x}$	training point location/vector
x	input estimate
Y	Z-transformed of LCS sensor data
Y	output of measurement model
y, $\mathbf{y}$	measured value/vector
y	output estimate
y^+	non-dimensional wall distance

Greek Symbols	**Denotation**
α	angle of attack
α	pitch angle
α_{20}	sensor temperature coefficient
β	angle of sideslip
β	yaw angle
β	bias error
β_b	blade pitch angle for blade b
δ	phase
δ	absolute error
ϵ	noise
ε	pre-specified margin for spatial calibration
ε	random/precision error
ε	dissipation rate

Greek Symbols	**Denotation**
$\varepsilon_{A/D,gain}$	gain error of A/D module
$\varepsilon_{A/D,offset}$	offset error of A/D module
η	cone angle
η	Kolmogorov length scale
θ	cone angle
θ_b	azimuthal blade position of blade b
$\boldsymbol{\theta}$	hyperparameter vector
κ	specific heat ratio/isentropic expansion exponent
λ	wavelength
λ	lag constant
λ	Taylor micro scale
λ_i	coefficient for f_n calculation
μ	dynamic viscosity
μ, $\boldsymbol{\mu}$	Gaussian process mean function/vector
ν	Poisson's ratio
ν	kinematic viscosity
ξ_z	normalized vorticity in z-direction
ρ	fluid/material density
ρ_{opt}	measured light intensity ratio, optical output
$\rho_{opt,0}$	optical output for no applied pressure
Σ	Gaussian process kernel/covariance matrix
$\tilde{\Sigma}$	approximated covariance matrix
σ	standard deviation
σ	solidity of the mesh
σ_f	kernel standard deviation (hyperparameter)
σ_l	kernel characteristic length scale (hyperparameter)
σ_n^2	noise variance
$\sigma_{n_u}^2$	noise variance from inducing points
τ	acoustic lag
τ_η	Kolmogorov time scale
ϕ	roll angle
ϕ	sigmoid/logistic activation function
ϕ, φ	phase shift
ω	angular frequency
ω_r	rotational angular frequency of the rotor

Greek Symbols	**Denotation**
ω_z	vorticity in z-direction

Subscript	**Denotation**
C	calibration point
c, cal, $calib$	calibrated data
$cavity$	cavity in the line-cavity system
$corr$	corrected value
$driver$, $driven$	data in driver or driven shock tube section
$FRAP$	fast-response aerodynamic probe
HW	hot wire
i, j, k	running indices
LCS	line-cavity system
max	maximum
m, $meas$	measured data
min	minimum
$recon$	reconstructed data
ref	reference data
sen, $sensor$	sensor data
$shock$	shock data
T	test point
$test$	test value
tip	tip data
0	zero/offset value
∞	atmospheric/free-stream condition

Modifier	**Denotation**
$\hat{\bullet}$	amplitude
$\hat{\bullet}$	average value
$\bar{\bullet}$	time-averaged value
$\bullet_{rms}$	root mean squared
$\bullet'$	fluctuation value
$\langle\bullet\rangle$	average value
$(\bullet)_\theta$	phase-locked/phase-averaged property

Abbreviations and Acronyms

Abbreviation	Meaning
A/D	Analog-to-Digital
AER	Chair of Aerodynamics and Fluid Mechanics
ANN	Artificial Neural Network
ASME	American Society of Mechanical Engineers
BFSL	Best Fit Straight Line
BIPM	International Bureau of Weights and Measures
CAD	Computer-Aided Design
CCA	Constant Current Anemometry
CCW	Counter Clockwise
CFD	Computational Fluid Dynamics
CTA	Constant Temperature Anemometry
CW	Clockwise
DAQ	Data Acquisition
DGLR	Deutsche Gesellschaft für Luft- und Raumfahrt
DIC	Dynamic Induction Control
DIC	Dynamic Individual Pitch Control
FBG	Fiber Bragg Grating
FFT	Fast Fourier Transformation
FIR	Finite Impulse Filter
FITC	Fully Independent Training Conditional
FO	Fiber-Optic
FOPS	Fiber-Optic Pressure Sensor
FRAP	Fast-Response Aerodynamic Probe
FSO	Full Scale Output
GP	Gaussian Process
GPML	Gaussian Processes for Machine Learning
HIT	Homogeneous Isotropic Turbulent
HW	Hot Wire
IFFT	Inverted Fast Fourier Transformation

Abbreviation	**Meaning**
ISO	International Organization for Standardization
LES	Large-Eddy Simulation
LCS	Line-Cavity System
LDA/LDV	Laser Doppler Anemometry/Velocimetry
LSB	Least Significant Bit
MEMS	Micro-Electro-Mechanical System
MHP	Multi-Hole Probe
MLP	Multi-Layer Perceptron
MOEMS	Micro-Opto-Electro-Mechanical System
MUSCL	Monotonic Upstream-centered Scheme for Conservation Laws
NTC	Negative Temperature Coefficient (Thermistor)
PIV	Particle Image Velocimetry
PR	Piezo-Resistive
PT	Potential (flow) Theory
RANS	Reynolds-Averaged-Navier-Stokes (equations)
RMS	Root Mean Squared
RSS	Root Sum Squared
SIMPLEC	Semi-Implicit Method for Pressure Linked Equations-Consistent
SLE	Selective Laser Etching
SLM	Selective Laser Melting
SST	Shear Stress Transport
STAB	Deutsche Strömungsmechanische Arbeitsgemeinschaft
TF	Transfer Function
TKE	Turbulent Kinetic Energy
TP	Terminal Point
TSR	Tip-Speed Ratio
TUM	Technical University of Munich
UDF	User Defined Function
UQ	Uncertainty Quantification
W/T	Wind Tunnel
ZPO	Zero Pressure Output
2D/3D	Two/Three dimensional

1 Introduction

This opening chapter of the dissertation *Multi-Hole Probes for Unsteady Aerodynamics Analysis* should give a first insight into the fundamental goals of this thesis. Besides a motivation for the execution of this research project, a brief review of developments and state-of-the-art solutions of pressure probes applied for the analysis of unsteady flow phenomena is given. Finally, the research objectives of this thesis are formulated and the thesis outline is presented.

1.1 Motivation

The description and the understanding of flows around and through objects is of great interest to many branches, especially in the aerospace and automotive industry. Hence, flows can be investigated by means of experimental measurements or numerical simulations. Even though the development and optimization of computational fluid dynamics (CFD) simulations enables the (unsteady) flow patterns to be handled numerically, experimentally gained data are still of interest for academic and industrial research. The reason why experiments can be still justified alongside numerical simulations is multilayered. Among other reasons, often, experimental results serve as a database for the validation for CFD codes/solutions. Moreover, sometimes live monitoring of machines/flows is only possible experimentally. And last, the investigation of complex flow phenomena typically involves computational resources or clusters with enormous computational power or, equivalently, very long simulation times. Hence, in the following, the experimental investigation of objects in a wind tunnel environment is of interest:

In the aerodynamic examination of objects in wind tunnels, engineers can choose from a wide range of different measurement tools for quantifying the flow in, on and around the object under investigation. The choice of the appropriate measurement methodology must therefore be made on the basis of various criteria. Often a prior knowledge or an anticipation of the expected flow is necessary in order not to measure the wrong quantity at the wrong place and at the wrong time. In many aerodynamic problems, in addition to the global/integral quantities, an in-depth understanding of the flow characteristics downstream of the object is also of great relevance. For example, in addition to the aerodynamic lift and drag of an aircraft or a car at a certain inflow velocity, the flow structures in the wake are also insightful and can be directly related to the integral behavior of the object.

Therefore, the acquisition of these wake structures is of great importance and an essential part of many wind tunnel investigations. In addition to the analysis of time-averaged flow fields, the observation of the transient phenomena can also help to interpret the physics. Highly fluctuating flow fields are for example caused by interactions of

rotating and non-rotating components, or disturbances introduced dynamically into the flow field, e.g. in form of active or passive actuators.

For aerodynamic measurements of flow fields, measurement techniques can basically be divided into non-intrusive/optical and intrusive techniques. Particle image velocimetry (PIV) and laser Doppler anemometry (LDA) are the main representatives of optical measurements, which are used to examine the velocity field. However, in some cases they are disadvantageous because of high calibration efforts and significant setup costs. Furthermore, the need for optical access in the test section rules out optical measurement techniques in various test situations.

For probe based measurement techniques, certain requirements have to be met in order to investigate unsteady flow quantities. This ensures that all sources of unsteadiness can be resolved precisely. For example, phenomena and their harmonics with bandwidths up to $f = 10\ kHz$ can be seen as the benchmark for the temporal resolution for measurements in subsonic wind tunnel facilities, as the ones that are operated at the Chair of Aerodynamics and Fluid Mechanics of the Technical University of Munich (TUM-AER).

Of the intrusive measuring methods, hot-wire probes and multi-hole pressure probes are most commonly used. On the one hand, hot-wire anemometry is characterized by its high temporal resolution. On the other hand, hot-wires lack of mechanical robustness when being set in harsh environments. In contrast, multi-hole pressure probes are cost-efficient and easy to use, but lack of a high temporal resolution in their standard versions, where distant pressure scanners are connected by long tubings to the probe in the measurement section. In this thesis, the properties of the two probes are to be combined and by the use of miniaturized sensors in the pressure probe body, a competitive solution is to be found.

1.2 Development of fast-response probes: review and state-of-the-art solutions

In this subsection, a short summary of developments of fast-response pressure probes in the literature is given. This short review does not give all details and state-of-the-art solutions of probes and sensor technology. The detailed state-of-the-art information of the respective topics can be found in the corresponding chapters and therefore it is emphasized here.

Since the 1990s research institutes worldwide developed multi-hole pressure probes for unsteady measurements, so-called fast-response aerodynamic probes (FRAP), which incorporate small pressure sensors in the probe assembly. Ainsworth et al. [1] describe the application of piezo-resistive silicon pressure sensors for unsteady measurements in turbomachines. Different designs of unsteady pressure probes, for example with respect to their shape, are discussed in Babinsky et al. [2]. The use of FRAPs in environments with high temperatures, varying pressure ranges or spatial restrictions of the installation space, require various design, assembly and calibration strategies. Meaningful and accurate measurement results can only be achieved if the probe is calibrated in representative conditions. Similarities in Reynolds number Re and Mach number M as well as dynamic

similarity have to be ensured during calibration and experiments. Several design trends can be observed in the literature. Especially sensor specific limitations or limits due to thermal durability are the main drivers for changes in probe design. Furthermore, fast-response pressure probes can be divided into real or virtual multi-sensor probes. Virtual probes use the periodicity of (turbomachinery) flows and are yawed to virtually simulate a multi-sensor probe [3].

At ETH Zurich, in various research projects, different researchers studied the behavior of FRAPs for their use in turbomachinery (see e.g. the dissertations by Gossweiler [4], Humm [5], Kupferschmied [6], and Gizzi [7]). Thus, Gossweiler et al. [8] developed single-sensor cylinder probes for turbomachinery measurements and placed micro-electro-mechanical system (MEMS) sensors in the probe tip. Humm et al. [9] studied various probe shapes and geometric parameters regarding their intrusive influence in flow fields. Further investigations based on the two aforementioned studies show the application of a fast-response cylinder probe in a centrifugal compressor [10–12].

Moreover, at Texas A&M University, Rediniotis et al. [13] built a MEMS based fast-response five sensor probe for subsonic measurements, in order to test the angular/spatial and temporal characteristics of the probe with signal frequencies of up to 400 Hz. A flush-mounted sensor experiences high loads, which can be reduced by placing the sensor farther inside the probe. However, by doing so, a characterization of the acoustic line-cavity system in the pressure channels is needed. A reconstruction procedure of the unknown flow parameters at the probe tip is introduced for a five-hole probe in References [14, 15]. Further research by this research group, especially by Johansen et al., covers the theoretical and experimental study of the unsteady calibration and use of fast-response probes in highly unsteady flow fields [16–19].

Persico et al. [20] developed cylindrical pressure probes and calibrated the pneumatic line-cavity system inside the probe in a low-pressure shock-tube. Sieverding et al. [21] and Brouckaert [22] developed single- and multi-sensor unsteady pressure probes for turbine test-rig experiments. Recent approaches towards fast-response probes include a waveguide approach by Fioravanti et al. [23] or studies on the probe head shapes by Liu and Paniagua [24]. Aspects in consequence of a probe miniaturization like the influences on the settling time in turbomachines on probe measurement accuracy are discussed by Grimshaw and Taylor [25].

1.3 Research objectives and thesis outline

There is a great need for probe-based measurement solutions for the experimental aerodynamic analysis in wind tunnels. Nevertheless, unresolved concerns remain with respect to the capabilities and limitations of such probes. In order to address those concerns, a novel design and assembly for a fast-response pressure probe is proposed in this thesis. The focus lies on the probe specifications which are to a large extent dependent on the applied sensors. Furthermore, for demonstration and validation purposes, several application cases are considered in this thesis. The following questions can be seen as the overall research objectives for this work:

Research Objective 1 With which means is it possible to develop a robust measurement device for transient flow phenomena for subsonic wind tunnels?

Research Objective 2 What are the limiting specifications and components related to spatial and temporal resolution and how can these limitations be addressed?

Research Objective 3 How can elaborate software solutions in data reduction or analysis facilitate the use of the probe or expand the range of possible applications?

Research Objective 4 Will the probe show appropriate performance and be able to replace or outperform other measurement techniques?

The following brief outline of the thesis gives a first glance of the scope of the covered topics. In addition, the thesis structure is also depicted in Figure 1.1. The structure of the work is divided twofold in several aspects. On the one hand, there is a separation between the theoretical part (Chapters 2 and 3), which is intended to clarify the fundamental mechanisms and relations, and an experimental part (Chapters 4, 5 and 6), in which tests are performed and measurements are analyzed and interpreted. On the other hand, in Chapters 2 and 4, a separation is also made between the investigations of the probe itself and studies on the applied sensor technology.

After the current introduction chapter, which mainly covers the motivation and structure of this thesis, Chapter 2 begins with the general theory about multi-hole probes. In addition to the operating principles, aspects of design and manufacturing are also discussed. Furthermore, theoretical fundamentals of pressure sensors are given. Here, special focus is devoted to the working principle of fiber-optic sensors based on the Fabry-Pérot interferometer.

Since the calibration of probes is a major part of characterizing and quantifying the performance of a pressure probe, Chapter 3 exclusively discusses different calibration and reconstruction approaches. Various methods for the spatial calibration of the probe are presented. A machine learning based algorithm is highlighted – the Gaussian process regression – which is expected to lead to a reduction in calibration time. Another part of the calibration process of a probe for transient applications is the temporal calibration, in which the acoustic system inside the probe is characterized.

After the theoretical basics have been explained in the aforementioned chapters, Chapter 4 deals with the characterization of the fiber-optic pressure sensors and the multi-hole probe. Various tests to determine the sensitivity of the sensor with respect to external effects and the characterization of the sensor behavior in installed conditions are explained and evaluated. The description of the probe behavior is divided into two parts, a numerical investigation of the flow around the probe and of the line-cavity system inside the probe, and an experimental evaluation of different probe calibrations.

Chapter 5 deals with the quantification of measurement resolution and uncertainties when measuring with fast-response pressure probes. After a brief overview of fundamentals in metrology and the necessary explanations for probe uncertainty quantification, Section 5.3 deals with the determination of the spatial and temporal resolution of the probe in grid-generated turbulence.

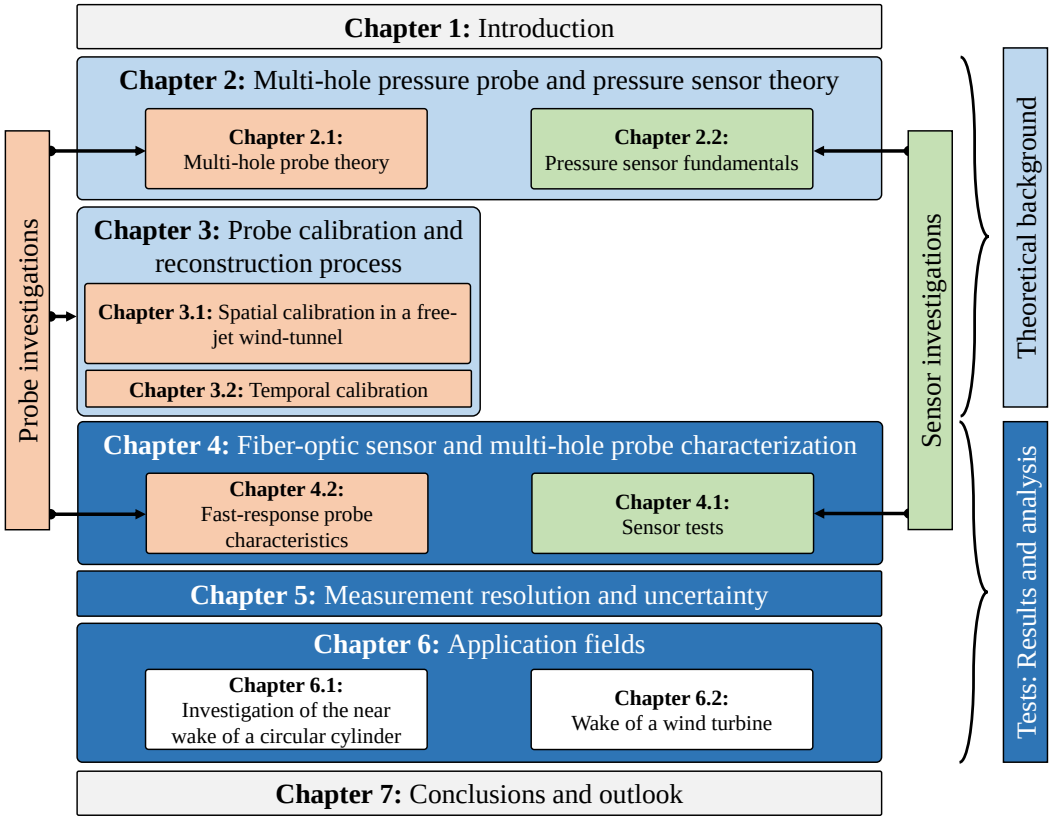

Figure 1.1: Thesis outline

While the previous chapters quantified the probe and determined its performance, the core task of Chapter 6 is to demonstrate the capabilities of the probe to provide a robust measurement of unsteady flow phenomena in different measurement scenarios in a wind tunnel environment. In two measurement campaigns – the wake of a circular cylinder and the wake of a dynamically actuated wind turbine – transient analyses of pressures and deduced velocities are performed in addition to time-averaged flow field quantities.

Last, the work is concluded by a summary on the researched problems concerning the development of a multi-hole probe for the measurement of unsteady aerodynamic phenomena in Chapter 7. In order to underline the main stages of the research, the obtained results are summarized and synthesized. The objectives, as stated in the previous paragraphs, are evaluated for fulfillment. Finally, recommendations for future developments are given for a) the probe and b) the sensor technology incorporated within the probe.

2 Multi-hole pressure probe and pressure sensor theory

This chapter has an introductory purpose and is intended to explain the basics of probe measurement. In addition to the presentation of the most important influencing factors in probe setup and design, the careful selection of a suitable pressure sensor also occupies a decisive role. The underlying theory of probe measurement with pressure sensors is presented in the respective sections. More detailed information on the probe calibration process can be found in the corresponding Chapter 3. The characterization and application of the probes and sensors used in this thesis is covered in detail in Chapters 4 and 5. However, before the probe theory is presented in the upcoming Section 2.1 and the sensor technology in Section 2.2, the application field of multi-hole probes is defined more precisely in the following paragraph and evaluated with regard to other measurement methods.

Intrusive and non-intrusive measurement techniques: Demarcating considerations

In order to get a better impression of how pressure probes can be classified within different velocity measuring techniques, other measuring methods are mentioned and their measuring principle is presented in a nutshell. Subsequently, a general judgement will be performed according to different evaluation criteria. However, the following discussion is constrained to the aerodynamic measurement operation in low speed wind tunnels, as otherwise the categorization would have to be broader and an evaluation would become rather difficult.

The various measurement techniques can most certainly be categorized in several different aspects. However, in the following, the four most common methods in the wind tunnel environment are classified into intrusive and non-intrusive methods. Examples for non-intrusive/optic measurement methods are the particle-image velocimetry (PIV), and the laser-Doppler anemometry/velocimetry (LDA). Intrusive measurement tools that involve the insertion of probes into the flow for example include hot-wire (HW) constant-temperature anemometry (CTA) and the use of pressure probes.

PIV and LDA are optical velocity measurement techniques which use seeding/tracer particles that are illuminated. Hence, properties of the flow can be deduced when extracting the particle information. In PIV measurements, the displacement of the seeding particles over a short time interval is measured. In the test setup, a pulsed light source produces a thin light sheet. In a stereoscopic PIV setup, two cameras record two subsequent image frames which show the scattered light of the seeding particles. Hence, by applying image processing and calibration routines, a three component velocity flow

field can be reconstructed and coherent flow structures can be visualized. PIV requires optical access for both the laser and the cameras. The more homogeneous – spatial and temporal – the particles are spread over the region of interest, the better the reconstruction algorithm can produce velocity readings with high accuracy. The application of PIV in TUM-AER wind tunnel facilities was studied for example in Hövelmann [26].

LDA is a point-wise velocity measurement technique. For each velocity component, a pair of laser beams cross under a certain angle and form a measurement volume. There, light is scattered at the particles in the flow. The scattered light is collected on a detector. Depending on the interference pattern due to the laser beam crossing and the flow/particle velocity, a Doppler frequency shift in the light spectrum is detected. The following advantages over intrusive probe-based methods can be named [27]: non-intrusive, directional sensitivity, high spatial and temporal resolution, high accuracy.

One of the most commonly used probe-based measurement techniques is hot-wire anemometry: Depending on the operating mode, a differentiation can be made between constant-current anemometry (CCA) and constant-temperature anemometry (CTA). At TUM-AER, exclusively CTA probes are operated. The measurement technique is based on the temperature control of a heated very thin tungsten wire (approximately 5 μm in diameter). The relationship between the voltage required to keep the wire at a predefined temperature while the incident flow velocity cools the wire can be described by a power law, the King's law. In the measurement system, the wire represents an arm of a Wheatstone full bridge. Due to the fast heat transfer at the miniaturized wire, the response time is very short and high-frequency phenomena $> 50kHz$ can be represented. However, the wire is very easily mechanically damageable and must also be protected against overvoltage which can cause a failure as well. Detailed information on the operation of hot-wire CTA probes at TUM-AER can be found in Breitsamter [28].

In comparison to standard pressure probes (Pitot or Prandtl probes), where pressure transducers/manometers are placed at the end of long tubings very distant from the probes themselves, here, fast-response pressure probes are of interest. Pressure sensors are incorporated inside the probe body to also account for transient measurements of the stagnation pressure. A more detailed introduction on the working principle of pressure probes is given in the subsequent sections. In Table 2.1, the various measurement techniques are compared, based in part on personal experience with the respective measurement techniques and in part on a purely objective assessment. The criteria for evaluating the different measurement methods and the associated questions are:

- **Calibration effort**: How difficult and time consuming is the calibration process? How often does it have to be done?
- **Intrusive effect**: Is the method invasive and therefore changing the flow behavior?
- **Robustness in harsh environment**: Does the method show sensitivities to external effects? Can it be damaged easily?
- **Ease of use**: Is it easy to use? How beginner friendly is the setup, the acquisition and the post-processing?
- **Spatial resolution**: How restrictive is the method towards spatial resolution?

Table 2.1: Distinction between the various measurement techniques

	Calibration effort	Intrusive effect	Robustness in harsh environment	Ease of use	Spatial resolution	Temporal resolution	Initial/ acquisition cost	Maintenance/ operating costs
PIV	--	+++	o	-	++	--	---	--
LDA	+++	+++	o	--	++	+++	---	--
CTA	---	--	-	o	+	++	o	-
MHP	++	--	++	+++	o	+	+	++

+++ very positive o neutral --- very negative

- **Temporal resolution**: How restrictive is the method towards temporal resolution?
- **Initial/acquisition costs**: How expensive is the needed equipment for measurements of the full 3D velocity vector?
- **Maintenance/operating costs**: Does the system need maintenance or are there any operating costs?

CTA and PIV both show a high calibration effort which has to be conducted before/while every measurement campaign. For some measurements, the need of optical access for LDA and PIV can be challenging, however due to their non-intrusive working principle, the influence of probe-based techniques has to be assessed for the respective measurement task. Hot-wires are easy to rupture and the need of repair and re-calibration is either time consuming or expensive. For the laser-based techniques, ensuring seeding concentration in specific areas of interest is difficult. In comparison to PIV and LDA, where laser safety regulations and the operation know-how can hinder the decision to measure, pressure probe measurements are easy to conduct even for beginners. The temporal resolution of a normal PIV system, as operated at TUM-AER, is very low compared to the other techniques. The spatial resolution of all probes is sufficiently accurate for most flow problems. The acquisition costs for PIV and LDA is very high due to the optic and laser components. However, CTA and a fast-response probe systems are significantly less expensive. In general, for pressure probes no maintenance is needed unless very strong mechanical damage is present. However, laser/optics based methods can be very cost intensive to repair and adjust the optics when damaged or misaligned.

To sum up, fast-response pressure probes combine good characteristics of a standard probe with the ability to measure with high spatial and temporal resolution. For low-speed wind tunnel tests of external flow scenarios, it is certainly one of the easiest to use and robust measuring devices.

2.1 Multi-hole probe theory

In the subsequent sections, the working principles of pressure probes, important design criteria, the manufacturing and the fast-response probe assembly are discussed. At last, the various probe designs used in this thesis are shown.

2.1.1 Working principle of pressure probes

The working principle of (multi-hole) pressure probes is based on the stagnation of the flow around the probe, when being inserted in a fluid flow. The pressure distribution around the bluff probe body varies from the maximum pressure at the location of stagnation to lower values, that can even drop below the static pressure in the undisturbed flow far upstream of the bluff probe body. For steady, incompressible flows, the specific energy along a streamline is constant and can be described by Bernoulli's equation. At the stagnation point, maximum pressure – the stagnation or total pressure p_t – is present and equals to the sum of the static pressure p_s and the dynamic pressure far away from the probe q:

$$p_t = p_s + q = p_s + \frac{\rho}{2} U_\infty^2 \tag{2.1}$$

Here, U_∞ is the free-stream velocity and ρ the density of the fluid. Depending on the orientation of the probe towards the direction of the flow, the probe experiences the maximal pressure at different locations. Similar to the well-known Pitot probe, where the stagnation pressure is measured at a single pressure port, multi-hole probes measure the total pressure of the flow at various locations at the probe tip. The increase in the number of pressure ports, where the total pressure of the flow is acquired, leads to the possibility of characterizing the flow direction besides the velocity magnitude, which can be deduced from the pressure distribution.

Figure 2.1a shows the schematic cross-section of a multi-hole probe under an angle-of-attack. In this flow situation, the bottom and central hole would experience higher pressures than the upper hole. By measuring all pressures and setting these pressures into relation within the calibration and reconstruction step, the flow properties at the location of the probe tip can be concluded. For a five-hole probe, which can measure both, pitch and yaw, angles, the pressures are measured at the depicted pressure ports in Figure 2.1b.

Within this thesis, multiple multi-hole pressure probes are developed, calibrated and assembled for the use in unsteady flows. In contrast to steady pressure measurements, long pressure lines cannot be used to connect the probe holes to the acquisition manometers/pressure sensors as the time-dependent pressure fluctuations would be attenuated entirely. Therefore, pressure sensors are installed in close proximity to the probe tip - often in the probe shaft. The goals for the temporal characteristics are mainly defined by turbomachinery use cases with signal frequencies of up to 10 kHz. Intrusive effects and considerations towards an increased spatial measurement resolution when inserting probes in flows are taken into account by miniaturizing the fast-response aerodynamic probe (FRAP) and its shaft. Additive manufacturing enables the realization of arbitrary probe shapes.

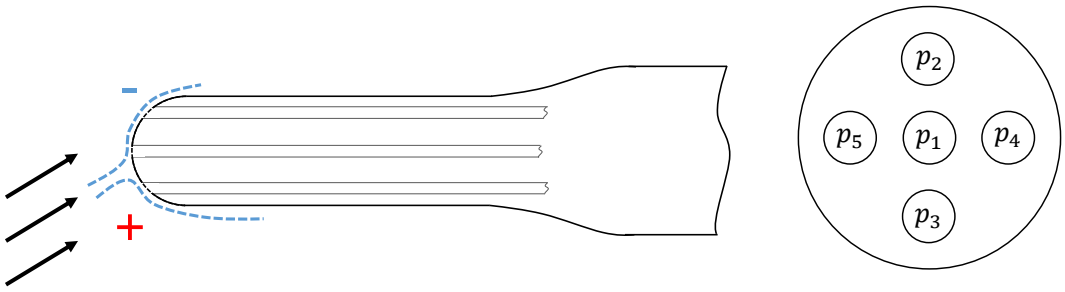

(a) Cross section of a probe with inflow under angle-of-attack

(b) Numeration of the five probe holes

Figure 2.1: Schematic sketch of a multi-hole pressure probe: a) side view and b) front view

During the calibration process of a pressure probe and the subsequent reconstruction routine, measured pressures p_1, p_2, ..., p_5 are mapped on the flow angles α and β and on the total and static pressure at the probe tip, p_t and p_s. Furthermore, by calculating the Mach number M and deducing the velocity magnitude also the velocity components $U = (u, v, w)^T$ are found. Depending on the number of pressure ports/holes, the maximum reconstruction angle is determined. Simple Pitot probes are limited to small angle ranges and solely show the total pressure and hence, the velocity magnitude when applying Bernoulli's equation. Three-hole probes can additionally acquire flow information, namely one flow angle. By incorporating even more ports, the 3D velocity vector can be reconstructed with higher resolution and range. Seven- or so-called omni-probes can resolve angles bigger than 70°. In addition, through the use of dedicated post-processing algorithms, a multi-hole probe can also be modeled by a simple single hole probe. Virtual multi-hole probes use the quasi-periodic flow behavior in known flows and are then rotated in different directions and can thus measure a quasi-3D flow through post-processing analysis.

In addition to the differences in spatial resolution due to the increase in the number of pressure ports, the influence of the probe geometry has also been extensively studied in the literature: Depending on the application and installation situation, L-shaped, straight or so-called cobra-shaped probe heads can be advantageous. Furthermore, the shape of the probe tip is also very relevant in the probe design. An overview of developments in multi-hole probe technology is given by Telionis et al. [29]. Dominy and Hodson describe the influence on multi-hole probe behavior under varying flow regimes, e.g. changing Mach number, Reynolds number or turbulence intensity [30]. They show that reconstructions accuracy of probes with different tip shapes can differ in their sensitivity due variations of the inflowing fluid. Humm investigates the influence of cylindrical stem probe head shape on aerodynamic measurements in highly fluctuating flows (turbomachinery applications) [5]. He comes to the conclusion, that circular cylinders show overall better properties than wedged probes but have downsides when being used in highly sheared flows. Crawford and Birk find that hemispherical tip shapes are ben-

eficial in most standard applications and outperform pyramidal or conical probe tip shapes [31]. This is due to a more consistent pressure distribution in inclined flow scenarios and thus show lower sensitivity towards Reynolds number variations. Therefore, all probes designed and manufactured in this thesis have exclusively hemispherical probe tips based on the findings in the literature and in-house pre-studies with different probe tip geometries.

Moreover, each probe shows different behavior due to smaller changes in the geometry or due to imperfections in the manufacturing process. Therefore, each probe has to be calibrated individually. Depending on the applied reconstruction algorithm and the calibration effort, the data reduction accuracy can be influenced. In addition to the spatial/aerodynamic calibration, for unsteady flows, it is also crucial to determine the acoustic behavior in the pressure tubings inside the probe, which connect the probe tip/pressure ports to the sensors. The determination of the behavior in this line-cavity system is investigated in the temporal/acoustic calibration.

Figure 2.2 shows a simplified external and internal view of a pressure probe assembly and is used to describe the main topics of interest when designing and assembling a multi-hole probe equipped with pressure sensors for the quantification of unsteady flow phenomena.

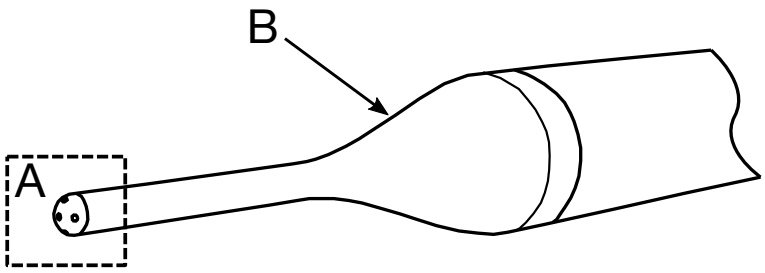

(a) External elements of interest

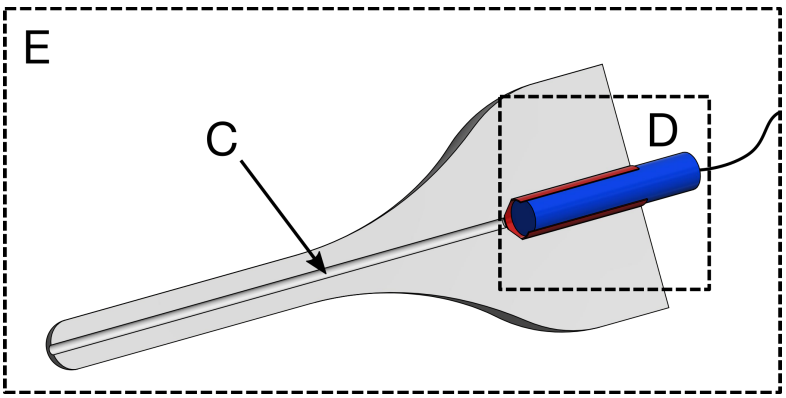

(b) Internal elements of interest

Figure 2.2: Sketch of the external and internal view of a pressure probe assembly

The following items describe the main tasks which are discussed within this thesis:

A Probe tip shape, spatial calibration and resolution.

B Additive manufacturing and mechanical restrictions.

C Line-cavity system description, temporal calibration and resolution.

D Pressure sensor choice and characterization.

E Pressure probe assembly and technical requirements.

Especially, the specification and characterization of suitable pressure sensors is of main focus and is described in detail in Sections 2.2 and 4. Furthermore, the calibration of the probe, both spatial and temporal, is investigated in Section 3. The other listed main tasks are either described in the upcoming subsections within this Chapter 2 or are also discussed partially in the following chapters.

2.1.2 Probe manufacturing and assembly

Several different design goals are pursued in the development and design of the multi-hole probe, which is intended to be used for highly unsteady flow phenomena. Often these objectives are difficult to harmonize with each other, since they have contradictory impacts on the fundamental characteristics of the probe.

Probably the most obvious design goal is the miniaturization of the probe. The narrower the size of the probe, the smaller the interfering effects in the flow when the probe is placed intrusively in the flow field. However, miniaturization is not possible without some restrictions. A suitable manufacturing method, namely additive manufacturing, allows a wide range of designs to be realized. In addition to the spatial resolution, the temporal resolution is also affected by miniaturization. For achieving a high temporal resolution, the placement of pressure sensors directly at the probe tip (flush mounted) would be the most promising approach. However, due to the physical size of the sensors, they are placed further backwards in the probe shaft and design compromises must be made. By placing the sensors slightly further back in the probe shaft, one can realize a small probe tip, consequently obtain higher spatial resolution, and still achieve high-frequency temporal resolution. However, the acoustic system between the probe tip and the sensor location must be characterized in the temporal calibration for this purpose, otherwise the measured values will be distorted. Thus, by a suitable improvement and reduction of pressure sensors, both the probe could be miniaturized and high frequency phenomena could still be detected without sacrificing temporal resolution because of the limitations due to the acoustic system. Therefore, the consideration of a sensor alternative to established pressure sensors available on the market is reasonable and will be carried out in this thesis, for example in Sections 2.2 and 4.1. Thus, the main geometric parameters that are determined in the design are the number of pressure ports, the probe tip diameter, the probe tip shape (conical, hemispherical), the probe head shape (L-shaped and straight), the probe head length, the probe shaft (length and diameter), the sensor size and, as already mentioned, the geometric parameters of the line-cavity system between tip and sensor position.

Additive manufacturing

For the manufacturing of the multi-hole probes in this thesis, the additive manufacturing *powder-bed fusion method*, more precisely the *selective laser melting (SLM)* method, is used by Vectoflow GmbH. Vectoflow GmbH is a Munich, Germany, based startup developing customer adapted pressure probe solutions and cooperated with TUM-AER within this thesis. In SLM, metal or ceramic powders are melted and sintered. Further terminologies for SLM in the literature are *direct metal laser sintering* or *laser cusing* [32]. In the SLM process, thin layers of powder are stacked on top of each other and selectively melted by a laser. Considering the design of aerodynamic probes, the narrow internal channels and the required tightness make certain manufacturing settings necessary. Layer thicknesses under 50 μm and focal laser diameters of around 100 μm provide good results with relatively small probe diameters [33]. The orientation of the probe during the additive manufacturing process is crucial to obtain a smooth surface. Furthermore, geometries with e.g. overhangs must be avoided if possible. Depending on the potentially harsh environments during probe applications, e.g. high temperatures, different materials can be used in the printing process. The materials, which can be used in the powder-bed-fusion process, have to show adequate melting and resolidifying properties [32]. Materials like titanium, Inconel 718, or stainless steel are most commonly used for aerodynamic applications [34]. For the FRAPs tested in this thesis, it was decided to use the standard alloy 316L, since no special temperature requirements were present in the wind tunnel facilities at TUM-AER. Nevertheless, there are still some limitations regarding the probe's geometry and its channel configuration when setting up the additive manufacturing process. Hence, many iterations are required to achieve acceptable results. These limitations range from powder accumulation within cavities to excessive porosity or rough surfaces in some structures [33]. Research efforts targeting those problems have enabled the manufacturing of arbitrary multi-hole probes with tip diameters of 1.2 mm and channel diameters of $D \ll 1$ mm [34].

Figure 2.3: L-shaped probe head comparison: probe after additive manufacturing (left) and after post manufacturing process (right)

After the additive manufacturing step, different details of the probe design can be realized in a post manufacturing cutting process (see Figure 2.3). Hence, for example, different probe tip shapes, which can vary from the application of the probe, or the connection to a probe holder are post-processed. Most commonly only the probe head is manufactured through SLM, since it is the critical part of the probe and sensible to geometric variations. Probe geometries can be further adopted to special measurement instrumentation. Therefore, Börner et al. realized a 3D-printed miniaturized wedge probe for transonic wake flows [35]. Furthermore, Bach et al. designed a SLM-manufactured guide vane with an integrated Kiel probe [36]. Improvements in the 3D-printing process can lead to further miniaturized probes, which reduce intrusive effects of the probe in the flow field.

Probe Assembly

The different generations of probes and the modifications made between the various prototypes are visualized chronologically in Figure 2.4. All probes have a hemispheric probe tip shape. As already discussed, hemispheric tip shapes reduce for example its sensitivity against Reynolds number changes and show good calibration/reconstruction behavior when exposed to high inflow angles.

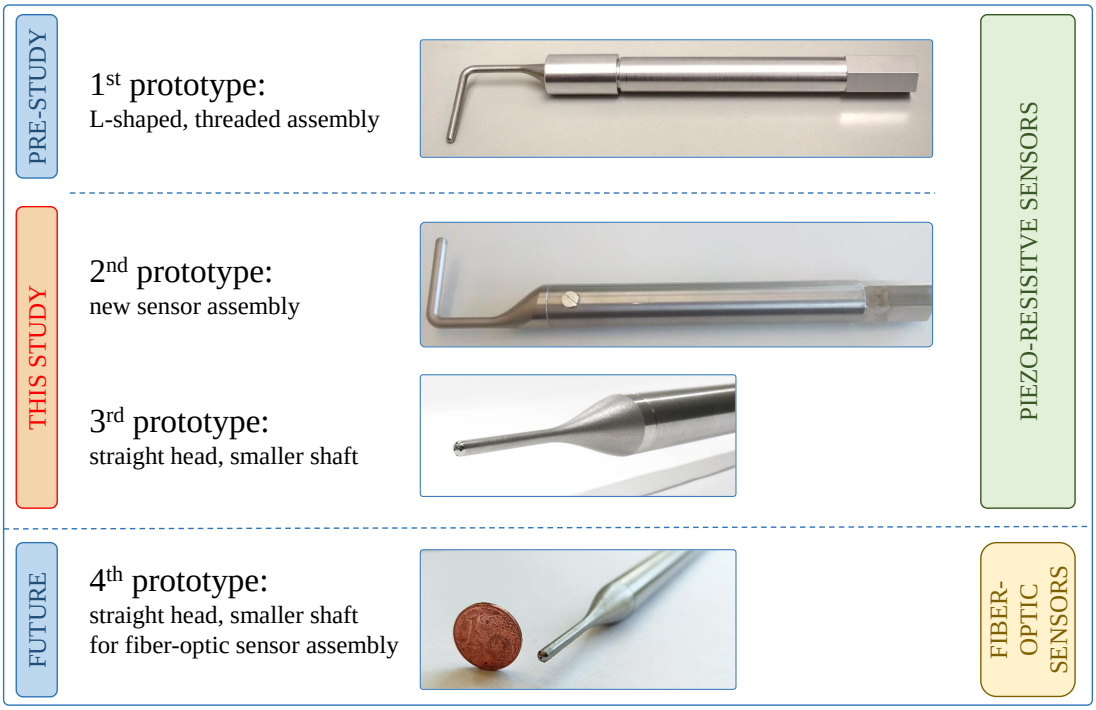

Figure 2.4: Chronological progress of the different fast-response aerodynamic probe prototypes produced in the course of the work

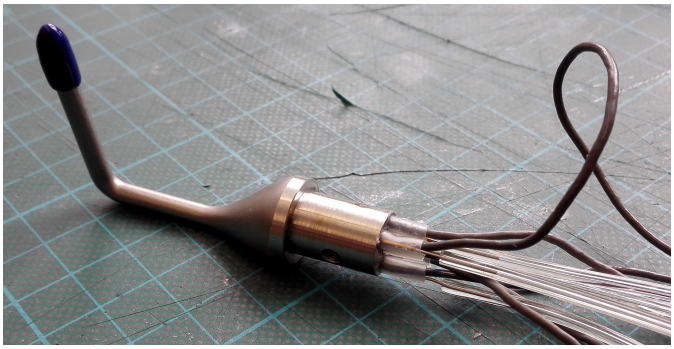

(a) Assembly: 2nd prototype and sensors

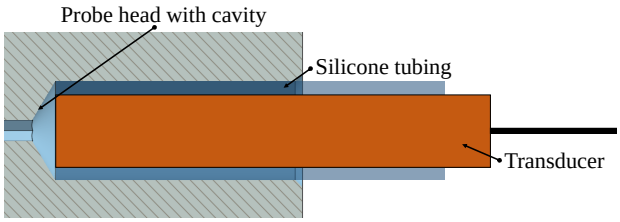

(b) Schematic visualization

Figure 2.5: Packaging problem: Sensor installation in the probe with a silicone tube

The fundamental background of the new developments is based on the preliminary research, which can be found in the respective diploma thesis by Decker [37]. The 1st prototype has a L-shaped probe head with a probe tip diameter of 4 mm. Several designs were investigated, such as the positioning of the sensor cavities in the probe shaft rather than in the additively manufactured probe head. In this case, the probe head was force-fitted onto the probe shaft with an additional screwed-on connector.

In the course of the doctoral thesis, the following prototypes were developed in co-operation with and manufactured by Vectoflow GmbH. In the second design iteration (2nd protoype), an optimized installation option for the piezo-resistive sensors was investigated on the one hand. On the other hand, the connection of the probe head and probe shaft was improved and realized by a lateral screw connection of the two parts by means of e.g. a grub screw. The L-shaped design and a tip diameter of 4 mm are chosen. The probe shaft has an outer diameter of 15 mm. At the end of the probe head, five cavities are drilled in a post-manufacturing cutting step in which the differential pressure sensors are packed. Five piezo-resistive Meggitt Endevco 8507C-2 (2 $psig$) transducers are chosen. For the packaging of the sensors inside the probe, the sensor is pressed into the cavity with a surrounding very thin silicone tubing in order to seal the probe and hence, avoid leakage (see Figure 2.5). The reference pressure lines of the five sensors are merged in a manifold. Thus, only one single pressure line is guided out of the probe.

Further miniaturization aspects were taken into account in the design of the third prototype. After measurements with the 2nd prototype showed promising results, a straight probe head was manufactured for the 3rd prototype. A further characterization of the probe and a comparison to other intrusive probes (hot wire CTA probe) is thus easier, since the probes in wind tunnel operation are usually placed in the flow with a straight probe holder construction that is fixed on a traversing system. The probe is once again equipped with the Endevco 2 *psig* sensors. The packaging is identical to the 2nd prototype. The probe tip diameter is reduced to 3 *mm*. All of the probe measurements in Chapters 5 and 6 are conducted with the 3rd prototype for the sake of consistency.

A logical next step is to further reduce the size of the probe which is only possible if the sensor size can also be reduced. The rather large sensors could, however, be placed farther away from the tip of the probe. This would be at the expense of the temporal resolution and the maximum achievable bandwidth of the probe, since the transfer function of the acoustic system between the probe tip and the sensor location would become worse. For the 4th prototype, a straight probe with reduced shaft diameter was additively manufactured, however not tested in the wind tunnel. A sensor size/cavity size of approximately 2 *mm* diameter was assumed, which corresponds to a possible sensor size of a fiber-optic sensor, see Section 2.2.2. Instead of press-fitting the sensor into the dedicated cavities in the probe head, either gluing or the use of modeling clay to fix and seal the sensor is intended. Extensive testing and validation of the probe with fiber-optic sensors will have to be performed in the future.

2.2 Pressure sensor fundamentals

In order to measure the physical quantity – the pressure – it must be converted to a measurable signal (e.g. a voltage) in a sensor. In the past, manual pressure gauges were used to read a known liquid displacement on a pre-calibrated scale, for example. Nowadays, however, transducers are used that transmit a digital output signal with the aid of suitable measurement technology. Unlike steady pressure probes, where time-averaged pressures are measured at distant pressure sensors connected to the probe by long tubes, FRAPs use sensors inside the probe. As explained in the previous section, this is due to the fact that the temporal signal of the pressure inside the probe channels is changed by acoustic effects (resonance and attenuation). It is therefore crucial that the distance between the probe tip and the location of the sensor is minimized in order to reduce this effect. The choice of the right sensor, speaking of its geometric properties and especially its specifications is of enormous significance when building a fast-response probe. In the following section, an introduction to pressure sensor basics is given, followed by a more detailed analysis of piezo-resistive pressure sensors. However, the main focus lies on the theoretical working behavior of fiber-optic pressure sensors, which are based on a Fabry-Pérot interferometer.

To begin, an initial segmentation is performed in three main measurement types, as visualized in Figure 2.6. In an absolute pressure sensor, the reference pressure p_0 is set to be (almost) vacuum. The sensor is exposed to the flow on the outer side,

while the medium inside the sensor is sealed. The gauge sensor measures the pressure relative to the surrounding/atmospheric pressure p_∞. The outer side of the membrane is again exposed to the flow of interest. On the contrary, the inner part is vented to the atmosphere with a pressure line. A differential pressure sensor takes the idea of a gauge sensor one step further, by pressurizing the sensor with a pre-defined reference pressure p_{ref} in the inner side of the membrane.

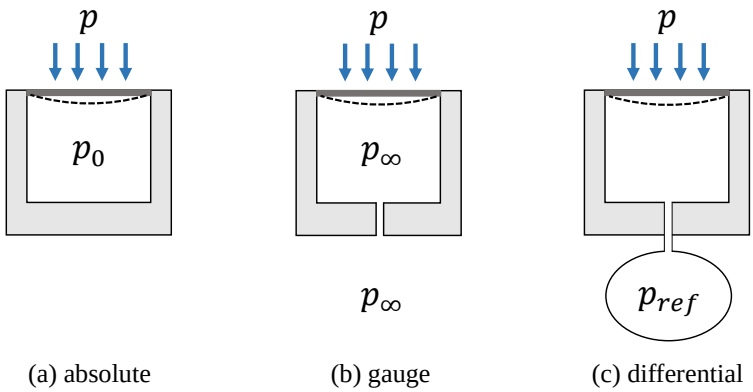

Figure 2.6: Pressure sensor types

For the integration of the sensor into a probe in a wind tunnel environment, an absolute sensor is not necessarily required, since the static/atmospheric pressure in/near the wind tunnel test section is usually known and also measured. By using a gauge sensor, the overpressure can be determined, which corresponds approximately to the dynamic pressure when the probe is exposed in the flow. In addition, a higher resolution is obtained when using a gauge sensor, since the pressure range only has to represent the possible overpressure.

Pressure sensors can be also separated by the involved technology that is used: As already described, pressure gauges measuring liquid displacements were used in the past to provide information about the applied pressure. Nowadays, electronic pressure sensors are used almost exclusively, e.g. resistive, piezo-resistive, capacitive, or piezo-electric ones. The respective sensor technologies all have their justification and can be selected on the basis of their specification for the appropriate measurement task. Key parameters are the measuring range, the measuring accuracy, sensitivities to (external) influences, the measurable bandwidth/response time or the natural frequency of the sensor/sensor membrane. The characterisation of some of these factors and the importance of some others are also addressed in chapter on measurement resolution and uncertainty, Chapter 5.

In the following sections, the pressure sensor technologies/designs used in this work are explained in more detail. On the one hand, piezo-resistive pressure sensors are briefly introduced, which can be regarded as the state-of-the-art technology. On the other hand, fiber-optic sensors are thoroughly discussed, which were developed in the course of this thesis in a collaboration by the company fos4X GmbH.

2.2.1 Piezo-resistive sensors

As a baseline/reference for the development of the fiber-optic differential pressure sensors, the commercially available state-of-the-art solution, namely piezo-resistive sensors, is introduced. This should give an impression of the advantages and disadvantages of this type of sensor and defines target specifications for the fiber-optic sensor. More information on piezo-resistive sensors is e.g given in Regtien and Dertien [38].

The working principle of a piezo-resistive sensor is illustrated in Figure 2.7a. Due to an applied pressure on the outer side of the membrane, the sensor membrane will be deformed. Therefore, bending stresses and, hence, changes in electrical resistivity of the sensor material due to the piezo-resistive effect appear. Those changes can be directly linked to the applied pressure. A Wheatstone bride is embedded in the piezoresistor membrane which is often made out of silicon. The change in resistance of the bridge leads to a change in the output voltage V_{out} (see Figure 2.7b).

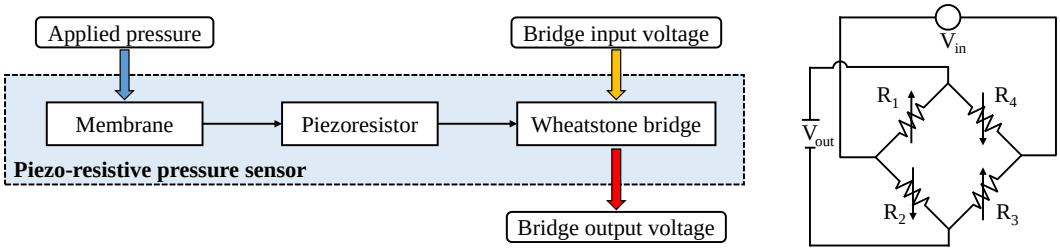

(a) Working principle **(b)** Circuit

Figure 2.7: Schematic working principle of a piezo-resistive sensor

Even though piezo-resistive sensors are easy to use and the state-of-the-art solution for pressure measurements, there are several downsides arising from the type of operation of the sensor: Due to the use of electronic (semiconductor) components, piezo-resistive sensors exhibit non-negligible cross-sensitivities to external influences such as temperature or humidity variations or electro-magnetic disturbance. In a calibrated specified temperature range, the components of the sensor are temperature compensated. This can be a plus, when using the sensor solely in this range, but can be crucial if temperatures outside this range are present. Moreover, the Wheatstone bridge has to be operated actively. An input voltage must always be applied and thus supplies the Wheatstone bridge. Due the spatial restrictions inside a pressure probe, the wiring of the multiple sensors is time-consuming and complex. Furthermore, the active operation of the sensor can also lead to cross talk and therefore increase the noise level of multiple sensors applied in close proximity to each other. Commercially available differential sensors are seldom smaller than 2-3 mm in diameter, considering the desired pressure range of up to 2 $psig$ for low-speed wind tunnel use-cases.

2.2.2 Fiber-optic sensors

One objective of the present thesis is to evaluated the possibility of applying fiber-optic pressure sensors in multi-hole probes as an alternative to state-of-the-art piezo-resistive sensors. Since the current state of development is still in the early stages, the first development steps have been initiated and basic tests have been carried out to specify the sensors within this thesis. In the following, the underlying theory of fiber-optic sensors will be discussed in more detail. In addition, the development steps in the course of the project will be outlined. The development was accomplished by the Munich-based company fos4X GmbH (now: Polytech A/S). Through constant cooperation (e.g. a joint student project [39]), first successes and ready-to-use sensor prototypes could be manufactured. The tests and characterization of the sensors can be found in Section 4.1.

Optical principles are applied to surpass the limits of conventional electrical pressure transducers with respect to resolution and cross-sensitivities. The characteristics of the optical sensors are expected to outperform state-of-the-art piezo-resistive sensors. In previous developments, fos4X GmbH has developed a durable pure glass absolute fiber-optic pressure sensor for surface pressure measurements [40–42]. The cuboid pressure sensor, which is wall mounted, operates without any conductive material. Due to its absence, the sensor is inherently immune to electro-magnetic interference. It is robust against water, humidity, and corrosion. The miniature sensor with dimensions of $1.6 \times 3 \times 10\ mm^3$ is capable of measuring aerostatic, aerodynamic and aeroacoustic events as a pressure sensor and as a microphone at the same time [40]. The flat design allows for integration in surfaces with minimal aerodynamic disturbance of the air flow. The fully exposed membrane of 1.65 mm diameter at the surface of the sensor enables pressure measurements without any spectral characterization, because of constant frequency response to 80% of the natural frequency of 250 kHz [40, 41]. In contrast to the existing cuboid absolute pressure sensor, a cylindrical, differential pressure sensor suitable for the application in multi-hole probes is developed and tested.

Fiber-optic pressure measurement theory

Basically, two measurement methods of fiber optic sensors can be distinguished: intrinsic and extrinsic sensing. In contrast to intrinsic measurements, where the light is modulated inside the fiber, extrinsic sensing involves the light exiting the fiber and being modulated outside in an off-fiber transducer [43]. After the light was modulated outside the fiber, it is either guided to a sensing device through another fiber or the original fiber. The modulation of light can be categorized into a modulation of intensity, phase, spectrum, polarization or frequency. In the intrinsic method the optical properties of the fiber itself are changed due to e.g. deformation of the fiber by external impact (e.g. temperature and pressure). An example for an intrinsic sensing is the fiber Bragg grating (FBG), where a variation of the refractive index is achieved by inscribing/grating directly into the fiber. An example for extrinsic sensing is the Fabry-Pérot interferometer and is described in more detail later, since it's the sensing method of choice in the manufactured fiber-optic pressure sensors in this thesis.

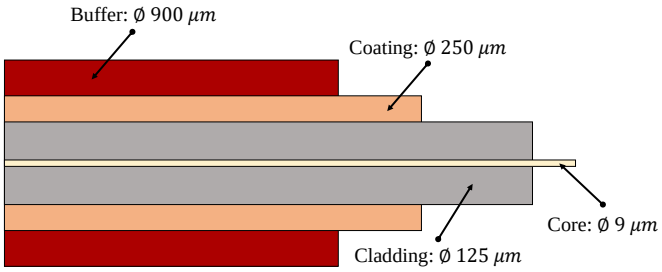

Figure 2.8: Schematic assembly of a single mode fiber

The most important component of fiber optic sensor technology is the optical fiber itself. This fiber assembly consists of the core, i.e. the transmission medium in which the light wave is guided, and the cladding. In addition, other components like buffers, coating material and additional layers providing extra strength solely add extra life expectancy but do not contribute to the transmission or modulation of the light signal [44]. A schematic drawing of the fiber assembly is given in Figure 2.8.

The fos4X GmbH sensors use standard telecommunication fibers, hence, single mode fibers. Single mode fibers have a rather small core diameter of a few micrometers, here approximately 9 μm, only transmit one light mode, and therefore, show greater bandwidth compared to multi-mode fibers (multi-mode step and graded index fibers) and experience low attenuation. However, due to the small core diameter the connection to light sources and within fiber couplings has to be addressed carefully [44].

The advantages of fiber-optic sensors over standard piezo-resistive sensors are manifold. The biggest advantage is probably the robustness against parasitic electromagnetic fields. Problems such as cross talk experienced by electrical sensors are therefore eliminated. Due to the employed materials, an increased temperature range, in which the sensor shows only low temperature sensitivity, is expected in future development steps (more on this in the later paragraph on sensor manufacturing). A summary of the key advantages of fiber-optic sensors compared to state-of-the-art piezo-resistive sensors is shown in Table 2.2 (adapted from Kienitz et al. [42]).

Fabry-Pérot sensor basics: Sensor working principle and data acquisition

In general, a fiber-optic pressure transducer at the end of a common telecommunication fiber works similar to their electrical counterparts: The fiber-optic sensor is a passive micro-opto-electro-mechanical-system (MOEMS) glass chip, which consists of a diaphragm/membrane, a resonance cavity and two mirrors. One mirror is attached on the diaphragm, while the second is half transparent and fixed. An applied pressure Δp bends the diaphragm and changes the cavity length L_c between the two mirrors by ΔL (see Figure 2.9). The end of the fiber and the inner part of the membrane represent the two mirrors.

The deflection ΔL due to the applied pressure Δp can be expressed with respect to the membrane radius r_m and thickness h_m, the material Poisson's ratio ν and the Young's

Table 2.2: Benefits of fiber-optic sensors over state-of-the-art piezo-resistive sensors, adapted from Kienitz et al. [42]

Fiber-optic sensor	Piezo-resistive sensor
High overload pressure: burst pressure > 30x full scale	Burst pressure > 3x full scale
Flush surface membrane	Protective mesh on top of membrane, reduction of bandwidth
Passive design, no electromagnetic coupling	Possible deviations by electromagnetic field or effects like cross talk
Ready for harsh environment	Limited usability e.g. in wet or humid flows
Low temperature dependency	High temperature dependency

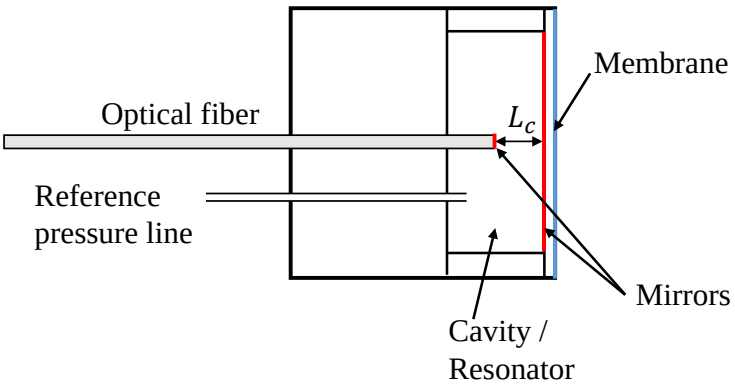

Figure 2.9: Schematic design of a differential fiber-optic pressure sensor; mirrors marked in red, membrane depicted in blue

modulus E [41, 45]:

$$\Delta L = \frac{3r_m^4(1-\nu^2)}{16Eh_m^3}\Delta p = \frac{r_m^4}{64K} \tag{2.2}$$

Hence, the bending stiffness K can be also expressed by the membrane geometric and material properties (see Hill et al. [46]):

$$K = \frac{Eh_m^3}{12(1-\nu^2)} \tag{2.3}$$

Thus, the performance of the measurement system, e.g. its sensitivity, is predominantly defined by the mechanical displacement of the membrane. The miniaturization of the sensor design will therefore considerably affect the sensitivity.

The sensor natural frequency f_n, as a limit of the sensor frequency response, can be estimated with the following equation, also considering the membrane material density ρ:

$$f_n = \frac{\lambda_i}{2\pi r_m^2}\sqrt{\frac{K}{h_m\rho}} \tag{2.4}$$

Yalcin et al. [47] give analytically derived approximations for the coefficients λ_i. For the first membrane bending, the first harmonic $i = 1$, the data from the literature gives $\lambda_1 = 10.22$.

The measurement principle of the sensors is based on the superposition of optical waves interfering in the sensor cavity: a Fabry-Pérot interferometer. A broadband infrared light source illuminates the transducer from the fiber-optic cable. Optical interference modulates the reflecting light spectrum depending on the cavity length and therefore, the deflection of the membrane due to the applied pressure. Each wavelength λ of incoming light, which fulfills the Fabry-Pérot resonance condition, being an integer multiple N, will interfere destructively [44, 48]:

$$N\lambda = 2n(L_c + \Delta L) \tag{2.5}$$

Here, n depicts the refractive index of the medium (air) inside the cavity and staying constant over time. The ratio of the reflecting light spectrum I_R to the incoming light spectrum I_0 is depending on the phase δ and the mirror reflection coefficients R_1 and R_2 and can be calculated as follows [46, 48, 49]:

$$\frac{I_R}{I_0} = \frac{M + F\sin^2(\delta/2)^2}{1 + F\sin^2(\delta/2)^2} \tag{2.6}$$

$$with \quad \frac{\delta}{2} = \frac{2\pi}{\lambda}n(L_c + \Delta L) \tag{2.7}$$

Here, F is the coefficient of finesse, which describes the quality of the Fabry-Pérot filter and can be calculated as:

$$F = \frac{4\sqrt{R_1R_2}}{(1-\sqrt{R_1R_2})^2} \tag{2.8}$$

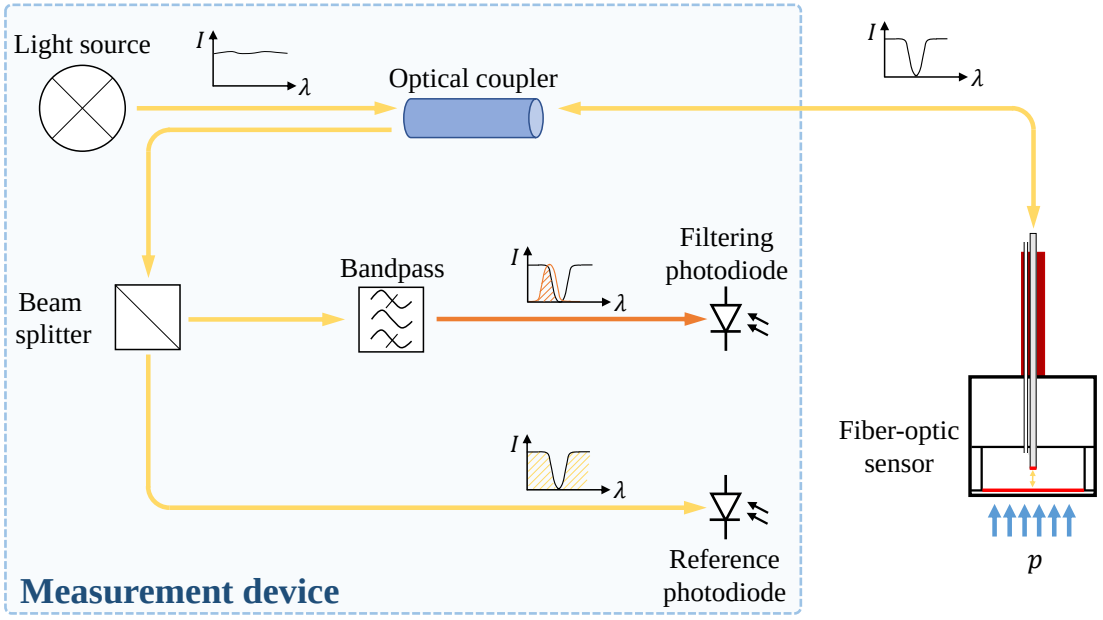

Figure 2.10: Schematic visualization of the fiber-optic measurement system and the light path through the edge-filter interrogator (based on Kienitz et al. [42])

The coefficient M refers to the "mismatch" of the reflectance values in the interferometer [50].

$$M = \frac{4\sqrt{R_1}\sqrt{R_2}}{1 - \sqrt{R_1 R_2}} \tag{2.9}$$

Since the spectrum is modulated outside the fiber, the sensor setup is referred to as an extrinsic fiber Fabry-Pérot interferometer. An increasing cavity length shifts the phase condition of the destructively interfered wavelength in the spectrum to larger wavelengths, while a smaller cavity length shifts the spectrum to smaller wavelengths [42, 51]. The modulated light is guided back in the same single fiber to the optical measurement device, the edge-filter interrogator, where it is split in two parts. While the first part is focused directly on a photodiode, the second part is optically filtered depending on the wavelength λ by an optical filter with a transmission spectrum $T(\lambda)$ and focused on a second photodiode (see Figure 2.10).

Thus, the measured light intensity ratio ρ_{opt} is the final measurand and is calculated as follows [49, 50]:

$$\rho_{opt} = \frac{\int_{\lambda_{min}}^{\lambda_{max}} I_R(\lambda) I_0(\lambda) T(\lambda)\, d\lambda}{\int_{\lambda_{min}}^{\lambda_{max}} I_R(\lambda) I_0(\lambda)\, d\lambda} \tag{2.10}$$

The reflected spectrum of the sensor is matched to the operating point of an edge-filter interrogator, also known as the quadrature Q-point of the device [50, 52]. Therefore, the edge-filter interrogator is filtering a single destructive interference in the optical spectrum in the C-band [40, 41]. The output of the measurement ρ_{opt} is set to be linear

near the Q-point of the sensor. The correlation of ρ_{opt} and the applied pressure can be determined in a sensor static calibration revealing its pressure sensitivity k_p, with an optical output value $\rho_{opt,0}$ for no applied pressure:

$$p = (\rho_{opt} - \rho_{opt,0}) \cdot \frac{dp}{d\rho_{opt}} = (\rho_{opt} - \rho_{opt,0}) \cdot k_p^{-1} \tag{2.11}$$

The optical filtering process ensures sampling frequencies up to $f_s = 50\ kHz$. Each analog signal is converted to a digital value by an analog to digital converter.

Sensor design, manufacturing and assembly

In the development process within this thesis, multiple iterations of gauge/differential fiber-optic pressure sensors have been developed by fos4X GmbH (see Figure 2.11).

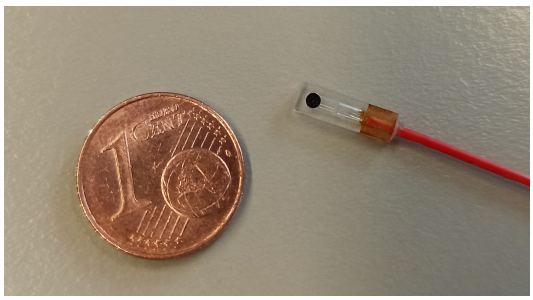

(a) Cuboid, absolute pressure sensor for flush surface mounting

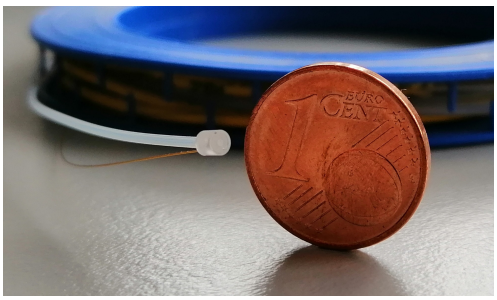

(b) Qualitative size comparison of a 1st gen sensor prototype and a Euro cent coin

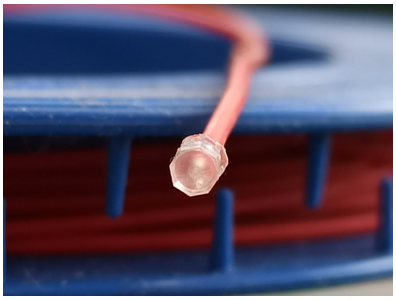

(c) 2nd generation differential pressure sensor

Figure 2.11: Various fiber-optic sensor generations

As stated in the previous section, the sensor working principle is based on the Fabry-Pérot interferometer. The fiber-optic sensor casing and membrane are fabricated out of two fused silica (SiO_2) wafers in order to reduce thermal sensitivities and have a very small coefficient of thermal expansion. In a first step, the three dimensional sensor inner structure is inscribed into the quartz glass wafer by pulsed laser radiation and thereby changes the glass properties [53–55]. In the next step, by introducing wet-chemical etching solvent, the irradiated material is washed out, which is called selective laser etching

(SLE). In order to have the same material properties as the sensor, a second very thin wafer representing the membrane is laser-welded on the sensor casing. Furthermore, a light diffusor is inscribed on the outside of the membrane. In the penultimate step, the outer sensor shape is either etched or cut. In the last processing step, the optical fiber is fixed to fit the Q-Point of the measurement device in the micromachined sensor. A capillary is bonded to either pressurize the cavity and therefore measure the differential pressure or work as a gauge sensor with the surrounding static pressure as the reference pressure (see Figure 2.9). In Figure 2.11, various fiber-optic sensor generations are displayed. Developments started with a cuboid, absolute pressure sensor for flush surface pressure measurements as discussed in Kienitz et al. [42]. However, for a higher measurement resolution and for a better possibility of exchange with state-of-the-art cylindrical piezo-resistive sensors, a cylindrical shape is desired. Therefore, the fiber-optic pressure sensor of the 1st generation comprises the desired specifications (see Figure 2.11b) [39]. It has a diameter of 2 mm and is operated as a differential/gauge sensor by having a reference pressure line installed in the sensor casing.

In Figure 2.12a, a sketch of the 2nd generation fiber-optic pressure sensor is shown, whereas in Figure 2.11c the actual sensor is depicted.

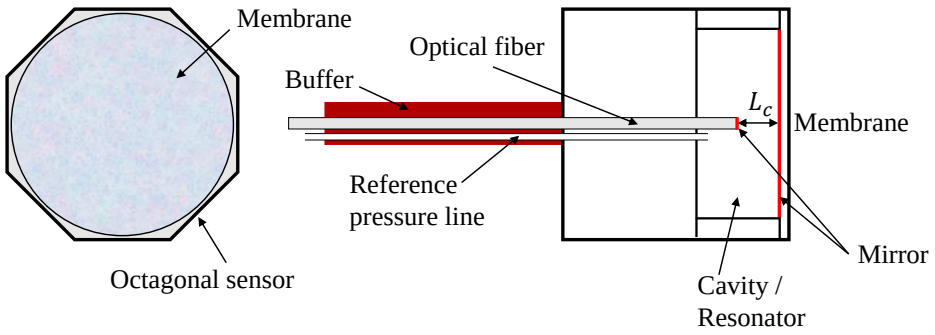

(a) 2nd generation sensor design

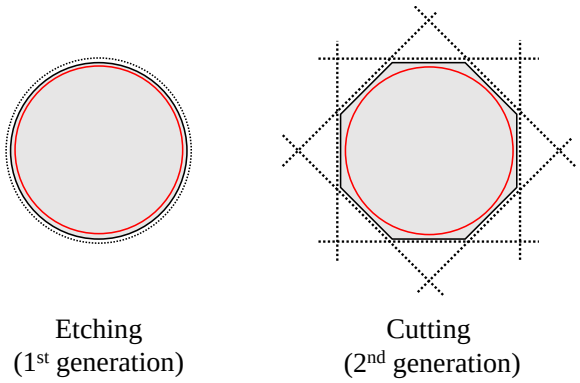

(b) Comparison of sensor outer shape

Figure 2.12: Sketch of the fiber-optic differential pressure sensor (FOPS)

The use of cutting in the manufacturing process of the sensor outer shape compared to the additional etching iteration leads to less scrap and has therefore been applied in the 2nd generation of sensors. Due to these manufacturing benefits, an octagonal shape is chosen (see Figure 2.12b). In addition, also tolerances in the fiber inlet should reduce the influence of the epoxy on e.g. the thermal stability. Furthermore, a bigger buffer is applied around the fiber and the pressure line for improved mechanical stability.

In Section 4.1, multiple tests to characterize the sensor behavior are discussed. Sensors of both sensor generations (1st and 2nd) are used.

3 Probe calibration and reconstruction process

In order to determine the flow quantities at the probe tip, the correlation between the sensor measurands and the flow quantities must be determined. This is achieved by a calibration procedure for the pressure probe. In an experiment with unknown flow conditions, the calibration data are used to reconstruct the flow properties the probe detects. In the calibration process, a separation of the spatial and temporal behavior of the probe is assumed. Therefore, besides an spatial/aerodynamic calibration, a temporal/dynamic calibration has to be conducted as well. In the spatial calibration, the time-averaged pressures measured at the pressure ports are correlated with the time-averaged flow properties (flow angles α and β and the flow velocity magnitude U_∞). Moreover, the temporal calibration characterizes the acoustic line-cavity-system in the channels between the tip and the sensors. Figure 3.1 schematically shows the procedure of the calibration and reconstruction steps. Both calibration and reconstruction approaches are described in detail in the following sections.

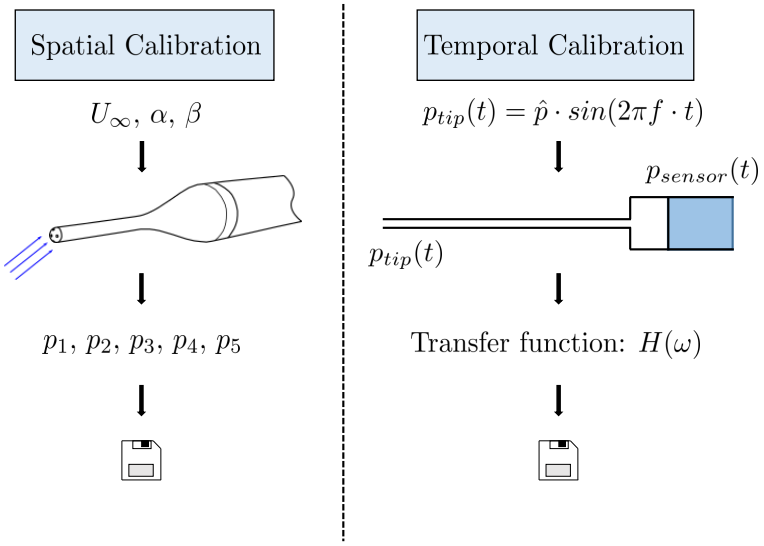

Figure 3.1: Calibration concept: Separation of the spatial/aerodynamic and the dynamic/temporal calibration

3.1 Spatial calibration in a free-jet wind-tunnel

For the spatial calibration, the probe is inserted into a known flow field in a free-jet wind-tunnel. By setting different angles and flow velocities in the wind tunnel, a large set of various combinations of pressure data which can be correlated to the flow field can be acquired. Besides uncertainties in the acquisition of pressure data and the wind-tunnel setup, the major driver for more accurate post-processing results is the applied reconstruction approach. In the following subsections, the basic theory of pressure probe calibration and its influencing factors are discussed. Most commonly, interpolation approaches are used to obtain the flow characteristics at the probe tip out of the five measured pressures. Furthermore, non-standard approaches are promising for an accurate reconstruction, for example system identification methods, like artificial neural networks, or the application of Bayesian statistics, in form of Gaussian process regression. Throughout the thesis, multiple equivalent formulations will be used for the post-processing step: reconstruction or data reduction. The overall calibration and reconstruction routines are visualized in the following flow chart in Figure 3.2, which should also demonstrate the interchangeability of different reconstruction approaches applied at TUM-AER.

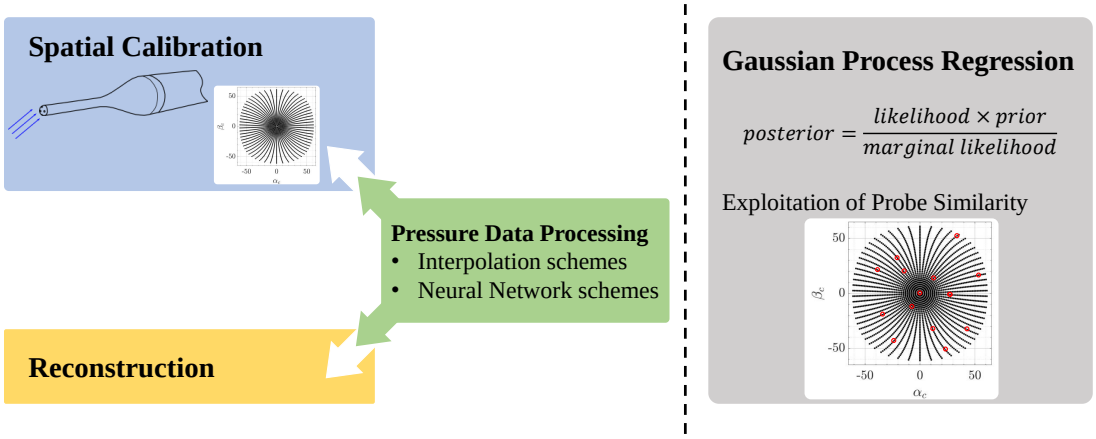

Figure 3.2: Overview of the presented spatial calibration approaches

3.1.1 General theory

In this section, a brief outline regarding the motivation of an experimental calibration task will be given. This is followed by a description of the experimental facilities and a clarification of the used coordinate system. In the subsections 3.1.1.1 and 3.1.1.2, the standard implemented data reduction approaches within this thesis are described.

The flow around bluff bodies has been investigated extensively analytically, experimentally, and numerically. From the steady, incompressible potential flow theory in axisymmetric flow, the velocity on the surface of a sphere $V(\theta)$ as a function of the cone

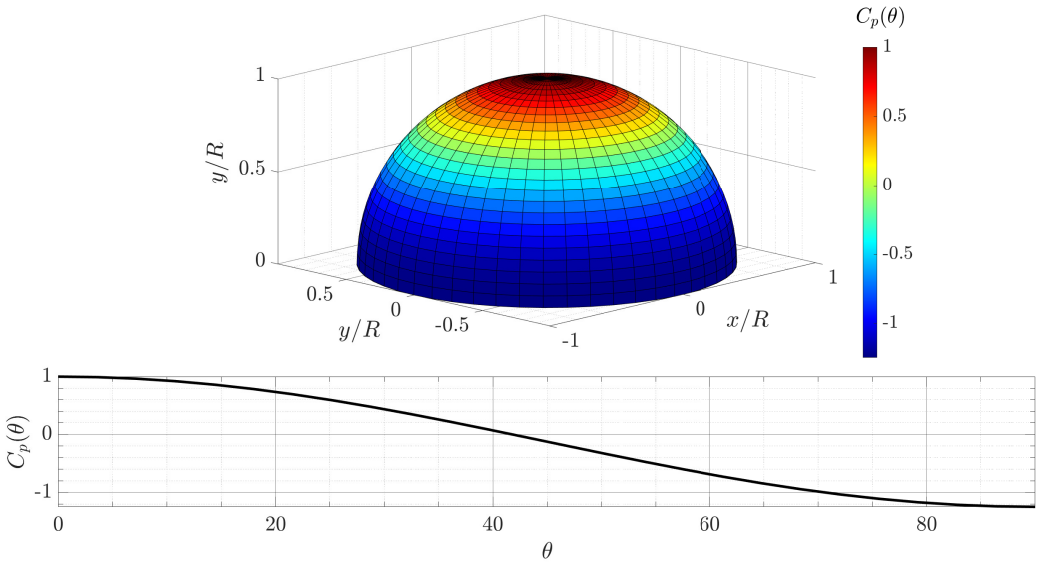

Figure 3.3: Pressure coefficient distribution C_p around a sphere as a function of the cone angle θ calculated with the incompressible potential flow theory

angle θ can be deduced from superposing a free stream flow U_∞ and a doublet flow:

$$V(\theta) = \frac{3}{2} U_\infty sin(\theta) \tag{3.1}$$

Incorporating Bernoulli's equation

$$p + \frac{1}{2}\rho V^2 = p_s + \frac{1}{2}\rho U_\infty^2 \tag{3.2}$$

with the local pressure p and calculation the pressure coefficient

$$C_p = \frac{p - p_s}{\frac{1}{2}\rho U_\infty^2}, \tag{3.3}$$

the axisymmetric pressure distribution $C_p(\theta)$ on a sphere reads:

$$C_p(\theta) = \frac{9}{4} cos^2(\theta) - \frac{5}{4} \tag{3.4}$$

This formulation serves as a first, idealistic guess for the pressure distribution on a pressure probe (see Figure 3.3). Nevertheless, since a) potential flow cannot be assumed when measuring real flows in wind tunnels, b) the dimensions of the probe differ from a sphere, c) the manufacturing of the probe having inaccuracies regarding symmetry and surface accuracy and d) the probe being exposed to (unsteady) flow phenomena, influencing the flow around the probe, a more precise and experimental acquisition of the pressure distribution around the probe is needed. A detailed analysis of the errors

Figure 3.4: Free-jet calibration facility at Vectoflow [34]

Table 3.1: Specifications of the Vectoflow GmbH calibration wind tunnel [34].

Velocity range	$M \leq 1.2$
Maximum power	90 kW
Angle range	$\pm 165°$ (yaw), $\pm 180°$ (roll)
Temporal speed non-uniformity	$\pm 0.25\%$ at $M = 0.1$
Nozzle diameter	$30 - 200$ mm

made, when relying on potential flow or numerical simulation instead of the actual experimentally acquired calibration characteristics, will be given in Section 4.2.1, which is dealing with numerical simulation of the flow around a straight pressure probe.

As already mentioned, in order to determine the actual flow conditions at the probe tip in an experiment, the acquired pressures have to be processed via a data reduction approach. Before delving into the mathematical expression of the reduction step, the calibration wind tunnel setup is shown and prerequisites are discussed.

Since the correlation between the mean free-stream flow conditions and the measured pressures at the probe have to be determined in the spatial calibration, various combinations of the free-stream velocity U_∞ and the flow angles α and β are set in the free-jet calibration wind tunnel. In this thesis, the major part of the calibration investigations have been executed in the calibration wind tunnel at Vectoflow GmbH [34]. In addition, a smaller calibration test rig adapted on a hot-wire calibration free-jet wind tunnel is used. The Vectoflow wind tunnel is illustrated in Figure 3.4.

In Table 3.1 the main specifications of the calibration free-jet facility are listed. Depending on the maximum calibration velocity (up to $M \leq 1.2$) and the probe size, different types of nozzles can be installed. The traversing unit moves the probe to match the dedicated calibration grid angles. Further details on the the calibration accuracy and uncertainties within the calibration process are given in Section 5.2.

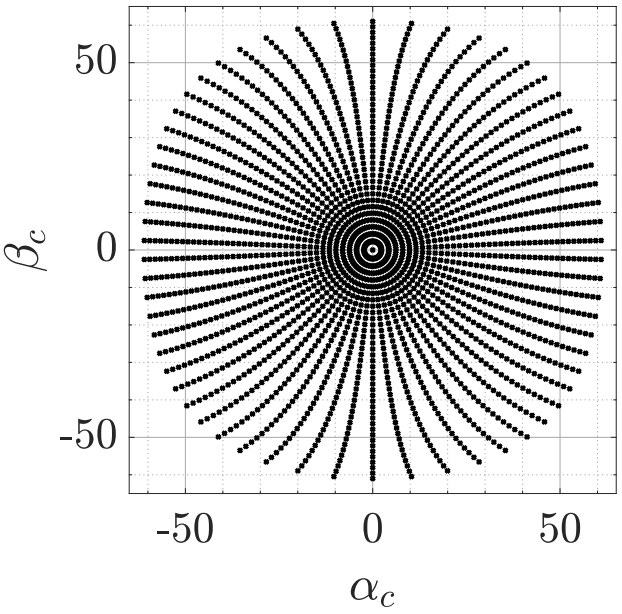

Figure 3.5: Calibration grid for $\alpha, \beta = \pm 60°$

Depending on the expected angle and velocity range the probe is exposed to in later experiments, angle combinations at specified velocities are calibrated. Figure 3.5 shows the calibration grid for the straight five-hole fast response probe, which is used for most of the experiments. This grid contains around 1000 points, with angles up to $|\alpha_c| = |\beta_c| = 60°$. In general, for an improved reconstruction accuracy, multiple velocities and a refined angle grid are calibrated.

The positioning of the probe can be described in two interchangeable coordinate systems, which are shown in Figure 3.6. The pitch(α)-yaw(β)-system can be transferred into the roll(ϕ)-cone(θ)-system by applying the following equations:

$$\alpha = \arctan\left(\tan(\theta)\sin(\phi)\right) \tag{3.5}$$

$$\beta = \arcsin\left(\sin(\theta)\cos(\phi)\right) \tag{3.6}$$

$$\theta = \arccos\left(\cos(\alpha)\cos(\beta)\right) \tag{3.7}$$

$$\phi = \arctan\left(\sin(\alpha)/\tan(\beta)\right) \tag{3.8}$$

For the description of the interpolation data reduction approach, both systems will be relevant and are therefore introduced here.

3.1.1.1 Interpolation schemes

At the beginning of this section, a brief literature review is given, discussing various important data processing approaches which base on interpolation schemes. The first notable studies have been published in the 1970's. New advances in the determination

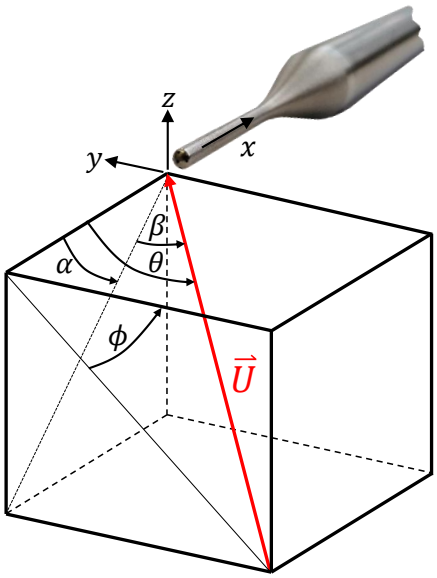

Figure 3.6: Schematic demonstration of the two interchangeable coordinate systems

of a fast and accurate reconstruction routine have lead to more recent publications. In most of the approaches non-dimensional calibration coefficients are calculated, which are the basis for the interpolation. Depending on the probe type, i.e. the number of pressure ports, the probe geometry, multiple coefficients for flow angles and for pressures are determined. The various publications often use polynomial based (global) interpolation approaches. Besides global interpolation approaches, local interpolation methods with an additional segmentation in various calibration flow regions/zones have been introduced, in order to enlarge the angular calibration range.
Starting in the mid 1970's, Bohn and Simon introduced a multi parametric approximation of calibration surfaces for multi-hole probes [56]. They defined non-dimensional angle coefficients, k_α and k_β, and the Mach number coefficient k_M and determined free parameters which contribute to polynomial function fits for each coeffient $f(k_M, k_\alpha, k_\beta)$. In order to extend the angular reconstruction range, Ostowari and Wentz reformulated the coefficient definition by taking the windward pressure port as the reference port instead of the stalled mid port [57]. Various further approaches deal with polynomial functions to describe the relation between pressure coefficients and the flow properties: Everett et al. apply three-variable third order polynomial functions representing the flow quantities for seven-hole probes [58], whereas Lee and Wood use an interpolation of 2D spline curve fitting data [59]. In the approach by Gameiro Silva et al., a linear interpoaltion of calibration data of a seven-hole probe is compared to a fourth order polynomial fit method [60]. Benay's reconstruction method is based on a global interpolation for seven-hole probes by using the Levenberg algorithm for the minimization procedure and a spline interpolation [61].
In addition to the definition of arbitrary coefficients, some authors considered theoretical

knowledge of potential flow: Houtman and Bannink deduced their method from potential flow and compressibility effects considerations [62]. Similar to the approaches discussed before, they then used a polynomial interpolation with constants derived from a least-squares method fit and performed a local interpolation with calibration data surrounding the test point. Likewise, Kjelgaard derived equations from potential flow theory over a sphere and approximated the probe behavior with a third order polynomial fit [63]. Furthermore, Pisasale and Ahmed followed a similar strategy by introducing theoretical knowledge into the relationship between the port pressures and the fluid properties from potential flow considerations [64, 65].
In order to enlarge the angular reconstruction range, various works deal with zoning/segmentation methods, which separate the flow behaviour around the probe and the definition of the respective calibration coefficients depending on the pressure port measuring the highest pressure in situations of higher flow angles: Zilliac and Field describe the calibration procedure and error analysis of a seven-hole probe. They use a sectional division and derive 28 coefficients [66, 67]. Thereby, they apply the Akima direct interpolation (see Akima [68]) and 5th degree interpolation polynomials with continuous first derivatives. Venkateswara Babu et al. also divide the seven-hole probe calibration data in zones and describe the data with a localized two-variable polynomial with surrounding points [69]. Furthermore, they use a zone extension approach that decreases the amount of points for the interpolation step compared to e.g. Everett [58], and hence, reduce the complexity of the problem. Argüelles Diaz et al. discuss the extension of the calibration angular range by zoning for a three-hole cylindrical probe [70]. In the study by Paul et al., a summary of various pressure normalization and data reduction methods, which also were named in the literature review in this section, is given [71]. Moreover, they compare a 4th order polynomial fit and the aforementioned Akima direct interpolation and also discuss a coefficient definition emphazising the importance of the central pressure port.
In addition to the enlargement of the angular range, the evaluation of sensitivities in various flow regimes is of great significance: Treaster and Yocum discuss Reynolds number and wall proximity effects of five-hole probes by introducing correction factors in their calibration, and define four non-dimensional pressure coefficients in an angular range of $\pm 30°$ within their non-nulling probe calibration approach [72]. Likewise, Smith and Adcock investigate Reynolds number and Mach number sensitivity of various multi-hole probes [73]. In the study by Clark et al., different formulation of non-dimensional calibration coefficients are given and their sensitivity to Mach number changes and measurement errors are discussed [74]. Furthermore, Ericksen et al. investigate the sensitivity of the reconstruction accuracy depending on the calibration test matrix size [75].
Besides the different concepts outlined so far, there are other studies that follow different reconstruction methodologies: Wenger and Devenport apply a two step calibration scheme. In addition to a least-squares curve fit with a higher order polynomial, lookup error tables are used to deduce the error of test point reconstruction with a polynomial of lower order [76]. In contrast to the definition of port pressure difference, Yasa and Paniagua directly handle the port pressures without taking left-right differences [77, 78]. By doing that, also in situation of blocked pressure ports, a reconstruction of the flow

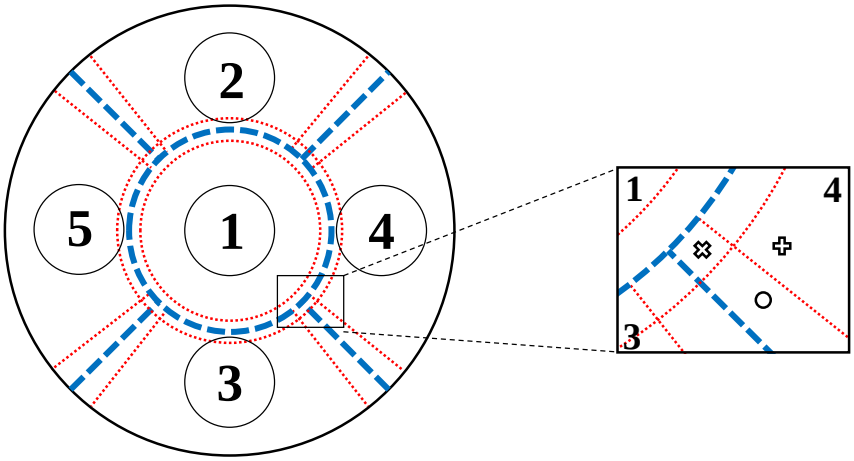

Figure 3.7: Schematic view of the five-hole probe head with numbered pressure ports and definition of flow regime regions/zones (blue) with overlap segments (red) including a zoomed view of a triple overlap region with three different test points

properties is possible. Finally, Shaw-Ward et al. introduce a polynomial response surface model [79]. Hence, a reduction of the amount of calibration points can be achieved due to a better calibration grid structure.

In the following, a detailed discussion of the applied data reduction approach for the spatial calibration and reconstruction in this thesis is given. The general scheme bases on Johansen's approach [80] which uses a local interpolation method with an additional zoning step. Hence, calibration data are divided in a low-angle and high-angle regime. The pressure port with the highest measured pressure determines the set of calibration coefficients, that are used for the reconstruction. In order to have sufficient information even for test points near the zone boarders, overlap segments are defined in case multiple ports are experiencing similar pressures within a pre-specified margin ε (see Figure 3.7). In the zoomed view, it can be seen that different calibration coefficients are needed for points located in the overlap regions: For example, test point (+) is solely defined for segment 4, test point (o) for segment 4 and 3, in case $\varepsilon > \frac{p_4 - p_3}{p_4}$, and finally, test point (x) for segment 4, 3, and 1, in case that $\varepsilon > \frac{p_4 - p_3}{p_4}$ and $\varepsilon > \frac{p_4 - p_1}{p_4}$ are both fulfilled. From pre-tests, it was observed that the overlap margin ε lies around $\varepsilon \approx 0.25$ for better reconstruction results. In the calibration routine, all acquired pressure combinations are processed as follows for all calibrated velocities/Mach numbers M_{calib}: First, four non-dimensional coefficients are calculated representing the probes behavior as function of $k_1 = f(\alpha)||f(\theta)$, $k_2 = f(\beta)||f(\phi)$, depending in which zone the highest pressure occurs, $k_t = f(p_t)$, and $k_s = f(p_s)$. Here, p_t ans p_s denote the total and static pressure, respectively. For the low-angle regime, where the central port p_1 measures the highest

pressure, the coefficients are as follows:

$$k_1 = b_\alpha = \frac{p_3 - p_2}{\bar{q}} \tag{3.9}$$

$$k_2 = b_\beta = \frac{p_4 - p_5}{\bar{q}} \tag{3.10}$$

$$k_t = \frac{p_1 - p_t}{\bar{q}} \tag{3.11}$$

$$k_s = \frac{p_t - p_s}{\bar{q}} \tag{3.12}$$

$$with \quad \bar{q} = p_1 - \frac{p_2 + p_3 + p_4 + p_5}{4} \tag{3.13}$$

Thus, $\bar{q}$ denotes the pseudo dynamic pressure, which is used to non-dimensionalize the coefficients.

The high-angle regime, where one of the circumferential ports p_i measures the highest pressure, can be described by the following coefficients:

$$k_1 = b_\theta = \frac{p_i - p_1}{\bar{q}} \tag{3.14}$$

$$k_2 = b_\phi = \frac{p^+ - p^-}{\bar{q}} \tag{3.15}$$

$$k_t = \frac{p_i - p_t}{\bar{q}} \tag{3.16}$$

$$k_s = \frac{p_i - p_s}{\bar{q}} \tag{3.17}$$

$$with \quad \bar{q} = p_i - \frac{p^+ + p^-}{2} \tag{3.18}$$

Thereby, p^+ and p^- denote the pressures at the circumferential pressure ports in clockwise and counter-clockwise direction. Figure 3.8 shows the flow regions and overlaps for a calibration grid at $M_{calib} = 0.1$ and an overlap threshold of $\varepsilon = 0.25$. As theoretically described before and in Figure 3.7, calibration points in the overlap region are used in multiple regions.

For feature scaling of k_1 and k_2 to similar ranges, the scaling factors for each flow regime region i is defined:

$$scale_i = \frac{\Delta k_{2,i}}{\Delta k_{1,i}} = \frac{k_{2,i,max} - k_{2,i,min}}{k_{1,i,max} - k_{1,i,min}} \tag{3.19}$$

As a next step, for each region, a Delauney triangulation is used to pre-process the calibration data in each flow regime region for the interpolation step in the data-reduction routine. Here, the MATLAB built-in Delauney triangulation function *delauneyTriangulation* is used to triangulate $(k_1|k_2)$-coordinates as seen exemplary in Figure 3.9a for region 1 of a five-hole probe. Furthermore, the calibration surface for $\alpha = f(k_1, k_2)$ is displayed in Figure 3.9b. Hence, α shows an almost linear dependency on k_1 and is barely varying with k_2, as expected.

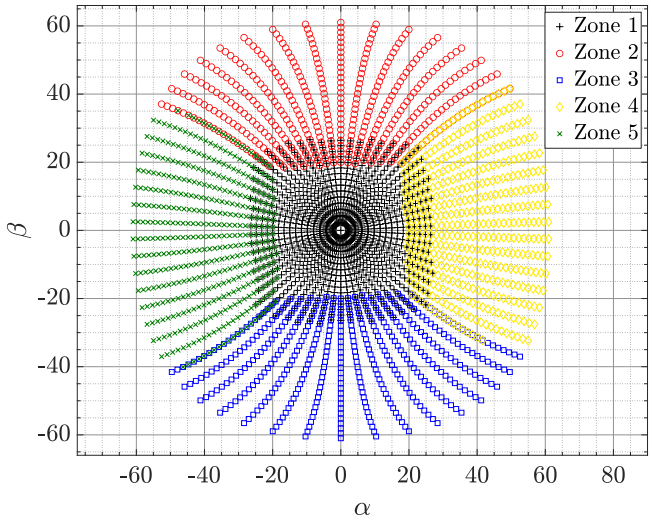

Figure 3.8: Flow regime regions/zones with overlap segments at $M_{calib} = 0.1$ and an overlap threshold of $\varepsilon = 0.25$

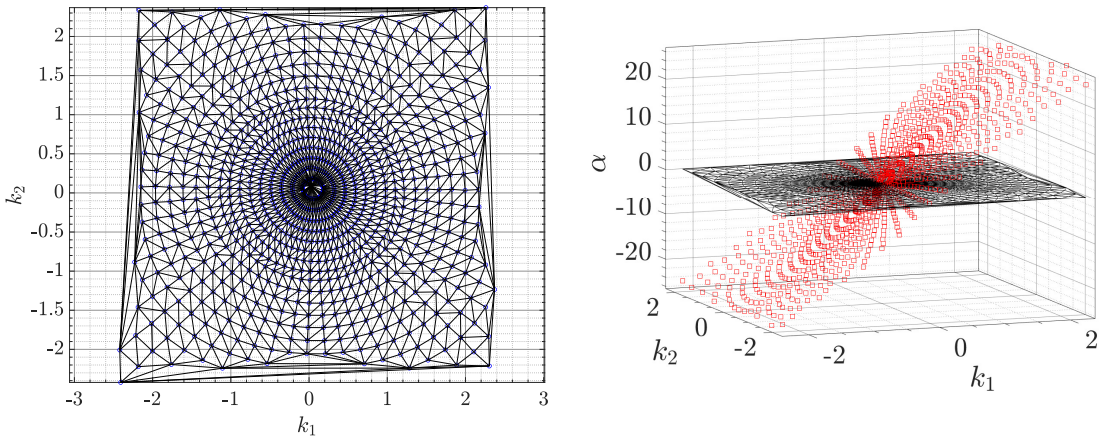

(a) Delauney triangulation

(b) Calibration surface $\alpha = f(k_1, k_2)$

Figure 3.9: a) Delauney triangulation of zone 1 calibration points and b) Calibration surface $\alpha = f(k_1, k_2)$ for $M_{calib} = 0.1$ and an overlap threshold of $\varepsilon = 0.25$

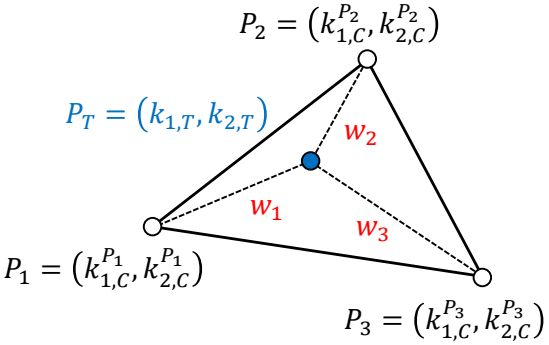

Figure 3.10: Schematic visualization of the concept of barycentric coordinates

When measuring in an unknown flow field, pressure data at the test point $p_{i,T}$ are acquired and have to be post-processed in the reconstruction procedure, which is described in the following. The subscript T and C denominates the values at the test point T and the calibration point C:
As a first step, the non-dimensional coefficients $k_{1,T}$ and $k_{2,T}$ for low- or high-angle regimes are calculated as defined above. Furthermore, an estimate for the Mach number $M_{estimate}$ is calculated based on the maximal measured pressure $p_{max} = max(p_{i,T})$, with κ being the isentropic expansion exponent:

$$M_{estimate} = \sqrt{\frac{2}{\kappa - 1} \cdot \left(\left(\frac{p_{max}}{p_s} \right)^{\frac{\kappa-1}{\kappa}} - 1 \right)} \tag{3.20}$$

Now, for each calibrated Mach number data set, the following steps are executed: In order to match the value range of $k_{1,C}$ and $k_{2,C}$, the test point coefficients are scaled with the calibration scaling factors $scale_i$. Using MATLAB's Delauney triangulation object function *pointLocation*, the triangle enclosing a test point can be found. In addition, the function provides the barycentric coordinates of the test point in the triangle, that can be seen as the weights w_1, w_2 and w_3 that solve this system of equations corresponding to the schematic visualization in Figure 3.10:

$$k_{1,T} = w_1 k_{1,C}^{P_1} + w_2 k_{1,C}^{P_2} + w_3 k_{1,C}^{P_3} \tag{3.21}$$

$$k_{2,T} = w_1 k_{2,C}^{P_1} + w_2 k_{2,C}^{P_2} + w_3 k_{2,C}^{P_3} \tag{3.22}$$

$$w_1 + w_2 + w_3 = 1 \tag{3.23}$$

In the following step, using the barycentric coordinates, the quantities $k_{t,T}$, $k_{s,T}$ and α_T, β_T or θ_T, ϕ_T, respectively, can be calculated by simple linear algebra calculations:

$$\begin{bmatrix} k_{t,C}^{P_1} & k_{t,C}^{P_2} & k_{t,C}^{P_3} \\ k_{s,C}^{P_1} & k_{s,C}^{P_2} & k_{s,C}^{P_3} \\ \alpha_C^{P_1} & \alpha_C^{P_2} & \alpha_C^{P_3} \\ \beta_C^{P_1} & \beta_C^{P_2} & \beta_C^{P_3} \end{bmatrix} \begin{bmatrix} w_1 \\ w_2 \\ w_3 \end{bmatrix} = \begin{bmatrix} k_{t,T} \\ k_{s,T} \\ \alpha_T \\ \beta_T \end{bmatrix} \tag{3.24}$$

The Mach number M can be determined by calculating p_t and p_s for the low-angle regime:

$$p_t = p_1 - k_{t,T} \cdot \bar{q}_T \tag{3.25}$$
$$p_s = p_t - k_{s,T} \cdot \bar{q}_T \tag{3.26}$$

Similar, it can be formulated for the high-angle regime:

$$p_t = p_i - k_{t,T} \cdot \bar{q}_T \tag{3.27}$$
$$p_s = p_i - k_{s,T} \cdot \bar{q}_T \tag{3.28}$$

With p_t and p_s, the Mach number M can be calculated:

$$M = \sqrt{\frac{2}{\kappa - 1} \cdot \left(\left(\frac{p_t}{p_s} \right)^{\frac{\kappa - 1}{\kappa}} - 1 \right)} \tag{3.29}$$

In the last step of the data reduction procedure, the results of the reconstructions for the various calibration Mach data sets, as described above, are used to linearly interpolate (and extrapolate) the final values for α, β, and M by using the Mach number estimate $M_{estimate}$.

In order to calculate the velocity magnitude and its components, the final calculation steps are needed:

$$U = M \cdot c = M \cdot \sqrt{\kappa \cdot R \cdot T} \tag{3.30}$$

Here, c is the speed of sound and R the specific gas constant. Lastly, the velocity components u, v and w can be derived:

$$u = U \cdot \cos(\alpha) \cdot \cos(\beta) \tag{3.31}$$
$$v = U \cdot \sin(\beta) \tag{3.32}$$
$$w = U \cdot \sin(\alpha) \cdot \cos(\beta) \tag{3.33}$$

3.1.1.2 Neural network-based scheme

In the reduction of the calibration data, knowledge about the flow physics around the probe is applied in the definition of the calibration coefficients. Another approach to the handling of the data is the application of system identification approaches, more precisely of artificial neural network methods. Resembling networks of complex-connected neurons in the brain, they can map complex mathematical relationships. After training the relations between the single neurons, the neural network can be applied as a black box. That means, that an exact description of the relationship between the input and output variables is no longer clearly apparent and needed for the user (see Figure 3.11).

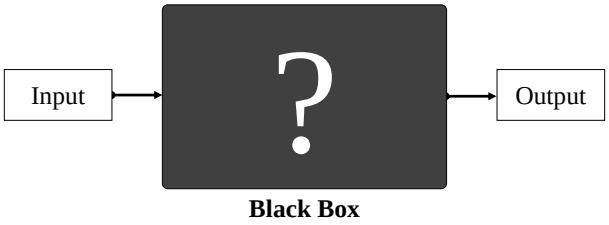

Figure 3.11: Black box models the identified system

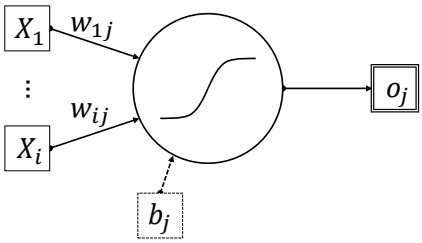

Figure 3.12: Node j of an ANN with inputs X_i, weights w_{ij}, a bias value b_j and the node output o_j

By incorporating theoretical knowledge, the neural network can be developed into a hybrid model, which can then be referred to as a "grey box". In the following, neural network approaches used for probe calibration from the literature are provided and the fundamentals of the neural network approach used in this thesis are discussed. An artificial neural network (ANN) is based on the architecture of biological neural system. The elements of the ANN which compare to brain neurons are depicted as nodes. The jth node can have multiple inputs X_i which are weighted with weights w_{ij} and processed within the node and lead to a single output o_j (see Figure 3.12). In addition, a bias value b_j is associated to every node. The processing of the data is carried out through the activation or transfer function of the node [81]. Activation functions are separated into linear and non-linear functions. A common non-linear function is the sigmoid or logistic activation function for an input z:

$$\phi(z) = \frac{1}{1 + e^{-z}} \tag{3.34}$$

The ANN consists of at least two layers of numerous nodes which are normally fully interconnected. The last layer is named output layer. The input data of the ANN are depicted as "features", whereas the outputs are often called "labels". In the supervised learning training step, known data pairs of features and corresponding labels are used to update the weights and biases of the neurons of the neural network until the network produces the "correct" output to a given input. Probably the most commonly employed technique for this updating task for feedforward neural networks is error backpropagation [81]. The aim is to update the (randomly set) initial parameters iteratively. In a forward propagation step, the neural network output is compared to the actual output

and an error is calculated. In the backpropagation step, the error is propagated back and the influences of each node in every layer on an overall cost function, i.e. gradients, can be determined. The weights and biases are then updated by incorporating the determined derivatives for example in a gradient descent approach.
In the literature, there are several studies that compare interpolation based reduction approaches with ANN based ones (see e.g. Franken and Ivey [82]). Vijayagopal et al. discuss a neural network based calibration of a seven-hole probe [83]. Their network uses two pressure coefficients as features/inputs and has four labels/outputs (A_t, A_s, α, and β). Based on this network approach, Rediniotis and Chrysanthakopoulos compare the ANN with a fuzzy logic approach [84]. Furthermore, Rediniotis and Vijayagopal claim a speed up of computation time of one order of magnitude when applying a neural network reduction in comparison to state-of-the-art interpolation algorithms [85]. Moreover, they introduce a backpropagation based neural network with a flexible architecture and apply it to calibration data of five- and seven-hole probes. Instead of using the backpropagation procedure for the ANN training, Fan et al. applied a differential evolution algorithm [86]. In order to further increase the reconstruction accuracy, Nikpey Somehsaraei et al. add a second multi-layer perceptron (MLP) neural network in their analysis [87]. The two MLPs comprise the calibration data processing and an error prediction. While the aforementioned studies are based on neural network schemes, Lee et al. incorporate an adaptive neuro-fuzzy inference system and claim an even faster reconstruction of the measured data [88, 89].
In this thesis, a basic MLP approach is chosen to compare its reconstruction accuracy and processing speed to the interpolation scheme in use. Therefore, the MATLAB neural network fitting application *nftool* [90] is applied. Figure 3.13 shows the architecture of the trained neural network for a single calibration Mach number. The five measured pressures are given as features. The output of the ANN are the flow angles (α and β) and the static and total pressure (p_s and p_t). Hence, no theoretical knowledge, like the definition of coefficients, is introduced in the black-box approach. The neural network is trained with the function *trainlm*, which trains a shallow two layer feed-forward network with sigmoid hidden neurons and linear neurons. For this purpose, the Levenberg-Marquardt backpropagation algorithm is applied to update the weight w_{ij} and bias b_j values [91]. The division between training, validation and test data for the neural network fitting is chosen to be random.

3.1.2 Gaussian process regression

In this subsection, the theory and motivation on Gaussian process regression for probe calibration, as an alternative to the classical methods described in the previous sections, is explained. The contents of this chapter have been published as a peer-reviewed research paper in the journal *Measurement Science and Technology* [92][1]:

[1] The journal article was published under the terms of the *Creative Commons* licence CC BY 4.0. The first author was responsible for the conception, the execution of the tests and the writing of the paper. The co-author has consented to publication, here.

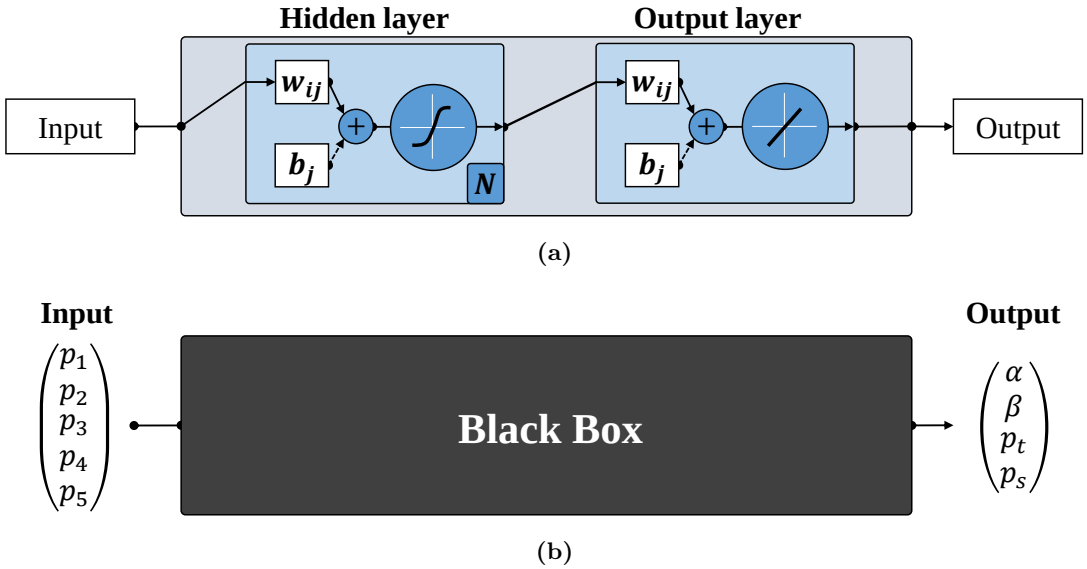

Figure 3.13: Sketch of the trained artificial neural network architecture

The analysis of the spatial calibration data indicates that the (multivariate) functions have a very similar shape. Since the aerodynamic probe calibration can be characterized as a regression problem, besides a standard polynomial regression approach – as seen in the discussion above – Bayesian statistics methods can be used. The basics of Bayesian statistics can be found in Gelman et al. [93]. Furthermore, Rasmussen applies *Gaussian processes* $\mathcal{GP}$ to machine learning problems, both for regression and classification problems [94]. In various research fields in the literature, Gaussian processes have been applied: in geostatistics, Gaussian process regression is better known as *kriging* [95]. During the application of $\mathcal{GP}$s, the placement of test point locations is crucial. Krause et al. describe an optimization routine for the placement of the locations in Gaussian process problems [96]. Furthermore, in engineering applications, Gaussian process regression has been used for the wind energy turbine power curve model prediction [97]. Its application on the calibration of spectroscopic sensors has also been shown [98]. In aerodynamic metrology, Garcia-Ruiz et al. show the application of Gaussian processes for the hot-wire temperature compensation [99]. Moreover, Agrawal et al. introduce a non-linear regression approach to minimize recalibration for non-thermal drifts [100].

Since aerodynamic probe calibrations a) require a regression within all measured data points, and b) show similarity among themselves, the idea of applying Bayesian statistics, namely Gaussian process regression, on aerodynamic probe calibration arises. Hence, the following governing hypotheses can be identified and are investigated within the thesis (see in the theoretical Section 3.1.2 and in the $\mathcal{GP}$ application Section 4.2.2.2):

Hypothesis 1. *The knowledge of former calibration data of various different shaped probes can be transferred to future probe calibrations incorporating the similarity among themselves.*

Hypothesis 2. *Bayesian statistics and machine learning algorithms, more precisely Gaussian process regression, are applicable on aerodynamic probe calibration data.*

Hypothesis 3. *The number of calibration points needed can be significantly reduced while still showing acceptable reconstruction accuracy, and thus, leading to a reduction of time consumption.*

Especially under the assumption that the first two hypotheses hold, a confirmation of the third hypothesis could result in a significant time saving in setup costs of a measurement campaign with aerodynamic probes.

Subsequently, the theoretical background to Gaussian process regression is explained: In Section 3.1.2.1, the principles of Bayesian statistics are outlined. The theory of the Gaussian process regression is introduced in Section 3.1.2.2. The upcoming sections are based on the more detailed discussion given by Rasmussen and Williams by addressing Gaussian processes in machine learning applications [94, 101]. Furthermore, general information on pattern recognition and machine learning is given by Bishop [81].

3.1.2.1 Theoretical background to Bayesian statistics

Engineering problems are often characterized by the lack of available information. This is where probability models provide a remedy when it comes to dealing with the challenge of missing information. In Bayesian statistics, the model based on existing data can successively be improved with new information by inference. The question on how probabilities change due to new information are thus brought into a mathematical framework by using the Bayesian theorem. The more general question on what can be inferred on the population based on samples is hereby answered. Hence, the Bayesian formalism introduces various probabilities, which are described in the following: A *prior* probability $P(H)$ has to be specified, expressing the belief about the hypothesis before incorporating observations. The *likelihood* probability $P(E|H)$ is the probability of the observations given the hypothesis. The *marginal likelihood* or evidence $P(E)$ is the normalizing constant. The *posterior* combines the likelihood and the prior and takes all information that is known into account. The posterior $P(H|E)$, the probability of the hypothesis given the evidence, can be calculated by Bayes' rule:

$$posterior = \frac{likelihood \times prior}{marginal\ likelihood} \tag{3.35}$$

$$P(H|E) = \frac{P(E|H) \times P(H)}{P(E)} \tag{3.36}$$

3.1.2.2 Gaussian processes

In the context of Bayesian statistics, multiple machine learning algorithms were developed in the past. One of them is the Gaussian process regression, which will be considered in more detail in the discussion hereafter. As noted, new information can be used to infer a new posterior Gaussian process model, which incorporates the observations by

updating the initial/prior Gaussian process. In contrast to basic (polynomial) fitting methods, for the Gaussian process regression, the expected order of the approximation does not need to be specified beforehand.

A Gaussian process ($\mathcal{GP}$) describes a distribution over functions and it is fully characterized by the mean function $m(\mathbf{x})$ and the covariance function $k(\mathbf{x}, \mathbf{x}')$ of a real process $f(\mathbf{x})$.

$$m(\mathbf{x}) = \mathbb{E}[f(\mathbf{x})] \tag{3.37}$$
$$k(\mathbf{x}, \mathbf{x}') = \mathbb{E}[(f(\mathbf{x}) - m(\mathbf{x}))(f(\mathbf{x}') - m(\mathbf{x}'))] \tag{3.38}$$

For noise-free observations, the Gaussian process can be written as:

$$f(\mathbf{x}) \sim \mathcal{GP}(m, k) \tag{3.39}$$

A distinct finite number n of locations is considered further:

$$\mu_i = m(x_i), \qquad i = 1, \ldots, n \tag{3.40}$$
$$\Sigma_{ij} = k(x_i, x_j), \qquad i, j = 1, \ldots, n \tag{3.41}$$

The joint distribution of n known training case function values, $\mathbf{f}$, and a set of n_* function values corresponding to the test set inputs, $\mathbf{f}_*$, gives:

$$\begin{bmatrix} \mathbf{f} \\ \mathbf{f}_* \end{bmatrix} \sim \mathcal{N}\left(\begin{bmatrix} \boldsymbol{\mu} \\ \boldsymbol{\mu}_* \end{bmatrix}, \begin{bmatrix} \Sigma_{\mathbf{f},\mathbf{f}} & \Sigma_{\mathbf{f},*} \\ \Sigma_{*,\mathbf{f}} & \Sigma_{*,*} \end{bmatrix} \right) \tag{3.42}$$

Here, for example $\Sigma_{\mathbf{f},*} = \Sigma(X, X_*)$ represents the $n \times n_*$ matrix of the covariances evaluated at all n training points X and n_* test points X_*.
The predictive joint posterior distribution can be used to sample function values $\mathbf{f}_*$ of test inputs X_* by evaluating the mean and covariance matrix:

$$\begin{aligned} (\mathbf{f}_* | X_*, X, \mathbf{f}) \sim \mathcal{N}\Big(& \boldsymbol{\mu}_* + \Sigma_{*,\mathbf{f}} \Sigma_{\mathbf{f},\mathbf{f}}^{-1} (\mathbf{f} - \boldsymbol{\mu}), \\ & \Sigma_{*,*} - \Sigma_{*,\mathbf{f}} \Sigma_{\mathbf{f},\mathbf{f}}^{-1} \Sigma_{\mathbf{f},*} \Big) \end{aligned} \tag{3.43}$$

The covariance of a Gaussian process random variable can be described by the *kernel* or *covariance function*. For a valid kernel function, the kernel matrix $\Sigma = k(X, X)$ has to be positive definite. This implies a symmetric covariance matrix. The prediction of the Gaussian process strongly depends on the choice of the covariance function. Instead of fixing it to a specific shape, usually a parametric family of functions is selected and its parameters are optimized by inferring with the training data. In the following, two commonly used families are introduced. Afterwards, a brief outline of the *hyperparameters* optimization is given.

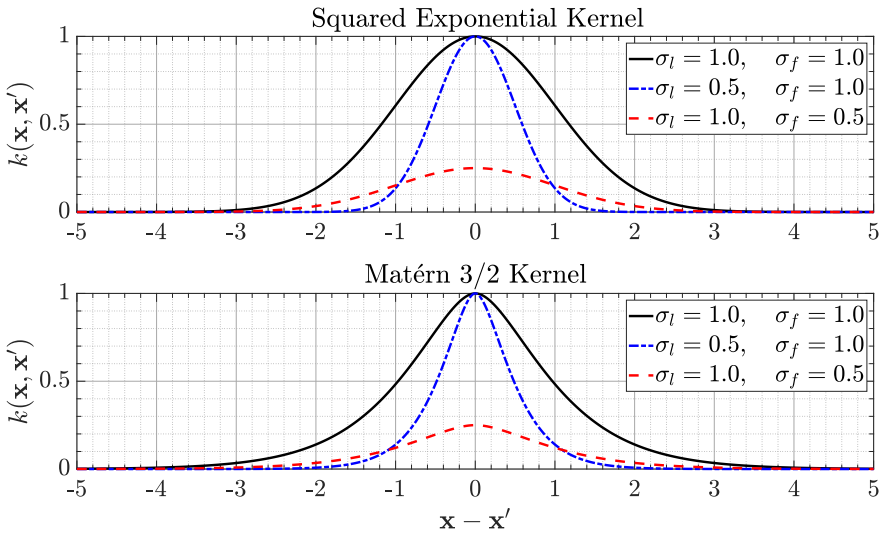

Figure 3.14: Squared exponential kernel (top) and Matérn kernel (bottom) for various hyperparameters σ_f and σ_l [92]

Kernel function families

One of the most basic kernel function families is the squared exponential kernel, or Gaussian kernel (see Figure 3.14 (top)):

$$k(\mathbf{x}, \mathbf{x}') = \sigma_f^2 \exp\left(-\frac{\|\mathbf{x} - \mathbf{x}'\|_2^2}{2\sigma_l^2}\right) \tag{3.44}$$

Here, σ_f denotes the signal standard deviation and σ_l the characteristic length scale. Another kernel function is the Matérn 3/2 covariance function (see Figure 3.14 (bottom)). This kernel function is also used for the $\mathcal{GP}$ applied on the multi-hole pressure probe data in Section 4.2.2.2:

$$\begin{aligned} k(\mathbf{x}, \mathbf{x}') &= \sigma_f^2 (1 + \sqrt{3}r) \exp\left(-\sqrt{3}r\right), \\ \text{with } r &= \frac{\|\mathbf{x} - \mathbf{x}'\|_2}{\sigma_l} \end{aligned} \tag{3.45}$$

Figure 3.15 shows a representation of the kernel matrix for both, the Gaussian and the Matérn 3/2, kernels with randomly chosen hyperparameters $\sigma_f = 1.0$ and $\sigma_l = 1.0$. Comparing both kernel functions, it can be seen that the squared exponential kernel shape has a broader peak in comparison to the Matérn kernel, but contrary flattens out earlier with increasing distance $\|\mathbf{x} - \mathbf{x}'\|_2$.
The set of hyperparameters is often pooled in the vector $\boldsymbol{\theta}$. For the previously defined kernel functions, $\boldsymbol{\theta}$ is defined as:

$$\boldsymbol{\theta} = \begin{pmatrix} \theta_1 \\ \theta_2 \end{pmatrix} = \begin{pmatrix} \sigma_l \\ \sigma_f \end{pmatrix} \tag{3.46}$$

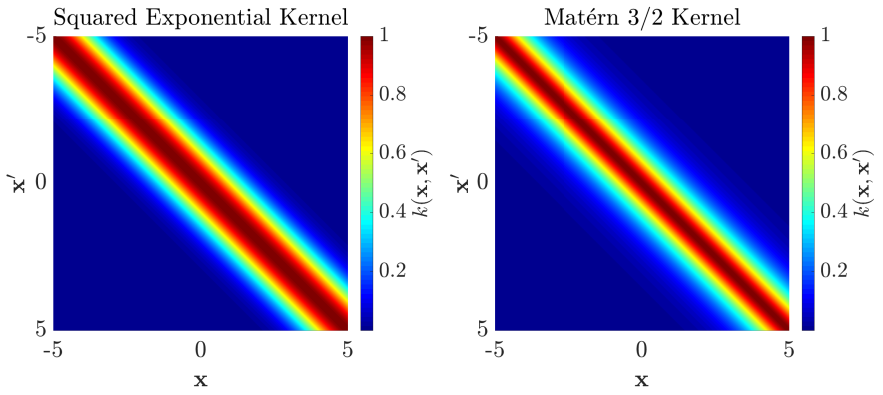

Figure 3.15: Squared exponential kernel matrix (left) and Matérn 3/2 kernel matrix (right) for hyperparameters $\sigma_f = 1.0$ and $\sigma_l = 1.0$ [92]

Depending on the mean and kernel function chosen in the prior step, different free parameters have to be set. The stated equations hold true for noise-free data. In real world problems, observations are subject to noise. This can be expressed in additional terms in the $\mathcal{GP}$ formulation. The measured value $\mathbf{y}$ with noise is defined as follows: $\mathbf{y} = \mathbf{f}(\mathbf{x}) + \epsilon$. Here, the noise ϵ is Gaussian distributed with a noise variance σ_n^2. Furthermore, the covariance also changes to $\Sigma_y = \Sigma_f + \sigma_n^2 I$, where Σ_f is the covariance matrix for noise-free observations.

Training of hyperparameters

The evaluation of the marginal likelihood function $p(\mathbf{y}|X, \boldsymbol{\theta})$ is the basis for the training of the hyperparameter vector $\boldsymbol{\theta}$. This can be done by maximizing the log likelihood function with efficient gradient-based algorithms, e.g. conjugate gradient solvers [102]. The log likelihood function for multivariate Gaussian distributions $\mathcal{L}$ is given by:

$$\begin{aligned} \mathcal{L} &= \log p(\mathbf{y}|X, \boldsymbol{\theta}) \\ &= -\frac{1}{2}\mathbf{y}^T \Sigma_y^{-1} \mathbf{y} - \frac{1}{2}\log|\Sigma_y| - \frac{n}{2}\log 2\pi. \end{aligned} \tag{3.47}$$

It has to be noted that $\log p(\mathbf{y}|X, \boldsymbol{\theta})$ is a non-convex function. Hence, it could have multiple maxima. Numerous methods in the literature cover the determination and optimization of this problems by inverting Σ_y efficiently while reducing computational costs of the order $\mathcal{O}(n^3)$ computation.
Furthermore, regarding non-linear optimization, the gradient of the log likelihood function is needed as well. This is done by seeking the partial derivatives of the marginal likelihood w.r.t. the hyperparameters θ_j:

$$\frac{\partial}{\partial \theta_j}\mathcal{L} = -\frac{1}{2}\left(\Sigma_y^{-1}\frac{\partial \Sigma_y}{\partial \theta_j}\right) + \frac{1}{2}\mathbf{y}^T \frac{\partial \Sigma_y}{\partial \theta_j}\Sigma_y^{-1}\mathbf{y}. \tag{3.48}$$

Sparse $\mathcal{GP}$ for large data sets

In the case of a high number of input/ training data sets, $\mathcal{GP}$ models experience a high computational effort due to matrix inversions in the inference step. Considering n training points $\mathbf{x}$, an exact inference via the Gaussian likelihood method is of $\mathcal{O}(n^3)$ for the standard $n \times n$ matrix inversion. In order to reduce the computational load, there are different methods to approximate the covariance matrix. Instead of using the full covariance matrix Σ, an approximate matrix $\tilde{\Sigma}$ is used for the inference. Quinonero-Candela and Rasmussen [103] give an overview of different methods. Generally, the approximation methods work with a set of m inducing points $\mathbf{u}$ with a reduced computational load of $\mathcal{O}(mn^2)$. In the GPML MATLAB toolbox the *Fully Independent Training Conditional* (FITC) approximation is applied, which is briefly explained in the following. The approximated covariance matrix $\tilde{\Sigma} \approx \Sigma$ can be expressed as [103–105]:

$$\begin{aligned} &\tilde{\Sigma} = Q + G, \quad G = diag(\Sigma - Q), \\ &Q = \Sigma_u^T \, Q_{uu}^{-1} \, \Sigma_u, \quad Q_{uu} = \Sigma_{uu} + \sigma_{n_u}^2 I, \end{aligned} \tag{3.49}$$

with $\sigma_{n_u}^2$ being the noise variance from the inducing points. The diagonal matrix $diag(A)$ comprises the diagonal elements of A. Besides the known $n \times n$ covariance matrix Σ, the formula also uses the $n \times m$ covariance matrix between the test points and the inducing points Σ_u and the $m \times m$ covariance matrix between the inducing points Σ_{uu}.

3.1.2.3 Exploitation for the calibration of aerodynamic probes: An introducing example

In the following, the procedure of the Gaussian process regression for the reduction in the number of the calibration points will be demonstrated in an introducing example, see Figure 3.16. Thereby, the application of the GPML MATLAB-toolbox implementation by Rasmussen and Nickisch [106] and the choice of the parameters will be discussed. In Section 4.2.2.2, the applicability of Gaussian process regression to real aerodynamic pressure probe data is shown.

Subsequently, the Gaussian process regression procedure from the flow chart in Figure 3.16 is explained step by step using generically generated univariate data. After starting the GPML MATLAB toolbox, the available calibration data are read in first. In this example, ten different input data sets are displayed in Figure 3.17 (left). Since the number of input data points within this example is very small, the normal $\mathcal{GP}$ approach is applied. A squared exponential kernel function and the Gaussian likelihood formulation is chosen for inference. The prior $\mathcal{GP}(0, k)$ is initialized with the initial hyperparameters in Table 3.2, and thereafter, a posterior $\mathcal{GP}$ is trained with the input data (see Figure 3.17 (right)).

In the optimization step, the hyperparameter vector $\boldsymbol{\theta}$ is optimized by maximizing the log marginal likelihood as described in Section 3.1.2.2. The optimized values in Table 3.2 show, that the initially chosen values were way off the optimized hyperparameters. The location of the first supporting point – the location of the first point to be calibrated in the new probe calibration – is determined. This is done manually or following a specific

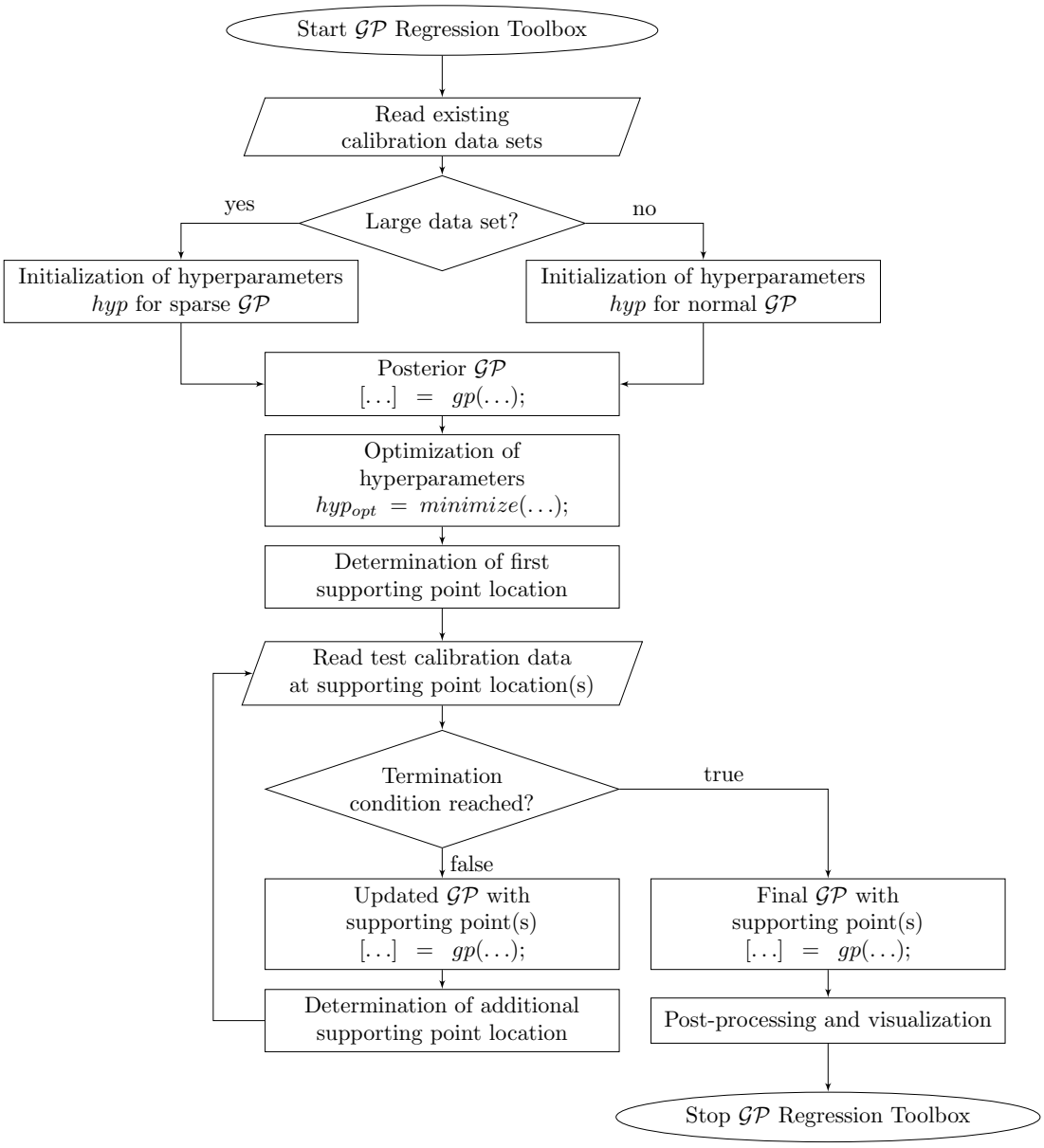

Figure 3.16: Flow chart of the Gaussian process regression applied on aerodynamic probe calibration data [92]

Table 3.2: Prior and optimized hyperparameters for the squared exponential kernel function in the example test case [92]

	initial hyperparameter hyp	optimized hyperparameter hyp_{opt}
σ_l	0.1	2.27
σ_f	0.1	1.61
σ_n	0.1	$2.2 \cdot 10^{-3}$

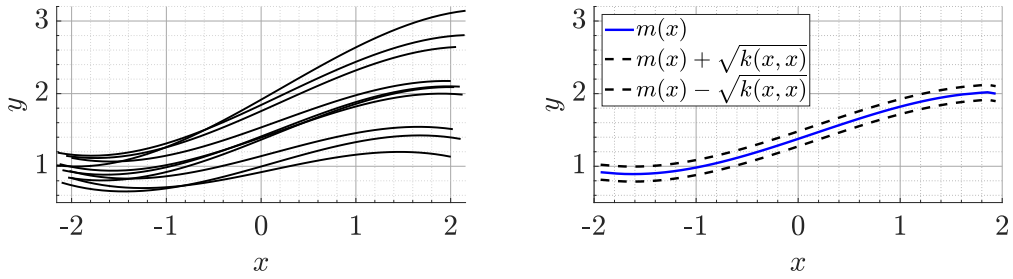

Figure 3.17: Input data sets for the introducing example (left) and the initial $\mathcal{GP}$ (right) [92]

rule for selection, e.g. by choosing the location of the highest predictive output variance, which is available as an output vector of the *gp*-routine. At this point, newly calibrated points of the probe under investigation are iteratively added to the $\mathcal{GP}$ regression approach: As long as the termination condition is not fulfilled, an updated conditional $\mathcal{GP}$ is formed with the available supporting points from the new calibration and new locations for further supporting points are determined. If the termination condition is reached, a final $\mathcal{GP}$ is formed with all newly calibrated supporting points. The results of the last step serves as the new calibration curve for the probe and can be used for post-processing or visualization. In Figure 3.18, the *gp*-routine outputs of the first three iterations and the final iteration are depicted. Besides the mean (blue) and the standard deviation of the updated $\mathcal{GP}$s (black), the test curve (red), which represents the probe calibration curve to be approximated, and the supporting points (red dots) are shown.

The introducing example was designed to show a high agreement between the output of the $\mathcal{GP}$ and the test function y_{test} already after two iterations. After five iterations, the selected termination condition is reached and the final $\mathcal{GP}$ is present, matching almost exactly the test curve y_{test}.

3.2 Temporal calibration

In addition to the spatial calibration (time-averaged correlation), the dynamic characteristics of the multi-hole probe, more precisely the acoustics of the line-cavity system (LCS) inside the probe, has to be determined to also resolve pressure changes with frequencies $f > 0\ Hz$. The acoustic system inside the pressure channels has a significant

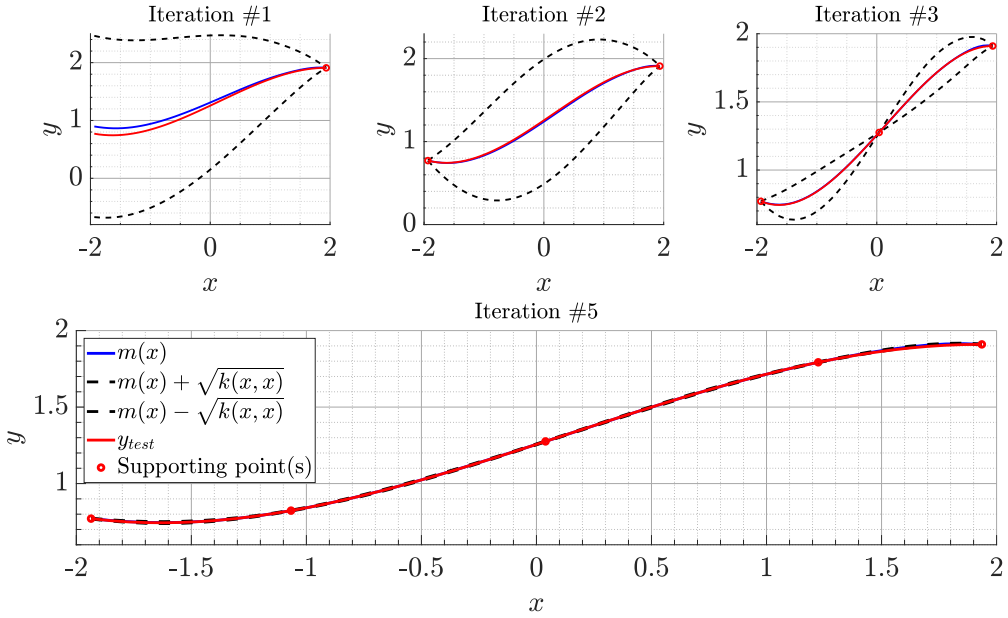

Figure 3.18: Output of the updated $\mathcal{GP}$s with supporting points in comparison to the test function y_{test} for the first three and the final iteration [92]

influence on the measurement of unsteady flow phenomena. In the following, a general introduction into the description of the line-cavity system is given in Section 3.2.1. Different analytic approximations of the acoustic behavior in the line-cavity system will be discussed. Furthermore, in sections 3.2.2 and 3.2.3 two different experimental approaches to quantify the system are given.

3.2.1 General theory of line-cavity systems

In Figure 3.19, the geometric properties of a line-cavity system are illustrated. The acoustic system between the tip and the location of the sensor is mainly described by the line length L, the line diameter $D = 2r$ and the cavity volume in front of the sensor V. Such acoustic systems are predominantly dominated by two different forms of pressure distortion, resonance and attenuation, depending on the pressure frequency f.

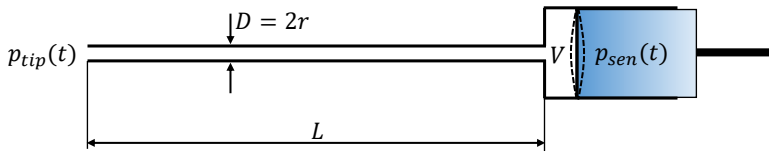

Figure 3.19: Schematic sketch of a pneumatic line system including the main geometric properties

In the literature, there are several analytic approaches to describe the dynamics inside

the LCS. Analytic solutions are often divided into approximations of the full Kirchhoff solution (see Kirchhoff [107] and Rayleigh [108]) and approaches introducing one or more simplifying assumptions. The following brief theoretical discussion deals with the latter. Wave propagation in a tubing can be described by the Navier-Stokes equations of momentum conservation and continuity. Furthermore, the fluid has to satisfy both the equation of state and the energy equation. The following equation describes the dynamics of acoustic wave propagation and represents a boundary value problem derived from the Navier-Stokes equations:

$$\frac{\partial^2 p(x,t)}{\partial t^2} + \frac{R_a}{\rho}\frac{\partial p(x,t)}{\partial t} = c^2 \frac{\partial^2 p(x,t)}{\partial x^2} \tag{3.50}$$

R_a denotes the acoustical resistance of the system. Iberall develops a fully theoretical model of the attenuation of a pressure signal through a connecting line [109]. Additionally, he introduces first order corrections if prerequisites for the full model can not be fulfilled, e.g. large perturbations or high reduced frequencies are present.

Further studies try to simplify the problem and reduce the order of the mathematical problem. Basically, the rigid cavity with an opening is modeled as a mass-spring system. The resonance frequency of the "Helmholtz resonator" system f_H is given by:

$$f_H = \frac{c}{2\pi}\sqrt{\frac{A}{L'V}} \tag{3.51}$$

Thereby, $A = \pi r^2$ denotes the cross-sectional area and L' the effective length of the tubing. Due to the oscillation of air in the system and the displacement of air at the opening, mass is added to the system, which is considered by calculating the effective length. For unflanged ends the effective length is given by $L' = L + 1.5r$ [110]. Whitmore and Leondest develop a second-order distortion model that accurately describes the behavior of the primary wave harmonic of the pneumatic tubing [111]. Rediniotis and Pathak [112] describe the system as a second-order dynamic system, as well:

$$p_{tip}(t) = mC\frac{\mathrm{d}^2 p_{sensor}(t+\tau)}{\mathrm{d}t^2} + RC\frac{\mathrm{d}p_{sensor}(t+\tau)}{\mathrm{d}t} + p_{sensor}(t+\tau) \tag{3.52}$$

Here, m is the mass of the system, $1/C$ the system elastic constant, R the viscous damping coefficient and τ the acoustic lag. For small tubing and volumes the system can be simplified to a first-order equation:

$$p_{tip}(t) = \lambda\frac{\mathrm{d}p_{sensor}(t)}{\mathrm{d}t} + p_{sensor}(t) \tag{3.53}$$

Thereby, $\lambda = RC$ depicts a lag constant, which can be determined analytically with simplifications or experimentally. Knowing the lag constant λ, the pressure at the tip can be corrected for systems, which follow the criterion for unsteadiness:

$$\omega \ll 32\mu/D^2\rho \tag{3.54}$$

Here, ω is the angular frequency of the unsteadiness, and ρ the air density. Nevertheless, due to the second-order dynamic approach, this correction method is limited to critically damped or overdamped systems.
One of the most often used correction methods for acoustic attenuation in line-cavity systems and the one that is seen as the state-of-the-art solution was introduced by Bergh and Tijdeman in 1965 [113]. They analytically formulated a recursive solution for multiple line-cavity systems in a row. Several simplifications and prerequisites were assumed:

- No steady flow in the line.
- The flow is laminar throughout the system, i.e. the Reynolds number is low enough.
- The gas properties are constant within each element of the system.
- Magnitudes of pressure, density, and temperature fluctuations (with time) are small compared to time-averaged values. If not, wave shape distortions and amplitude-dependent nonlinear attenuation occur and have to be corrected (see e.g. Blackshear et al. [114])
- The line diameter is small compared to the line length $L/D \gg 1$ and small compared to acoustic wavelengths of interest.
- The thermal conductivity of the system wall is large and temperature fluctuations at the wall are zero.
- The wall material is rigid.
- The cross-flow velocity at the entrance is assumed to be small.
- Expansions occur isentropically.

The attenuation and phase shift for the acoustic wave propagation inside a single-tube system is formulated as the complex ratio $H(\omega) = P_{sensor}(\omega)/P_{tip}(\omega)$ and is denoted as transfer function (TF):

$$H(\omega) = \frac{P_{sensor}(\omega)}{P_{tip}(\omega)} = \left[\cosh(\psi L) + \frac{V\eta\psi}{\kappa\pi r^2}\sinh(\psi L)\right]^{-1} \tag{3.55}$$

$$\text{with} \qquad \psi = \frac{\omega}{c}\sqrt{\frac{\kappa}{\eta}\frac{J_0(\gamma)}{J_2(\gamma)}} \tag{3.56}$$

$$\eta = \left[1 + \frac{\kappa - 1}{\kappa}\left(\frac{J_2\left(\gamma\sqrt{Pr}\right)}{J_0\left(\gamma\sqrt{Pr}\right)}\right)\right]^{-1} \tag{3.57}$$

$$\gamma = i^{3/2} r\sqrt{\frac{\rho\omega}{\mu}} \tag{3.58}$$

Thereby, J_i denotes the Bessel function of i^{th} order, κ the specific heat ratio and Pr, ρ and μ the Prandtl number, the density and dynamic viscosity of the fluid, respectively. In a study by Nyland et al., Iberall's and Bergh and Tijdeman's approaches

are tested experimentally, showing good correlation between the tests and the predicted solutions [115]. In the case of longer pneumatic lines, the signal noise can get dominant in the deconvolution. Semaan and Scholz compare the Bergh and Tijdeman correction with a method using a Wiener filter. This approach is called Wiener deconvolution [116]. They come to the conclusion that only for a length bigger than $L > 150\ mm$ the Wiener deconvolution is beneficial. Since the probe presented in this thesis has shorter tubes, the considerations made by the Bergh and Tijdeman solution are sufficient enough for estimating the general acoustic behavior inside the LCS. Moreover, Tijdeman discusses two main parameters of very high importance in cylindrical tubes, the shear wave number and the reduced frequency [117].
Richards' approach describes the line-cavity system by using an analogy to electrical transmission lines [118]. In his analysis for the propagation of sound waves in tubes, he discusses non-circular cross sections, as well, whereas Bergh and Tijdeman's approach is only valid for circular cross-sections. In the transmission line approach for one dimensional wave propagation in ducts, the underlying equations are based on electrical transmission lines, using the ABCD matrix formalism. It is claimed that by using this approach, which can be mathematically transformed into the Bergh and Tijdeman solution when assuming circular tubing, a faster and easier computational effort is achieved. However, experiments have shown that due to imperfections in the probe manufacturing or due to a more complex probe assembly, analytic solutions can solely serve as a first guess: Irwin et al. try to digitally correct the attenuation by incorporating an experimentally determined transfer function [119]. Also, the inclusion of a restrictor in the assembly is discussed. Holmes and Lewis observe a good agreement between the theoretical and experimental solutions with long tubings [120]. However, they note that for sensors with flexible diaphragms, an equivalent volume has to be considered in the approach. Kobayashi et al. determine the effects on the transfer function due to compressibility effects and conduct a lumped-parameter analysis [121].
A similar, but slightly different probe assembly, leads to the determination of the transfer function in so called waveguide or infinite line pressure probes [23, 122, 123]. Whitmore and Fox introduce a less complex, time domain solution, based on an improved accuracy second-order response model [124]. Hall and Povey review existing approaches and suggest a new method, which is also based on electric transmission theory [125]. Kutin and Svete discuss the downsides of Bergh and Tijdeman's approach with respect to thermodynamic effects [126]. They introduce a second-order lumped-parameter model and analytically derive approximations for these parameters (natural frequency, damping ratio and time constant).
As seen in the recent years, an experimental determination of the transfer function is absolutely necessary, when dealing with a more complex probe setup. Two experimental realizations for the TF determination are explained in more detail in the following subsections.

3.2.2 Experimental determination in the frequency domain: Frequency test-rig

The transfer function can be determined experimentally in a frequency test-rig, where the investigated object (e.g. the multi-hole probe) and a reference sensor are mounted in close proximity to each other (see Figure 3.20). Furthermore, the rig contains a speaker connected to an an amplifier and placed directly facing the test object and the reference sensor.

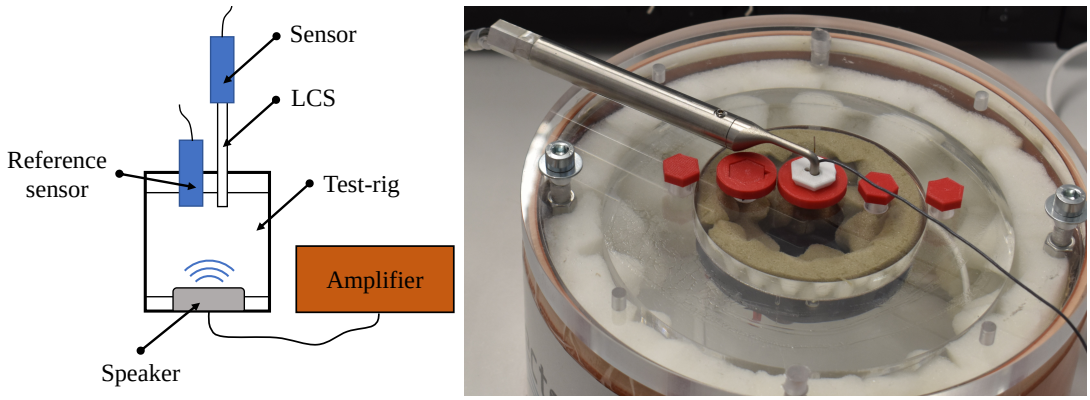

Figure 3.20: a) Sketch of the frequency test-rig assembly and b) frequency test-rig for the determination of the transfer function $H(\omega)$

During the calibration step, sinusoidal waves are emitted by the speaker at specified frequency steps Δf up to a predefined maximal calibration frequency $f_{cal,max}$. By evaluating the reference sensor signal and the sensor signal at the end of the LCS, the transfer function of the LCS, more precisely the amplitude ratio as well as the phase shift, is deduced.

$$H(\omega) = \frac{P_{sensor}(\omega)}{P_{tip}(\omega)} = \frac{\hat{p}_{sensor}(\omega)}{\hat{p}_{tip}(\omega)} \cdot e^{i\omega t + \varphi(\omega)} \tag{3.59}$$

The set Δf and $f_{cal,max}$ are dependent on the speaker and amplifier specifications. Furthermore, $f_{cal,max}$ is chosen to suit the expected frequency content of the flow.

Due to the closed test-rig assembly, acoustic modes can develop or resonate in the cavity between the speaker and the test object, and thus, distort the pressure signals sensed by the pressure sensors. For this reason, a) damping material is used in the rig cavity and b) the test object and reference sensor mount is rotated in several calibration runs to compensate for modes.

3.2.3 Experimental determination in the time domain: Quantification in a Shock-tube

In cooperation with Thomas Hopfes from the gas dynamics group at TUM-AER, investigations on the acoustic behavior of line-cavity systems (LCS) are conducted in the shock tube facility at TUM-AER [127]. The aim is to determine the transfer function of the LCS and to acquire measurement characteristics of the fiber-optic pressure sensors. The contents of this theoretical section are widely extracted from the peer-reviewed research article that has been submitted in the Springer conference proceedings of the STAB/DGLR Symposium 2020 "New Results in Numerical and Experimental Fluid Mechanics XIII" [128][2]. In the shock tube experiments, a shock wave that provides a step change in pressure is generated. Sensors are flush mounted to the wall of the test section for reference, and at the end of a given line-cavity system, respectively. Within a system identification step, the discrete-time pressure signals acquired due to the pressure step are measured and set into relation (see experiments in Section 4.1.4). In contrast to the determination in the frequency test rig, which shows a bandwidth restriction due to the selected speaker, the shock allows to also identify high frequencies.

System identification

The time-discrete signals can be Z-transformed (i.e. time-discrete equivalent of the Laplace transform) and the transfer function of the linear system can be expressed by two polynomials of order m and n [129]:

$$\frac{Y(z)}{U(z)} = \frac{b_0 \cdot z^{-d} + b_1 \cdot z^{-1-d} + \cdots + b_m \cdot z^{-m-d}}{1 + a_1 \cdot z^{-1} + a_2 \cdot z^{-2} + \cdots + a_n \cdot z^{-n}} \tag{3.60}$$

Here, $Y(z)$ and $U(z)$ are the Z-transformed of the time series data of the line-cavity and the reference sensor signals, respectively. The exponent d depicts the delay between the input and output signal.

After the identification of the unknown parameters a_i and b_i, the amplitude ratio and phase lag corresponding to the transfer function can be computed at any frequency f

[2]The article was published with copyrights staying at the authors, under exclusive license to Springer Nature Switzerland AG 2021. The co-authors have consented to publication, here.

for a specific sampling rate f_s.

$$\left|\frac{Y(f)}{U(f)}\right| = \sqrt{\frac{B_1^2 + B_2^2}{A_1^2 + A_2^2}} \tag{3.61}$$

$$\varphi(f) = atan(B_2/B_1) - atan(A_2/A_1) \tag{3.62}$$

$$A_1 = 1 + \sum_{i=1}^{m} a_i \cdot \cos(2\pi f/f_s \cdot (-i)) \tag{3.63}$$

$$A_2 = \sum_{i=1}^{m} a_i \cdot \sin(2\pi f/f_s \cdot (-i)) \tag{3.64}$$

$$B_1 = \sum_{i=0}^{m} b_i \cdot \cos(2\pi f/f_s \cdot (-i-d)) \tag{3.65}$$

$$B_2 = \sum_{i=0}^{m} b_i \cdot \sin(2\pi f/f_s \cdot (-i-d)) \tag{3.66}$$

Hence, for following measurements, the transfer function can be applied to correct the pressures attenuated in the line-cavity system, as described in [33]. In this work, the MATLAB built-in system identification functions are used [130]. Before applying the signal identification functions, the acquired signals are divided into a training and validation set. The delay d between the input and output signal is estimated with the function *delayest*. By using the function *tfest*, the free parameters a_i and b_i of the transfer function identification can be calculated depending on the chosen number of poles and zeros. In order to achieve a good fit for the training signal, various combinations of the number of poles and zeros are tested. In addition to the estimated fit of the *tfest*-output, the estimated transfer function is applied on the validation data set. The combination of poles and zeros with the best fit/correlation to the reference pressure signal is chosen and the transfer function parameters are stored.

3.2.4 Reconstruction process using the transfer function

When measuring in unknown unsteady flows, the time signal at the tip has to be reconstructed from the sensor signal acquired inside the probe. Therefore, the reconstruction process described in this section is applied. The schematic work flow is shown in Figure 3.21, which is adapted to the approach by Rediniotis et al. [15].

The quasi-periodic signal at the sensor $p_{sensor}(t)$ represents the input. Before the time-domain signal is processed into the frequency domain by applying a fast Fourier transformation (FFT), a windowing function can be applied. Often, rectangular windowing is already included in the FFT-realization in many coding languages (as e.g. in MATLAB's *fft* function). Other windowing functions countering the spectral leakage effect can be chosen in order to either ensure a better conversation of magnitudes or phase shifts of the transformed signal. Windowing ensures a quasi-periodic input signal for the Fourier transformation, which suppresses higher frequency artefacts when transformed into frequency domain. After the input signal is transformed into the frequency domain,

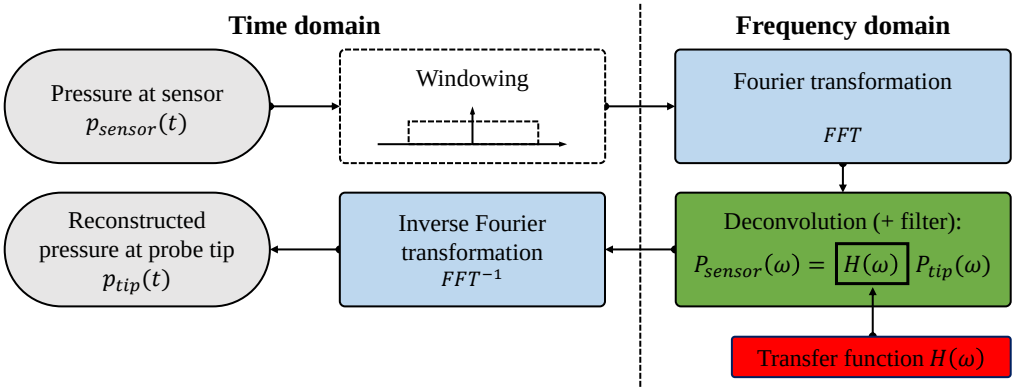

Figure 3.21: Pressure reconstruction routine

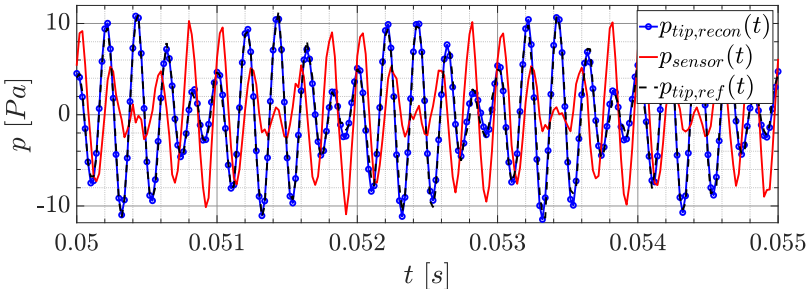

Figure 3.22: Pressure reconstruction example of a narrow tubing: Superposition of signals with $f_1 = 4.0\ kHz$ and $f_2 = 5.0\ kHz$

the TF is used to calculate the Fourier-transformed pressure at the tip $P_{tip}(\omega)$ from the Fourier-transformed pressure at the sensor $P_{sensor}(\omega)$:

$$P_{sensor}(\omega) = H(\omega) P_{tip}(\omega) \tag{3.67}$$

Furthermore, digital signal conditioning, like low-pass filtering, can be applied in this step. Lastly, the signal is transferred into time domain by applying the inverse FFT. The pressure at the tip $p_{tip}(t)$ is obtained as the output and can be further processed by utilizing the spatial calibration data, as seen in the respective Section 3.1.
In order to show the functionality of the reconstruction procedure, the transfer function of a narrow silicone tubing is determined and tested: two sinusoidal signals with $f_1 = 4.0\ kHz$ and $f_2 = 5.0\ kHz$ with differing magnitudes are superposed and emitted by the speaker in the frequency test-rig. In Figure 3.22, the reconstructed pressure at the tubing tip $p_{tip,recon}$ after applying the TF on the pressure detected at the sensor p_{sensor} is depicted. It is compared to a reference signal measured in close proximity to the tubing tip with another reference sensor $p_{tip,ref}$. The reconstructed signal matches the reference signal very well.

4 Fiber-optic sensor and multi-hole probe characterization

In this chapter, several qualification and characterization tests are shown for a) the fiber-optic pressure sensor and b) the fast-response multi-hole probe (see schematic overview in Figure 4.1).

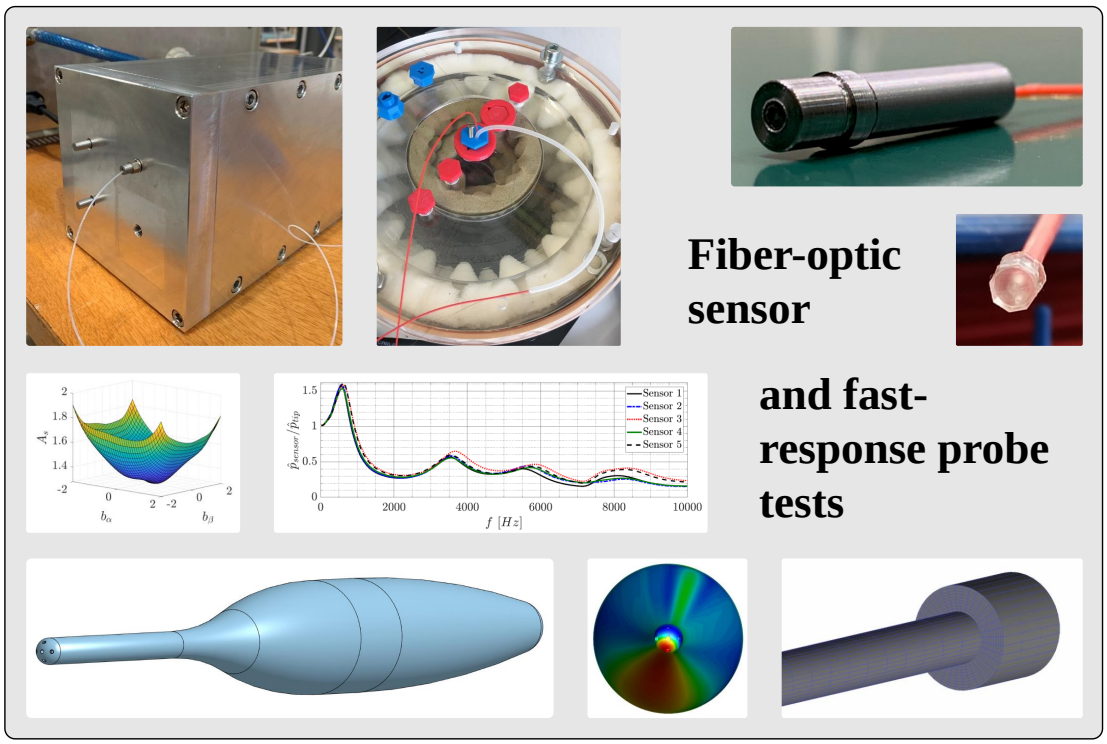

Figure 4.1: Overview of various covered topics within this chapter on the characterization of the fiber-optic sensor and the multi-hole pressure probe

In the first part in Section 4.1, the behavior of the fiber-optic sensor is investigated regarding its pressure and thermal sensitivity. Furthermore, tests in the two different transfer function determination scenarios – in a frequency test rig and in a shock tube – are discussed.

In Section 4.2, some findings and analyses of the fast-response probe behavior are shown. In addition to experimentally determined characterizations of the probe, computational fluid dynamics (CFD) simulations are shown that describe the spatial and

temporal behavior of a generic probe, with equivalent dimension as the one used for the more elaborate application studies in this thesis in Chapters 5 and 6.

4.1 Sensor tests

In this section, several tests are presented in order to characterize the fiber-optic behavior. Besides the static and thermal calibration of the sensor, the following sections cover the transfer function determination in the frequency test rig and in a shock tube applying fiber-optic sensors.

4.1.1 Static calibration of the sensor

In the static calibration, the sensor is pressurized at multiple pressure levels. As a result, the correlation between the optic output parameter ρ_{opt} and the applied pressure p is determined to find the function $\rho_{opt} = f(p)$.

As already mentioned in the theoretical part, covering the fiber-optic sensor basics in Section 2.2.2, around the operation point and in the pressure range of the sensor, the output should be linear:

$$p = (\rho_{opt} - \rho_{opt,0}) \cdot \frac{dp}{d\rho_{opt}} = (\rho_{opt} - \rho_{opt,0}) \cdot k_p^{-1} \tag{4.1}$$

Here, $\rho_{opt,0}$ is the zero output at 0 Pa gauge pressure, and k_p^{-1} is the slope fit of the linear regression.

The schematic test setup is depicted in Figure 4.2. The fiber-optic sensor is connected to a channel of the FOPS DAQ which in turn is controlled via National Instrument LabVIEW. A pneumatic pressure controller (Druck DPI 520, up to ± 1 $psig$) is also controlled via a serial connection to LabVIEW. A pressure chamber, in which multiple sensors can be inserted simultaneously, is either pressurized or depressurized. The optic output values ρ_{opt} and the set applied static pressure are recorded.

In Figure 4.3, the principle hardware components are visualized. Here, the sensor is mounted inside a metal sensor housing, that is used for an easier flush mounting in the wind tunnel, when measuring surface pressures.

Figure 4.4 visualizes the static calibrations for a 2nd generation fiber-optic sensor (FOPS-19E3). Multiple positive pressures in the range between $p = (0,\ 4000)$ Pa are set in the pressure chamber. The optical output value ρ_{opt} is plotted over the applied pressure p. A linear correlation between the two variables can be identified. The linear fit with a negative slope is plotted in the figure. The slope of the fit gives the static pressure sensitivity coefficient $k_p = d\rho_{opt}/dp$. The coefficient of determination $R^2 = 1$ indicates a very pronounced degree of linearity of the sensor.

The sensor under investigation FOPS-19E3 shows a pressure sensitivity coefficient of

$$k_{p,FOPS-19E3} = -3.4529 \cdot 10^{-6}\ 1/Pa. \tag{4.2}$$

Nevertheless for some sensors, significant changes in the pressure sensitivity coefficient are detected when disassembling the sensor from its mount or a test object and

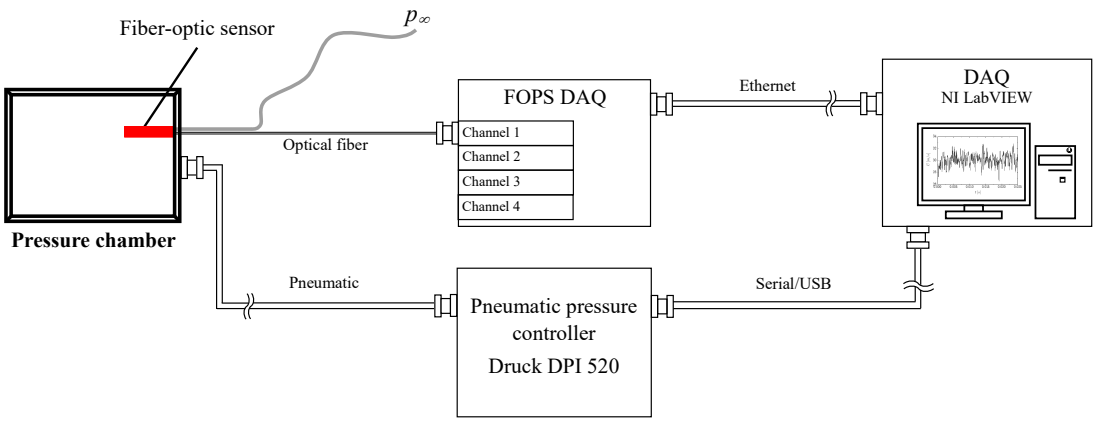

Figure 4.2: Schematic setup for the determination of the pressure sensitivity coefficient $k_p = d\rho_{opt}/dp$

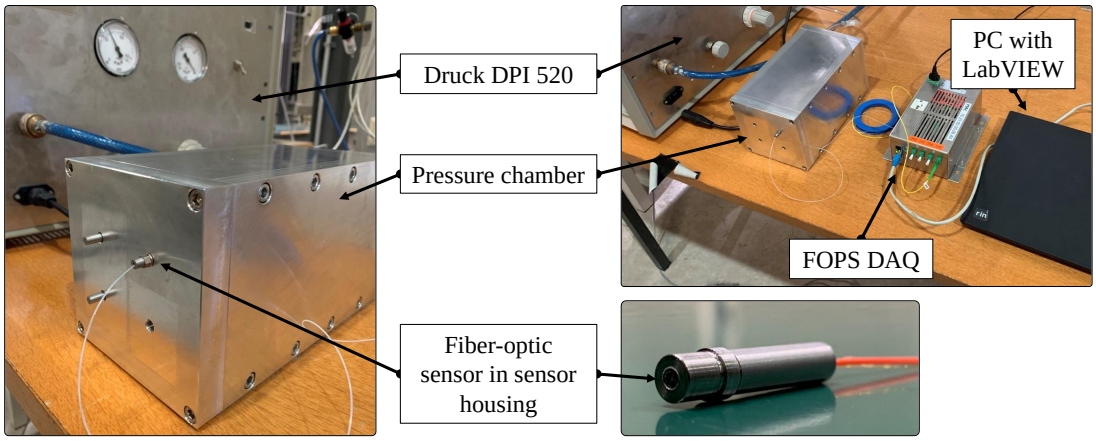

Figure 4.3: Measurement hardware for the determination of the pressure sensitivity coefficient $k_p = d\rho_{opt}/dp$

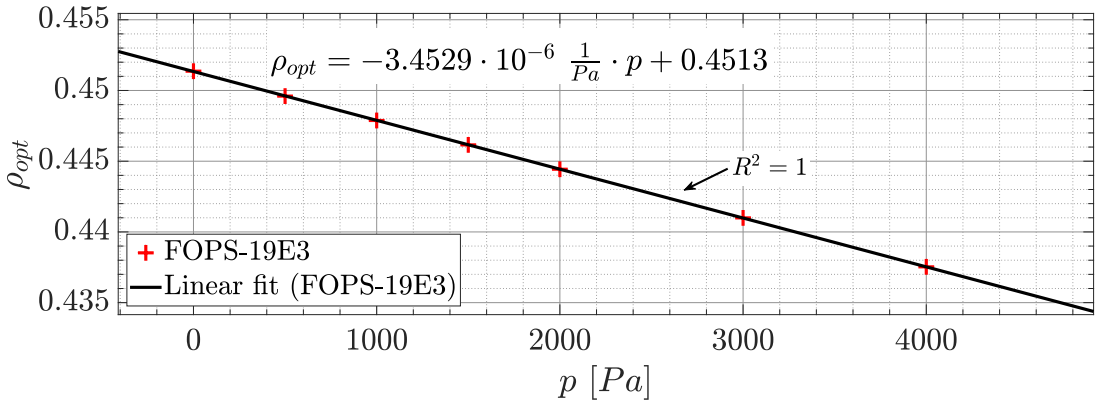

Figure 4.4: Determination of the pressure sensitivity coefficient $k_p = d\rho_{opt}/dp$ for a fiber-optic sensor (2nd generation, FOPS-19E3)

re-assembling and hence re-calibrating it. This could be due to forces and loads on the sensor ferrule applied through the assembly situation. Hence, a calibration in the mounted stage is necessary. However, the calibration of the sensitivity coefficient is reproducible in the mounted assembly and should be performed carefully for this reason.

4.1.2 Determination of the temperature sensitivity

Within this section, the focus lies on the determination of the temperature sensitivity of the fiber-optic pressure sensor. Sensors are mainly designed to only show a significant change for a unique quantity of interest. They should be solely slightly dependent or unaffected by other quantities (see discussion in Section 5.2). Hence, pressure sensors should mainly show a strong dependence on the applied pressures. Due to the manufacturing, assembly and the underlying physics of the sensor also other stronger sensitivities can be detected. One of them is the ambient temperature or the thermal behavior of the sensor material.

In contrast to the stated correlation between the applied pressure and the optical output quantity ρ_{opt} in the previous section, the optical output can be seen as a function of the pressure and the temperature $\rho_{opt} = f(p, T)$. Before delving into the characterization of the thermal sensor behavior, some possible underlying influencing considerations are discussed. Since the sensor is manufactured out of fused silica wafers, no differences in material thermal conductivity is expected. The fiber and the pressure line are glued into the fused silica sensor ferule. The orientation of the optical fiber within the ferule is extremely critical for a clean and repeatable signal. Thus, if different expansion coefficients cause the fiber to lie only marginally altered for changed temperatures and therefore light exits the fiber at an offset angle, strong thermal sensitivities of the optical output value are to be expected. In contrast to piezo-resistive pressure sensors, no active temperature compensation is present.

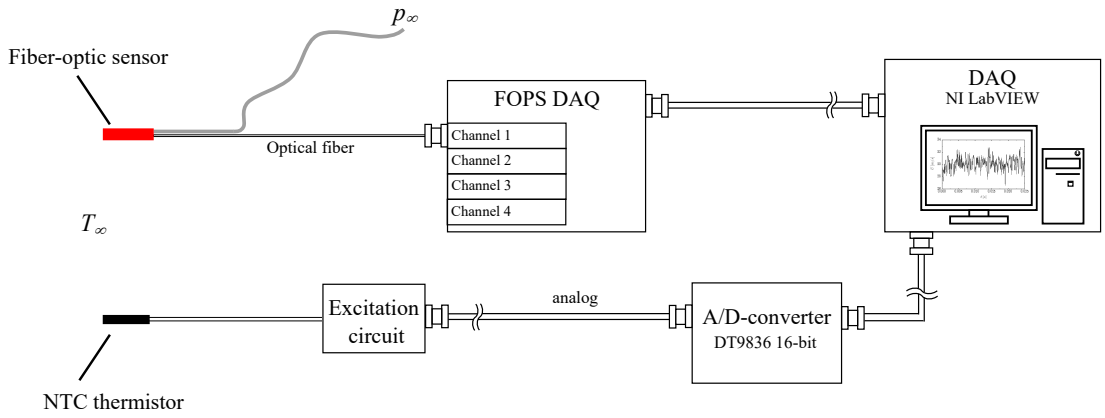

Figure 4.5: Schematic setup for the determination of the thermal sensitivity coefficient $k_T = d\rho_{opt}/dT$

In the following, the test setup and an exemplary determination of the temperature sensitivity of fiber-optic sensors are shown. The tests were performed in the context of a supervised student research project by Niklas Mooshofer [131]. Here, sensors of the 1st development generation are investigated since those sensors showed a non-negligible sensitivity with varying temperatures. The 2nd generation was improved in such a way that the temperature sensitivity was considerably reduced.

The aim of the tests is to determine the thermal sensitivity coefficient $k_T = d\rho_{opt}/dT$, which is part of the extended equation for calculating the applied pressure p from the optical output value ρ_{opt}:

$$p = (\rho_{opt} - \rho_{opt,0} - \Delta T \cdot \frac{d\rho_{opt}}{dT}) \cdot \frac{dp}{d\rho_{opt}} = (\rho_{opt} - \rho_{opt,0} - \Delta T \cdot k_T) \cdot k_p^{-1} \tag{4.3}$$

The schematic test setup is visualized in Figure 4.5. The fiber-optic sensor is connected to a channel of the FOPS DAQ which in turn is controlled via LabVIEW. In addition, a state-of-the-art temperature sensor (NTC thermistor) measures the ambient temperature.

Figure 4.6 shows the temperature calibrations for two fiber-optic sensors. Different ambient temperatures in the range between $T_\infty = (12,\ 25)°C$ are measured, which represents the common temperature range in the wind tunnel measurements at TUM-AER. The optical output value ρ_{opt} is plotted over the temperature. Since no pressure is applied on the sensor membrane, the change in ρ_{opt} comes only from the the temperature changes. A linear correlation is detected. Linear fits are also plotted for both sensors. The slope of the fits represent the thermal sensitivity coefficient $k_T = d\rho_{opt}/dT$. Besides the linear fit, also the coefficient of determination R^2 is shown in the figure and show a high linearity of the measured values.

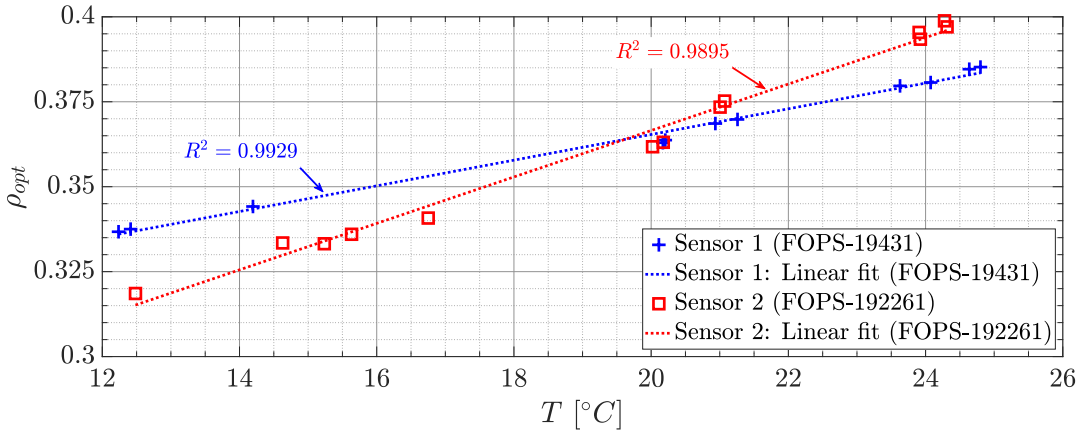

Figure 4.6: Determination of the thermal sensitivity coefficient $k_T = d\rho_{opt}/dT$ for two fiber-optic sensors

Here, sensor 1 (FOPS-19431) and sensor 2 (FOPS-192261) show a thermal sensitivity coefficient of

$$k_{T,FOPS-19431} = 3.779 \cdot 10^{-3}\ 1/K \qquad k_{T,FOPS-192261} = 6.835 \cdot 10^{-3}\ 1/K. \tag{4.4}$$

When multiplying the thermal coefficient with the inverse of the pressure coefficient, a measure for the virtual increase of the applied pressure coming from a temperature change can be calculated which is corrected by applying the extended formula introduced in Equation 4.3.

$$\frac{dp}{dT} = \frac{d\rho_{opt}}{dT} \cdot \frac{dp}{d\rho_{opt}} \tag{4.5}$$

For the two sensors the following dp/dT coefficients are calculated:

$$\left.\frac{dp}{dT}\right|_{FOPS-19431} = 448.43\ Pa/K \qquad \left.\frac{dp}{dT}\right|_{FOPS-192261} = 511.66\ Pa/K \tag{4.6}$$

Compared to the low dynamic pressures that the sensors are designed to measure, pressure changes due to a temperature change would be very significant. This demonstrates the huge significance of determining the thermal sensitivity and show a major development potential for future sensors. By modifying and adapting the gluing concept in the 2nd generation sensor, this value could be reduced by at least one order of magnitude. Furthermore, future sensor developments could further reduce this value or allow a sensor assembly without any glue.

4.1.3 Transfer function determination in the frequency test rig

In this section, the application of the fiber-optic sensors is shown when determining the transfer function of a silicone tubing in the frequency test rig. In Figure 4.7, the

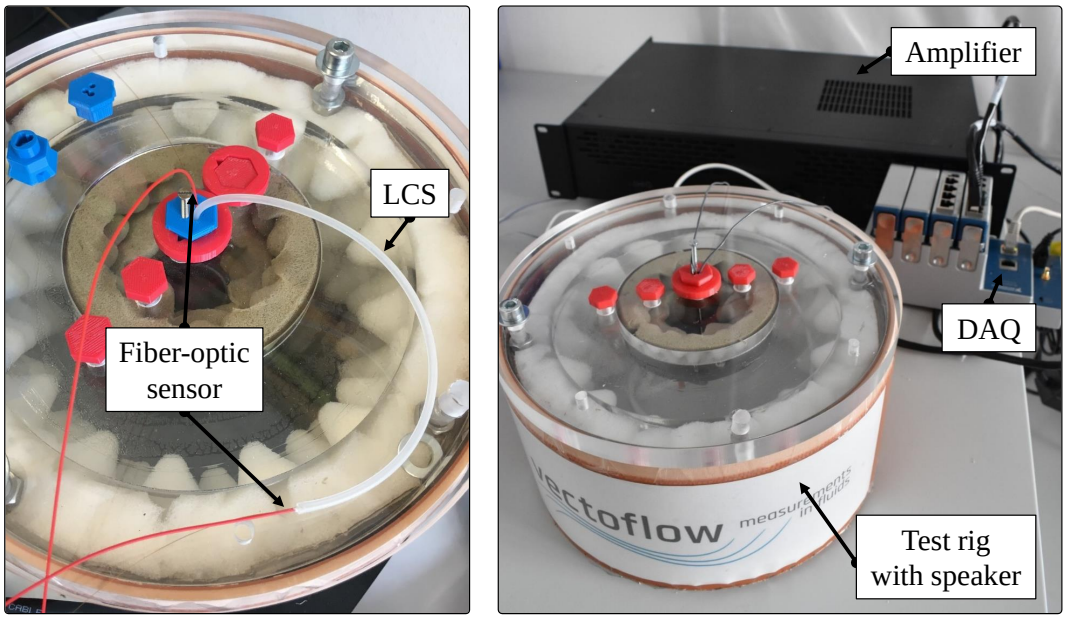

Figure 4.7: Hardware components for the transfer function determination in the frequency test rig

frequency test rig setup is visualized. By using different sensor/object holders, various sensor combinations can be tested. The setup for a silicone tubing LCS transfer function determination is shown on the left. On the right hand side, the measurement hardware, including the amplifier, the DAQ and the test rig, is visualized.

First, the dynamic behavior of the fiber-optic sensor (1st generation) is compared to a state-of-the-art piezo-resistive sensor. The sensors are placed next to each other in the frequency test-rig. Sinusoidal excitations in the frequency range of $f_e = (100,\ 1000)\ Hz$ are applied, measured, and compared. The signal frequencies are exactly reproduced by both sensor types with relative errors smaller than 1 % in the whole frequency range. Figure 4.8 shows the pressure amplitudes measured by both sensors. Furthermore, the relative deviation of the fiber-optic sensor to the piezo-resistive sensor is depicted. The amplitudes match very well at most frequencies. Larger errors at $f_e = \{100,\ 400\}\ Hz$ could be due to acoustic modes in the frequency test-rig, that have been observed in previous measurements.

Second, in order to test the fiber-optic sensor in a more realistic application, the transfer function of a silicone tubing (line-cavity system, LCS) with $L = 200\ mm$ and $d = 1.5\ mm$ is determined in the aforementioned frequency test-rig. Multiple variations of the combination of the reference sensor and the sensor at the end of the tubing are compared (see Figure 4.9). The excited frequency step size is 20 Hz and 100 Hz for the PR-PR case and cases including a fiber-optic sensor (PR–FO and FO–FO), respectively. Moreover, the analytic estimate by Bergh and Tijdeman is included in the figure, where

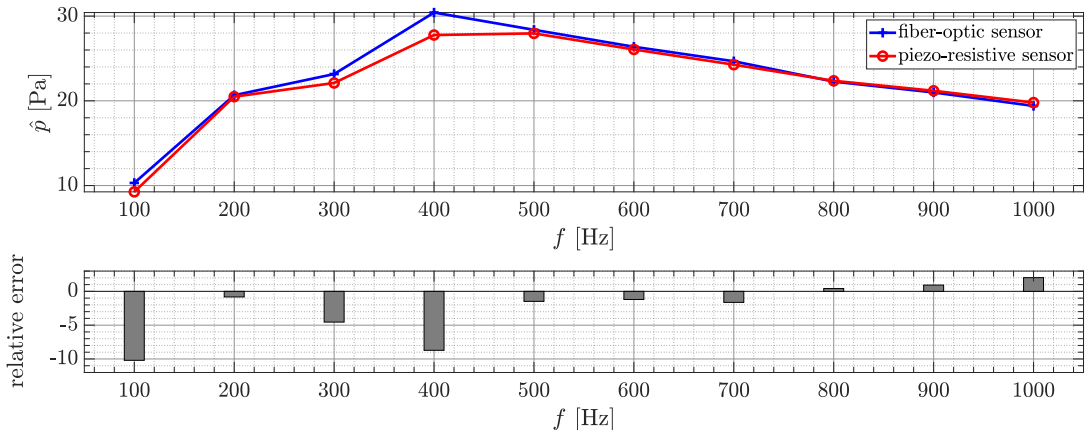

Figure 4.8: Acquired pressure amplitudes of a fiber-optic sensor placed next to a piezo-resistive sensor in the frequency test-rig

only the amplitude ratio $\hat{p}_{sensor}/\hat{p}_{tip}$ is displayed. For both cases, where the fiber-optic sensor is mounted at the end of the tubing, the resonance frequencies match the ones of the analytic estimate and the PR-PR solution, which can be seen as the state-of-the-art, and validated solution. The qualitative trend is reproduced very well, however,

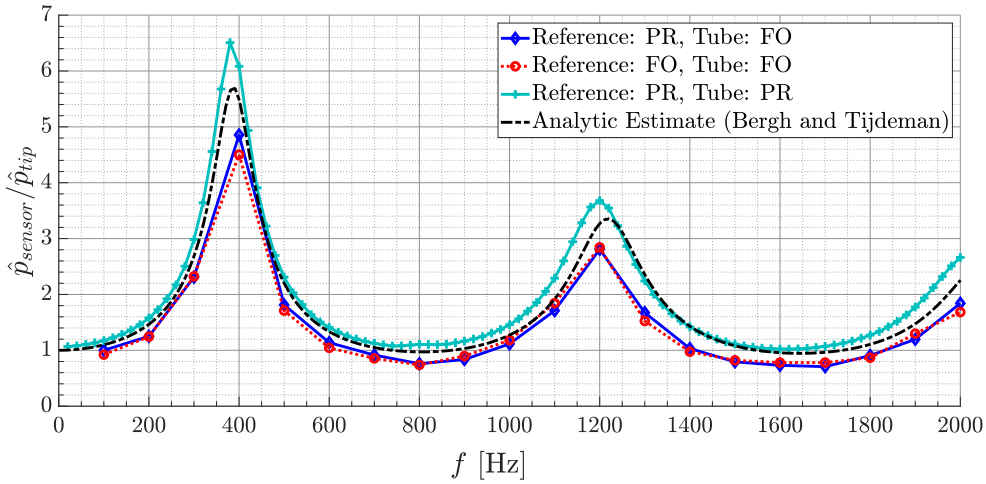

Figure 4.9: Amplitude ratio $\hat{p}_{sensor}/\hat{p}_{tip}$ for a silicone tubing with geometric parameters $L = 200\ mm$ and $d = 1.5\ mm$: PR – piezo-resistive; FO – fiber-optic

the amplitudes of the attenuation are partly underpredicted. A possible reason for this behavior is a systematic error, which can be attributed to a modification of the operating point of the sensor. The fiber-optic sensor is deformed by the surrounding silicone tubing marginally but sufficient enough to cause a change in the calibration coefficient. This leads to the conclusion that the assembly of the sensor into a test object is crucial for its behavior. As already seen in the static calibration in Section 4.1.1, the determination of

the pressure sensitivity should be repeated in the assembled configuration to counteract those effects.

4.1.4 Transfer function determination in the shock tube

The contents of this section are widely extracted from the peer-reviewed research article published in the Springer conference proceedings of the STAB/DGLR Symposium 2020 "New Results in Numerical and Experimental Fluid Mechanics XIII" [128][3]. The underlying theory on the shock tube test and the identification process is presented in Section 3.2.3. In contrast to the experiments in the frequency test-rig, the excitation signal in the shock-tube not only contains one distinct frequency per run, but a large frequency bandwidth corresponding to the shock traveling downstream the shock tube. In the following sections, the experimental setup in the shock tube facility and selected results are presented.

Experimental setup of the shock tube

In Figure 4.10, the layout of the shock tube and the connected systems for the current experiments are depicted. The shock tube has an overall length of 24 m, an inner diameter of 290 mm, and is segmented into a driver, a driven, and a test section. A cookie-cutter is installed upstream of the test section to remove boundary flows and to enable the transition from the tube to the 190 $mm \times 190$ mm square test section. Static conditions are monitored with thermocouples and absolute pressure transducer. A 0.2 mm-thick PVC diaphragm is clamped between the driver and driven sections

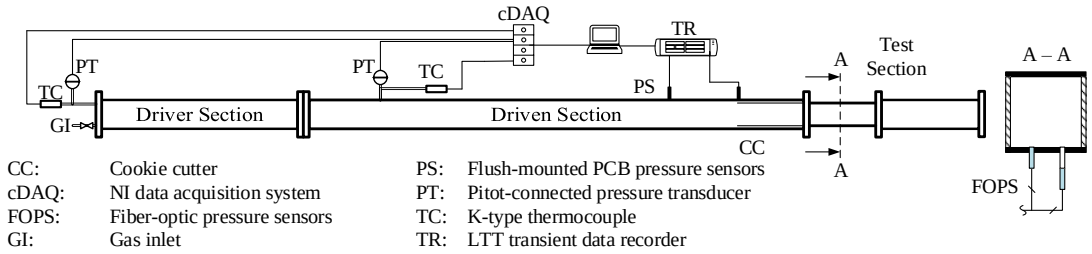

Figure 4.10: Schematic layout of the shock tube facility at TUM-AER [128]

with a pair of crossed 0.1 mm thick heating wires in direct contact. While the driven section is kept at atmospheric conditions, the driver section is filled with air to a level of 1.15 bar. By supplying an electric current to the heating wires, the diaphragm is melted locally and ruptures. Subsequently, a planar shock wave forms, propagates towards the downstream test section and induces a uniform flow along with a step change in pressure, temperature, and density. Pressure and flow conditions remain steady for approximately 2 ms before reflected waves alter the conditions. Two pressure sensors are flush mounted along the tube and allow to calculate the shock velocity shortly upstream of the test

[3]The article was published with copyrights staying at the authors, under exclusive license to Springer Nature Switzerland AG 2021. The co-authors have consented to publication, here.

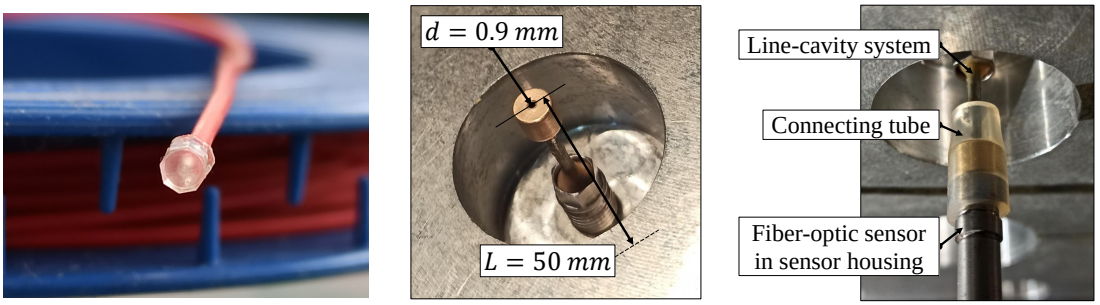

(a) Fiber-optic pressure sensor **(b)** Line-cavity system **(c)** Line-cavity system with attached sensor

Figure 4.11: Line-cavity system and sensor assembly [128]

Table 4.1: Test plan for all conducted measurements in the shock tube [128]

L	M_{shock}	p_{driver}	p_{driven}	# experiments
50 mm	$1.0291 - 1.0389$	$1.1 - 1.15$ bar	96.5 kPa	3
100 mm	$1.0374 - 1.0399$	1.15 bar	96.4 kPa	3

section based on the time lag between the signals. Along with pre-shock conditions, this allows to calculate post-shock flow properties based on moving shock relations.

Figure 4.11a depicts one of the fiber-optic differential pressure sensors that are used to determine the transfer function. The octagonal shape of the 2nd generation fiber-optic sensors is clearly visible. The sensor housing for the fiber-optic sensors mimics the shape of the regular PCB sensors of the shock-tube facility and the sensor is sealed and fixed into the housing with modeling clay. While the housing is rather big, it enables a fast installation of the fiber-optic sensor at desired locations. For the experiment, two sensors are mounted in parallel in the test section as indicated by the cutting plane A – A in Figure 4.10. One of them is flush-mounted and serves as a reference, while the other is connected to the LCS under investigation (see Figure 4.11c). The LCS consists of a tube with a diameter of $d = 2r = 0.9$ mm and a length of $L = \{50, 100\}$ mm which is fixed in a housing similar to that of the sensors. At the end of the tube, a brass connector with the same outer diameter as the sensor housing is attached to the LCS (see Figure 4.11c). The brass connector is used together with a silicone tube to connect the LCS to the sensor in order to achieve a negligible cavity volume V and enable a fast replacement of various sensors and LCSs. In total, six experiments are conducted, varying the length of the LCSs L as summarized in Table 4.1. Here, besides the variation in length, the shock Mach number M_{shock} and the pressures of the driver and the driven section, p_{driver} and p_{driven}, are shown, respectively.

Results and discussion

In the following, the results of the shock-tube tests for the determination of the transfer

Table 4.2: Overview of the acquired shock tube test results [128]

#	L	M_{shock}	p_{driver}	usage	correlation [%]
1	50 mm	1.0291	1.10 bar	generalization	99.90
2	50 mm	1.0389	1.15 bar	training + validation	99.90
3	50 mm	1.0370	1.15 bar	generalization	99.93
4	100 mm	1.0399	1.15 bar	generalization	98.52
5	100 mm	1.0384	1.15 bar	generalization	99.28
6	100 mm	1.0374	1.15 bar	training + validation	99.97

function of the LCS are discussed. In Figure 4.12a, the acquired pressure signals of the flush-mounted reference sensor p_{ref} and the sensor signal at the end of the LCS p_{sen} are shown for test case #2 (see Table 4.2). All signals are sampled with a sampling rate of $f_s = 50\ kHz$, which is currently the maximum achievable sampling rate of the DAQ system for the fiber-optic pressure sensors. The data are separated into three parts: The first pressure rise, which corresponds to the initial shock (see Figure 4.12b), is used for the system identification training as described in Section 3.2.3. Furthermore, a validation data set is chosen independently in order to identify the best number of poles and zeros for the system identification. For the generalization, the entire signal is reconstructed. With the delay estimation function *delayest*, the delay d is estimated to be 40 samples. Fitting the free transfer function parameters and cross-checking it with the validation data, the optimal number of poles and zeros is identified for this LCS with $L = 50\ mm$ to be 19 poles and nine zeros. A fit factor of 97.51% is achieved which estimates the training input data. Moreover, the correlation of the reconstructed validation data is above 99%. Figure 4.12c shows the amplitude ratio of the discrete-time identified transfer function for the LCS under investigation along with the analytic solution by Bergh and Tijdeman [113]. In contrast to the analytic solution, which shows resonance at very similar frequencies, the attenuation is more pronounced in the actual acquired and post-processed data. In Figure 4.13, the identified transfer function is applied to reconstruct the signal, which is the final generalization step: Apart from the shock moment with not negligible overshoots before the shock (see Figure 4.13a), the reconstructed pressure curve shows a very high agreement with the measured reference signal, as depicted in Figure 4.13b.

Furthermore, the transfer function that was identified with test case #2 can be applied on other cases. Figure 4.14 shows the reconstructed signals of case #1 and #3 at different signal locations. Again, a very high agreement between the reconstructed signal and the reference signal is clearly visible. In order to quantify the quality of the transfer function determination and to show the reconstruction accuracy, Table 4.2 gives the correlation of the reconstructed with the reference pressure signal for all test cases. Furthermore, the usage of the data set, namely training, validation or generalization, is mentioned. For both LCS lengths, a very high reconstruction accuracy is achieved. Thus, the determination of the transfer function via a system identification process

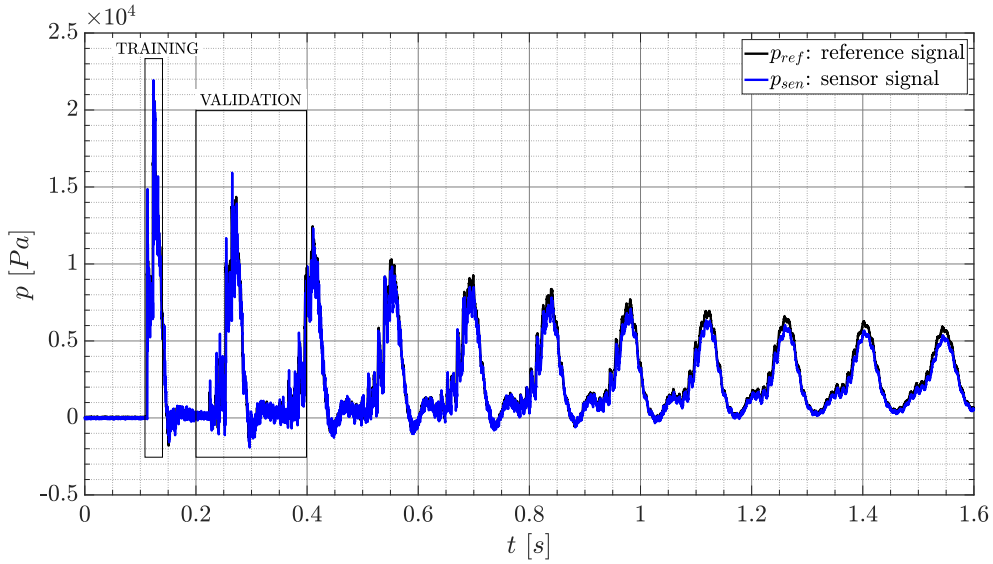

(a) Division of the input/output data: training and validation data sets indicated by the boxes

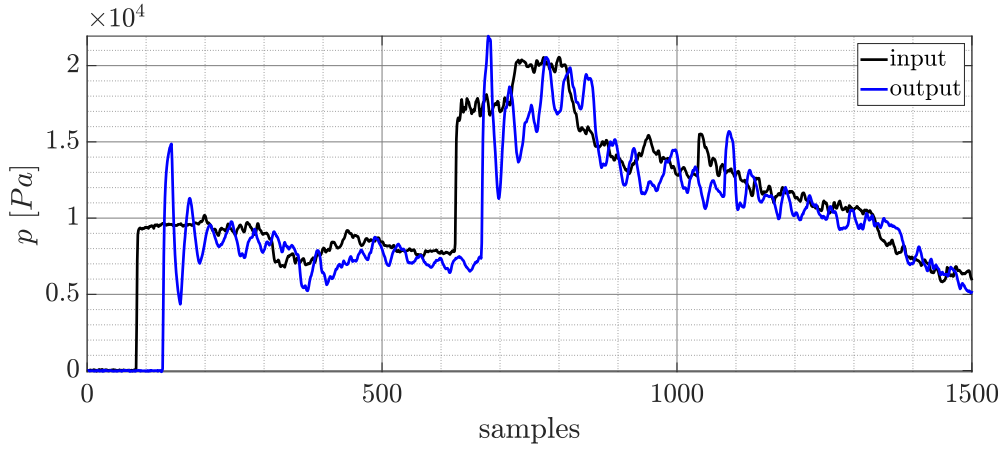

(b) Training input and output data

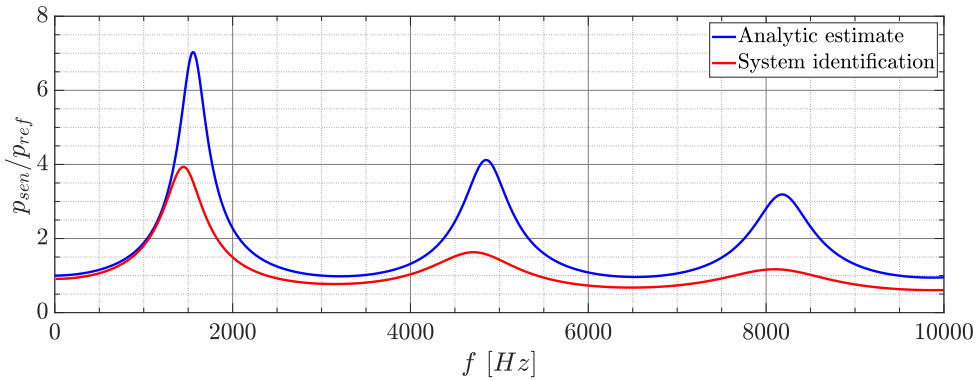

(c) Amplitude ratio of TF

Figure 4.12: Post-processing for the transfer function determination of the signal acquired for test case #2 [128]

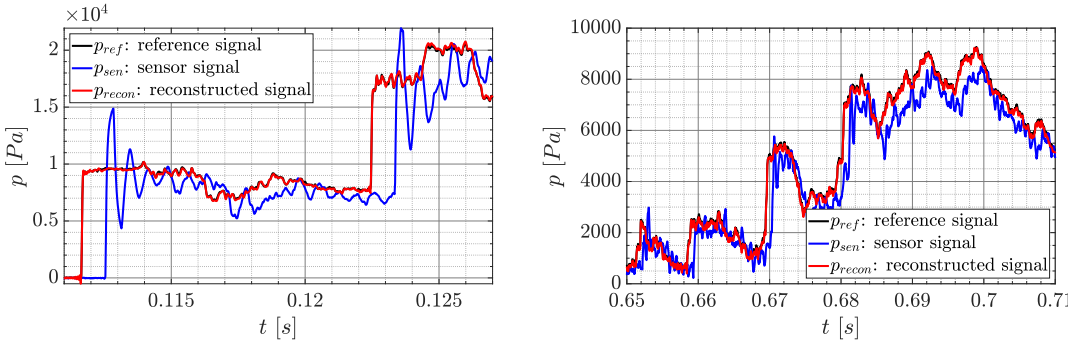

(a) Test case #2: Initial pressure step

(b) Test case #2: Generalization

Figure 4.13: Reconstruction of the pressure signal for case #2 [128]

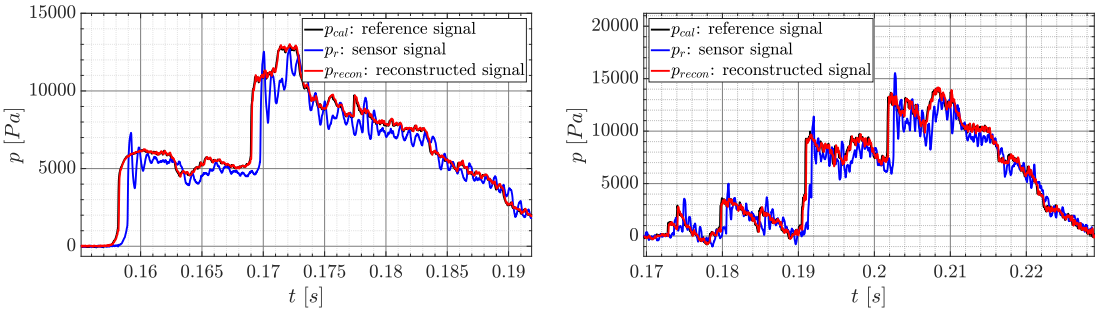

(a) Test case #1: Generalization

(b) Test case #3: Generalization

Figure 4.14: Generalization for different cases #1 and #3 [128]

shows very promising results and can be used in addition to the rather time consuming determination in the frequency test-rig [33].

Conclusion

Summing up the experimental results within this section, a discrete-time system identification approach can be applied in order to investigate the acoustic transfer function in a pneumatic line-cavity system (LCS). Fiber-optic differential pressure sensors are used in the shock tube facility at TUM-AER. The sensors acquire the high bandwidth pressure signal data resulting from the pressure change due to the shock. Various LCSs with differing dimensions are tested. Post-processed data show a high agreement and reproducibility when comparing it to reference data: A frequency range up to 10 kHz can be captured. Moreover, a reconstruction accuracy in the application of the estimated transfer function on new pressure data (generalization) is higher than 99 %. Furthermore, the 2nd generation fiber-optic pressure sensors show a good dynamic behavior. The linear pressure range of the sensor is confirmed up to 20 kPa.

4.2 Fast-response probe characteristics

After the fiber-optic sensor behavior was characterized in the section before, this section provides investigations on the general behavior of the flow around and inside the fast-response probe. First, a generic counterpart of the additive manufactured FRAP is investigated numerically in Section 4.2.1. Data from numerical simulations are compared to data from analytic theory and from experiments. In Section 4.2.2, the FRAP calibration behavior is shown. Besides the determination of the spatial and temporal calibration data set, the focus lies also on the application of the Gaussian process regression theory from Section 3.1.2 in order to faster generate the spatial calibration data set.

4.2.1 Numerical simulations

This section deals with the numerical treatment of the flow around and inside the multi-hole probe. CFD simulations are performed within the ANSYS CFD framework. Additional details can be extracted from the supervised student thesis (see Molz [132]) where multiple simulation approaches were tested and which led to the results presented in this thesis.

4.2.1.1 Five-hole probe spatial flow pattern

In this section, numerical simulations of the flow around a generic five-hole probe with a spherical probe head are performed and discussed. Especially, results of the numerical data, the analytic potential flow solution and the experimental calibration of an additive-manufactured five-hole probe are compared.

Design and geometric properties of the five-hole probe

The numerical simulations are performed with a generic five-hole probe, which is illustrated in Figure 4.15. In contrast to the fast-response probe, that is experimentally tested, several simplifications in the design process are made. For a faster convergence, a smooth shape for the back part of the probe was chosen. It also reduces the formation and excitation of a von Kármán vortex street. The outer dimensions are similar to the real, additively manufactured probe (see Figure 4.15c): The probe tip diameter is $d_{tip} = 3\ mm$ and the maximum probe shaft diameter is $d_{shaft} = 15\ mm$. All five pressure channels have a diameter of $d_{LCS} = 0.5\ mm$. The four circumferential pressure ports are placed in a cone angle of $\eta = 53°$ (see Figure 4.15d). Here, the five pressure channels run straight to the approximate location of the sensors and are designed as cylindrical holes with a fixed length of $L_{LCS} = 66\ mm$. In the additively manufactured probe, the pressure channels cannot be designed as straight tubes due to the spatial restrictions when assembling the sensors.

Mesh generation and numerical setup

After the generation of the probe CAD model, a numerical mesh is needed. All meshes are generated in ANSYS ICEMCFD (Version 2020 R1). The numerical block-structured mesh consists of H- and O-grids (see Figure 4.16). The size of the boundaries of the numerical domain are depicted in Figure 4.16a. By increasing the overall domain, a reduction in the influence of the flow around the probe in up- and downstream direction is achieved. The resolution around and inside the probe is adapted to the test case velocity, to obtain a non-dimensional wall distance $y^+ \approx 1$.

A grid independence study was performed resulting in the following numerical mesh: In total, the mesh consists of approximately 3.81 million hexahedral cells. A visualization of the mesh at the boundaries of the farfield and on the surface of the probe are given in Figure 4.17. The mesh is optimized for a high numerical mesh quality (determinants and angles of the cells). Furthermore, cell sizes at the respective block boundaries are adapted for better smoothness and transition between cells of different blocks.

CFD calculations are performed in ANSYS Fluent (Version 2020 R2). For the steady calculations, the pressure-based solver is chosen. The fluid is assumed to follow the ideal gas law with an ambient temperature of $T_\infty = 15°C$ and an operating pressure of $p_\infty = 1013\ hPa$. For the closure of the Reynolds-averaged-Navier-Stokes (RANS) equations, the k-ω shear stress transport (SST) turbulence model is chosen.

The following boundary conditions for the mesh boundaries are set: The probe outer surface and its pressure channels are modeled as *no slip* walls. The inlet is a *velocity inlet* with a fixed velocity magnitude and changing inflow angles, α and β. Here, the default settings for the inflow turbulence intensity and viscosity ratio are kept. For the other three surfaces in the farfield, a *pressure outlet* boundary condition with no gauge pressure is set. Table 4.3 shows the relevant settings for the flow solver, including the pressure-velocity coupling methods and the discretization schemes.

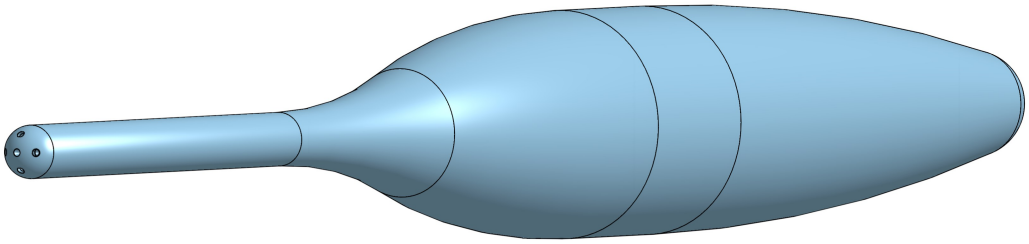

(a) Outer view

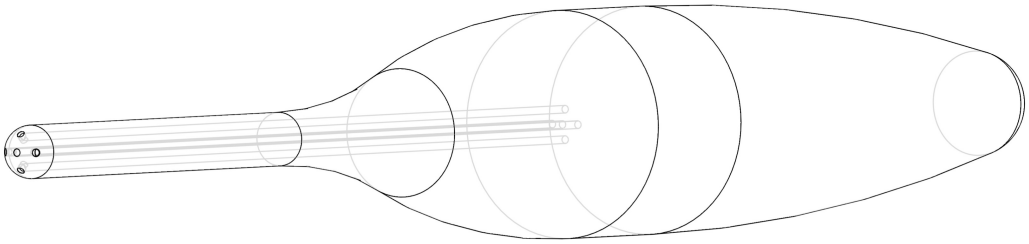

(b) Outer view - transparent

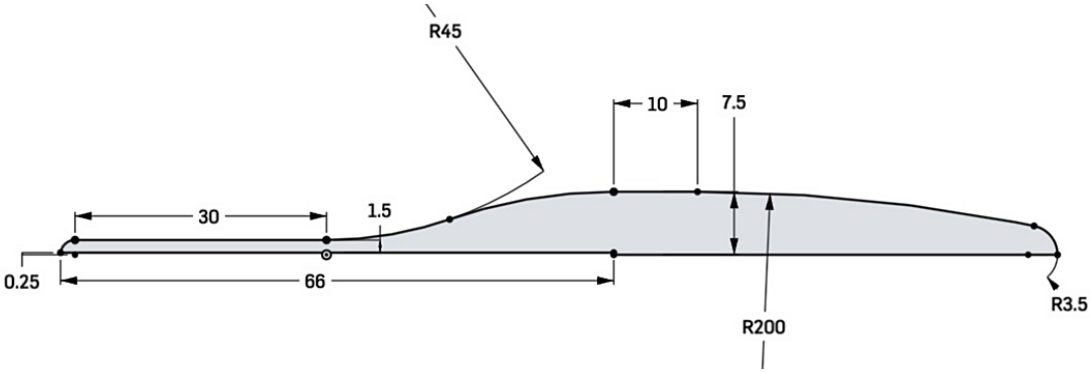

(c) Geometric properties in $[mm]$

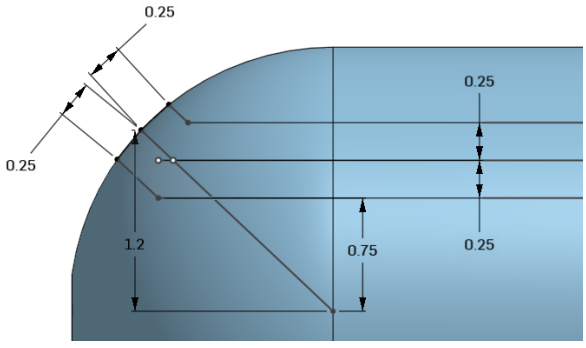

(d) Dimensions of the holes in $[mm]$

Figure 4.15: Design and size of the generic five-hole probe

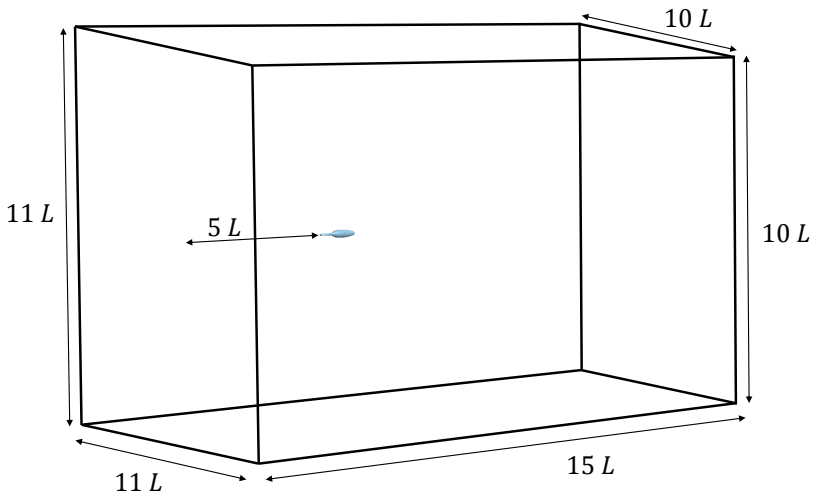

(a) Dimensions of the CFD domain in multiples of the probe length $L = L_{probe}$

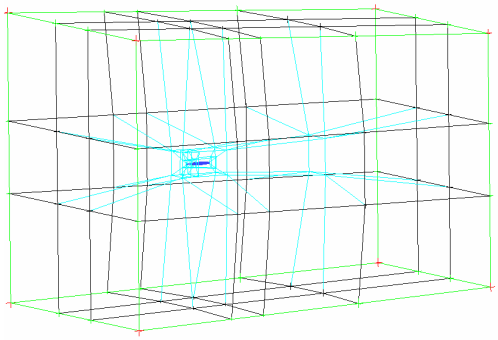

(b) Block structure: farfield

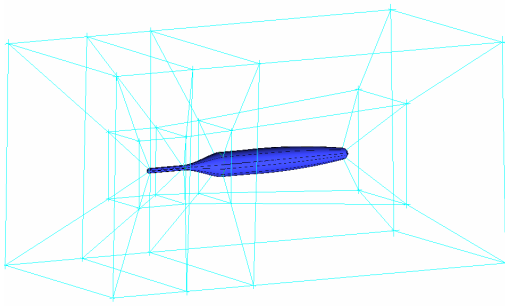

(c) Block structure: probe

Figure 4.16: CFD domain and block structure

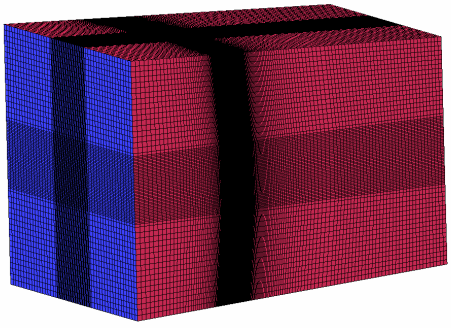

(a) Grid: farfield

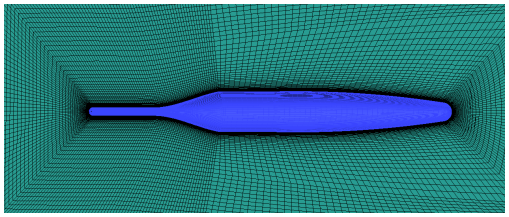

(b) Grid: probe

Figure 4.17: CFD domain and block structure

Table 4.3: Flow solver settings for the flow around the five-hole probe

Pressure-velocity coupling	SIMPLEC
Pressure	2nd order
Density	2nd order upwind
Momentum	2nd order upwind
Turbulent Kinetic Energy	2nd order upwind
Specific Dissipation Rate	2nd order upwind
Energy	2nd order upwind
Gradient	Least squares cell based

Analysis of the CFD results

The analysis comprises multiple simulations carried out with the mesh and the setting explained before. Two sweeps in the angle-of-attack α at fixed yaw angles $\beta = \{0, 10\}^\circ$ have been performed to investigate the flow field around the generic five-hole probe. The simulations have a fixed velocity magnitude at the inlet boundary condition of $U_\infty = 34\ m/s$ (at around a Mach number $M = 0.1$) to match the experimental calibration data of the similar fast-response pressure probe.

Figure 4.18 shows the surface pressure contour on the probe in form of the pressure coefficient $C_p = (p - p_s)/(0.5\rho U_\infty^2)$ for the case at $\alpha = \beta = 0^\circ$. The central port sees the maximum stagnation and hence experiences a value of $C_p = 1$. All circumferential ports measure the same pressure due to an axisymmetric flow field. In Figure 4.19, the contour plot of the velocity component in x-direction u is visualized in the x-z-plane at $y = 0$. Here, it can be seen, that the flow can follow the probe geometry, no separation occurs, and only a small recirculation area behind the probe is present.

In contrast to the aligned flow discussed before, the flow at large incidence angles is visualized in the following. Figure 4.20 depicts the surface pressure distribution on the probe at $\alpha = 40^\circ$ and $\beta = 10^\circ$. It is clearly visible how the stagnation point moved downwards in comparison to an aligned inflow. The lower pressure port (seen from the front) reads the highest pressure, whereas the pressure in the upper pressure channel is negative. For a better impression of the flow field around the probe, the pressure coefficient C_p contour plot in the x-z-plane at $y = 0$ is shown for a very similar, symmetric case at $\alpha = 40^\circ$ and $\beta = 0^\circ$ in Figure 4.21. Similar to the case in Figure 4.20, the stagnation point on the probe tip lies near the lower pressure port. A small separation bubble can be seen near the upper pressure port resulting in negative pressures at the upper sensor location.

For a more quantitative analysis, Figures 4.22 and 4.23 sum up the simulation results of the two angle-of-attack α-sweeps: Figure 4.22 depicts the pressure coefficients at the pressure ports for a fixed yaw angle $\beta = 0^\circ$ for various angle-of-attacks α. Besides the CFD-simulation results, also results from the potential flow theory (cf. Section 3.1.1 and Figure 3.3) and the experimental calibration of the additive-manufactured probe are presented. It is clearly visible, that the results from the three different sources follow the same trend. Nevertheless, significant differences in C_p are present. Especially, the results

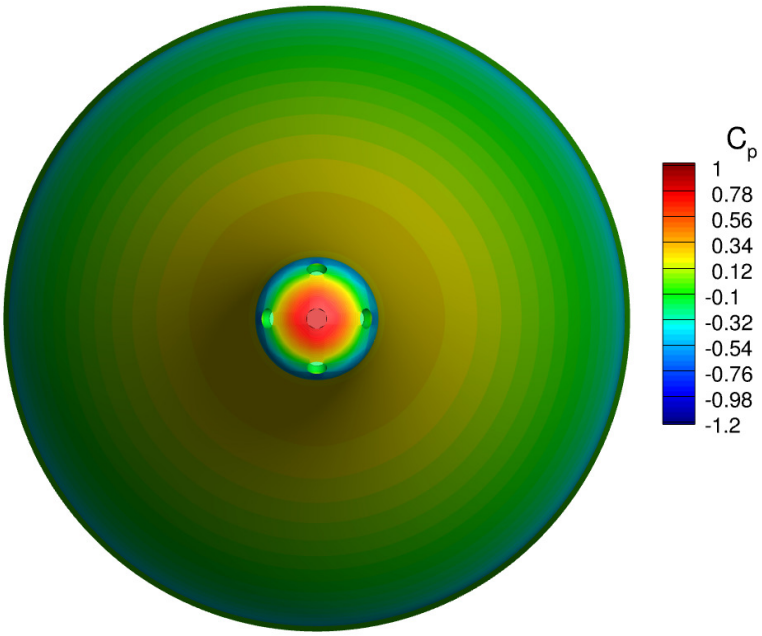

Figure 4.18: Surface pressure distribution C_p on the probe for $\alpha = \beta = 0°$

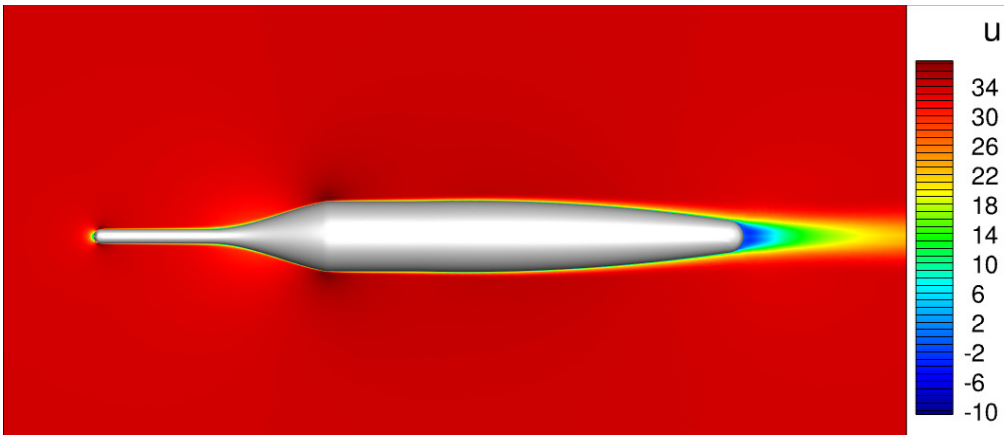

Figure 4.19: Contour plot of the velocity component in x-direction u in the vicinity of the probe for $\alpha = \beta = 0°$

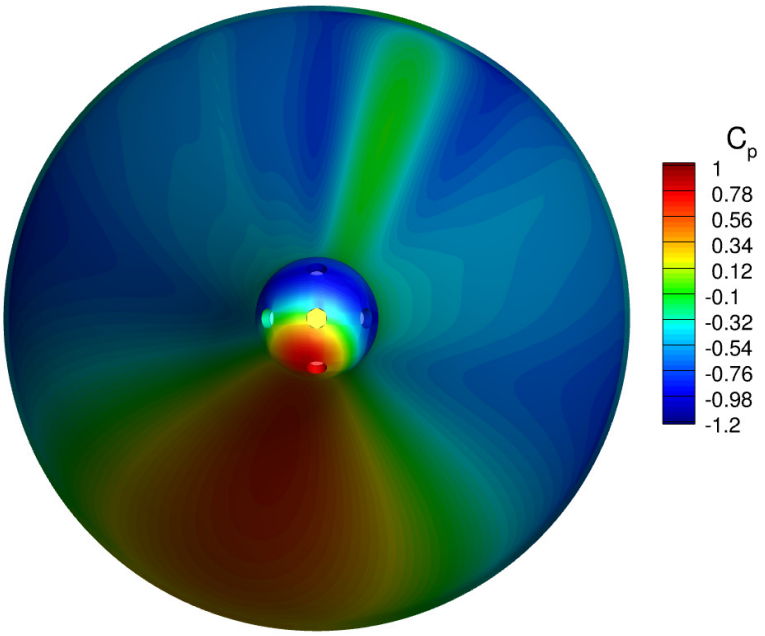

Figure 4.20: Surface pressure distribution C_p on the probe for $\alpha = 40°$ and $\beta = 10°$

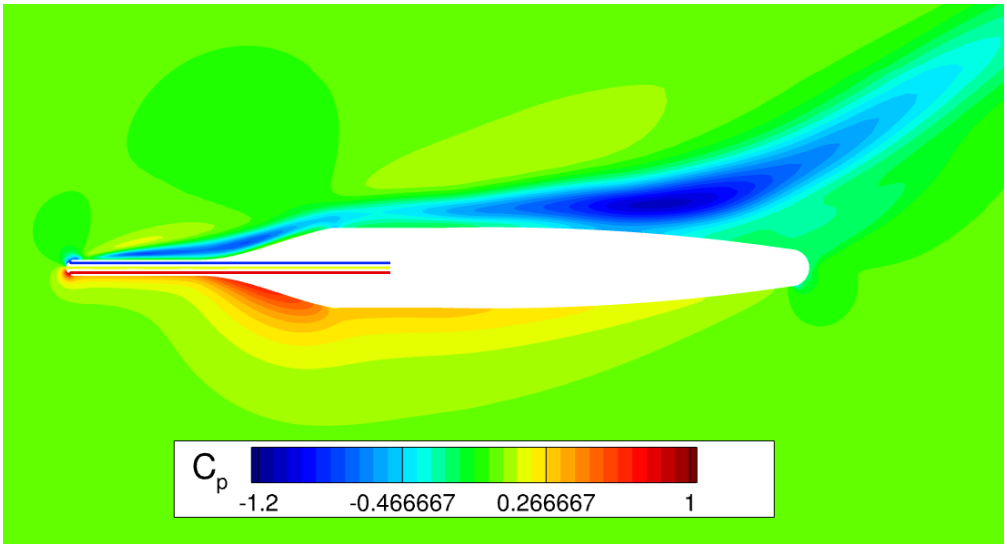

Figure 4.21: Contour plot of the pressure coefficient C_p in the vicinity of the probe for $\alpha = 40°$ and $\beta = 0°$

from the potential flow theory cannot follow the real flow behavior/pressure distribution on the probe. When comparing the CFD results with the experimental calibration data, a smaller discrepancy and partly a very good match between the data is noticeable. In general, the central pressure port shows the best agreement, while the circumferential ports are more sensitive to differences in the probe design (e.g. drill shape, cone angle η) and imperfections in the additive manufacturing leading to deviations between the two methods.

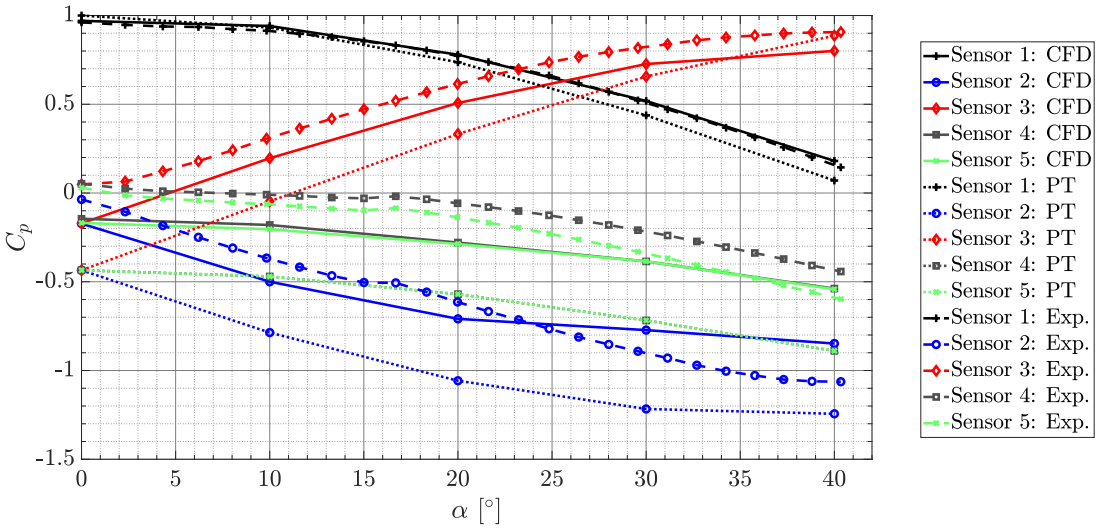

Figure 4.22: Pressure coefficient C_p at all five pressure sensors for an α-sweep at $\beta = 0°$

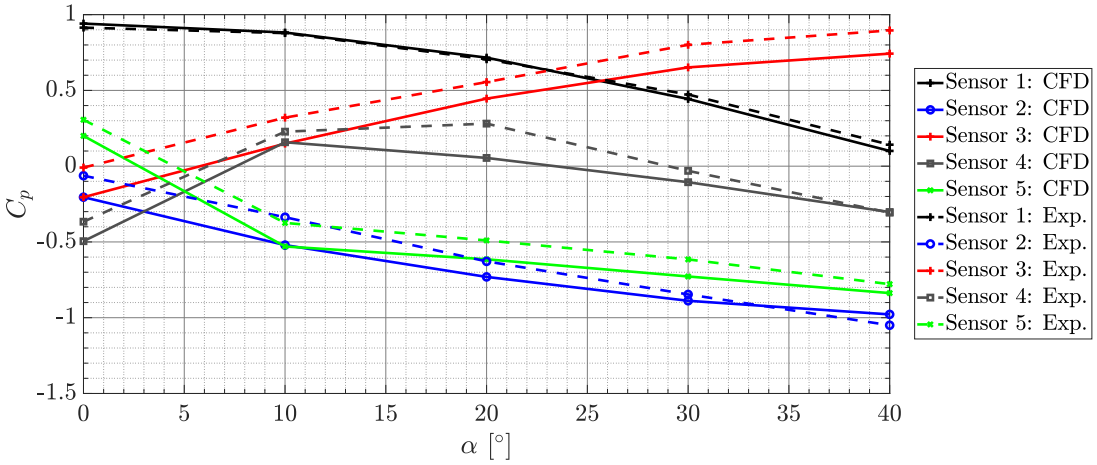

Figure 4.23: Pressure coefficient C_p at all five pressure sensors for an α-sweep at $\beta = 10°$

Figure 4.23 shows an α-sweep for $\beta = 10°$ for the CFD simulations and the experimental calibration tests. Similar to the α-sweep discussed before, both curves follow

the same trend with an almost constant offset within all sensors except sensor 1. This can be attributed to the higher sensitivity of the sensed pressure due to the design and placement of the circumferential pressure ports.

To conclude the analysis of the CFD simulation of the flow around the generic five-hole probe, it can be stated that an experimental determination of the spatial calibration characteristics is inevitable regardless of a good replication of the general behavior of the pressure distribution at the probe. Asymmetries and imperfections in the manufacturing process will change the probe calibration and cannot be mapped correctly by CFD analyses.

4.2.1.2 Transfer function determination

In this section, it is evaluated if a numerical treatment of the line-cavity system acoustics inside the pressure probe is sufficient enough to model the transfer function.

Therefore, a similar approach as in the experimental determination of the transfer function in the frequency rig is chosen. A generic 3D line-cavity system is subject to a sinusoidal pressure excitation at a distinct excitation frequency f. The dynamic system is investigated until the system response (resonance and/or attenuation) stays at an dynamically converged value. Both the pressures at the line inlet and at the location of the sensor are probed. By iterating through multiple frequencies, the full temporal characteristics of the LCS can be determined.

Geometric properties, mesh generation and numerical setup of the LCS

The 3D geometry and the numerical mesh of the LCS is set up in ANSYS ICEMCFD. The focus of this section lies on two generic tubings similar to the one experimentally testes in Section 4.1.3: a full LCS and a truncated one which lacks a cavity but otherwise is equivalent to the full LCS. The geometric properties of the LCSs are captured in Figure 4.24 and read: line diameter $d_{LCS} = 1.5\ mm$, line length $L_{LCS} = 200\ mm$, and cavity volume $V_{LCS} = \pi \cdot (D_{cavity}/2)^2 \cdot L_{cavity} = 21.21\ mm^3$ (only for the full LCS).

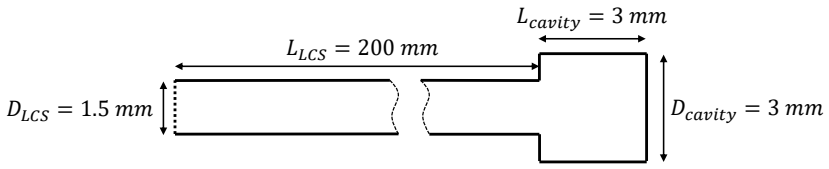

(a) Full LCS

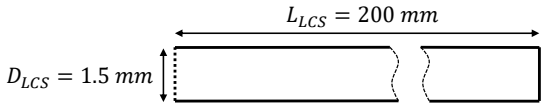

(b) Truncated LCS

Figure 4.24: Dimensions of the generic LCSs for the CFD analysis

Table 4.4: Flow solver settings for LCS simulations

Pressure-velocity coupling	Coupled
Pressure	2nd order
Density	3rd order MUSCL
Momentum	3rd order MUSCL
Turbulent Kinetic Energy	3rd order MUSCL
Specific Dissipation Rate	3rd order MUSCL
Energy	3rd order MUSCL
Gradient	Least squares cell based
Transient Formulation	Second Order Implicit

For both configurations, a grid independence study was performed. The full LCS configuration results in a mesh that consists of approximately 77000 hexahedral cells. Figure 4.25 visualizes the block structure and the mesh on the LCS walls. The cell size in the line direction is estimated by the minimum propagation distance of a disturbance at a given frequency $f = 2\ kHz$ – being the maximum tested excitation frequency – at speed of sound.

CFD calculations of the LCSs are performed in ANSYS Fluent (Version 2020 R2). For the unsteady/transient calculations, the pressure-based solver is chosen. The fluid is assumed to follow the ideal gas law with an ambient temperature of $T_\infty = 15°C$ and an operating pressure of $p_\infty = 1013\ hPa$. For the closure of the Reynolds-averaged-Navier-Stokes (RANS) equations, the k-ω shear stress transport (SST) turbulence model is chosen.

The pressure channel side walls in the line and all surfaces in the cavity are modeled as *no slip* walls. Since the transient solution of the pressure fluctuation traveling through the LCS is of interest, an unsteady *pressure inlet* boundary condition is set for the inlet surface. Hereby, a so-called *User Defined Function* (UDF) is set up and hooked to the inlet boundary condition. In the UDF, at every new time step, a new gauge pressure is calculated and is prescribed on the boundary surface with the UDF-function *DEFINE_PROFILE*. The applied pressure $p(t)$ is calculated depending on the CFD simulation current flow time t, the chosen excitation frequency f, a mean pressure p_0, and a pressure amplitude $\hat{p}$:

$$p(t) = p_0 + \hat{p} \cdot \sin(2\pi f \cdot t) \tag{4.7}$$

In addition, the default settings for the inflow turbulence intensity and viscosity ratio are kept. Table 4.4 shows the relevant settings for the flow solver, including the pressure-velocity coupling methods and the discretization schemes.

The time step is chosen to be $\Delta t = (\frac{1}{f})/40$ to adequately resolve the changing sinusoidal pressure input. For each time step 100 inner iterations are set in order to reach the residuum, which was chosen to be 10^{-7}, since bigger residuals led to differing results. After an initial transient response in the CFD solution, which for some simulations took

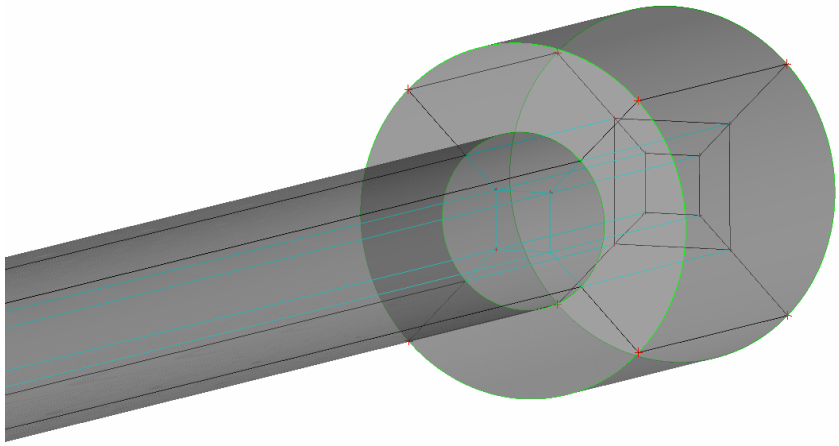

(a) Block structure LCS

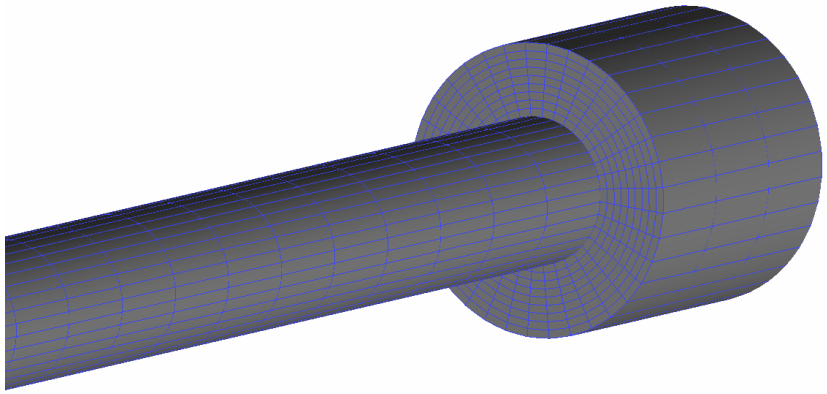

(b) Mesh on LCS walls

Figure 4.25: Full line-cavity system meshing in ANSYS ICEMCFD

several periods, the pressure signals at the inlet and at the sensor surface are used for the analysis within the next paragraph.

Analysis of the CFD results

In the ANSYS Fluent analysis of the two LCS configurations, the surface averaged pressures are recorded at the inlet domain and at the location of a fictive sensor, hence, at the end of the LCS. Figure 4.26 depicts the time series data for the full LCS configuration at an excitation frequency $f = 2\ kHz$. After the initial transient response, the simulation takes a not negligible amount of excitation periods to dynamically converge to the solution that can be further processed. The converged time series data are post-processed and transferred into frequency domain. In the frequency domain, the amplitude ratio $\hat{p}_{sensor}/\hat{p}_{tip}$ at the excited frequency and the phase shift ϕ between the two signals are calculated.

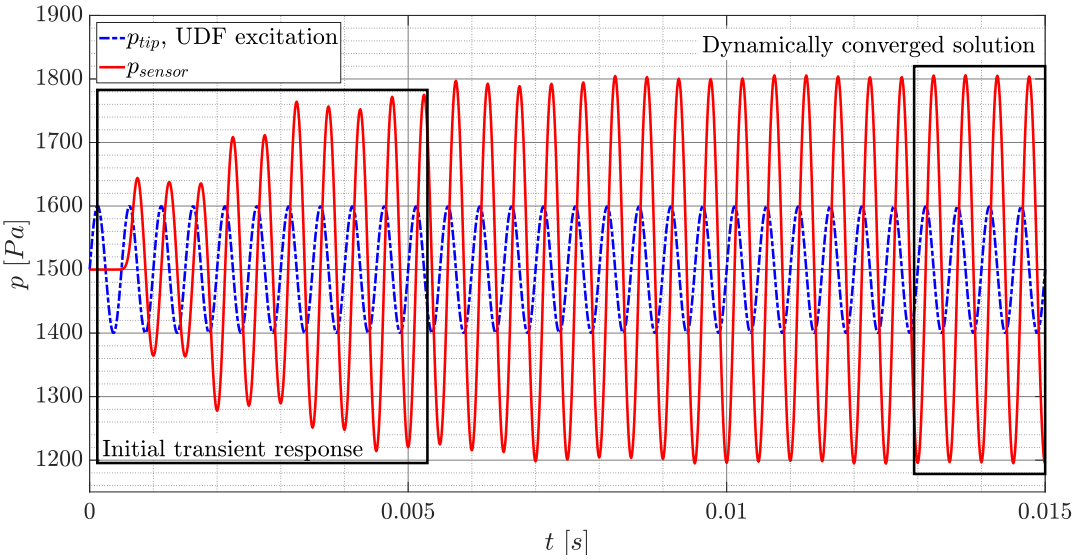

Figure 4.26: Time series data of a $f = 2\ kHz$ UDF excitation of the full LCS configuration

The following results show the post-processed data in comparison to the analytic solution, derived from the Bergh and Tijdeman approach (cf. [113] and Section 3.2.1), and also to experimentally obtained data. Figure 4.27 shows the results of the simulations of the truncated LCS setup. Besides the Bergh and Tijdeman solution, also experimental data from investigations in the frequency test rig (see also Section 4.1.3) are used for a comparison of the amplitude ratio in Figure 4.27a. Simulations are performed for excitations every $\Delta f = 100\ Hz$ with an additional refinements around the resonance peaks. The general LCS behavior – resonance and attenuation – is reproduced in the CFD simulations. The first resonance peak is detected at $f = 400\ Hz$ in the numeric simulation. However, the findings in the experiment and the analytic estimate show the peak at a lower frequency of around $f = 380\ Hz$, resulting in an 5.2% relative error of the CFD solution. The amplitude ratio at the resonance peak is overestimated by

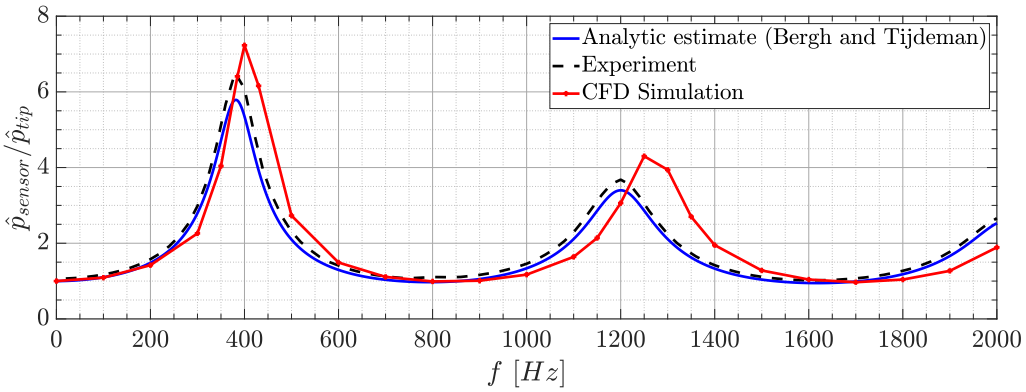

(a) Amplitude ratio

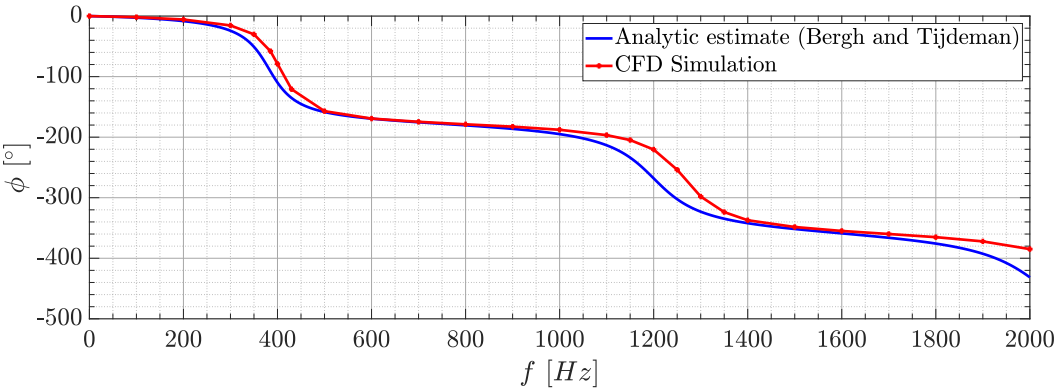

(b) Phase shift

Figure 4.27: CFD results for the transfer function determination of the truncated LCS

$\Delta\hat{p}_{sensor}/\hat{p}_{tip} = 0.723$, which constitutes to a 11.1% relative error. The simulation results deviate more at the second peak at around $f = 1200\ Hz$. Here, again, the simulation peak is located at a higher frequency than the experimental and analytic data. The amplitude ratio of the peaks deviates by $\Delta\hat{p}_{sensor}/\hat{p}_{tip} = 0.620$ which is a relative error of 16.8%. The trend for the phase lag in Figure 4.27b is similar. The change of phase at the resonance peak locations is shifted to higher frequencies within the CFD simulations. However, the slope of the curves match very well and the overall agreement is good.

Figure 4.28 shows a comparison of the aggregated results of the simulations of the full LCS system to the analytic estimate for excitations every $\Delta f = 100\ Hz$ up to $f = 2200\ Hz$. No experimental data are available. A similar behavior compared to the truncated case can be seen. The amplitude ratios $\hat{p}_{sensor}/\hat{p}_{tip}$ are amplified at the resonance peaks. Furthermore, the peaks occur at slightly higher frequencies compared to the analytic solution. The first resonance peak is detected at $f = 380\ Hz$ in the numeric simulation. In the analytic solution, the peak is located at a lower frequency of around $f = 360\ Hz$, resulting in an 5.6% relative error of the CFD solution. The amplitude ratio at the resonance peak is overestimated by $\Delta\hat{p}_{sensor}/\hat{p}_{tip} = 1.59$, which

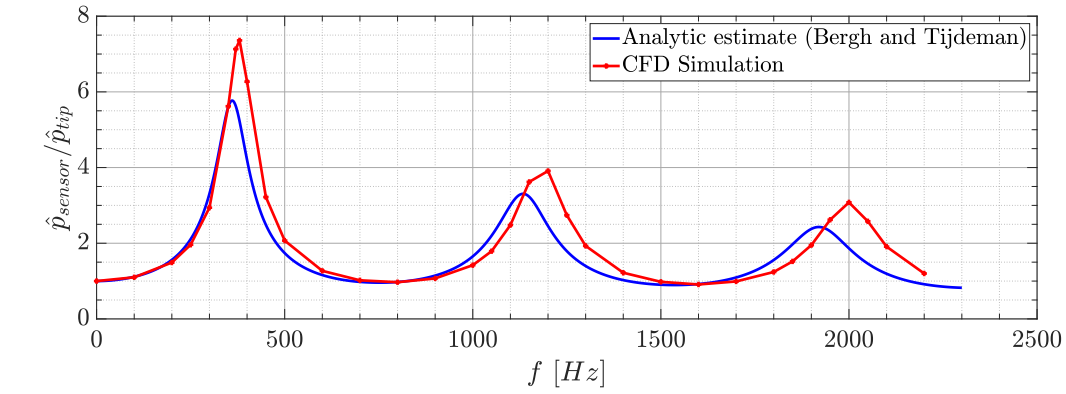

(a) Amplitude ratio

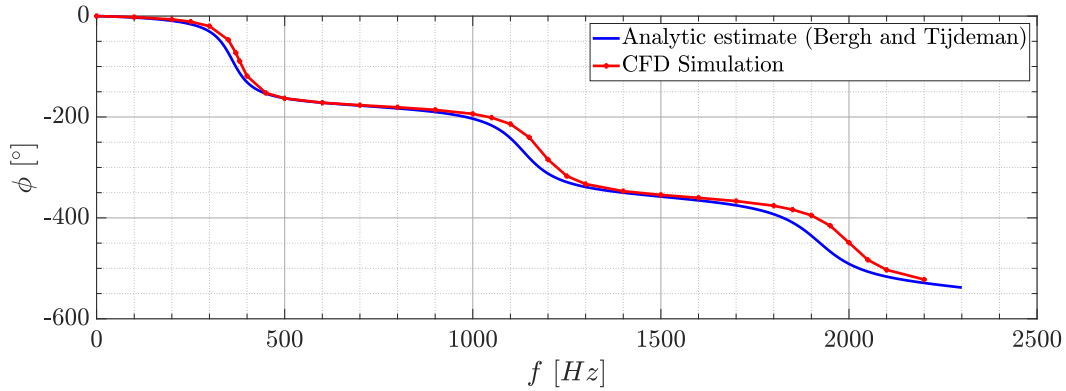

(b) Phase shift

Figure 4.28: CFD results for the transfer function determination of the full LCS

constitutes to a 27.6% relative error. For the second and third resonance peak, a relative error in the detected peak frequency of 6.2% and 4.2% is detected, respectively. Again, the amplitude ratio seems to be overestimated for the second and third peak which results in a larger relative error of 18.1% and 26.8%, respectively. As already seen for the truncated case, the change of phase of the CFD simulations matches well with the analytic solution.

For the identification and numerical determination of the LCS behavior, the simulations show acceptable results in comparison to the experimentation. Simulations accurately predict the general behavior of resonance and attenuation. With higher excitation frequencies, however, smaller simulation time steps are needed and a refinement of the grid is necessary. This in turn leads to very high computational costs for the determination of the transfer function. Nevertheless, as described, a realistic treatment of the LCS in CFD simulations can be achieved by introducing unsteadiness into the simulation using the UDF implementation.

4.2.2 Spatial and temporal calibration

In this section, selected results describing the FRAP calibration behavior are shown. Both spatial and temporal characteristics are addressed in the following. First, results from the spatial calibration are discussed, also comparing the different reconstruction approaches. Second, the application of Gaussian process regression on probe calibration data is shown. The last part discusses the temporal calibration of the FRAP and the thereby identified transfer functions of the LCS inside the probe.

4.2.2.1 Spatial calibration: Interpolation and ANN approach

As a test for the spatial calibration, data for 258 test points (α-β-combinations) are acquired after the probe calibration for a defined Mach number of $M = 0.10$. As already introduced in the theoretical Section 3.1.1.1, a pre-specified overlap margin ε in the calibration coefficient definition has to be set. Therefore, Figure 4.29 shows the dependency of the spatial reconstruction accuracy as a function of the margin ε. In the subfigures, the maximum absolute (maxabs) errors and the root-mean-squared (rms) values of the flow angles α and β, and the flow velocity magnitude U are depicted. When looking at the maximum absolute deviations $max(|*|)$ of the three variables, it is noticeable that a minimum is reached at $\varepsilon = 0.25$ for α. The other two variables have an almost constant value in the range $\varepsilon = (0.1,\ 0.25)$. The analysis of the RMS values shows an inconsistent result: while the $(\Delta\alpha)_{rms}$ slightly decreases with increasing margin, the $(\Delta\beta)_{rms}$ shows an opposite trend. It can be concluded that a margin value in the range between $\varepsilon = (0.1,\ 0.25)$ is preferable. Hence, in the following, a margin value of $\varepsilon = 0.25$ is assumed for all FRAP applications.

Figure 4.30 depicts the post-processed angles considering three calibration Mach numbers $M_{calib} = \{0.05,\ 0.1,\ 0.2\}$. The post-processed angles are compared to the actual angles set in the free-jet wind tunnel. Furthermore, the test point locations are marked with the highest α and β reconstruction errors, respectively.

Table 4.5 gives a summary of the dependence of the reconstruction accuracy of α, β and U on the number of calibration Mach number data sets. By incorporating, more than one calibration data set, the accuracy significantly increases, hence, the deviations decrease. For the usage of all three Mach number calibration data sets, the RMS errors decrease below 0.2° or 0.2 m/s for the angles and the velocity magnitude, respectively. The values in the bottom row correspond to the results in Figure 4.30.

The following discussion compares the post-processing accuracy and time consumption of the two different spatial reconstruction approaches, the local interpolation and neural network. The ANN has $N = 25$ neurons in the hidden layer (see Figure 3.13a). Both methods show mean absolute errors below 1° for both angles. Table 4.6 shows maximum absolute (maxabs) errors, root-mean-squared (rms) values and standard deviations (std) for both angles. The Delauney triangulated interpolation calculation results in smaller deviations compared to the ANN approach. This is due to a rather low amount of neurons in the ANN architecture ($N = 25$ neurons). Nevertheless, both methods show acceptable errors for tested angles up to 60°.

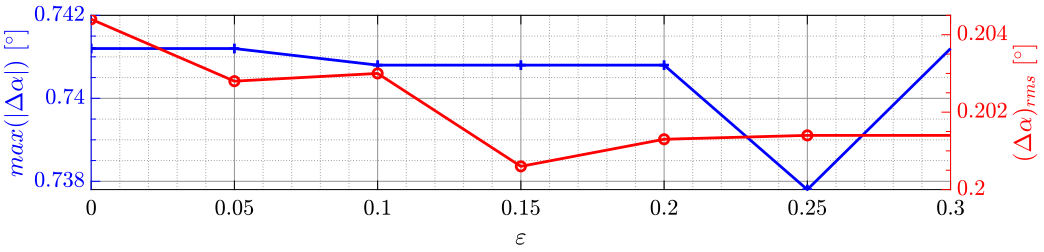

(a) Flow angle α

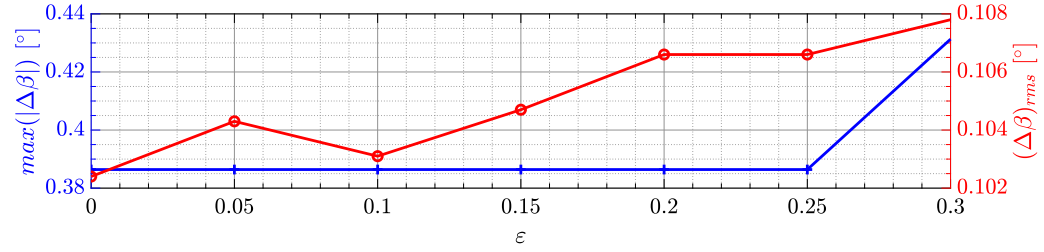

(b) Flow angle β

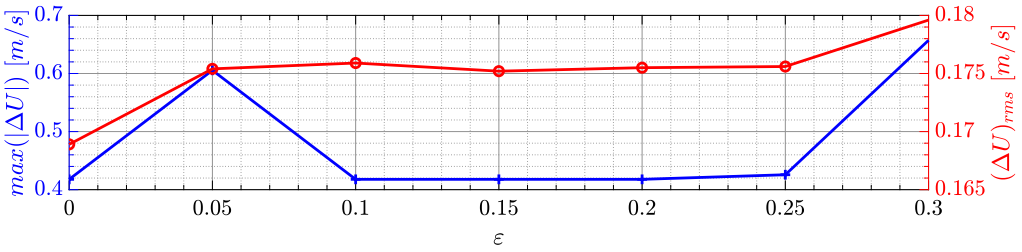

(c) Flow velocity magnitude U

Figure 4.29: Dependency of the spatial reconstruction accuracy as a function of the margin ε for α, β, and U

Table 4.5: Reconstruction accuracy dependence on the number of calibration Mach number data sets

M_{cal}	$\Delta\alpha$ [°]		$\Delta\beta$ [°]		ΔU [m/s]	
	maxabs	*rms*	*maxabs*	*rms*	*maxabs*	*rms*
0.05	2.41	0.47	0.93	0.31	1.65	0.57
0.2	1.65	0.43	2.44	0.53	1.73	0.24
{0.05, 0.2}	2.12	0.42	0.96	0.30	1.11	0.40
{0.05, 0.1, 0.2}	0.74	0.20	0.39	0.11	0.43	0.18

The reconstructed velocities match the fixed velocity in the free-jet with relative errors smaller than 1% for both methods. Applying the MATLAB built-in functions for both

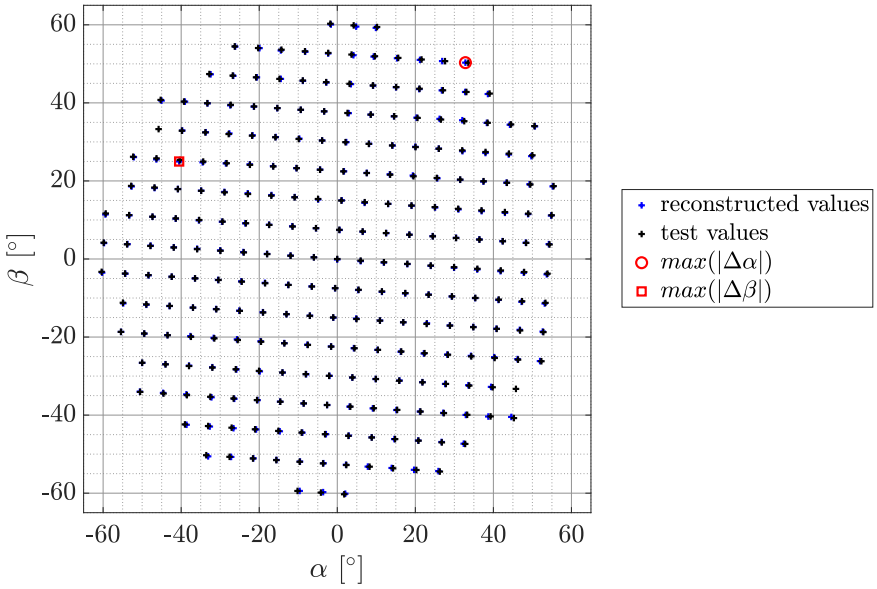

Figure 4.30: Reconstructed/post-processed flow angles compared to test angles set in the free-jet wind tunnel

Table 4.6: Spatial reconstruction results for both approaches

	$\Delta\alpha$ [°]			$\Delta\beta$ [°]		
	maxabs	*rms*	*std*	*maxabs*	*rms*	*std*
Interpolation	0.74	0.20	0.20	0.39	0.11	0.11
ANN	1.80	0.53	0.50	1.13	0.35	0.35

methods results in a speed-up factor of up to 5 for the neural network processing, in contrast to the Delauney triangulated interpolation method. The demand of fast data processing increases, when measuring in highly unsteady flows with sampling frequencies bigger than $f_s > 10\ kHz$. Interpolation methods are optimized and represent the state-of-the-art solution for multi-hole probe post-processing. However, the neural network approach may lead to reduced calculation times. All results in the Chapters 5 and 6 are post-processed with the interpolation reconstruction due to an increased accuracy.

4.2.2.2 Gaussian process regression for five-hole pressure probes

In this subsection, the results of the Gaussian process regression approach for probe calibration, as described in Section 3.1.2, are shown. The contents of this chapter have been published as a peer-reviewed research paper in the journal *Measurement Science*

and Technology [92][4]:

As described in Section 3.1, the spatial calibration of five-hole probes results in four calibration surfaces for α, β, A_t and A_s as functions of $f(b_\alpha, b_\beta)$. Therefore, four $\mathcal{GP}$ regressions will be investigated simultaneously in this section. The determination of the supporting points of the updated $\mathcal{GP}$s will be evaluated globally, but the updating of every single $\mathcal{GP}$ itself is handled independently.

As a first step, all available calibration data sets are read in: They consist of data of 24 five-hole probes, which are shaped differently. The probe stem shape varies between straight, L-shaped and cobra-shaped probe stems and conical and hemispheric probe tip shapes are present. For some of the calibrated probes, data for multiple inflow Mach numbers are available. Therefore, 45 input data sets in the Mach number range between $M = (0.024,\ 0.95)$ are used to train the initial $\mathcal{GP}$. When concatenating the input data sets, with $n = 47577$ calibration points, the number of points exceeds the limit for the standard $\mathcal{GP}$ regression due to limitation of the necessary $\mathcal{O}(n^3)$ matrix manipulations (cf. $\mathcal{GP}$ theory in Section 3.1.2.2). Hence, the sparse approximation with $m = 1681$ locations $(b_\alpha|b_\beta)$ is applied which in turn reduces the costs to $\mathcal{O}(mn^2)$. As the covariance function, the Matérn 3/2 kernel is used for the four $\mathcal{GP}$s and is initialized with the initial hyperparameters in Table 4.7. After initialization, the $\mathcal{GP}$ is updated with the sparse input values. Figure 4.31 shows the initial $\mathcal{GP}$s for the four calibration surfaces.

Table 4.7: Prior and optimized hyperparameters for the Matérn 3/2 kernel function in the five-hole pressure probe test case [92]

	initial hyperparameter hyp				optimized hyperparameter hyp_{opt}			
	$\mathcal{GP}_\alpha$	$\mathcal{GP}_\beta$	$\mathcal{GP}_{A_t}$	$\mathcal{GP}_{A_s}$	$\mathcal{GP}_\alpha$	$\mathcal{GP}_\beta$	$\mathcal{GP}_{A_t}$	$\mathcal{GP}_{A_s}$
σ_l	50.0	50.0	50.0	50.0	8.06	7.00	7.82	9.20
σ_f	10.0	10.0	10.0	10.0	4.28	4.53	0.21	0.29
σ_n	0.1	0.1	0.1	0.1	$2.55 \cdot 10^{-5}$	$2.06 \cdot 10^{-6}$	$1.59 \cdot 10^{-6}$	$4.02 \cdot 10^{-6}$

In order to better compare the output of the $\mathcal{GP}$ regression, the probe under investigation was fully calibrated to serve as a reference: The straight five-hole probe with a hemispheric probe tip was calibrated for three inflow velocities. Two of these calibration data sets are part of the input data sets and the remaining one is the *test* calibration, denoted either as *full* calibration or with the index $*_{test}$.

In the next step, optimized hyperparameters for the four $\mathcal{GP}$s are found by optimizing the log marginal likelihood $\mathcal{L}$. The optimized hyperparameters are gathered in Table 4.7 and remain unchanged during the upcoming updating routine. In the updating pro-

[4]The journal article was published under the terms of the *Creative Commons* licence CC BY 4.0. The first author was responsible for the conception, the execution of the tests and the writing of the paper. The co-author has consented to publication, here.

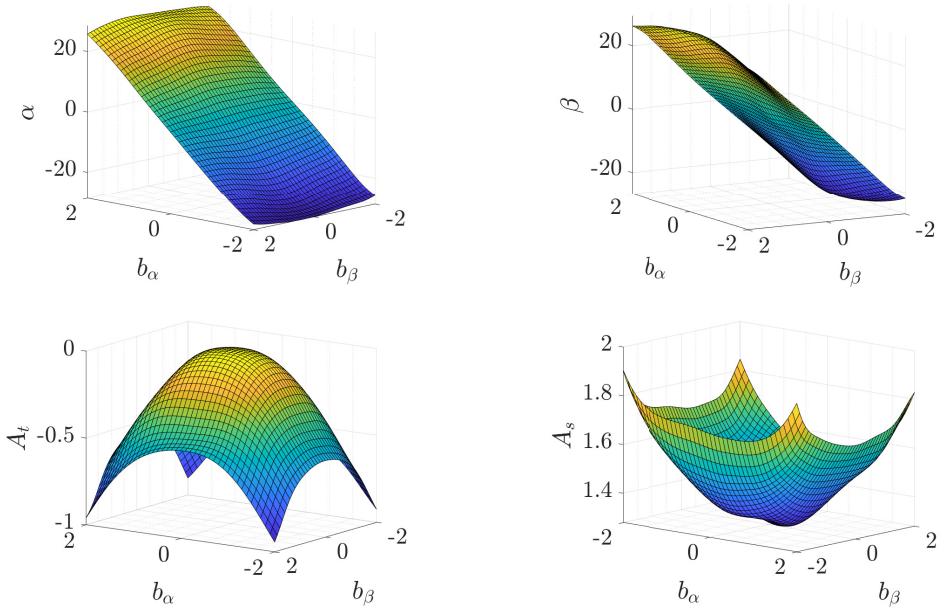

Figure 4.31: Initial $\mathcal{GP}$s for the four calibration surfaces [92]

cedure, supporting point locations are added to the $\mathcal{GP}$. Due to the fact, that four $\mathcal{GP}$s are updated simultaneously, a criterion is defined which $\mathcal{GP}$ contributes the next supporting point. For each $\mathcal{GP}$, the location is calculated which shows the maximum standard deviation of the updated $\mathcal{GP}$ normalized by the standard deviation of the first iteration. Depending which of the four $\mathcal{GP}$s experiences the highest normalized standard deviation, the location of the additional supporting point is chosen for the next iteration for all $\mathcal{GP}$s. A termination criterion stopping the iterative updating process can be applied. For example, one could choose the maximum normalized standard deviation or the RMS value of the sum of standard deviations for the four $\mathcal{GP}$s as an indicator. If that indicator falls below a pre-defined margin, the termination criterion is met. In the presented case, the full calibration for the multi-hole probe is available for comparison to the results of the $\mathcal{GP}$. The number of iterations is fixed to 300 steps for the first part of the investigation. After each iteration, the RMS error between the $\mathcal{GP}$ output data and the reference calibration data is displayed in the semi logarithmic plot in Figure 4.32. In the $rms(\beta_{\mathcal{GP}} - \beta_{test})$ plot, the RMS value drops from around 1° for the 20th iteration to 0.2° after approximately 80 iterations, until it asymptotically converges to a value near 0.1° for 250+ iterations.

Figure 4.33 visualizes the $\mathcal{GP}$ outputs of the 80th iteration of the four calibration surfaces. Furthermore, the 80 supporting points and the full calibration test surfaces are shown by red circles. Visually there are only very small deviations in the A_t and A_s plot noticeable. The errors between the α and β $\mathcal{GP}$ output and the full calibration seem negligible.

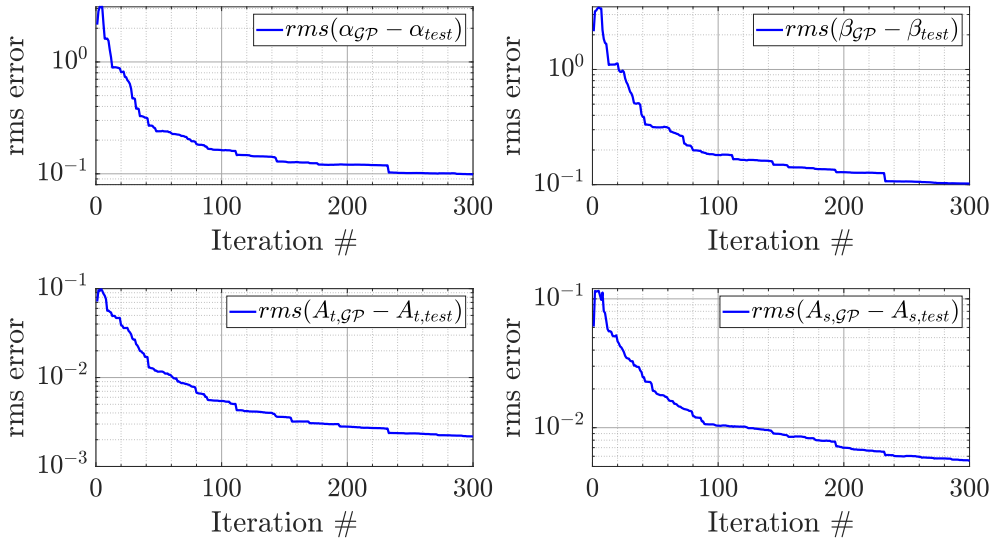

Figure 4.32: RMS error convergence of the $\mathcal{GP}$ outputs and the full calibration values with increasing iterations [92]

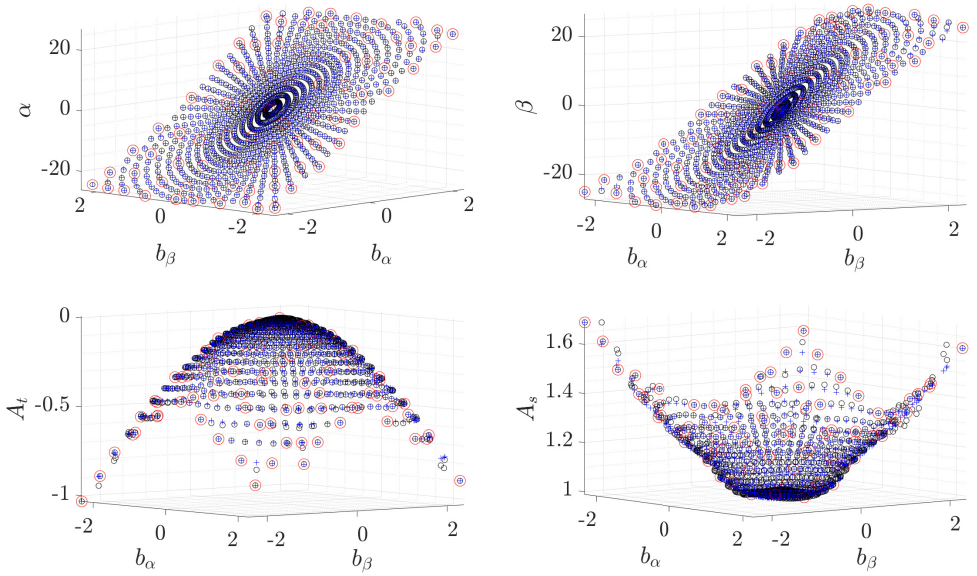

Figure 4.33: Updated $\mathcal{GP}$s for the four calibration surfaces after the addition of 80 supporting points: +(blue) - $\mathcal{GP}$ output, ∘(black) - full calibration, ◯(red) - supporting points [92]

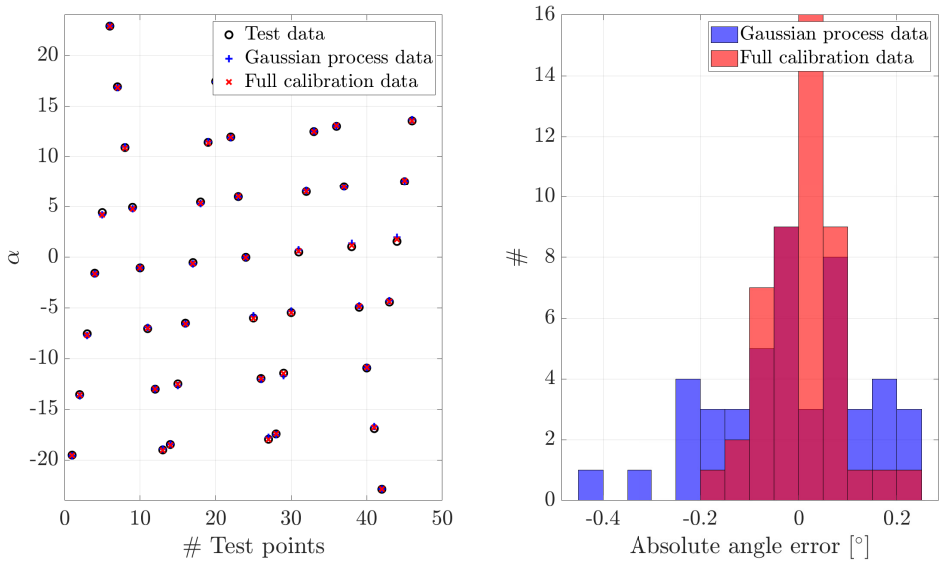

Figure 4.34: Test point reconstruction of the angle α with the updated $\mathcal{GP}$ after the addition of 80 supporting points compared to the full calibration reconstruction [92]

Table 4.8: Spatial reconstruction results for the $\mathcal{GP}$ after the 80th iteration compared to the full calibration data [92]

	$\Delta\alpha$ [°]			$\Delta\beta$ [°]			$\Delta\ M\ [\cdot 10^{-3}]$		
	maxabs	*rms*	*std*	*maxabs*	*rms*	*std*	*maxabs*	*rms*	*std*
$\mathcal{GP}$	0.41	0.14	0.15	0.27	0.13	0.13	1.07	0.42	0.40
Full calibration	0.23	0.08	0.08	0.26	0.09	0.08	0.63	0.36	0.21

For quantifying the visually perceived deviations in Figure 4.33, a reconstruction of unknown test points is performed in the next step, also known as *generalization*. In this process 47 test data points, which were measured independently of the determination of the calibration surfaces, are post-processed with the final $\mathcal{GP}$ output and the full calibration data. The test points comprise pressure measurements $\mathbf{p}_T$ of different angle combinations at a fixed Mach number of $M = 0.1$. Figure 4.34 and Figure 4.35 show the results of the post-processing step conducted with the $\mathcal{GP}$ and the full calibration data, visualizing the reconstructed angles. In addition, a histogram shows the absolute angle errors in [°], calculated with the true angle values set in the calibration wind tunnel as reference values.

The quantified results are summed up in Table 4.8: Apart from the maximum absolute occurring error among the test results *maxabs*, the RMS errors *rms*, and the standard deviation *std* are calculated for all test points for the angles α and β as well as for the reconstructed Mach number M.

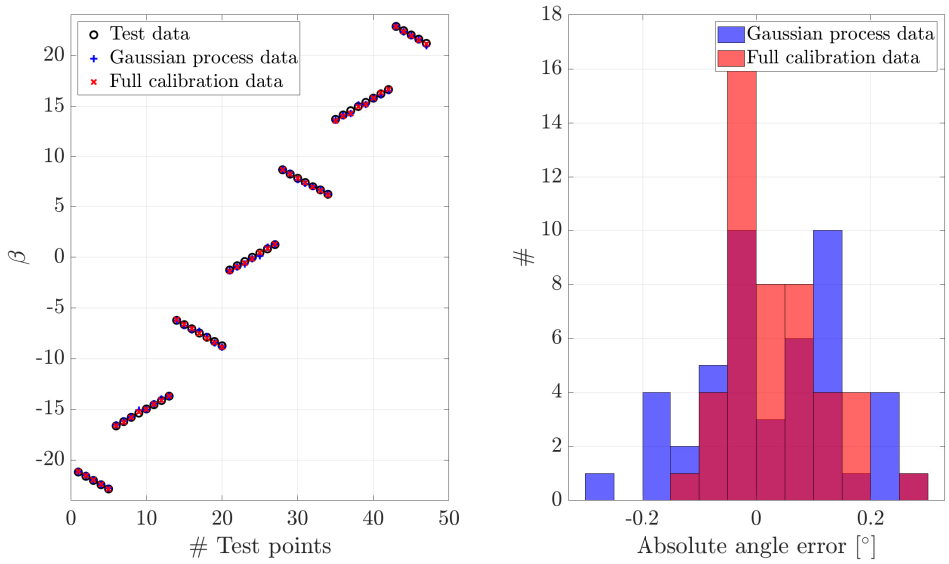

Figure 4.35: Test point reconstruction of the angle β with the updated $\mathcal{GP}$ after the addition of 80 supporting points compared to the full calibration reconstruction [92]

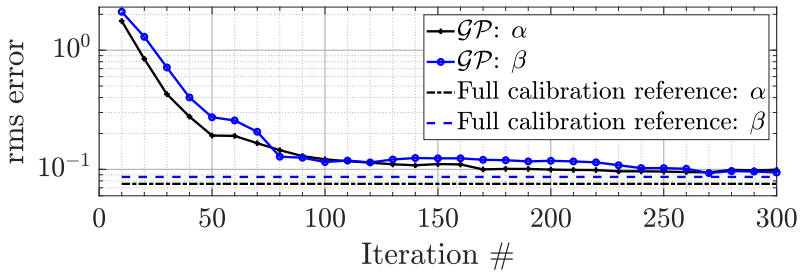

Figure 4.36: RMS errors of the test point reconstruction of the angles α and β when increasing the number of updating iterations of the $\mathcal{GP}$ [92]

A series of reconstructions/generalizations with different sized $\mathcal{GP}$ models concludes the $\mathcal{GP}$ investigations. Thereby, the number of supporting points was increased in steps of 10 up to 300 supporting points. The reconstruction accuracy in terms of the RMS error of the $\mathcal{GP}$ α and β is displayed in the semi logarithmic plot dependent on the number of supporting points/iterations in the $\mathcal{GP}$ updating process in Figure 4.36. With an increasing number of supporting points, the RMS errors asymptotically approach the reference values of the full calibration reconstruction. After 80 to 100 supporting points, only marginal improvements are noticeable. In order to make this statement more quantifiable in terms of the counteracting evaluation criteria – calibration time savings vs. a worsened reconstruction accuracy – the following can be concluded: the number of actually measured points to build a calibration surface can be decreased over one order of magnitude by applying the $\mathcal{GP}$ regression. The calibration surface is still

capable to reconstruct the properties with almost the same accuracy as with the full data set. If even lower requirements are made in terms of reconstruction accuracy, the number of supporting points can be reduced by a multiple of the already made savings. Hence, calibration setup costs, expressed by the number or time of measured points, could be reduced in this example by the factor of $F = 1014/80 = 12.68$ for high reconstruction accuracy (angle RMS below 0.15°) or the factor of $F = 1014/40 = 25.35$ for lower reconstruction accuracy (angle RMS below 0.5°).

4.2.2.3 Temporal probe calibration in the frequency test-rig

For the straight FRAP in this thesis, the transfer function is determined experimentally in the frequency test-rig (see Section 3.2.2). Sinusoidal signals are emitted by a speaker and recorded at specified frequency steps ($\Delta f = 20\ Hz$). Consequently, the transfer function is obtained. The temporal calibration is performed for frequencies up to $f_{cal,max} = 10\ kHz$.

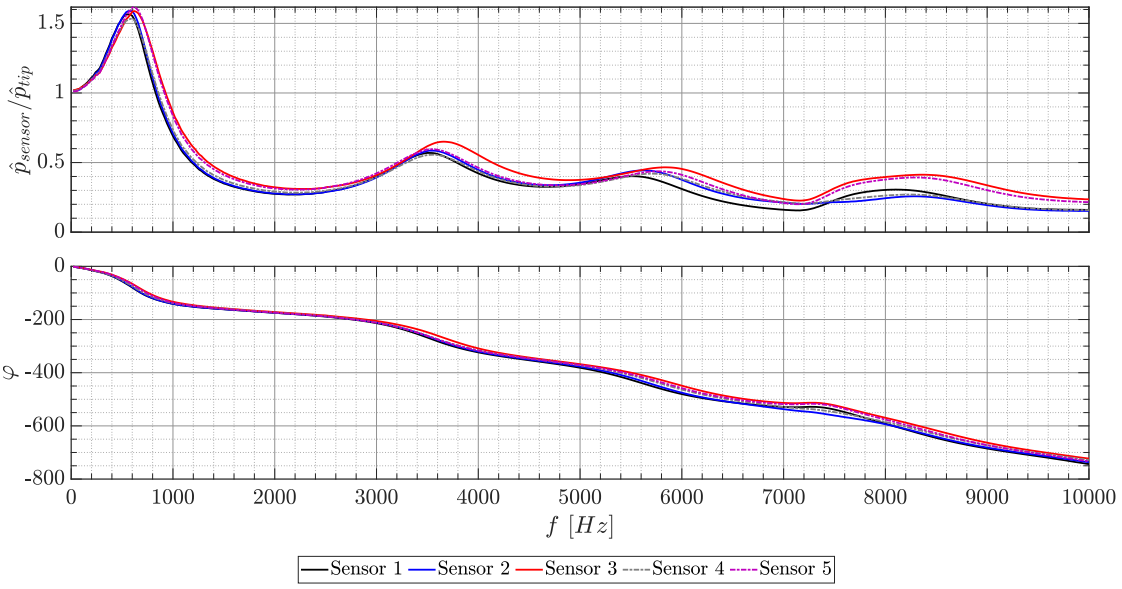

Figure 4.37: Attenuation and phase shift of the probe tip signal in the line-cavity system as a result of the transfer function determination in the frequency test rig

Figure 4.37 depicts the attenuation and phase shift of the five line-cavity systems of the FRAP. When the transfer function characteristics of all five sensors/LCSs are compared, a very high degree of similarity can be observed. This is obviously due to the geometric shape of the mostly straight tubings. Small discrepancies between the different sensors indicate that a purely analytical determination of the transfer function is not sufficient. Therefore, an experimental analysis is required to correctly calculate and reconstruct higher-frequency signals. It is clearly visible, that for some higher frequency ranges the amplitude is attenuated to $\leq 25\%$ of the initial pressure signal magnitude at the probe

tip. In particular, if the high-frequency parts of the signal are only represented very weakly (very small pressure fluctuation magnitudes of $p' \approx 10^{-3}\ Pa$), this can produce problems in the reconstruction. Due to the minimal resolution of the DAQ measurement system, further attenuation of the signal within the TF reconstruction may even lead to unphysical reconstructions of the real signal. This problem will be discussed in more detail in Section 5.3 on the spatial and temporal resolution of the FRAP in grid-generated turbulence [133].

5 Measurement resolution and uncertainty

The focus of this section lies on the quantification and discussion of the measurement resolution and uncertainty when conducting measurements with fast-response multi-hole probes. Since the unsteady flow field in the wake of objects is of great interest in experimental aerodynamics, the understanding of the characteristics and limits of the applied measurement techniques can help to cover the highly fluctuating phenomena to a very large extent with the measured data.
As an introduction into the topic, Section 5.1 discusses fundamentals of metrology and uncertainty quantification. In order to cover different sources of measurement uncertainty, in Section 5.2, some considerations are given concerning the influencing parameters and their uncertainties when calibrating and applying aerodynamic probes. Moreover, Section 5.3 deals with spatial and temporal resolution limitations of the FRAP inserted in grid-generated turbulence. Figure 5.1 presents an overview of the governing key words which determine the characteristics of the probe.

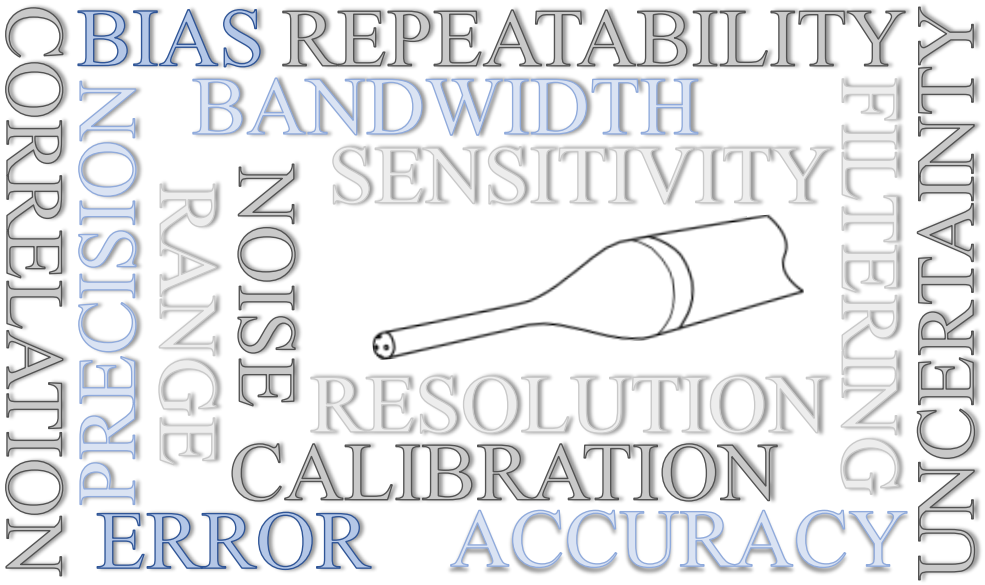

Figure 5.1: Common terms in metrology

In the next sections, the focus lies on the observations made with the presented FRAP assembly. Nevertheless, a differentiation from other probes and CTA hot-wire probes is added in the discussion.

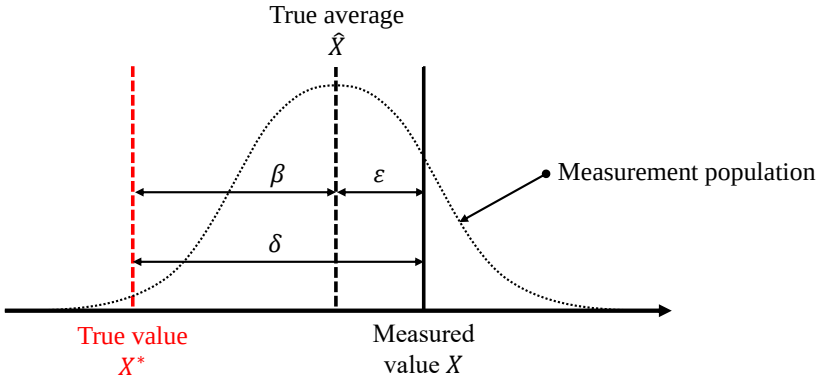

Figure 5.2: Visualization of measurement errors

5.1 Fundamentals of metrology and uncertainty quantification

In this section, a general introduction into the world of uncertainty quantification (UQ) is given. This also includes the definition of important terms and results in a better understanding and differentiation between some of the expressions in Figure 5.1. In the past, several groups and societies in the engineering community have tried to standardize common terms and dependencies in metrology, resulting in an acknowledged technical language. For example, Abernethy et al. define standards for the *American Society of Mechanical Engineers* (ASME) [134]. The guideline that is used within this thesis, was published by the *International Organization for Standardization* (ISO) and the *International Bureau of Weights and Measures* (BIPM). It is called "Guide to the expression of uncertainty in measurement" and is freely available with explanatory extensions [135–137].

The quantity of interest is called *measurand*, when performing a measurement. The measured value is called *indication value*. All measurements are subject to measurement errors, which is the difference between the true value X^* and the measurement population (see Figure 5.2). When measuring multiple times, an *estimate* of the true value, or *true average*, can be calculated as

$$\hat{X}_i = \frac{1}{n} \sum_{k=1}^{n} X_{i,k}. \tag{5.1}$$

Furthermore, the absolute error δ can be divided into two sources of error: the systematic error, or bias error β, and the random error, or precision error ε. The systematic error denotes the (constant) offset between the true value and the true average. The random error will differ between repeated measurements.

Formulation stage

In general, the measurand – the quantity of interest – is not measured directly but as a result or deduced from other quantities, which are often correlated to each other. In a calibration routine, the functional relationship between these quantities is deter-

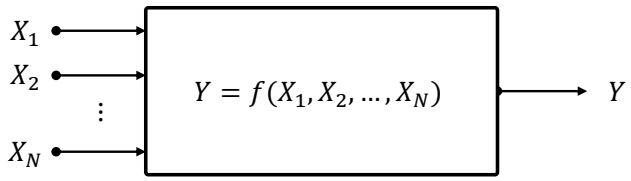

Figure 5.3: Sketch of the measurement model

mined and is formulated as a *measurement model* (see Figure 5.3). The output of the measurement model Y is a function of the input quantities X_i, which are represented by probability functions around the their true averages:

$$Y = f(X_1, X_2, \ldots, X_N) \tag{5.2}$$

As mentioned, the input quantities are subject to errors. Estimates x_i of the input quantities X_i are used for determining the output estimate y:

$$y = f(x_1, x_2, \ldots, x_N) \tag{5.3}$$

Calculation stage

In order to characterize the input quantities X_i uncertainties, knowledge about the probability distribution is needed. There are two types of evaluation methods:

- *Type A evaluation of uncertainty*: repeated indication values obtained independently, often Gaussian shaped or t-distribution
- *Type B evaluation of uncertainty*: scientific judgement or other information (e.g. manufacturer's specification or certificate), often rectangular probability distribution with limits

For a type A distribution, the *standard uncertainty* $u(X_i)$ can be calculated with the standard deviation of the measurements s as

$$u(X_i) = \frac{s}{\sqrt{n}} = \sqrt{\frac{1}{n(n-1)} \sum_{k=1}^{n} \left(X_{i,k} - \hat{X}_i \right)^2}. \tag{5.4}$$

In addition, *sensitivity coefficients* c_i that describe the influence of changes in the input estimate x_i on the output estimate y are the partial derivative of first order of $f(X_1, X_2, \ldots, X_N)$ with respect to X_i:

$$c_i = \frac{\partial f}{\partial x_i} = \left. \frac{\partial f}{\partial X_i} \right|_{x_1, x_2, \ldots, x_N} \tag{5.5}$$

Hence, the measurement model can be reformulated, e.g. for a linear measurement function:

$$Y = f(X_1, X_2, \ldots, X_N) = c_1 X_1 + \ldots + c_N X_N \tag{5.6}$$

Next, a *combined uncertainty* $u_c(y)$ can be obtained by a combination of the single uncertainty terms in quadrature (law of propagation of uncertainty):

$$u_c^2(y) = \sum_{i=1}^{N} \left(\frac{\partial f}{\partial x_i} \right)^2 u^2(x_i) = \sum_{i=1}^{N} \left(c_i u(x_i) \right)^2 \tag{5.7}$$

In order to provide an uncertainty interval, the *expanded uncertainty* U can be obtained by multiplying the combined standard uncertainty $u_c(y)$ by the *coverage factor* k:

$$U = k u_c(y) \tag{5.8}$$

Here, k is chosen on the basis of the level of confidence (e.g. 95% or 99%), and lies in the range between 2 and 3, in many examples [135]. Finally, the measurement can be expressed with the expanded uncertainty as $Y = y \pm U$.

Further information on the limitations and differences in the calculation stage of the UQ, e.g. in case multiple inputs are dependent on each other, can be found in the respective literature [135].

5.2 Uncertainty quantification of aerodynamic probes

After the more general introduction to the metrological description, this section is dedicated to the uncertainty evaluation of aerodynamic probes. The primary aim is to identify possible sources of errors in the calibration and reconstruction. In addition, a degree of awareness of levers for future probe optimization is given, as possible key drivers for uncertainty are identified. Moreover, studies in the literature on the uncertainty evaluation of pressure probes and hot-wire probes will be given.

Many of the thoughts and results were developed and elaborated in the course of supervised final thesis by Jonas Bauer [138]. For further information, please refer to the thesis and the more detailed discussion in the studies given in the literature review.

Literature review on uncertainty quantification for aerodynamic probes

Moffat developed a constant odds approach combining uncertainties of various error sources [139]. The constant odds approach includes the instrument calibration uncertainty, as well as the unsteadiness of the flow, and the uncertainties due to the interpolation. The uncertainty of the quantity R can be calculated by a summation of the contributions $\frac{\partial R}{\partial x_i}\delta x_i$ to the absolute uncertainty δR as follows:

$$\delta R = \sqrt{\sum_{i=1}^{N} \left(\frac{\partial R}{\partial x_i} \delta x_i \right)^2} \tag{5.9}$$

Here, x_i are independent variables and are Gaussian distributed. The odds for all input uncertainties must be constant. Based on Moffat's formulation, Zilliac stated that the greatest gains in measurement accuracy can be made by applying better transducers [67]. A gain in 0.1% full scale accuracy or better can be achieved with an even better

calibration of pressure transducer, with more powerful A/D-converters and by enlarging the probe stem stiffness, in order to mitigate vibrations. Reichert and Wendt discuss the influence of various parameters on the propagation of uncertainty in five-hole probe measurement [140]. They give details on the relationships between the probe geometry, the calibration technique, the data reduction algorithm, and the resulting measurement uncertainty. Johansen et al. show that the often made assumption of a near Gaussian distribution of measurements may be not sufficient enough to describe the true uncertainty of the measurement [80]. An estimate uncertainty with the standard deviation $\hat{x} \pm 2\sigma$ is compared to Moffat's single-sample theory estimate for the uncertainty. They further investigate the uncertainty of the local-least squares data reduction algorithm. Furthermore, it is noted that bias errors should be identified and accounted for by experimenters and should not be involved in an uncertainty analysis. The study by Sumner compares various reconstruction algorithms for the spatial calibration and shows that the measurement uncertainty of the data-reduction methods is sensitive to the calibration grid spacing [141]. In addition, Argüelles Diaz et al. investigate the influence of the construction angle of the three-hole probe – the angles between the pressure ports [70]. Hence, by changing the geometric properties the uncertainties of the flow angle and the dynamic and static pressure can significantly be influenced. The studies by Dell'Era et al. show the determination of the measurement uncertainties for a single sensor probe and a three-hole probe based on the ASME UQ method [142,143]. Finally, Hölle et al. introduce a Monte-Carlo based uncertainty evaluation for multi-hole probes, also covering non-linearity effects, too [144]. Similar investigations were made in the hot-wire probe community. Yavuzkurt studied standard sources of uncertainty during the calibration of a single wire and stated, that in a well-designed calibration process low uncertainty levels for velocities can be achieved [145]. Rezaeiravesh et al. analyse uncertainties of hot-wire anemometry and oil-film interferometry for wall-bounded turbulent flows [146]. They identify that the power law/King's law exponent n is the parameter with highest influence on the overall uncertainty when performing a local sensitivity analysis of the flow velocity. Nevertheless, in a global sensitivity analysis (over the whole parameter range), the measured wire voltage is found to be the variable with the most significant contribution.

Summing up the main findings of the literature review, four areas with major influence on the sensitivity of measured uncertainties are identified:

- Geometric and material properties of the probe
- Measurement system: sensors and data acquisition
- Calibration technique/facility (incl. grid spacing)
- Data reduction algorithm

Fast-response probe uncertainty quantification

In order to identify causes that contribute to the measurement uncertainty of the FRAP in this thesis, there are several well documented methodologies to do so. One of them is a *cause and effect* diagram which is also known as an Ishikawa or fishbone diagram. Possible cause categories can be divided into the so-called *5M*s [137]:

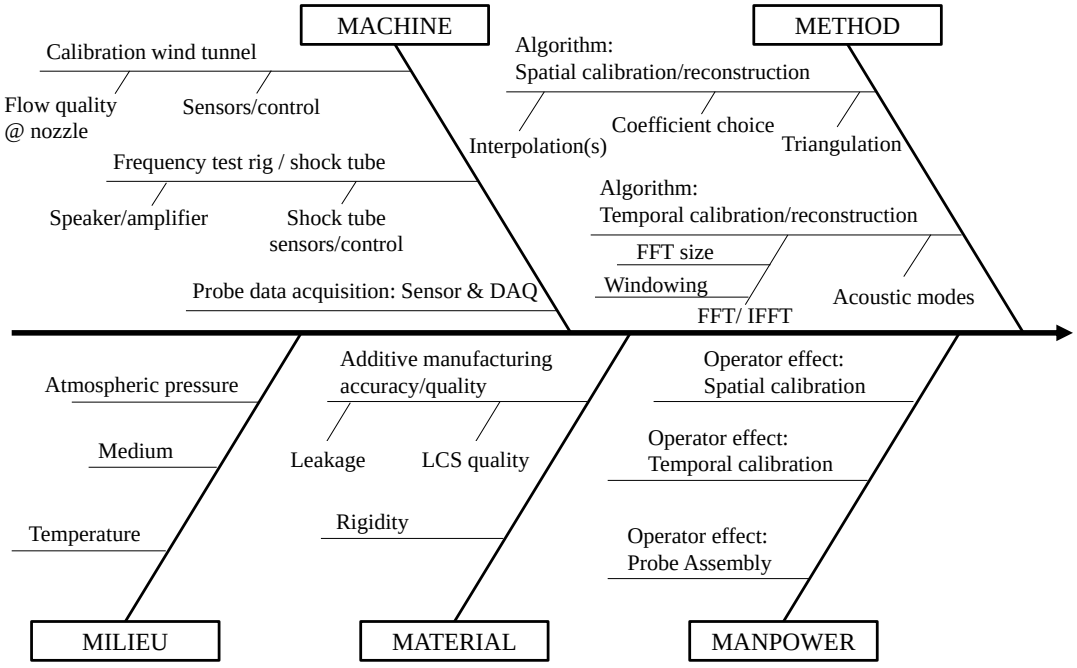

Figure 5.4: 5M fishbone diagram with the main influencing parameters

- Machines: effects related to machines and measurement instrumentation
- Method: effects related to the measurement model
- Milieu (Environment): effects related to the environment,
- Material: effects related to the material properties
- Manpower: effects related to the operator

A representation of factors influencing the calibration and operation of the fast-response pressure probe is visualized in Figure 5.4. The biggest contributors to the increased uncertainty are most certainly the *Machine* and *Method* options. Especially, the calibration measurement setup and all thereby applied sensors and controls can introduce significant uncertainties. Furthermore, the data reduction process contains uncertainties depending on the strengths and weaknesses of the underlying algorithms. Some details are discussed in this thesis. Nevertheless, an in-depth analysis of the errors introduced by the calibration facilities are presented in Bauer [138].

An essential aspect contributing to the overall measurement uncertainty is the pressure sensor and its uncertainties when converting pressure into an analog output signal. Some of the key features and sensitivities have been already treated when designing and characterizing the fiber-optic pressure sensor in Chapters 2.2 and 4. Figure 5.5 shows possible error sources for a differential pressure sensor. Depending on the sensor type choice (absolute, differential, or gauge), different sensor characteristics may contribute differently on the sensor uncertainty. However, the key figures that contribute to the sensor accuracy are listed below. Accuracy is normally quantified either as a percentage of the full-scale range (% F.S.) or as a percentage of the actual reading.

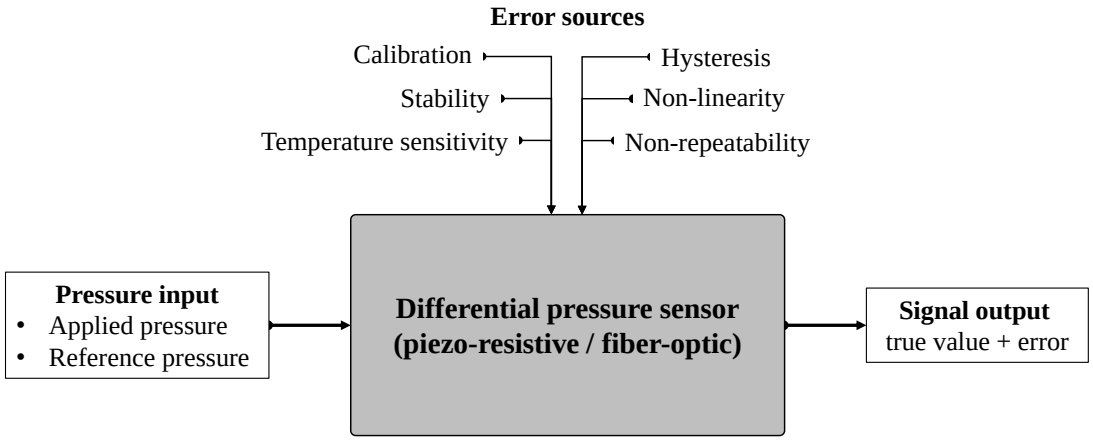

Figure 5.5: Error sources for the differential pressure sensor

- Full scale output (FSO),
- Zero pressure output (ZPO),
- Sensitivity S,
- Non-linearity,
- Hysteresis,
- Non-repeatability, and
- Thermal zero shift.

One of the most crucial metric of a sensor is its linearity towards the main input quantity – the applied pressure. In the best case, a pressure sensor operates linear in the pressure range it will be used in the experiments. In Figure 5.6, the occurrence of a linearity error is shown. Here, the sensitivity of the (piezo-resistive) sensor can be calculated by dividing the span by the range of the sensor:

$$S = \frac{\text{span}}{\text{range}} = \frac{E_{max} - E_0}{p_{max} - p_{ref}} \tag{5.10}$$

There are different ways to indicate non-linearity of a sensor. The most common linear fits are the best fit straight line/least squares (BFSL) and the terminal point (TP) methods. In this manner, different values of for non-linearity can be calculated for the same sensor. The linearity error can then be calculated by taking the voltage difference between the sensor response and the linear fit value at $p_{max}/2$. Non-linearity can also be influenced by various secondary factors, like temperature or humidity. Furthermore, depending on the design and assembly of a differential sensor, different levels of non-linearity can occur on the front or backside of the sensor. In the optimal case, however, these two are identical.

Assuming a linear sensor behavior with sensitivity S, the sensor output voltage can be calculated as:

$$E = E_0 + S \cdot p \tag{5.11}$$

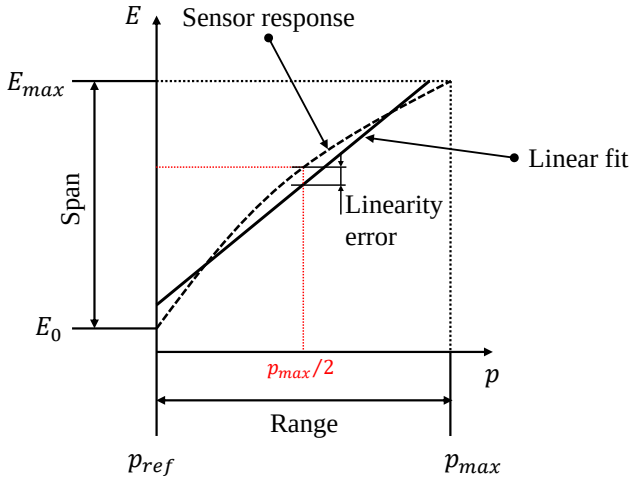

Figure 5.6: Visualization of the linearity error for a piezo-resistive sensor

In addition to the linearity error, errors regarding non-repeatability and hysteresis are determined (see Figure 5.7). The combination of the three errors is often reported as the combined uncertainty on the sensor data sheet. Therefore, two different metrics – the RSS (root sum squared) or the RMS (root mean squared) error – are usually used:

$$RSS = \sqrt{(\text{non-linearity})^2 + (\text{hysteresis})^2 + (\text{non-repeatability})^2} \tag{5.12}$$

$$RMS = \sqrt{\frac{(\text{non-linearity})^2 + (\text{hysteresis})^2 + (\text{non-repeatability})^2}{3}} \tag{5.13}$$

The uncertainty is often strongly influenced by the sensor behavior towards temperature changes. A temperature sensitivity coefficient could help to compensate for thermal induced effects.

Taking all metrics from the data sheet into account, the reading/output of the sensor comprises the true value and the determined error: $E_{sensor} \pm \delta E_{sensor}$.

In addition, for dynamic measurements, a fast response time of the sensor is desired. The response time is defined as the time required to change from an initial state to a final value. Often the response time is quantified as a time constant T which is the time the sensor needs to change to $\approx 65-70$ % F.S. when an instantaneous full-range pressure is applied. Furthermore, depending on the natural frequency of the sensor membrane, the dynamic response can be characterized. However, for the measurements conducted within this thesis, the natural frequency lies higher than the fluctuation bandwidth of the signals. Besides the specifications of the sensor, the complete measurement system including DAQ system has to be investigated. The finest and most advanced sensor is ineffective, if a poor DAQ system introduces the majority of the uncertainties into the reading. Possible sources of uncertainty and error are a reduced bandwidth, a limited resolution of the A/D conversion, or an additionally introduced thermal sensitivity of the DAQ system, for instance. Exemplary, the thermal sensitivity on the accuracy of the

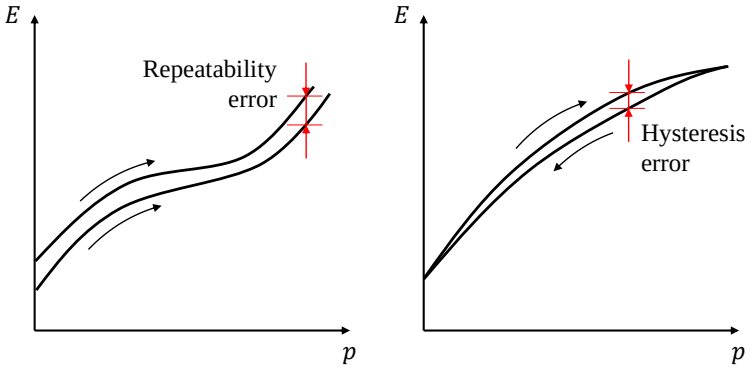

(a) Non-repeatability **(b)** Hysteresis

Figure 5.7: Non-repeatability and hysteresis error visualization

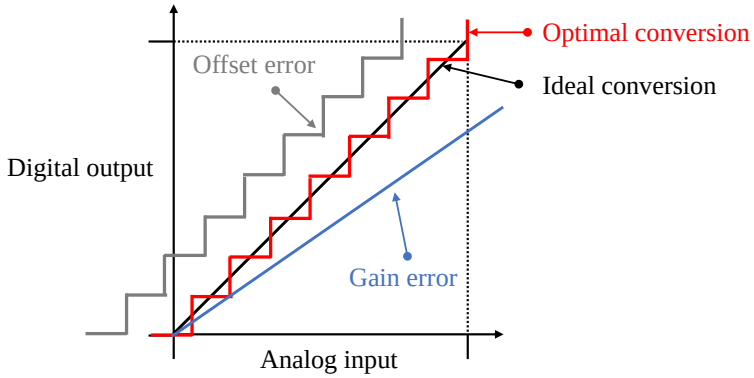

Figure 5.8: Visualization of the offset and gain errors in the A/D conversion

applied DAQ module NI-9237 is given in the following discussion: Figure 5.8 visualizes the offset and gain errors in the A/D conversion. The gain error of the module in percent of reading is:

$$\varepsilon_{A/D,gain}(T) = \begin{cases} 0.05\ \%, & \text{for } T = (20, 30)\ ^\circ C, \\ 0.20\ \%, & \text{else.} \end{cases} \tag{5.14}$$

The offset error in percent of range reads:

$$\varepsilon_{A/D,offset}(T) = \begin{cases} 0.05\ \%, & \text{for } T = (20, 30)\ ^\circ C, \\ 0.25\ \%, & \text{else.} \end{cases} \tag{5.15}$$

Coming back to the 5M fishbone diagram: How could the applied *Methods* influence possible uncertainties and errors? As described in Chapter 3, the spatial calibration contains the triangulation of the calibration surface and a weighted interpolation based on the barycentric coordinates of points surrounding the measurement point. Thereby,

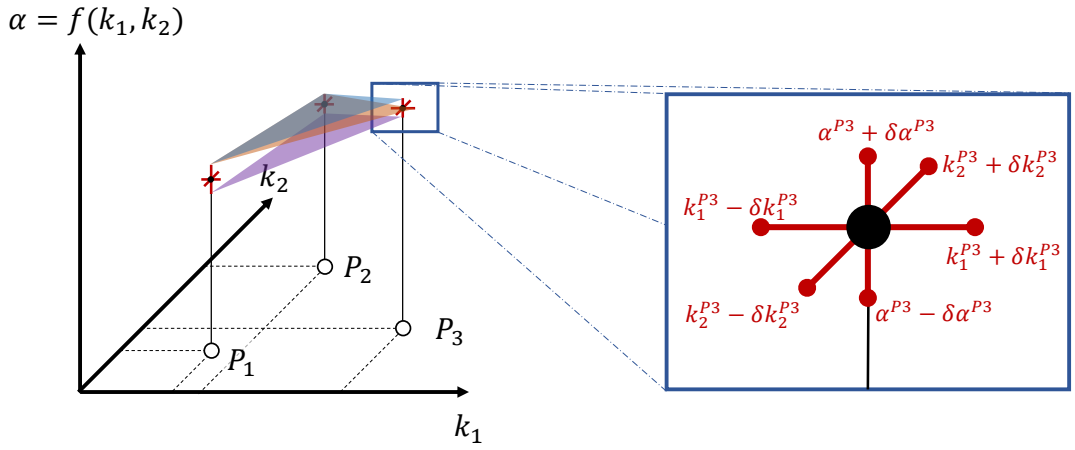

Figure 5.9: Calibration surface errors

the assumption that a locally linear surface can map the real probe calibration behavior was introduced and can lead to errors in the estimation of the reconstructed values. Furthermore, Figure 5.9 demonstrates the variations that are possible due to uncertainties in a) the pressure readings p_i of the FRAP or b) the set velocities and angles in the calibration wind tunnel. Here, three different linear surfaces are depicted that could occur for the same three calibration points. In the subsequent reconstruction in an unknown flow field, the FRAP readings propagate this error further.

To sum up, an insight into various sources of uncertainty was given in the course of the section. Important adjustment parameters were identified and the metrological handling of measurements and their associated uncertainties was introduced. The following sections captures the spatial and temporal limits that are present in the measurement with a fast-response five-hole probe.

5.3 Spatial and temporal resolution in grid-generated turbulence

In this section, the spatial and temporal characteristics and limits of a fast-response probe are studied in the well-documented case of grid-generated turbulence. The contents of this chapter have been published as a peer-reviewed research paper in the journal *Experiments in Fluids* [133][5]:

Spatial and temporal filtering effects of the velocity fluctuations are expected when measuring with the FRAP in unknown flows. This is due to resonance and damping

[5]The journal article was published under the terms of the *Creative Commons* licence CC BY 4.0 (`http://creativecommons.org/licenses/by/4.0/`). The first author was responsible for the conception, the execution and evaluation of the tests (shared with co-author S. Hayböck) and the writing of the paper. The co-authors have consented to publication, here.

effects in the acoustic system and due to the outer dimensions of the probe. The measurement of turbulent flows is challenging where turbulence length and time scales (e.g. Kolmogorov length scale η) are smaller than the corresponding probe sensing length and bandwidth. In order to quantify hot-wire probe resolution, Ashok et al. [147] and Bailey et al. [148] examined various hot-wire CTA probes with different wire lengths in grid-generated turbulence. In this work, a similar wind-tunnel setup is used to characterize and validate the FRAP spatial and temporal measurement behavior. A comparison between the FRAP data, hot-wire data and data from the literature is conducted.
The following discussion is divided into several subsections: The first Subsection 5.3.1 gives a theoretical introduction on grid-generated turbulence. Thereafter, general information on the specification and assembly of the FRAP and the used hot-wire probes are discussed in Subsection 5.3.2. The experimental setup in the wind tunnel TUM-AER is described. In the last part, the results regarding spatial and temporal resolution of the probe are discussed and an outlook is given in Subsection 5.3.3.

5.3.1 Grid-generated turbulence theory

Grid-generated turbulence is well documented in the literature: Essentially, a statistical analysis of grid-generated turbulence can be performed by evaluating higher order moments (like second and third central statistical moment) [149, 150]. The nomenclature for the velocity vector is (u_1, u_2, u_3), and the velocity can be expressed by its mean value and the fluctuation around the mean $u_i = \langle u_i \rangle + u_i'$. The magnitude of the velocity vector is denoted as U. In grid-generated flows, the mean velocity component in streamwise direction is approximately the mean velocity magnitude $\langle u_1 \rangle \approx \langle U \rangle$. The degree of anisotropy DA measures if isotropy is given and relates the variances of the velocity component fluctuations $\langle u_i'^2 \rangle$:

$$DA = \frac{2\langle u_1'^2 \rangle}{\langle u_2'^2 \rangle + \langle u_3'^2 \rangle} \tag{5.16}$$

For an isotropic flow, the velocity component variances are similar $\langle u_1'^2 \rangle = \langle u_2'^2 \rangle = \langle u_3'^2 \rangle$ and DA approaches 1. For grid-generated turbulence, values $DA > 1$ are stated in the literature (see Ting [151]). As a measure for the homogeneity, the third central moment of the velocity fluctuation can be used. When both isotropy and homogeneity can be assumed, the turbulent kinetic energy (TKE) K is approximated by the following equation:

$$K = \frac{\langle u_1'^2 \rangle + \langle u_2'^2 \rangle + \langle u_3'^2 \rangle}{2} \approx \frac{3}{2} \langle U'^2 \rangle \tag{5.17}$$

Additionally, the decay of turbulent kinetic energy can be expressed as a function of the normalized distance x/M downstream of the grid:

$$\frac{K}{\langle U \rangle^2} = A \left(\frac{x - x_0}{M} \right)^{-n} \tag{5.18}$$

Here, x_0 describes the virtual origin of the turbulent kinetic energy decay. The coefficients A and n can be fitted with measurement data. The coefficient A depends on

the grid dimensions and the applied Reynolds number. According to the literature, the exponent lies between $1.15 < n < 1.45$ (see Pope [152]).

By using Taylor's hypothesis of *frozen turbulence*, the dissipation rate ε for homogeneous, isotropic turbulence can be calculated and the spatial development of the flow can be inferred from the temporal properties. Furthermore, the dissipation rate can be approximated by assuming a homogeneous isotropic turbulent (HIT) flow. The dissipation rate ε corresponds to the decay of the TKE over time:

$$\varepsilon = -\langle U \rangle \frac{d}{dx_1} \frac{\langle u_1'^2 \rangle + \langle u_2'^2 \rangle + \langle u_3'^2 \rangle}{2} \approx -\langle U \rangle \frac{d}{dx_1} \frac{3}{2} \langle U'^2 \rangle \tag{5.19}$$

Hereby, turbulent length scales can be defined, which describe the size of eddies in the turbulent energy cascade. The Taylor micro scale λ indicates the size of the largest vortex structures in the dissipative range and can be expressed as a function of the dissipation rate ε and the kinematic viscosity ν [153]:

$$\lambda = \sqrt{15\nu \frac{\langle u_1'^2 \rangle}{\varepsilon}} \tag{5.20}$$

Then, a turbulence Reynolds number Re_λ, calculated with the Taylor micro scale, can be used as a figure of similarity for turbulent flows and is given by:

$$Re_\lambda = \frac{\lambda \cdot \sqrt{\langle u_1'^2 \rangle}}{\nu} \tag{5.21}$$

As a measure for the lower size limit of the dissipation range, the Kolmogorov length scale η is defined. Here, the turbulent kinetic energy is dissipated into heat due to dominating viscous effects.

$$\eta = \left(\frac{\nu^3}{\varepsilon} \right)^{1/4} \tag{5.22}$$

Further turbulence measures, the Kolmogorov velocity u_η and time scales τ_η, as functions of ε and ν can be deduced by dimensional analysis:

$$u_\eta = (\varepsilon \nu)^{1/4} \tag{5.23}$$

$$\tau_\eta = \left(\frac{\nu}{\varepsilon} \right)^{1/2} \tag{5.24}$$

For the spectral examination of the grid-generated turbulence, the normalized kinetic energy is calculated and shown as a function of the non-dimensional variable $k\eta$. Hereby, the wave number k is defined as:

$$k = 2 \cdot \pi \cdot f / \langle U \rangle \tag{5.25}$$

For de-noising the measured signals, the following procedure is applied on all hot-wire and FRAP signals ensuring an analogous post-processing workflow: The velocity signal

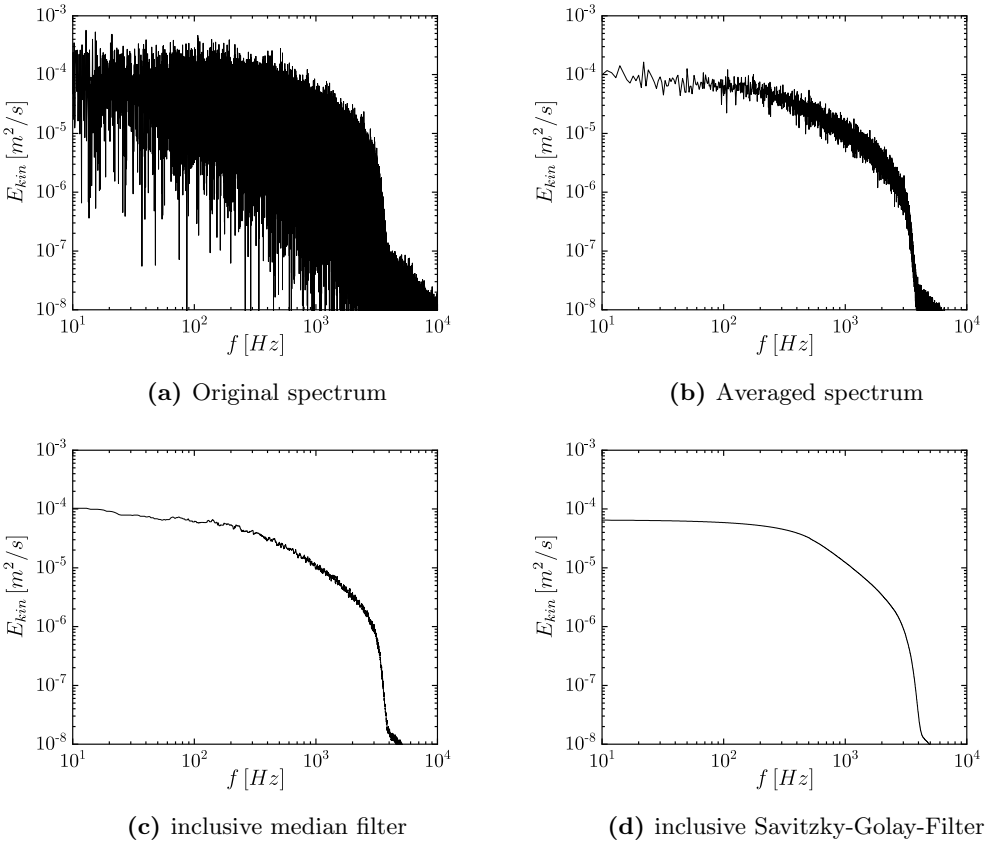

(a) Original spectrum

(b) Averaged spectrum

(c) inclusive median filter

(d) inclusive Savitzky-Golay-Filter

Figure 5.10: Application of averaging and filtering for de-noising the non-dimensional kinetic energy spectra [133]

is split in evenly distributed parts of $\Delta t = 1\ s$ and averaged in the time domain. With a sampling rate of $f_s = 50\ kHz$, this step results in $f_s/\Delta t = 50k$ averaged samples. Moreover, further filtering in the frequency domain is applied. Figure 5.10 shows the filtering procedure exemplary for a measurement downstream of the grid. The noisy initial signal is averaged and filtered after transformation into the frequency domain. A 1-D median filter of 20th order and a Savitzky-Golay finite impulse filter (FIR) of 1st order and a frame length of 999 Hz are further applied on the signal, using MATLAB's inbuilt functions *medfilt1* and *sgolayfilt*, respectively [154].

5.3.2 Experimental setup

In the first part of this subsection, the measurement equipment for the grid-generated turbulence investigations is explained. Since the pressure probe data are compared to hot-wire CTA probe measurements, the basic characteristics of the used CTA equipment is given. In the second part, the wind tunnel setup with the grid is documented. A fast-response five-hole probe, as depicted in Figure 5.11a, is assembled to measure the flow

field downstream of the grid. The probe head of the FRAP is additively manufactured. The hemispheric probe head and the cavities for the placement of the pressure sensors are post-manufactured in a cutting step. The probe is equipped with five differential piezo-resistive pressure sensors (Meggitt Endevco 8507C-2), which are pressurized with the ambient pressure outside of the wind tunnel as reference pressure. The sensors are surrounded with a silicone tubing and pressed into the cavities in order to avoid leakage [33]. The reference pressure lines of the differential transducer are merged in a manifold, so only one pressure tubing is connected to the reference pressure. The sensors are connected to NI 9237 data acquisition cards, which transmit the data to the LabVIEW controlled computer. The 24-bit A/D-conversion of the typical input voltage range of $\pm 25\ mV/V$ for $3.3\ V$ excitation voltage yields a least significant bit (LSB) of $E_{LSB} \approx 9.8\ nV$, resulting in a minimal detectable pressure of around $p_{LSB} \approx 5 \cdot 10^{-4}\ Pa$ depending on the linear calibration coefficient (in $[Pa/V]$) of the respective pressure sensor. A sketch of the measurement setup for the FRAP is shown in Figure 5.12.

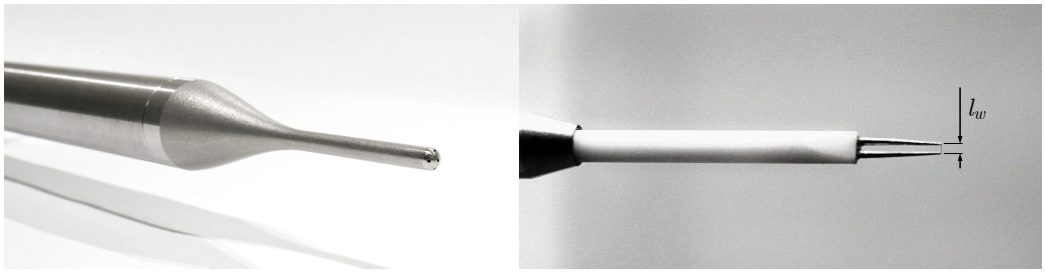

(a) FRAP **(b)** Dantec 55P11 with $l_w = 1.25\ mm$

Figure 5.11: a) Fast-response five-hole probe equipped with piezo-resistive sensors and b) single-wire probe [133]

Before the usage of the FRAP, it has to be calibrated for a) its spatial/aerodynamic and b) its temporal/transient characteristic, when exposed into unknown flow fields. The exact procedure is given in Chapter 3, which covers the calibration and reconstruction processes in detail. Table 5.1 shows the pressure probe properties including some geometric dimensions.
For the reconstruction of the flow-field properties, the measured pressures are post-processed taking the calibration data of both, temporal and spatial calibrations, into account. A high reconstruction accuracy can be achieved, as shown in the sensor and probe characterization Chapter 4. Accuracy lies below 0.2° in both flow angles and $0.1\ m/s$ in the reconstructed velocity.
Pre-tests have shown that the temporal characteristics of the probe is limited due to bandwidth restrictions of the transfer function in the temporal calibration. The speakers in the frequency test-rig ensured good quality sound emission only up to $10\ kHz$. Furthermore, the minimal resolution of the sensor and the DAQ-card p_{LSB} must be taken into account, since the expected pressure fluctuations attenuated in the line-cavity system in the higher kHz-range could be lower than the minimal resolvable pressure fluc-

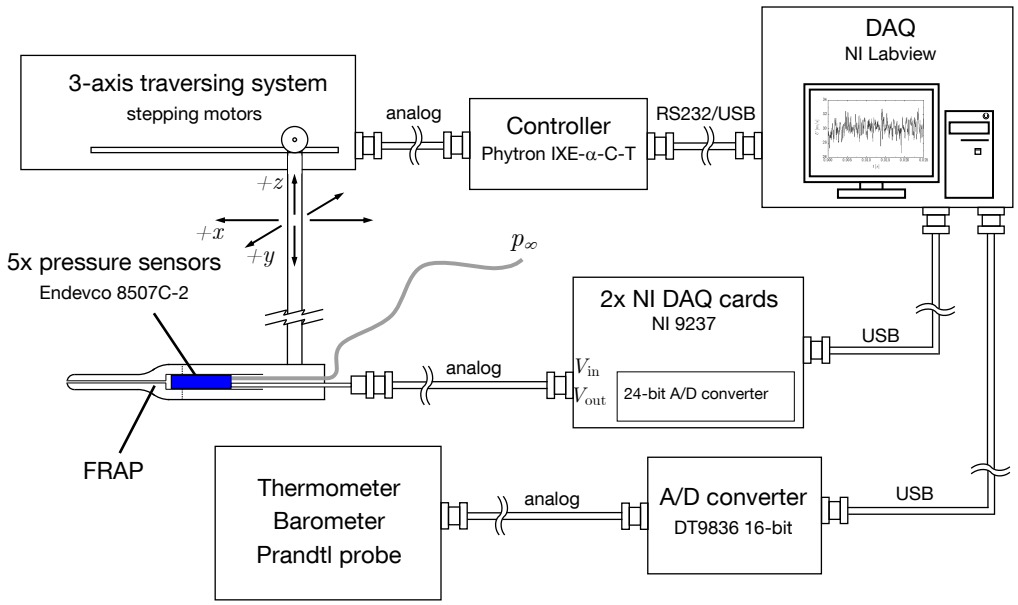

Figure 5.12: Fast-response five-hole probe measurement setup [133]

tuation. For this case, an additional digital low pass filter is applied on the pressure data before reconstruction of the flow field properties. For example, if the pressure fluctuation of sensor 1 lies in the range of 10^{-3} Pa, the signal is further attenuated in the frequency range around 7 kHz of almost one order of magnitude, and thus, cannot be resolved due to the LSB-restriction, mentioned before. Hence, the temporal resolution restriction comes either from the bandwidth of the temporal calibration or the minimal resolvable pressure fluctuation.
As a counterpart to pressure measurement systems, hot-wire probes are used to validate the FRAP results. A Dantec 55P11 single-wire probe with a standard wire length of

Table 5.1: Five-hole probe properties [133]

Tip diameter d_{tip}	3 mm
Channel diameter	≤ 1 mm
Sensor type	differential, piezo-resistive
Sensor gauge pressure range	2 $psig$
Sensor diameter	2.3 mm
Voltage LSB E_{LSB} $[V]$	≈ 9.8 nV
Pressure LSB p_{LSB} $[Pa]$	$\approx 5 \cdot 10^{-4}$ Pa
Spatial/angular calibration	$\pm 60°$
Temporal calibration	10 kHz

Table 5.2: Single-wire probe properties P11 [133]

Wire diameter d_w		5 μm
Wire length l_w	shortened	0.7 mm
	standard	1.25 mm
l_w/d_w ratio	shortened	140
	standard	250
Sensor temperature coefficient α_{20}		0.0036 K^{-1}
Overheat ratio		1.8

$l_w = 1.25\ mm$ (see Figure 5.11b) and a retrofitted, shortened probe with a wire length $l_w = 0.7\ mm$ are compared (see Table 5.2).

The CTA hot-wire probe is operated with a Dantec StreamLine Pro constant temperature anemometer. The signal is digitized by a Data-Translation DT9836 16-bit A/D-converter. After bridge-balancing of the CTA-bridges, the probes are calibrated in the desired velocity range. The cut-off frequency inferred from a square-wave test lies above the set low-pass frequency of the CTA. In order to compensate for temperature changes during the calibration and the wind tunnel measurements, the voltages are corrected as described in Bearman [155]:

$$E_{corr} = C \cdot E_{HW} - (1 - C) \cdot O \cdot G \tag{5.26}$$

where:

$$C = \sqrt{\frac{T_w - T_{ref}}{T_w - T_{meas}}} \tag{5.27}$$

Here, O is the voltage offset, G the gain, T_w the wire temperature, T_ref the reference temperature and T_{meas} the temperature during the actual measurement. The experiments on the grid-generated turbulence are conducted in a low-speed wind tunnel (W/T-B of TUM-AER), which is of Göttingen type (closed-loop) and has a cross section of $h \cdot b = 1.20\ m \cdot 1.55\ m$. Turbulence intensity without the grid lies below $Tu = 1\ \%$. At the nozzle section, a weaved grid with a mesh size $M = 6.4\ mm$ and a wire diameter of $d = 1.6\ mm$ is installed (see Figure 5.13). The solidity of the mesh is $\sigma = \left(\frac{d}{M}\right)\left(2 - \frac{d}{M}\right) = 0.438$. The free-stream velocity is monitored with a Prandtl probe that is installed upstream of the grid near the nozzle. The free-stream velocities are set to match the Reynolds numbers $Re_M = \{4300, 12800\}$. For all types of probes, measurements are acquired along an x-traverse downstream of the grid. The x-positions are normalized by the mesh size M and lie between $x/M = (20, 100)$. Both hot-wire and FRAP data are sampled with a sampling frequency of $f_s = 50\ kHz$. In order to account for aliasing problems, a low-pass filter below the Nyquist frequency ($f_{lp} \leq f_s/2$) is set for both acquisition setups. The measurement time was set to $t_s = 15\ s$.

5.3.3 Results and discussion

In a first evaluation step, the assumptions of homogeneous and isotropic turbulence are evaluated as a prerequisite for the application of Taylor's frozen turbulence hypothesis.

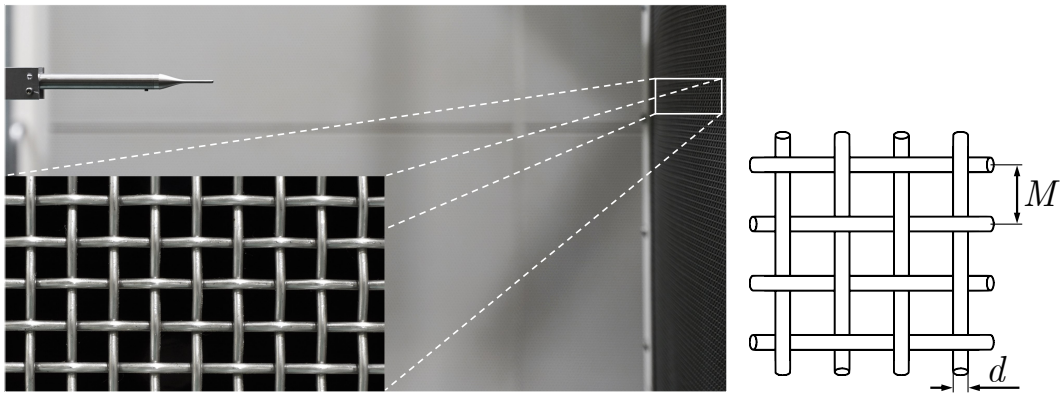

Figure 5.13: a) Wind tunnel setup with the FRAP being installed downstream of the grid in the nozzle section and b) sketch of the mesh [133]

The stated equations in Section 5.3.1 are only valid if both homogeneity and isotropy are present in the flow field. In the literature, Ashok et al. [147] and Bailey et al. [148] solely assume a homogeneous, isotropic flow without any validation. In this study, the usage of a fast-response five-hole probe giving the 3D velocity vector enables a closer look on the evaluation of the stated prerequisites:

The first assumption is the homogeneity of the flow field. Hence, three measurement planes with a very fine measurement grid resolution ($\Delta y = \Delta z = M/8 = 0.8\ mm$) are measured in the near wake of the grid at $x/M = \{2, 10, 20\}$. Contour plots of the turbulence intensity Tu at the measurement planes at $Re_M = 4300$ are shown in Figure 5.14. The turbulence intensity Tu is defined as:

$$Tu = \frac{\sqrt{\frac{1}{3}\left(\langle u_1'^2\rangle + \langle u_2'^2\rangle + \langle u_3'^2\rangle\right)}}{\langle U\rangle} \tag{5.28}$$

In the near-field of the grid, the flow field is very inhomogeneous due to the separation and acceleration of the flow at the grid. At $x/M = 10$, the flow field is still strongly influenced by the grid, resulting in a more homogeneous flow field at $x/M = 20$. In the backmost measurement plane in Figure 5.14 at $x/M = 20$, repeat measurements indicated that turbulence intensities lie between $Tu = 0.05$ and $Tu = 0.1$, which is approximately one order of magnitude higher than the undisturbed flow at the nozzle in W/T-B at TUM-AER.

In order to investigate the assumption of isotropy, the degree of anisotropy is observed with the FRAP downstream of the grid. In Figure 5.15, the degree of anisotropy and the variances of the three velocity fluctuation components are depicted. As described in the literature, the component in streamwise direction is higher compared to the lateral and vertical components. The difference is decreasing with a larger distance from the grid. From $x/M \geq 40$, the flow gets more and more isotropic. The variance of the velocity component in streamwise direction $\langle u_1'^2\rangle$ matches the variance of the velocity

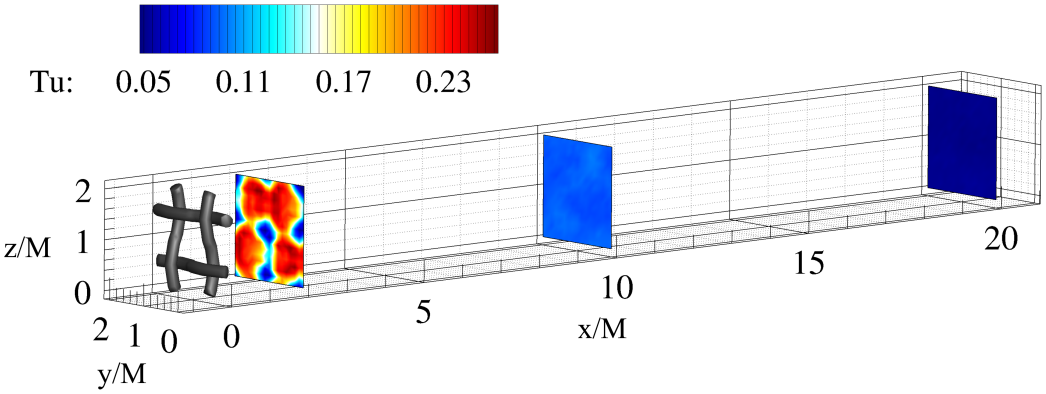

Figure 5.14: Homogeneity of the flow downstream of the grid at $x/M = \{2, 10, 20\}$ indicated by the turbulence intensity Tu [133]

magnitude $\langle U'^2 \rangle$ to a very high extent (see Figure 5.15b). Further evaluations on grid-generated turbulence are based on the velocity magnitude and its variance, as $\langle u_1'^2 \rangle \approx \langle U'^2 \rangle$. However, a certain degree of anisotropy is still present in the wake of the grid: The degree of anisotropy never falls below $DA = 1.3$. In the literature, similar values for DA have been noted for grid-generated turbulence by Ting [151]. For further evaluations steps, the degree of anisotropy is seen as acceptable. For higher Reynolds numbers, the degree of anisotropy decreases as expected.

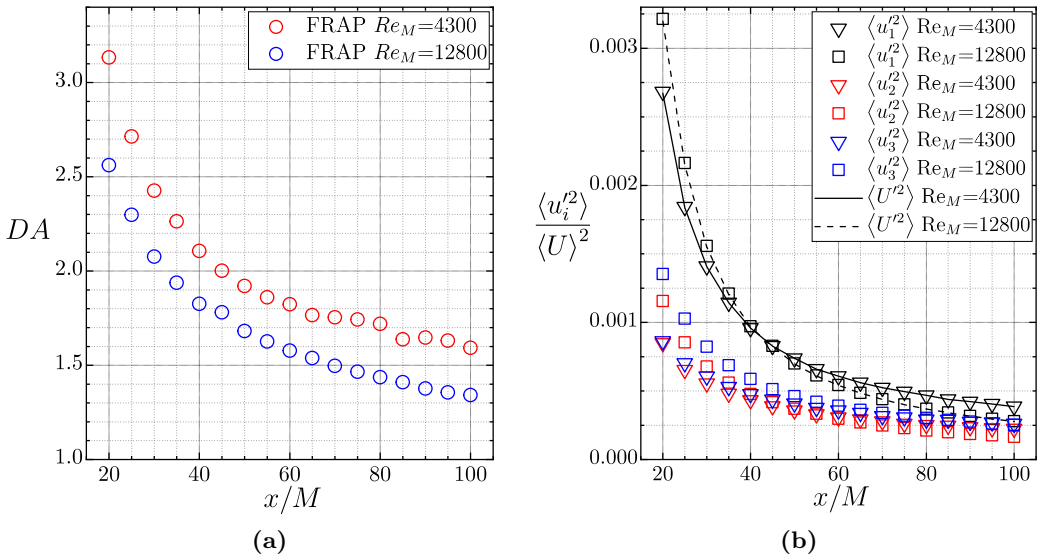

Figure 5.15: a) Degree of anisotropy and b) velocity components variance downstream of the grid as a characteristics for isotropy [133]

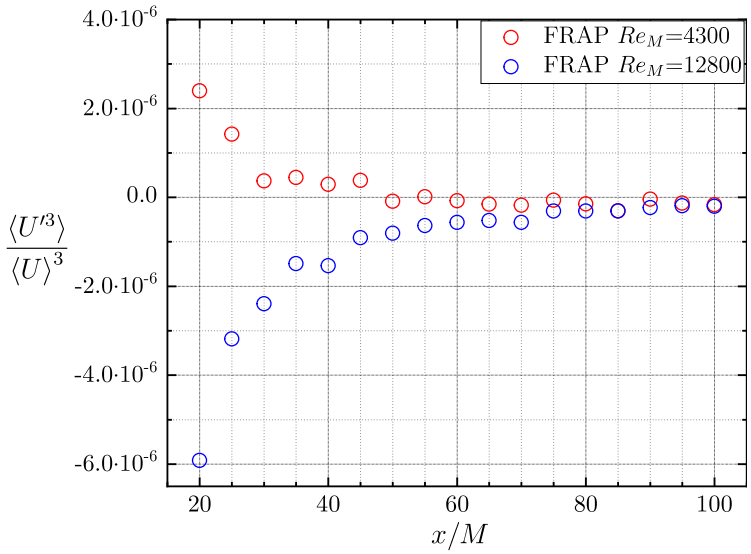

Figure 5.16: Normalized third order statistical moment for $Re_M = 4300$ (red) and $Re_M = 12800$ (blue) [133]

Another indication which justifies the assumption of homogeneity at distances $x/M \geq 40$ is the investigation of higher order statistical moments of the velocity magnitude, like the non-dimensional third order moment in Figure 5.16 for both Reynolds numbers. The third order statistical moment is very low and almost constant for farther downstream measurement points.

The lack of full isotropy, as seen in the discussion before, leads to the investigation of the introduced errors. The following paragraph discusses the application of the HIT approximation for the calculation of the TKE and all deduced quantities: Figure 5.17 shows the decay of the turbulent kinetic energy K as a function of the normalized distance x/M downstream the mesh with and without the HIT approximation. Furthermore, the fit parameters are investigated when fitting the measurement data to the power law in Equation 5.18. The fitted exponent $n = 1.26$ fulfills the assumptions as mentioned in Pope [152]. Using the aforementioned approximation, the TKE is overestimated. The relative error for the TKE is more than 40% in the near wake of the mesh and decreases with increasing distance. Since Ashok et al. [147] solely use data from a single wire CTA probe, it is assumed that they come to a similar error when calculating deduced quantities in grid-generated turbulence, approximating U with u_1.

As described in Equation 5.19, the dissipation rate of the flow can be deduced from the spatial derivative of the velocity components variances, when assuming homogeneous, isotropic turbulence and Taylor's frozen turbulence hypothesis. In Figure 5.18a, the dissipation rate for both Reynolds number cases is displayed for a) the dissipation rate calculated with the present 3D variances, namely without the homogeneous isotopic turbulence (HIT), and b) with the HIT approximation. Due to the described higher

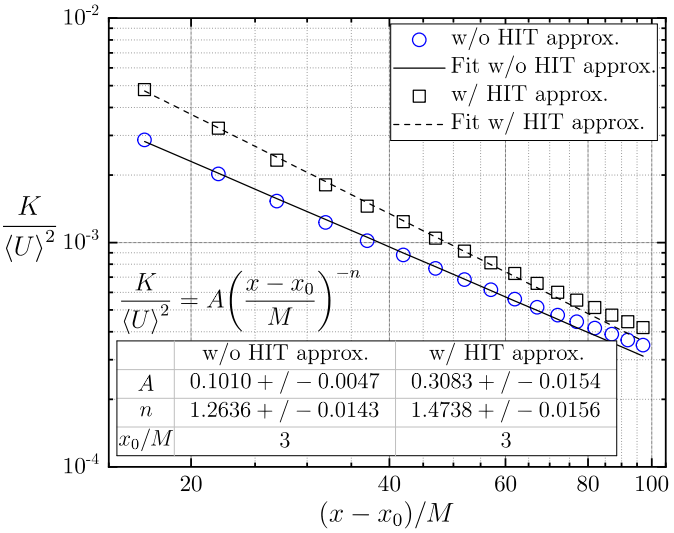

Figure 5.17: Decay of the turbulent kinetic energy K as a function of the normalized streamwise distance $(x - x_0)/M$ [133]

degree of anisotropy in the near wake, the approximation overestimates the dissipation rate throughout the full traverse in downstream direction, but still follows the estimated trend. The error made in the calculation of the Kolmogorov length scale η is shown in Figure 5.18b. The relative error is lower compared to the dissipation rate plot, due to the fact that $\eta \sim \varepsilon^{1/4}$. The Kolmogorov scale is underestimated when applying the HIT-approximation. This is also important for single-wire CTA-probe measurements since there this assumption also holds, as stated before by assuming $U \approx u_1$.

In the literature, values for the Reynolds number based on the Taylor micro scale lie in the range $Re_\lambda = (30, 80)$ (see Ashok et al. [147]). The measurements from the FRAP $Re_\lambda = (20, 70)$ match the reference data. The Kolmogorov length scale η, calculated as defined in Equation 5.22, is shown in Figure 5.19a for both Reynolds numbers. For $Re_M = 12800$, the data for both measurement techniques match very well in the entire x/M range downstream of the grid. For the lower Reynolds number, deviations between the hot-wire measurements and the FRAP occur in the far wake at distances $x/M > 80$. This is mainly due to the low velocity fluctuation magnitudes. Small velocity fluctuations around a low mean velocity correspond to even smaller pressure changes, and therefore can not be resolved appropriately. It can be seen that the Kolmogorov length scale increases with increasing distance from the grid. Furthermore, it increases with decreasing Reynolds numbers. The same trend is shown in the literature with Kolmogorov length scales of $\eta = (0.04, 0.275)\ mm$ for an equivalent Re_M (see Ashok et al. [147]). The same trend can be observed for the Taylor micro scale λ in Figure 5.19b. For measurements farther away from the grid, larger deviations between the various probes are present for $Re_M = 4300$. Here, the absolute velocity and the respective velocity component fluctuations are very small. The fluctuations of the measured total pressure lie below $\Delta p \ll 1\ Pa$ and the probe reconstruction accuracy is influenced, which

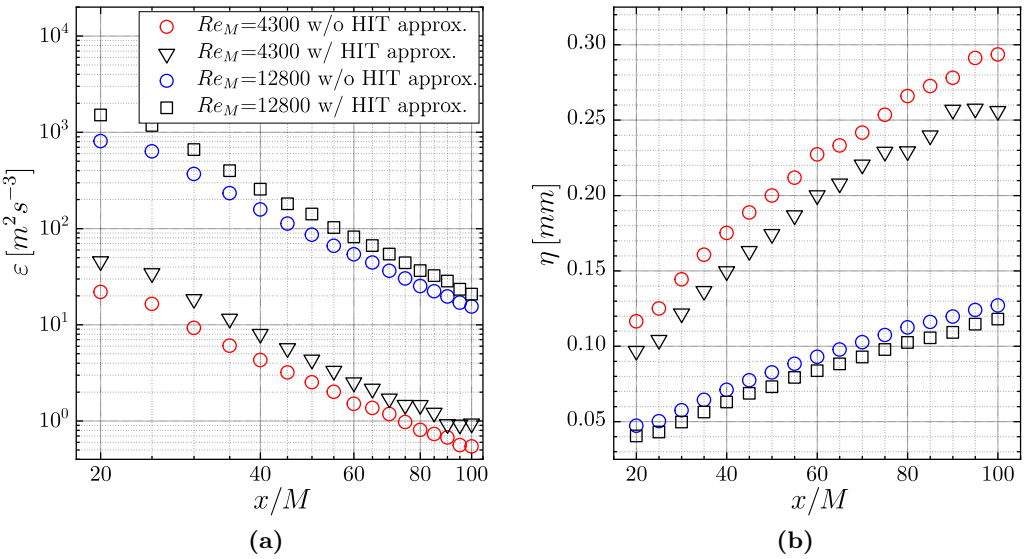

Figure 5.18: a) FRAP dissipation rate ε and b) Kolmogorov scale η for $Re_M = 4300$ (red) and $Re_M = 12800$ (blue) with and without the homogeneous isotropic turbulence (HIT) approximation in Equation 5.19 [133]

can lead to inaccurate results. For the higher Reynolds number case $Re_M = 12800$ this mismatch is less pronounced.

Figure 5.20 shows the local, normalized velocity variance for all probes under investigation and validation data from the literature (see Ashok et al. [147]). The trend that the smaller the spatial filtering due to the probe size, the higher the measured variance, can be observed in both, the literature and the measurement data in this study. Interestingly, the five-hole probe with a head diameter of 3 mm lies between the two single-wire probes used for validation purposes. The reason why the TUM-AER single-wire probe with a wire length of 0.7 mm lies below the 1 mm probe in the literature is due to the lack of comparability in the length to diameter ratio of the various probes. Ashok et al. used wires with smaller diameters to compensate for 3D flow effects around the hot-wire. The ratio of the wire length to the wire diameter l_w/d_w is larger by a factor of at least 2 for all measurements of Ashok et al. Ligrani and Bradshaw showed that at ratios $l/d > 200$ 3D effects are negligible and, thus, the influence of the hot-wire prongs are less prominent [156]. The TUM-AER hot-wire probe l_w/d_w-ratios, $l_w/d_w = 250$ and $l_w/d_w = 140$ for the standard and shortened probe, respectively, are in the same range as this lower limit. An additional reason for the deviation of the measurements from the literature to the measurements in this study is related to the differences in the flow in the wind tunnel, i.e. wind tunnel effects.

In the spectral analyses, the acquired signals are post-processed (averaging and filtering) as described in Figure 5.10. Figure 5.21a shows kinetic energy spectra as a function of the frequency. The influence of the digital low-pass filter is visible for the FRAP data. The spectra approach a nonphysical near constant value near the low-pass frequency

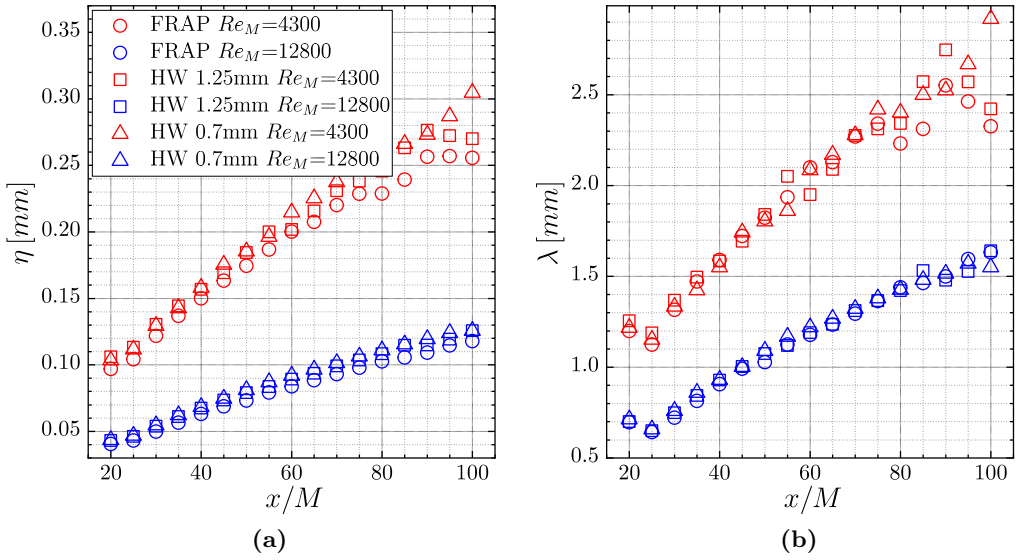

Figure 5.19: a) Kolmogorov length scale η and b) Taylor micro scale λ for $Re_M = 4300$ (red) and $Re_M = 12800$ (blue) for the FRAP and both single-wire probes [133]

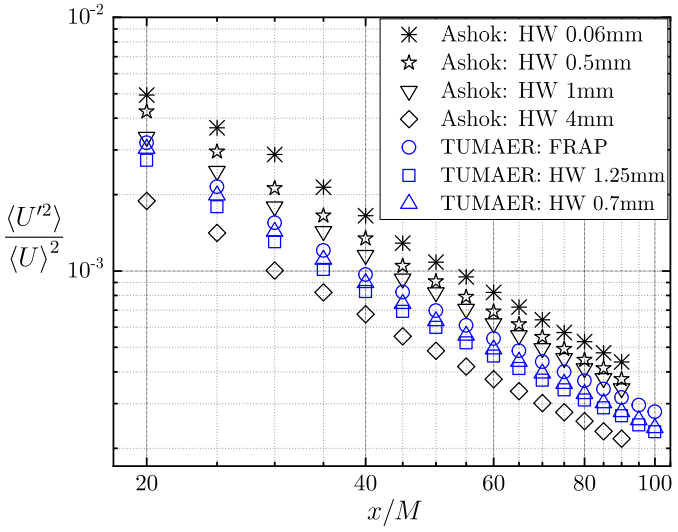

Figure 5.20: Local normalized velocity variance at $Re_M = 12800$ [133]

of the DAQ system at $f \approx 25\ kHz$, which shows the minimal resolution restrictions of the FRAP sensors and measurement cards. In Figure 5.21b, normalized kinetic energy spectra $\hat{E}_{kin}/(\varepsilon\nu^5)^{1/4}$ for the FRAP at various downstream positions as a function of $k\eta$ at $Re_M = 12800$ are depicted. As a reference, the energy spectra for the single-wire measurement at $x/M = \{40, 60, 80\}$ are given, as well. In addition, the $k^{-5/3}$ slope in the inertial range of the energy cascade is included, which applies for flows with $Re_\lambda \to \infty$. After the near constant trend in the low bandwidth region, the inertial subrange is clearly visible. For flows with small Reynolds numbers Re_λ, the exponent p of the k^{-p} dependency deviates from the ideal value of $p = 5/3$ [152]. Due to the minimal resolution of the sensor-DAQ-system, the FRAP signals have been additionally low-pass filtered. Therefore, the inertial subrange can not be fully resolved by the FRAP. Since the abscissa is non-dimensionalized with the Kolmogorov length scale, which increases with the distance from the grid, the cut-off value $k\eta$ for the FRAP measurements is shifted for measurements farther downstream. In comparison, the single-wire measurement with a wire length of $l_w = 1.25\ mm$ additionally resolves even smaller scales in the dissipative range of the energy cascade. A linear fit in the log-log-scale between $k\eta = [0.04, 0.1]$ results in fitted exponents p for the measurements, that were carried out at $Re_\lambda \approx 50$: Following the proposed experimentally derived dependency for $p(Re_\lambda)$ by Mydlarski and Warhaft [157] $p(Re_\lambda) = 5/3 - 5.25Re_\lambda^{-2/3}$, the exponent for FRAP and for the HW measurements are $p_{FRAP} \approx 1.3$ and $p_{HW} \approx 1.47$, respectively. The discrepancy between the two measurement techniques can be attributed to effects due to the filtering process and the assumptions made concerning homogeneous, isotropic flows.

In Figure 5.22, the pre-multiplied energy spectra $kE_{kin}/(\varepsilon\nu^5)^{1/4}$ are shown for all measured distances downstream the grid. It can be seen that the energy decreases with the distance from the grid. For all measurements, the FRAP cannot fully resolve the decay in the high bandwidth region $k\eta > 10^{-1}$.

In the last step of the grid-generated turbulence evaluation, an equivalent wire length is calculated for the FRAP in order to make the pressure probe dimensions comparable to single-wire probes. The flow around the bluff FRAP body leads to a spatial filtering effect and can be made comparable to the spatial filtering due to the wire length of the single-wire CTA probe. Ashok et al. investigate the ratio between the wire length and the Kolmogorov length scale l_w/η [147]. As a reference, Ashok et al. use a miniature hot-wire probe with a wire length $l_w = 0.06\ mm$. This miniature wire size is in the same order of magnitude as the Kolmogorov scale $l_w \sim \eta$ and spatial filtering hardly occurs. Thus, they postulate an exponential trend of the spatial filtering as a function of the ratio l_w/η:

$$\frac{\langle U_m'^2 \rangle}{\langle U_{hw0.06}'^2 \rangle} = \exp^{-0.0175\ l_w/\eta} \tag{5.29}$$

Here, U_m denotes the measured velocity and $U_{hw0.06}$ the reference value measured with a miniature hot-wire probe. Consistent to the findings in Figure 5.20, where the FRAP data lie nearer to the 1 mm HW than the 4 mm one from the literature, an equivalent wire length $l_{w,equi.}$ can be found for the FRAP. The measured FRAP data can be fitted

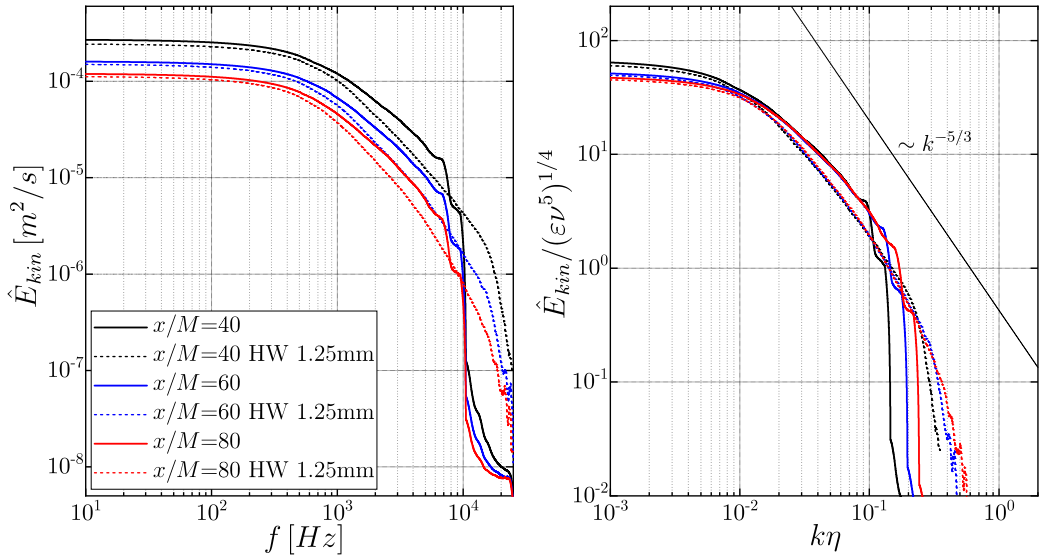

Figure 5.21: a) Kinetic energy spectra and b) normalized kinetic energy spectra at downstream positions $x/M = \{40, 60, 80\}$ for $Re_M = 12800$ for both, FRAP and HW, probes [133]

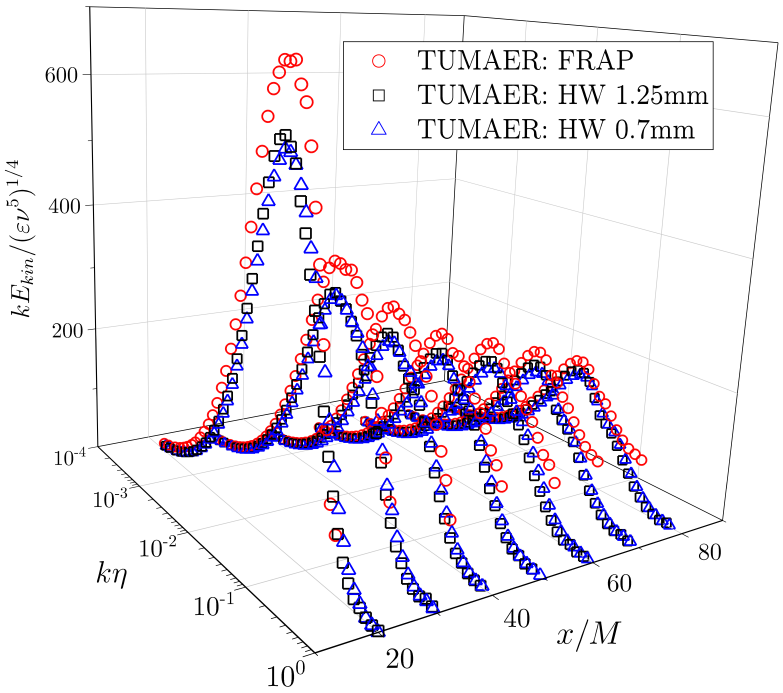

Figure 5.22: Pre-multiplied normalized kinetic energy spectra as a function of $k\eta$ for $Re_M = 4300$ [133]

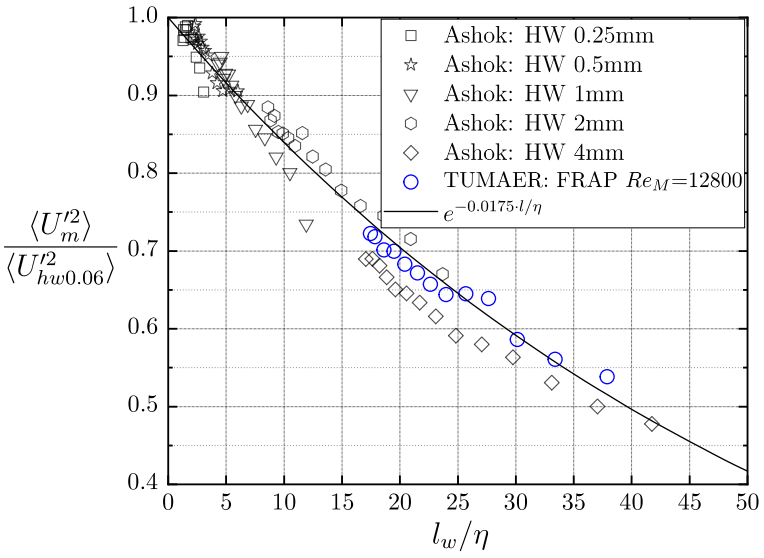

Figure 5.23: Variance normalized by hot-wire variance values with a wire-length of $l_w = 0.06\ mm$ [147] as a function of l_w/η [133]

to the exponential trend. Figure 5.23 shows the variance normalized by hot-wire variance values with a wire-length of $l_w = 0.06\ mm$ [147] as a function of l_w/η. For the depicted values of the FRAP, an equivalent wire length of $l_{w,equi.} = 2.0\ mm$ is assumed and lies below the outer dimension of the probe tip, which reads $d_{tip} = 3\ mm$.

To conclude, grid-generated turbulence data from a fast-response multi-hole pressure probe were compared to data from single-wire CTA probes and data from the literature. The underlying assumptions of homogeneity and isotropy have been studied thoroughly. The evaluation of higher order statistics show a good agreement between the different measurement methods. Solely, minor deviations in regions with small velocity fluctuations around a low wind speed could be observed in the FRAP data. In the spectral investigations, the limits of the FRAP have been shown. These are mainly due to the minimal resolution of the FRAP sensors/DAQ system and the bandwidth limit of the experimentally acquired temporal calibration. Future developments concerning those issues should overcome the problems: Smaller probe dimensions could further reduce spatial and temporal filtering. Moreover, the limits of the piezo-resistive sensor should be avoided by the application of newly developed fiber-optic pressure sensors in the future. The measurements have shown that the FRAP can be used for turbulence measurements. In comparison to state-of-the-art hot wire CTA probes, FRAP offer a reduced setup time (no recurring calibration needed), the full 3D velocity vector and a more robust probe design, which can also be used in harsh environments.

6 Application fields

In this section, a demonstration of the measurement capabilities of the fast-response aerodynamic probe is given. Special focus lies on the determination of unsteady aerodynamics when operating the probe in wind tunnel setups. Within the FRAP development and studies conducted at TUM-AER, different opportunities to validate and compare the FRAP to other intrusive and non-intrusive measurement techniques occurred (see overview in Figure 6.1).

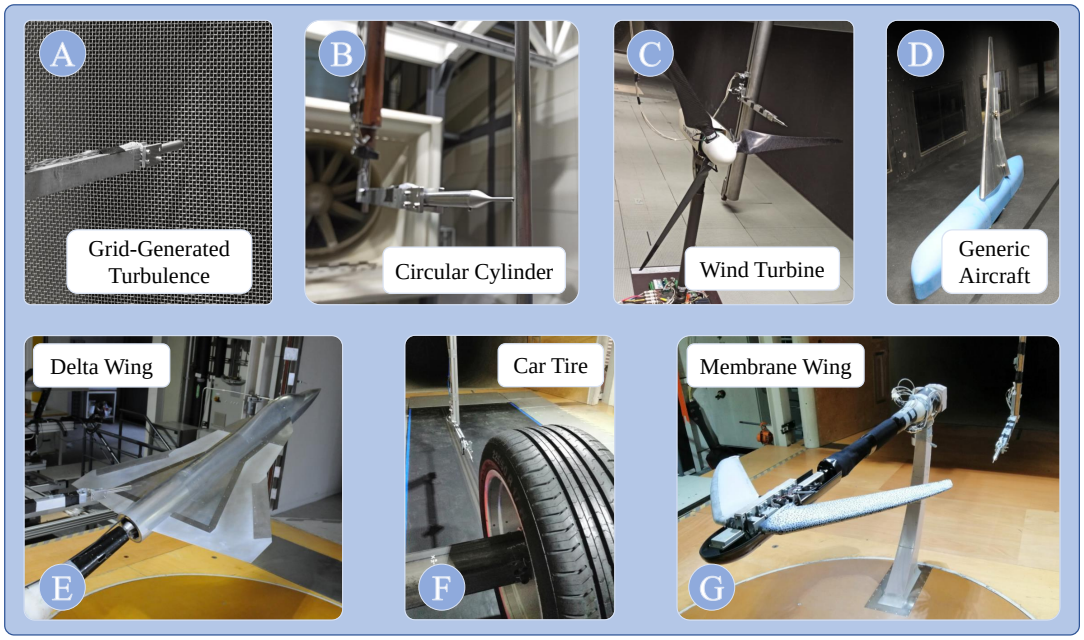

Figure 6.1: Overview over conducted measurements with the FRAP

At this point, a brief explanation is given of why FRAP measurements are superior to other measurement techniques for the subsequent measurement tasks. Besides the ability to be employed quickly and the ease of use, a strong focus will be put on a high spatial as well as temporal resolution in the following measurement campaigns. Especially for strongly unsteady flows the consideration of merely averaged flow fields as they are obtained from stereo PIV measurements is not sufficient enough. The analysis of frequency spectra for the identification of characteristic flow phenomena or the observation of phase-averaged, quasi-transient flow fields can be easily realized with a FRAP. Since measurements are also made in very close proximity to measurement objects, the robustness of FRAPs compared to hot-wire probes is thus also an important advantage.

Besides the already thoroughly described grid-generated turbulence measurement setup (Figure 6.1 (A)) which was mainly used to quantify the spatial and temporal characteristics of such a fast-response pressure probe (see Section 5.3), there were further studies to be mentioned here, before delving into two major application scenarios in the following. In cooperation with other research groups and colleagues at TUM-AER, the FRAP was used for example to quantify the wake of car tires (see Figure 6.1 (F)), the wake of transport aircraft with actuated flaps (see Figure 6.1 (D) and Ruhland et al. [158]), the wake of a delta wing (see Figure 6.1 (E) and Sedlacek et al. [159]), or the wake of a membrane wing (see Figure 6.1 (G)).

Nevertheless, two bigger wind tunnel measurement scenarios are investigated in more detail in the following. Beginning with the well known and documented test case of a (quasi 2D) circular cylinder (see Figure 6.1 (B)) with sub-critical Reynolds number inflow in Section 6.1, a more complicated wake analysis of a wind turbine with dynamically actuated blades serves as the benchmark test for the FRAP in Section 6.2 (see Figure 6.1 (C)).

6.1 Investigation of the near wake of a circular cylinder

The first application of the FRAP within this thesis covers a quasi 2D flow over a circular cylinder. This flow is well-known and described in the literature. Besides experimental data of the near cylinder wake, also CFD simulations in the literature can be used for comparison.

As depicted in Figure 6.2, the flow over a cylinder is mainly characterized by three different flow regions in the vicinity of the cylinder: the boundary layer on the cylinder (A), the shear layers demarcating the recirculation area (B) and the near wake (C).

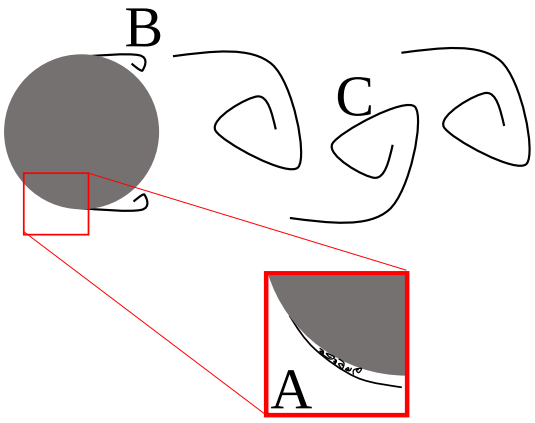

Figure 6.2: Schematic view of the dominant flow regions in the vicinity of the circular cylinder

Furthermore, depending on the Reynolds number Re_D, three flow regimes can occur - the laminar, transitional or turbulent regime [160]. Here, the Reynolds number is

therefore defined as a function of the cylinder diameter D, the freestream velocity U_∞ and the kinematic viscosity ν:

$$Re_D = \frac{U_\infty \cdot D}{\nu} \tag{6.1}$$

The flow regimes can be further divided in sub-ranges: In the sub-critical Reynolds number range $Re_D = [4 \cdot 10^2, 2 \cdot 10^5]$, a transitional mechanism from laminar to turbulent flow is observed. The measurements conducted within this thesis specifically cover the sub-critical Re_D-range where a regular vortex shedding pattern, the so-called von Kármán vortex street, occurs and is mainly described by the vortex shedding frequency f_{vs}. In order to make measurements comparable, the non-dimensional Strouhal number St is introduced as

$$St = \frac{f_{vs} \cdot D}{U_\infty}. \tag{6.2}$$

In the literature, multiple studies cover the shedding behavior downstream of a cylinder either experimentally or numerically. Predominantly, a generic benchmark case with the Reynolds number $Re_D = 3900$ is documented very well. Ong and Wallace conducted hot-wire measurements in the near wake of a circular cylinder and acquired velocity data with different hot-wire probes [161]. In contrast to intrusive hot-wire measurements by Ong and Wallace, Norberg acquired laser Doppler velocimetry (LDV) measurements in the near wake and discussed the statistical moments of the streamwise and lateral velocity components [162]. Furthermore, Parnaudeau et al. compared experimental and large-eddy simulation (LES) results of the cylinder wake flow at $Re_D = 3900$ [163].

Experimental studies with invasive measurement techniques of the very near wake (non-dimensional streamwise distances $x/D <= 4$) are very rare due to the occurrence of low or even negative velocities and high local flow angles in the recirculation area. The latter are very difficult to resolve with standard probes. Therefore, the usage of non-intrusive techniques like particle image velocimetry (PIV) or LDV is advantageous when measuring in close proximity to the cylinder [162].

Furthermore, flow interference of the intrusive measurement device and the objects of interest are present. Interference effects between the probe and the cylinder can influence the vortex shedding behind the cylinder, depending on the gap size between the two bluff bodies [164].

Within the presented investigations on the circular cylinder wake, fast-response aerodynamic pressure probe (FRAP) measurements are presented. In detail, measurements are conducted in the near wake of the cylinder at various Reynolds numbers $Re_D = \{3900, 5000, 10000\}$ and at downstream positions $x/D = [1,\ 10]$, where $x/D = 0$ refers to the position of the axis of the cylinder. Further measurements and a comparison to a triple wire CTA probe have been published in Heckmeier et al. [165]. The pressure probe measurements of the von Kármán vortex system in the wake of the cylinder are compared with numerical and experimental results from the literature. Besides the evaluation of time-averaged flow quantities in the wake and higher order statistical properties, emphasis lies on a specification of the shedding behavior. Table 6.1 gives an overview of the conducted measurements and the used data from the literature.

Table 6.1: Overview of measurements in the near wake of a circular cylinder

	Re_D	x/D	Measurement technique
FRAP	$[3900, 10000]$	$[1, 10]$	FRAP
Ong and Wallace [161]	3900	$[3, 10]$	hot-wire
Norberg [162]	$[3000, 8000]$	$\{0.6, 1, 2\}$	LDV
Parnaudeau et al. [163]	3900	$\{1.06, 1.54, 2.02\}$	LES, PIV, hot-wire

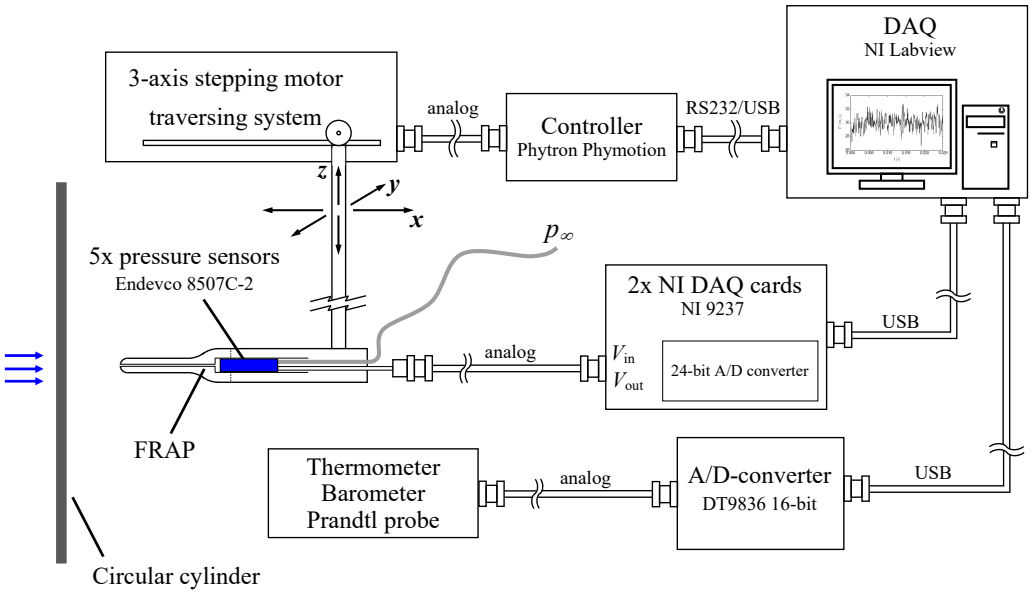

Figure 6.3: Fast-response five-hole probe measurement setup in the wake of the cylinder

The experiments on the near wake of a circular cylinder are conducted in the TUM-AER *Wind Tunnel B*. The Göttingen type wind tunnel (closed-loop) has an open test section with a cross section of $h \cdot b = 1.20\ m \cdot 1.55\ m$. The maximal velocity is $U_\infty = 65\ m/s$. Turbulence intensity lies below 1%.

Near the nozzle, the circular cylinder is vertically installed and clamped on both sides. Two circular cylinders with different diameters $D_1 = 5\ mm$ and $D_2 = 10\ mm$ are chosen to fulfill the Re_D requirements and also accomplish high vortex shedding frequencies. The ratio between the diameter and the length of the cylinder is $D/l < 1/120$. Therefore, 3D-effects due to the clamping are negligible in the conducted measurements. The incoming free stream velocity U_∞ is monitored with a standard Prandtl probe installed at the nozzle exit, acquiring the dynamic pressure q_∞. Furthermore, a temperature probe (PT100) is installed to acquire flow temperature data T. Hence, together with the output of the Prandtl and the temperature probes, the atmospheric pressure signal p_s is digitized by a Data Translation DT9836 16-bit A/D-converter.

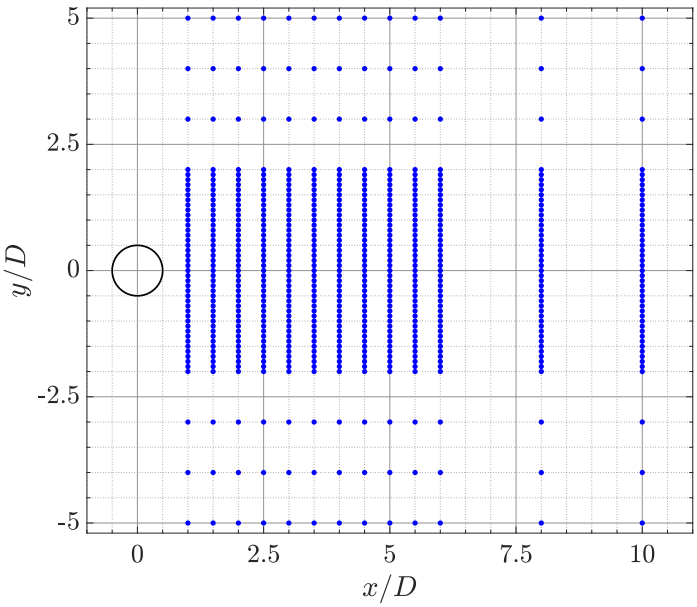

Figure 6.4: Measurement grid in the wake of the cylinder

The probe is equipped with five differential piezo-resistive pressure sensors (Meggitt Endevco 8507C-2), which are pressurized with the ambient pressure outside of the wind tunnel as reference pressure. The sensors of the FRAP are connected to two National Instruments modules NI 9237 which are placed in a NI-chassis cDAQ-9174, which transmits the data to the LabVIEW controlled computer (see wind tunnel setup in Figure 6.3). The signals are sampled with $f_s = 10\ kHz$ for a total acquisition time of $t_s = 5\ s$. By applying an internal low-pass filter, frequencies higher than the Nyquist frequency ($f_N = f_s/2$) are filtered.

The probe is positioned in the near wake of the cylinder with a three-directional traversing system. Therefore, Figure 6.4 shows the traversing grid while the x-y-locations are normalized with the cylinder diameter D. In total, data at 611 measurement locations are acquired for each Re_D configuration.

6.1.1 Time-averaged results of the wake flow

In this part, time-averaged results of the near wake flow field are shown and discussed. To give an overview over the flow field in the circular cylinder wake, Figure 6.5 shows a contour plot of the normalized time-averaged streamwise velocity $\bar{u}/U_\infty$ for $Re_D = 3900$. Due to the displacement of the fluid around the cylinder, the flow is accelerated and values $\bar{u}/U_\infty > 1$ are present. The velocity deficit decreases at the centerline for larger downstream distances. In addition, the lateral expansion of the velocity deficit enlarges with increasing distances downstream the circular cylinder.

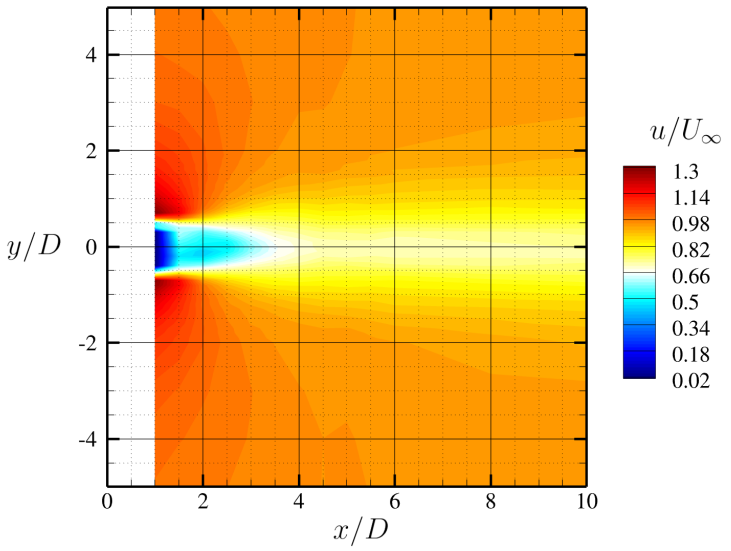

Figure 6.5: Contour plot of the normalized time-averaged streamwise velocity $\bar{u}/U_\infty$ for $Re_D = 3900$

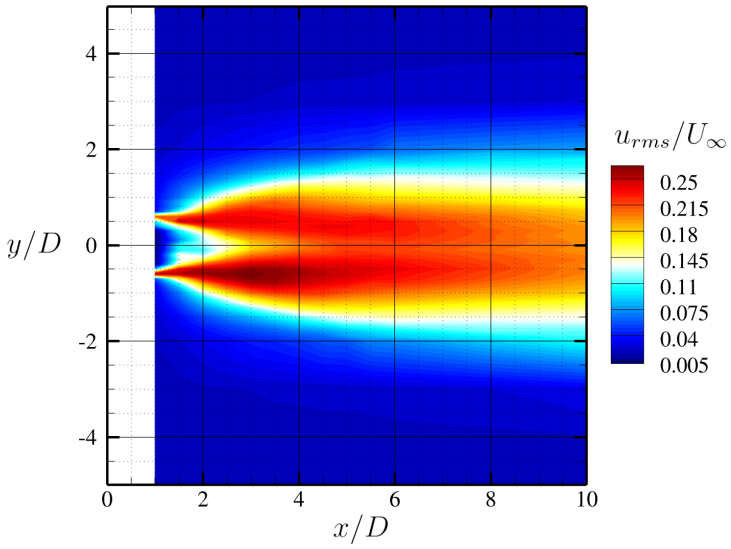

Figure 6.6: Contour plot of the normalized time-averaged RMS-values of the streamwise fluctuations u_{rms}/U_∞ for $Re_D = 3900$

In order to show the level of unsteadiness and identify regions of specific interest for further spectral analysis, Figure 6.6 depicts the contour plot of the normalized time-averaged RMS-values of the streamwise velocity fluctuations u_{rms}/U_∞ for $Re_D = 3900$. At $y/D = \pm 0.5$ strong peaks in the RMS-values are significant, which can be correlated to the von Kármán vortex shedding behind the cylinder. Furthermore, it can be seen that the flow field is not perfectly symmetric as it could be expected. This can be related to a not perfectly uniform inflow and systematic errors introduced by circular cylinder manufacturing and the cylinder mounting into the W/T. However, those smaller differences are negligible and a quasi-symmetric flow can be assumed. For this reason and for better visualization, for the treatment of the lateral velocity profiles, only one half of the symmetric profiles ($y/D \geq 0$) is depicted in the following.

In Figure 6.7, normalized time-averaged streamwise velocities $\bar{u}/U_\infty$ in the wake centerline are presented for the $Re_D = 3900$ case. The FRAP measurements are compared to HW, PIV and LES data from Parnaudeau et al. [163], further HW data by Ong and Wallace [161] and PIV data by Lourenco and Shih [166]. At the location of the cylinder wall at $x/D = 0.5$, the velocity is zero. Data from the literature shows backflow in the recirculation region until approximately $x/D \approx 2$. Due to the limitations in the calibration and data reconstruction routine of invasive probes, the FRAP can not reproduce the negative velocities or angles corresponding to backflow. Hence, FRAP data in the very close proximity of the circular cylinder are subject to higher uncertainties, difficult to accurately assess and serve only as a rough estimate for the trend in the region at $x/D < 3$. Hence, FRAP results in very close proximity to the cylinder $x/D < 2$ are not presented in Figure 6.7 since they could be misleading. An indication for this behavior is an almost identical value at $x/D = 2$ and $x/D = 2.5$ within the FRAP data, which is non-physical. However, with increasing distance to the cylinder the measurements show a good agreement compared to data from the literature, coming both from experimental and numerical simulations. In Figure 6.8, a comparison of the centerline streamwise velocity $\bar{u}/U_\infty$ and its fluctuation RMS-value u_{rms}/U_∞ is given for the three measured Reynolds numbers Re_D. In general, the three Reynolds number trends show a similar behavior. However, the recirculation region is smaller and lower velocity deficits at close distances to the cylinder can be seen for larger Reynolds numbers. Furthermore, an increase in the velocity fluctuation RMS-values at downstream distances $x/D \leq 4$ are present for higher Reynolds numbers. These effects are more pronounced for $Re_D = 10000$ and lead to the assumption that the sub-critical regime can be further divided in sub-regimes, which will be further discussed in the spectral investigation part later.

In Figure 6.9, normalized time-averaged streamwise velocities $\bar{u}/U_\infty$ are depicted in lateral direction in a more downstream position at $x/D = 10.0$. The FRAP measurements are compared to hot-wire anemometry data [161,167] and to numerical simulation data [168]. The symmetric profile measured with the FRAP is in good agreement with data from the literature. As already mentioned, solely half of the symmetric profile $y/D > 0$ is shown. Lateral profiles of the normalized time-averaged streamwise velocity $\bar{u}/U_\infty$ and of the RMS-values of the streamwise fluctuations u_{rms}/U_∞ are shown for increasing distances $x/D = \{2.5,\ 4.0,\ 10.0\}$ and for various Reynolds numbers

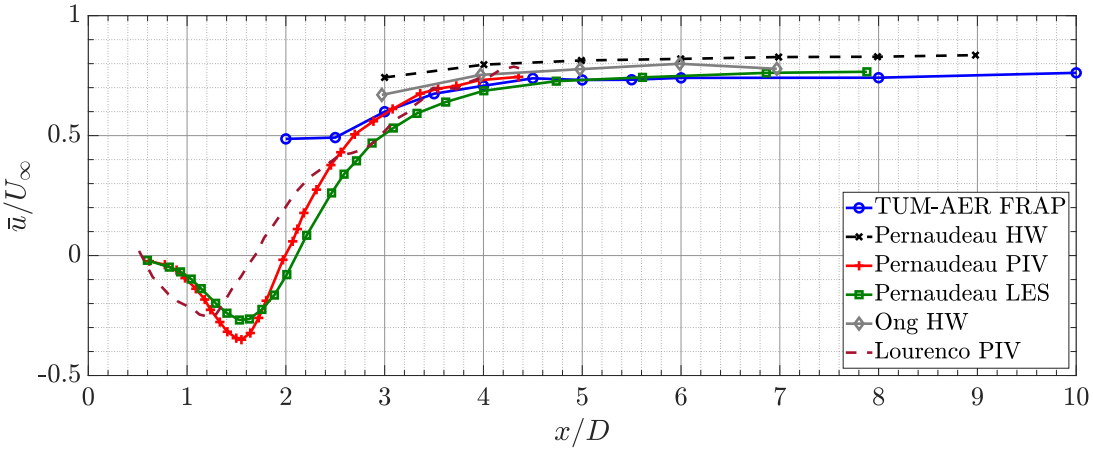

Figure 6.7: Normalized time-averaged streamwise velocities $\bar{u}/U_\infty$ at the centerline at $Re_D = 3900$, compared to Parnaudeau et al. [163], Ong and Wallace [161] and Lourenco and Shih [166]

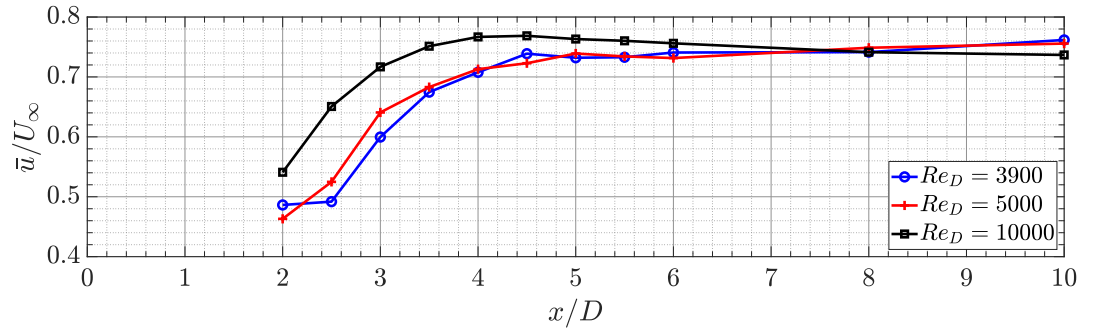

(a) $\bar{u}/U_\infty$ at $y/D = 0$

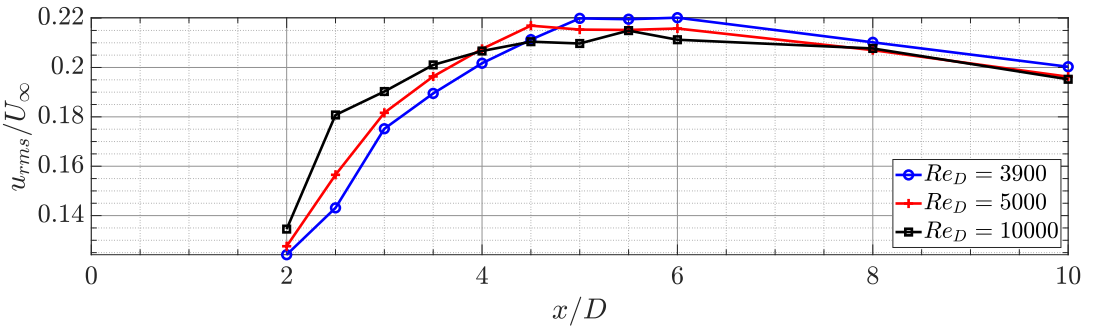

(b) u_{rms}/U_∞ at $y/D = 0$

Figure 6.8: a) Normalized time-averaged streamwise velocities $\bar{u}/U_\infty$ and b) RMS-values of the streamwise fluctuations u_{rms}/U_∞ at the centerline $y/D = 0$ for various Reynolds numbers

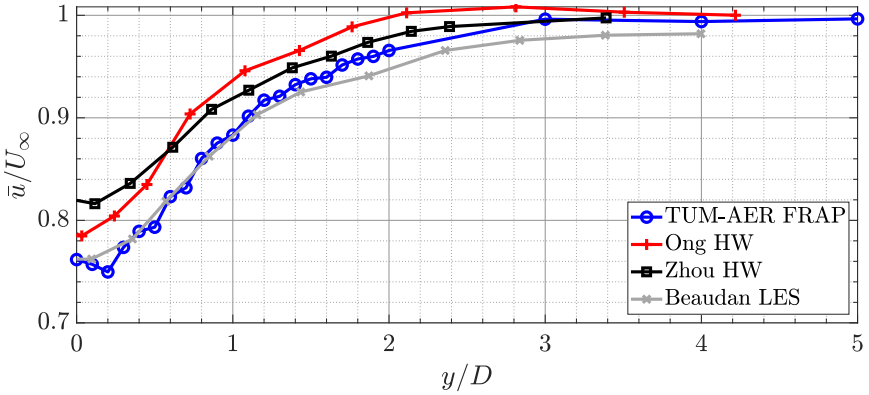

Figure 6.9: Normalized time-averaged streamwise velocities $\bar{u}/U_\infty$ in lateral direction at $x/D = 10$ at $Re_D = 3900$, compared to Ong and Wallace [161], Zhou and Antonia [167] and Beaudan and Moin [168]

$Re_D = \{3900,\ 5000,\ 10000\}$ in Figure 6.10. Furthermore, in good agreement with findings in the literature [161], the velocity profiles show a smaller but broader velocity deficit when increasing the streamwise distance to the cylinder. Considering the RMS-values of the streamwise fluctuations, in closer distance to the cylinder a bump can be seen at $y/D = [0.5, 0.7]$ which corresponds to a transition state in the boundary layer, and thus, an increase in the RMS-values (see Figure 6.10b) and d)). This bump was also observed in the literature [162, 163]. Farther downstream, this effect vanishes and the RMS values flatten to a an lower, almost constant value in the inner section.

6.1.2 Spectral investigations: Vortex shedding and gap effect

In this section, various spectral investigations with the acquired FRAP data are conducted. Most of the results were generated by an analysis of the velocity magnitude fluctuations $U'(t) = U(t) - \bar{U}$ at the respective measurement locations. Similar to the post-processing approach explained in Section 5.3, visualized in Figure 5.10, the Fourier-transformed data can be denoised. Here, only the averaging step is applied – the velocity signal is split in evenly distributed parts of $\Delta t = 0.5\ s$ and the spectra are averaged thereafter.

Figure 6.11 shows the dependency of the Strouhal number St on the Reynolds number Re_D for circular cylinders. For sub-critical Reynolds numbers a Strouhal number around $St \approx 0.2$ can be assumed. Nevertheless, as stated for example in Norberg [169], the shedding behavior follows the depicted trend. The measured shedding behavior for the three test Reynolds numbers are consistent with the data from the literature. In Table 6.2, the respective measured values for the Strouhal number St are listed.

In the following, kinetic energy spectra E_{kin} are shown at various locations in the measurement grid. Frequencies are normalized with the detected von Kármán vortex shedding frequency f_{vs}. Higher harmonics are thereby easily detectable. In Figure 6.12, multiple selected kinetic energy spectra at different lateral measurement locations y/D

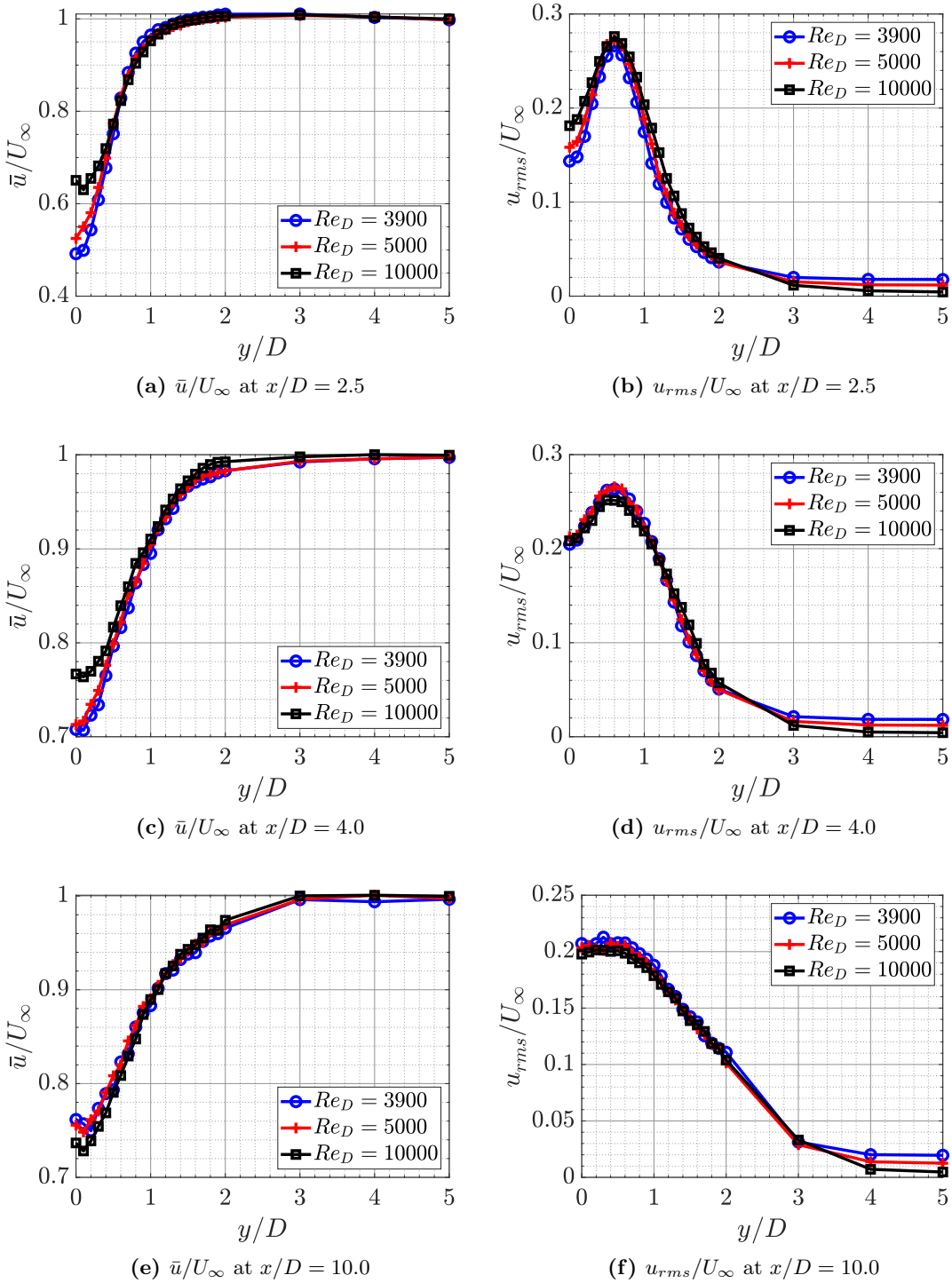

(a) $\bar{u}/U_\infty$ at $x/D = 2.5$

(b) u_{rms}/U_∞ at $x/D = 2.5$

(c) $\bar{u}/U_\infty$ at $x/D = 4.0$

(d) u_{rms}/U_∞ at $x/D = 4.0$

(e) $\bar{u}/U_\infty$ at $x/D = 10.0$

(f) u_{rms}/U_∞ at $x/D = 10.0$

Figure 6.10: a), c), e) Normalized time-averaged streamwise velocities $\bar{u}/U_\infty$ and b), d), f) RMS-values of the streamwise fluctuations u_{rms}/U_∞ at multiple downstream positions $x/D = \{2.5,\ 4,\ 10\}$ for various Reynolds numbers $Re_D = \{3900,\ 5000,\ 10000\}$

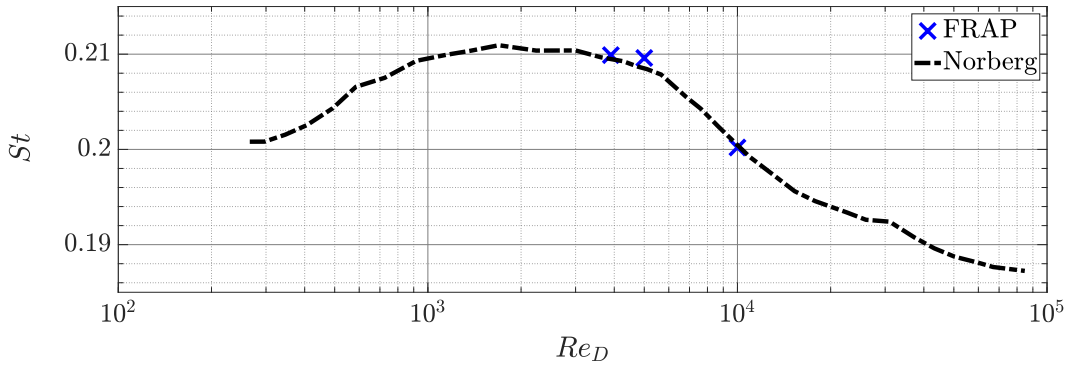

Figure 6.11: Strouhal number St over Reynolds number Re_D. Reference data are extracted from Norberg [169]

Table 6.2: Measured Strouhal number St for the three test Reynolds numbers Re_D

Re_D	3900	5000	10000
St	0.2099	0.2096	0.2002

for $Re_D = 3900$ and $x/D = 2.5$ are shown. Energy content is remarkably higher in the inner locations $|y/D| < 1$ in contrast to measurements farther outside. Besides the dominant first harmonic peak at the vortex shedding frequency $f/f_{vs} = 1$, several higher harmonic shedding frequencies – $f/f_{vs} = \{2,\ 3,\ 4\}$ – can be seen. Throughout all measurements, the second harmonic is present. However, especially near the centerline $y/D = 0$, even harmonics of higher order (3rd and 4th harmonic) are still detectable.

In order to better visualize the aforementioned observations, Figure 6.13 shows three selected kinetic energy spectra extracted from Figure 6.12 at the lateral locations $y/D = \{0.0,\ 0.5,\ 1.5\}$. The magnitude of the peaks decreases and the peak bandwidths get broader for harmonics of higher order. Highest kinetic energy magnitudes can be observed in the lateral region around $|y/D| = 0.5$ which corresponds to the circular cylinder outer dimensions. In the inner region, an almost constant high base kinetic energy level $E_{kin} \geq 10^{-4}$ is present in the frequency range under observation. In outer measurement locations, the kinetic energy spectrum decreases rapidly after the first harmonic peak, showing a kinetic energy level of around $E_{kin} \sim 10^{-6}$.

In order to evaluate the changes of the frequency content in the flow with increasing distances downstream the circular cylinder, the kinetic energy spectra E_{kin} at three downstream measurement locations $x/D = \{2.5,\ 4.0,\ 10.0\}$ are visualized for $Re_D = 3900$ and $y/D = 0.5$ in Figure 6.14. The peak corresponding to the vortex shedding frequency is more pronounced for closer locations. The second harmonic is barely measured at $x/D = 4.0$ or $x/D = 10.0$. However, the third harmonic is most distinct at $x/D = 4$.

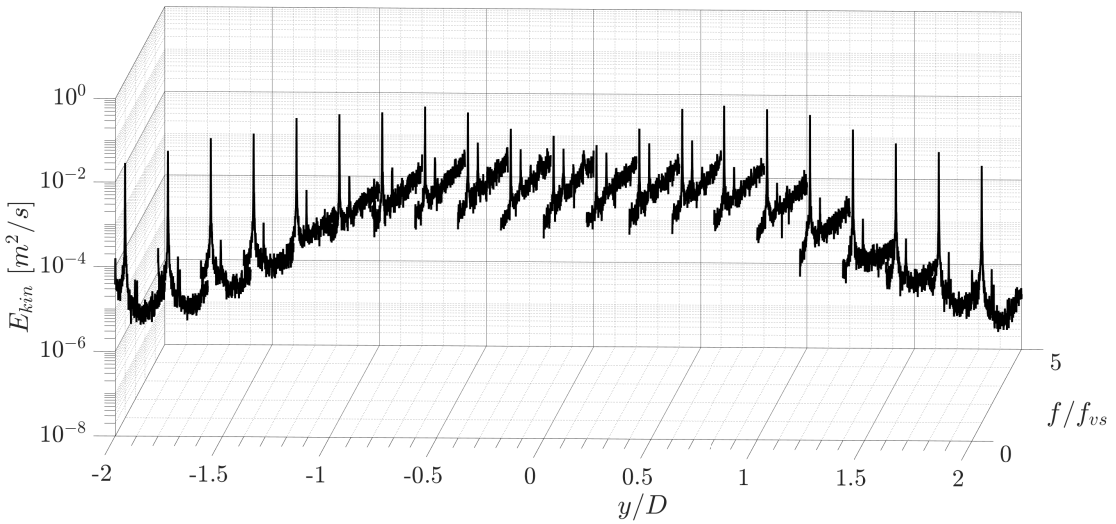

Figure 6.12: Kinetic energy spectra E_{kin} at different lateral measurement locations y/D for $Re_D = 3900$ and $x/D = 2.5$

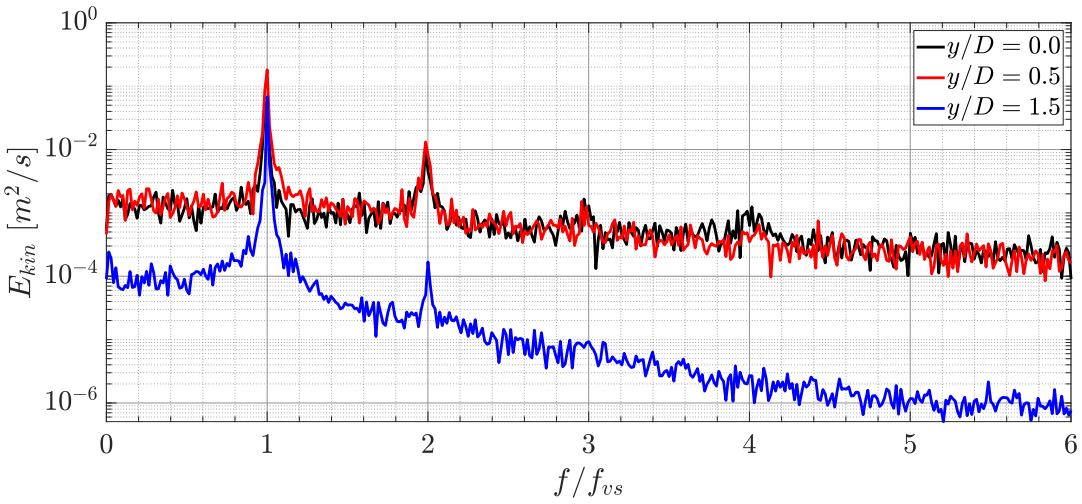

Figure 6.13: Kinetic energy spectra E_{kin} at three lateral measurement locations $y/D = \{0.0,\ 0.5,\ 1.5\}$ for $Re_D = 3900$ and $x/D = 2.5$

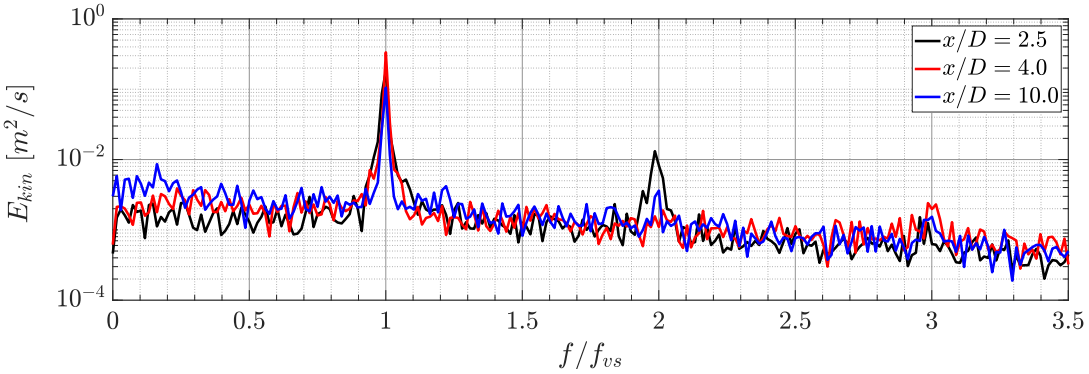

Figure 6.14: Kinetic energy spectra E_{kin} at three downstream measurement locations $x/D = \{2.5,\ 4.0,\ 10.0\}$ for $Re_D = 3900$ and $y/D = 0.5$

Furthermore, it can be seen that the kinetic energy level at low frequencies increases with larger distances downstream the cylinder.

As can be concluded from Figure 6.15, an enlargement of the relative bandwidth of the detached vortex system in the energy spectra for Reynolds numbers $Re_D \geq 5000$ is present. Especially, the data from the $Re_D = 10000$ case show a broader relative bandwidth throughout all downstream locations x/D. Hence, as noted in the literature [169,170], a further division of the sub-critical regime in a lower and upper part at around $Re_D \approx 5000$ is reproduced by the FRAP measurements in this thesis.

In close proximity to the cylinder, an attenuation of the actually measured shedding frequency is observed. Therefore, Figure 6.16 shows a contour plot of the vortex shedding frequency, depicted as the non-dimensional Strouhal number, in the near wake of the circular cylinder. It is clearly visible that the shedding frequency near the cylinder ($x/D < 2$ and $|y/D| < 1$) deviates from an almost constant value in the rest of the measurement grid. A possible reason for this phenomenon are interference effects between the probe and the cylinder. As it was noticed by Hetz et al. [164], the shedding depends on the gap size between multiple bluff bodies of similar dimension in a row. The FRAP having a tip diameter size in the same order of magnitude as the cylinder diameter interferes with the cylinder, leading to a drop in the shedding frequency up to $\Delta f_{vs} = 10\%$ in the vicinity of the circular cylinder.

6.1.3 Concluding remarks

Measurements in the near wake of a circular cylinder were conducted in the sub-critical Reynolds number regime at Reynolds numbers $Re_D = \{3900, 5000, 10000\}$ and at downstream positions $x/D = [1,\ 10]$. Experimental data measured with the FRAP are in agreement with data from the literature. Time-averaged data are shown for various sections and kinetic energy spectra allow a conclusion to be made regarding the frequency content of the periodic flow field, showing the vortex shedding behavior downstream the cylinder. The dependency of the Strouhal number St on the Reynolds number Re_D for

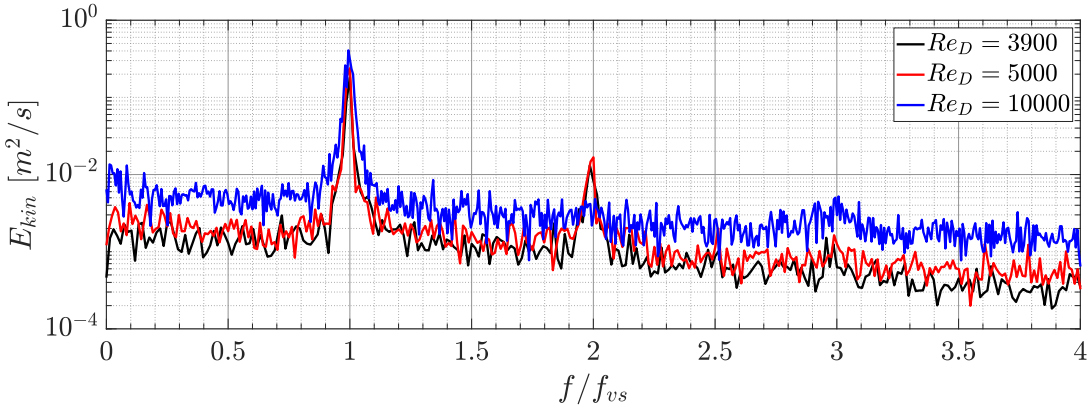

(a) E_{kin} at $x/D = 2.5$

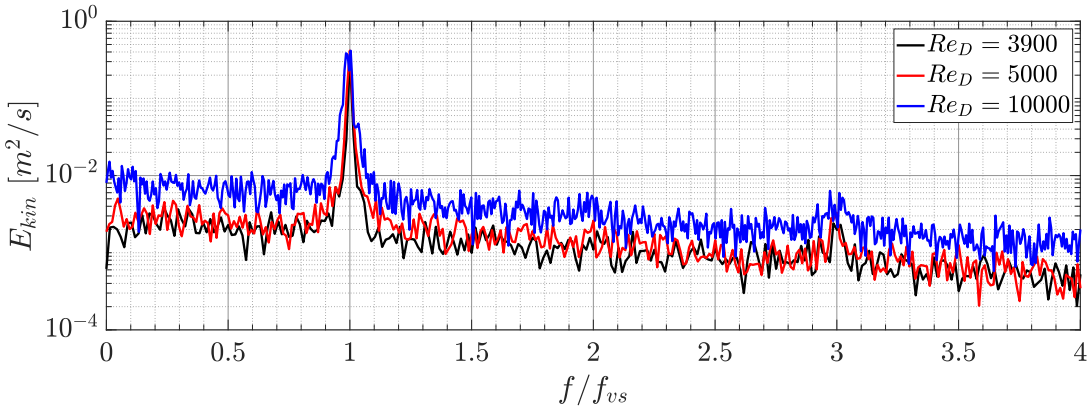

(b) E_{kin} at $x/D = 4.0$

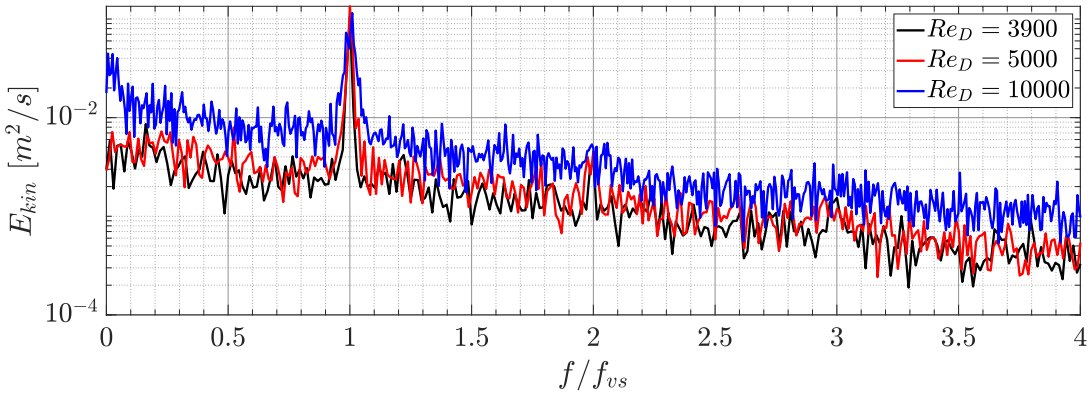

(c) E_{kin} at $x/D = 10.0$

Figure 6.15: Kinetic energy spectra E_{kin} at three downstream measurement locations $x/D = \{2.5,\ 4.0,\ 10.0\}$ for the tree test Reynolds numbers $Re_D = \{3900,\ 5000,\ 10000\}$ at $y/D = 0.5$

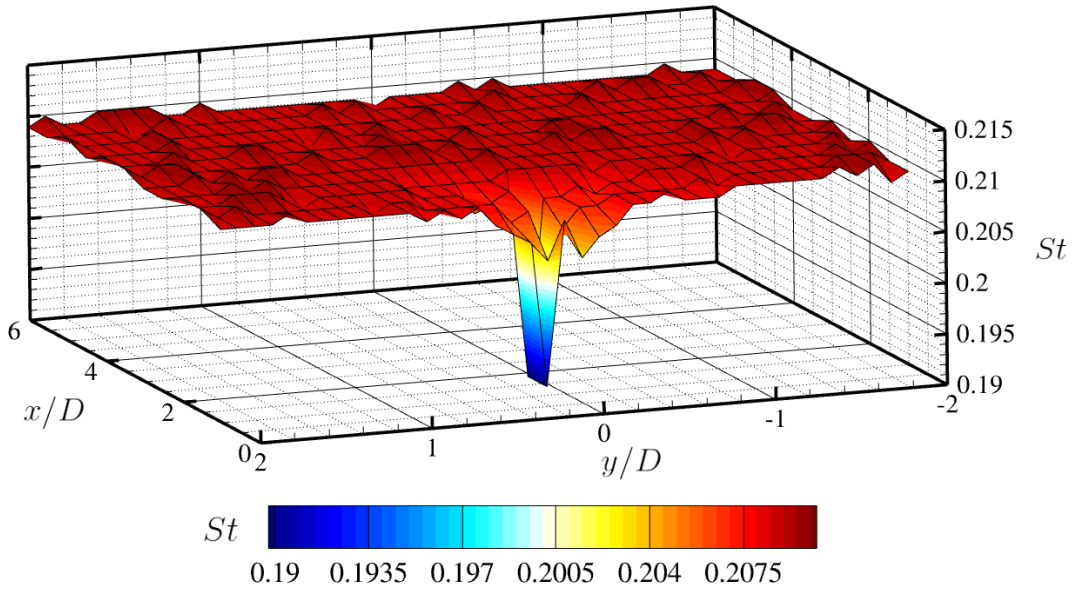

Figure 6.16: Contour plot of the measured shedding frequency, depicted as the non-dimensional Strouhal for $Re_D = 3900$

circular cylinders, which lies approximately around $St \approx 0.2$ for sub-critical Reynolds numbers, could be reproduced. It could also be confirmed that a further division of the sub-critical regime in a lower and upper part at around $Re_D \approx 5000$ is present, which corresponds to an enlargement of the relative bandwidth of the detached vortex system in the energy spectra. In the very near wake inside the recirculation region, where back-flow occurs, intrusive probes have drawbacks to non-intrusive measurement methods. Furthermore, interference effects between the five-hole probe and other objects in close distance are detected and restrict the usage of the FRAP very close to similar sized objects.

6.2 Wake of a wind turbine

This section describes the second major application case for the FRAP in a wind tunnel setup. The wake of a wind turbine shows highly unsteady 3D-flow structures which are worthwhile to analyze in more detail to understand the physics when operating wind turbines either on- or offshore. In the demonstrated case, a novel dynamic individual pitch control strategy is of interest, which was analytically described by Frederik et al. [171] and named *Helix approach* due to the corresponding wake structure movement. The aim of the study is to influence the wake vortex breakdown and therefore enhance wake mixing and faster recovery for higher power readings of successive wind turbines in wind farm scenarios. A schematic visualization of the near wake flow inclusive the vortex pairing and vortex breakdown is given in Figure 6.17.

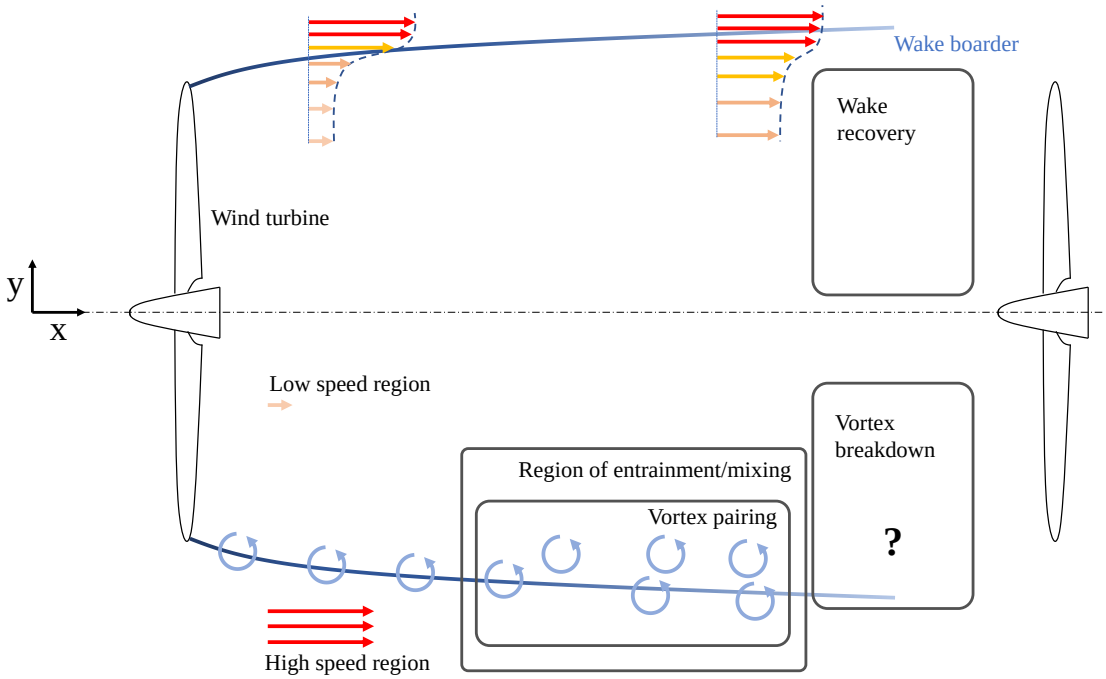

Figure 6.17: Schematic visualization of the near wake flow of a wind turbine with labeling of the zones of particular interest (e.g. possible vortex breakdown region)

In addition to the investigations shown in this section, some results were presented at the *Wind Energy Science Conference 2021* and a research journal article covering the tests and results is currently in work and under review [172]. The following discussion is segmented as follows: Beginning with a motivation and the basic theory on turbine wake instabilities and the Helix approach in Section 6.2.1, the wind tunnel setup and wind turbine power data are shown. This is followed by turbine wake investigations conducted with the FRAP. As already seen in the previous section on the wake of the circular cylinder, the discussion is split into a time-averaged part in Section 6.2.4 and a transient, phase-locked discussion in Section 6.2.5.

6.2.1 Motivation and theory of the Helix approach

This section should give a brief introduction into the wind turbine wake theory. Furthermore, the dynamic individual pitch control is introduced.

In order to optimize the power output of wind farms, it is essential to understand the aerodynamics in the wind turbine wake. The low speed region governing the wake is the reason that multiple successive wind turbines need to be separated with a certain spatial distance between each other. By controlling the upstream turbine wake, e.g. introducing additional instabilities into the flow, synergistic effects on the entire wind turbine farm can be achieved. Hence, controlling and influencing the wake recovery has a huge potential for wind farm power optimization. Basically, the flow behind a wind turbine is defined by the continuous sheet of vorticity which rolls up to two bigger vortices, the tip vortex and the root vortex. The root vortex imposes a rotary movement on the wind turbine wake that is counter rotating to the turbine rotation. The tip vortices build a helical system in the wake of the wind turbine. The wake aerodynamics can be separated into three main phenomena, the vortex shedding, the tip-vortex pairwise instability – also known as leapfrogging instability –, and the turbulent mixing (see Lignarolo et al. [173], Sarmast et al. [174] and Sørensen [175]). If it is possible to influence the tip-vortex breakdown, and thereby increase the net entrainment of kinetic energy, the wake can be re-energized and therefore, recovers earlier. The predominant instability mode in wind turbine wakes is the mutual-inductance instability, where adjacent helical filaments influence each other and start to roll up which results in the leapfrogging phenomenon [173].

In the literature, several control strategies which aim to influence the turbulent mixing of wind turbine wakes are presented. An example for such a control strategy is the dynamic induction control (DIC), where the induction factor is varied over time (see Munters and Meyers [176] and Frederik et al. [177]). Another control strategy was introduced by Frederik et al. [171]. In the so-called *Helix approach*, the wind turbine blades experience a dynamic individual pitch control/excitation (DIPC) resulting in a variation of the fixed-frame tilt and yaw moments. Thereby, they show a meandering of the wake in either clockwise (CW) or counter clockwise (CCW) direction, depending on the slightly out of sync excitation frequency. If this technique is applied, a faster wake recovery is detected. However, in the literature, merely results of computational simulation are present. For this reason, in this thesis, the potential of the Helix approach is experimentally investigated in a wind tunnel (W/T) and should give a more thorough insight in the wake aerodynamics.

In the Helix approach, the blades are controlled with a sinusoidal excitation with a frequency $f_\beta = f_r \pm f_e$, which is out of sync with the rotational frequency $f_r = \omega_r/60 = 1P$. The additional excitation f_e is either added or subtracted to the rotational frequency, leading to the CCW or CW wake meandering, respectively. The following equation shows

the transient blade pitch angle $\beta_b(t)$ for each of the three blades $b = \{1,\ 2,\ 3\}$:

$$\beta_b(t) = \beta_{b,0} + \overbrace{\hat{\beta} \cdot \sin\left(2\pi \underbrace{(f_r \pm f_e)}_{f_\beta} t + \theta_{b,0}\right)}^{\Delta\beta} \tag{6.3}$$

Here, the blade pitch excitation amplitude is denoted as $\hat{\beta}$, the respective blade pitch offset $\beta_{b,0}$, and the azimuthal blade position $\theta_{b,0} = -(2\pi/3) \cdot (b-1)$ at $t = 0\ s$.

6.2.2 Wind tunnel setup

The wind tunnel experiments are carried out in the closed-loop (Göttingen-type) low-speed wind tunnel C (W/T-C) of the Chair of Aerodynamics and Fluid Mechanics of the Technical University of Munich (TUM-AER) to conduct transient fast-response five-hole pressure probe measurements in the wake of the wind turbine model. The W/T-C closed test section has a size of $1.8 \times 2.7 \times 21.0\ m^3$ (height x width x length). The ceiling of the wind tunnel is adjustable to minimize the pressure gradient in the longitudinal direction. Turbulence intensity lies below $Tu < 0.5\%$. In general, in order to simulate the atmospheric boundary layer as seen in the real world case, it is possible to equip the wind tunnel with a vortex generator and roughness elements. Nevertheless, in this study this was omitted in order to emphasize the aerodynamic effects of the actuation while operating the wind tunnel with low turbulence intensity.

The experiments are performed at low speeds $U_\infty \approx 5.3\ m/s$ to operate the turbine in its optimal tip-speed ratio. The turbine wake is captured at the one side of the turbine only in the x-y-plane (see Figure 6.18).

For the wind tunnel tests, two identical scaled wind turbine models with a rotor diameter of $D = 1.1\ m$ are used. They are depicted as *G1 model*s in the following. A brief summary of the applied sensors and controls is given in the following. Nevertheless, a detailed description of the wind turbine setup is given by Campagnolo et al. [178,179]. The rated rotor speed of the three bladed G1 is 850 *rpm*. The blades are manufactured out of unidirectional carbon fiber. Each blade is equipped with an individual pitch actuator and a built-in relative encoder measuring the pitch angle $\beta(t) = \beta_0 + \Delta\beta$. The azimuthal position of the blades/rotor θ is detected via an optical encoder. Furthermore, a torque-meter can measure the torque in front of the torque generator. Moreover, shaft strain gauges are used to measure forces and moments at the shaft. The G1 model is controlled with an industrial real-time Bachmann M1 controller. The controller is connected to a supervisory PC, where all settings and recordings concerning the wind turbine can be done.

The measurement campaign is divided into two scenarios/stages: In the first stage, two turbines are placed in line at $x/D = 0$ and $x/D = 5$ (see Figure 6.18 a)). The upstream turbine is actuated following the control strategy introduced in Section 6.2.1. The downstream turbine acts as a sensor, providing insight on the wake recovery of the first turbine. A series of different actuation frequencies and amplitudes are tested in order to identify the actuation scenarios with the most prominent effects. In the second

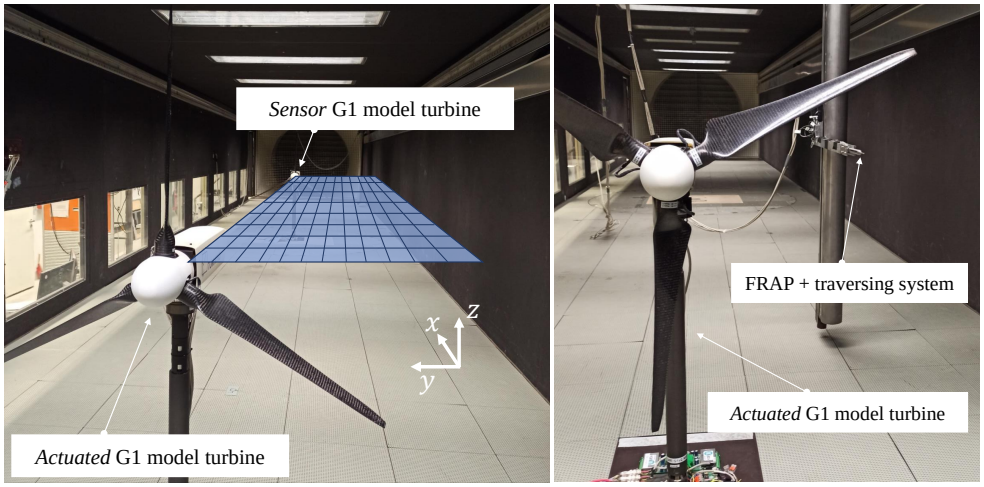

(a) 1. stage setup: two turbines **(b)** 2. stage setup: one turbine + FRAP

Figure 6.18: Wind tunnel setup for the two measurement stages: a) two G1 wind turbine models and a schematic representation of the FRAP measurement grid and b) one G1 turbine and the FRAP in TUM-AER W/T-C

stage (see Figure 6.18 b)), the downstream turbine is removed from the wind tunnel and the FRAP is being traversed in the turbine wake. Thereby, a better understanding of the underlying physics of the identified actuation scenarios should be achieved.

In Figure 6.19, a schematic visualization of the W/T measurement setup for the FRAP wake measurements is given. The FRAP is mounted on a three-axes traversing system. The servo traversing motors are controlled with an Isel servo-controller that can be automatically controlled within the LabVIEW measurement program. Moreover, the ambient air properties (static pressure p_s and temperature T_∞) and the dynamic pressure of the undisturbed inflow q_∞ are measured. The free-stream velocity is monitored with a Prandtl probe that is installed approximately two diameters upstream of the first turbine at hub height. Data are acquired with a Data Translation 16-bit A/D-converter. The FRAP pressure data are sampled with NI cDAQ-9237 full-bridge modules operated at a sampling frequency of $f_s = 10\ kHz$. In order to account for aliasing problems, a low-pass filter below the Nyquist-Shannon frequency ($f_{lp} \leq f_s/2$) is applied in the NI measurement card. The measurement time is set to $t_s = 40.0\ s$. In addition to the acquisition of the five pressure sensor signals, the azimuthal position θ and the blade pitch β of blade 1 are digitized with a NI-9215 analog input cDAQ module in order to synchronize the independent FRAP measurements later. Hence, all measurements can be synchronized in the post-processing routine correlating the different measurements. This phase-locking technique allows for a transient investigation of the full wake of the wind turbine. A similar approach has been followed by Mühle et al. [180] studying the effects of winglets on the tip vortex interaction in a model wind turbine wake.

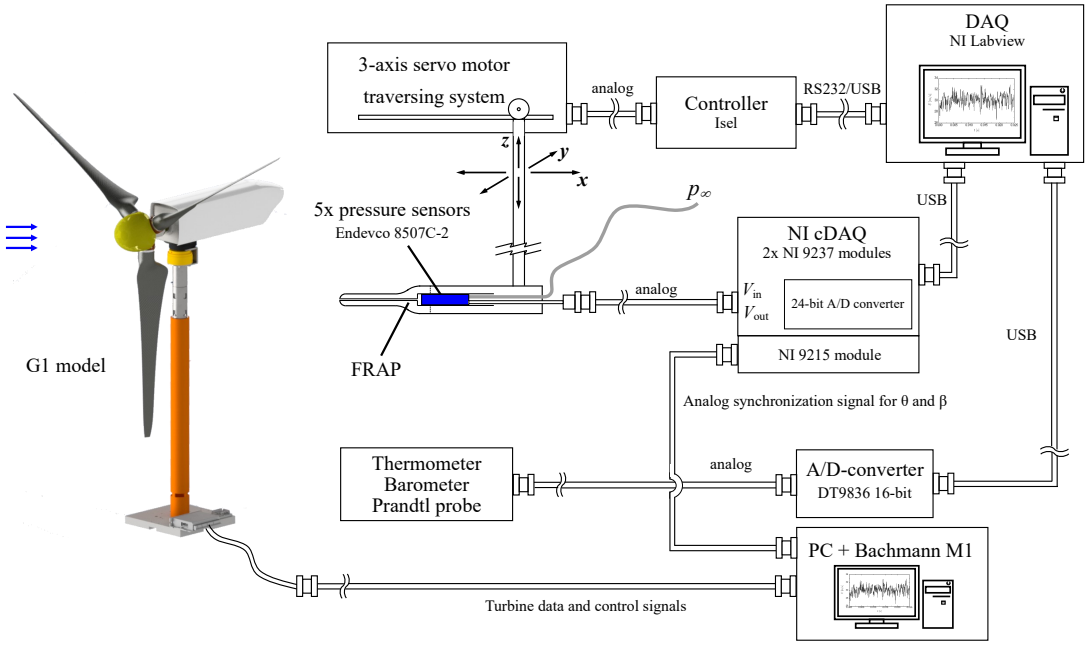

Figure 6.19: Schematic fast-response five-hole probe and G1 wind turbine model measurement setup for TUM-AER W/T-C

6.2.3 Wind turbine data

In this section, the results of the first measurement stage are presented. In the following, the rather short discussion should solely serve as an identification and clarification of the choice of actuation frequencies. For this part of the investigations, the inflow velocity is set to $U_\infty = 5.3\ m/s$ in order to match the optimal tip-speed ratio (TSR) of the turbine. Within the presented investigation, the upstream turbine (actuated G1) is actuated in the dynamic individual pitch mode with a pitch excitation amplitude of $\hat{\beta} = 4°$ in order to magnify the aerodynamic effects downstream the actuated turbine. The degree of freedom here is the excitation frequency f_e, which is controlled by setting a desired pitch frequency f_β in the Bachmann M1 controller. It is operated with a constant rotational frequency $f_r = 840\ rpm/60 = 14\ Hz$ and an optimal pitch offset of $\beta_0 = 0.4°$. The downstream turbine (sensor G1) serves as a sensor and is downrated with $f_r = 750\ rpm/60$ and a pitch offset $\beta_0 = 0°$. The extracted powers of both wind turbines can be seen as an integral metric for the turbine performance. The summation of the two powers shows the overall performance of the whole setup. Figure 6.20 depicts the results of the power investigations by changing the actuation frequency in the range of $f_\beta/f_r = (0.72 : 0.02 : 1.28)$. The extracted powers P are normalized by the power of the upstream/actuated turbine in the baseline scenario P^*, where no actuation is present and the pitch is kept constant to $\beta = \beta_0 \neq f(t)$. In general, the extracted power of the actuated turbine is decreased for all test frequencies, since it is operated in a non-optimal operating point. However, the higher the actuation frequency gets, the lower

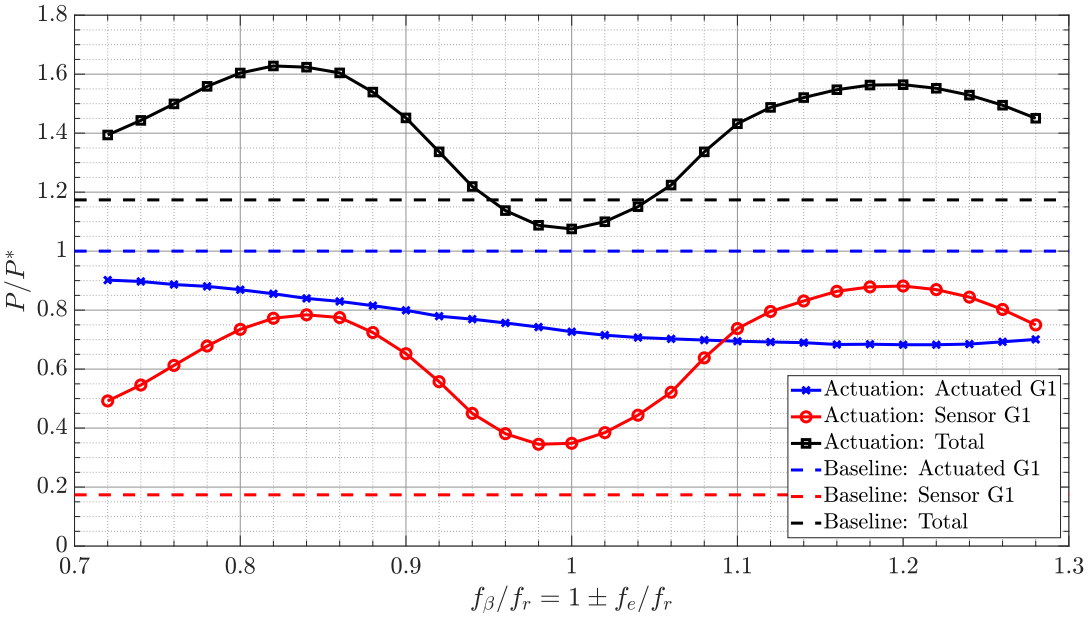

Figure 6.20: Extracted power of the upstream/actuated and downstream/sensor turbine for changing pitch frequencies $f_\beta/f_r = (0.72 : 0.02 : 1.28)$ compared to the baseline case without any actuation $f_\beta = 0$

the power of the actuated turbine becomes. The behavior in terms of extracted power of the downstream/sensor turbine shows a remarkable trend. Clearly, two distinct local maxima can be identified. The two frequency ranges with maximum extracted power are chosen for the wake investigations in the next section. As already discussed in Frederik et al. [171], these two peaks are located at the identical additional excitation frequency of $f_e = 0.18 f_r$. Likewise, the two scenarios are named corresponding to the intended helical movement of the wake in either clockwise (CW) or counter-clockwise direction (CCW). The identified pitch frequencies are $f_\beta|_{CW} = 0.82 f_r$ and $f_\beta|_{CCW} = 1.18 f_r$, and are hereafter referred to as *Helix 0.82* and *Helix 1.18*, respectively.

Figure 6.21 shows a) the nodding moment the hub experiences during 14 rotor revolutions (equivalent to one second of measurement) and b) the Fourier transformation single sided amplitude spectra of the nodding and yawing moments in the fixed-frame coordinate system of the upstream turbine for the baseline and the identified extreme actuation cases. In addition to the peaks at the rotational frequency $f_r = 14\ Hz$ and its higher harmonics, the Helix cases also experience an significant peak at the additional frequency $f_e \approx 0.18 f_r = 2.5\ Hz$ which is more than one order of magnitude bigger than the rotational frequency events. Therefore, the wake investigations in the following sections should clarify the impact of this actuation strategy, and hence, demonstrate whether these perturbations with the detected frequency are induced into the flow and contribute to an faster wake recovery.

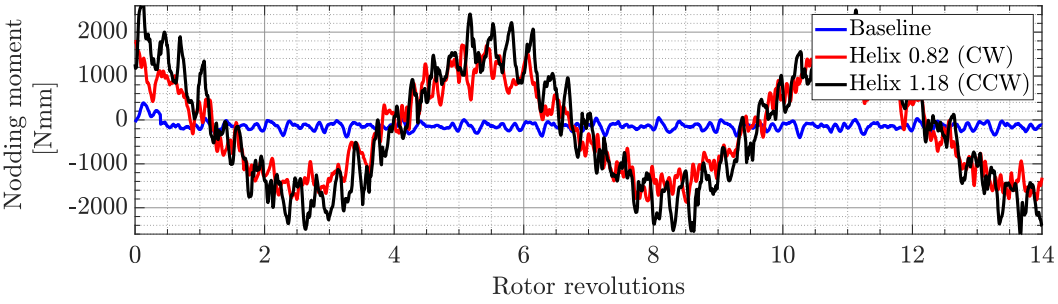

(a) Nodding moment (time domain)

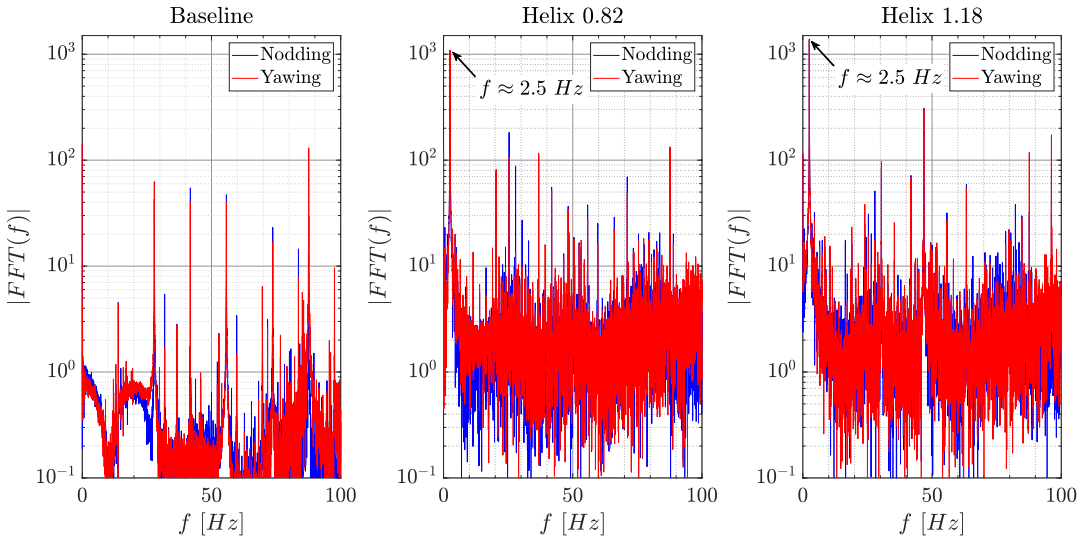

(b) Single sided amplitude spectra (frequency domain)

Figure 6.21: FFT nodding and yawing moments, single sided amplitude spectra for baseline, Helix 0.82, and Helix 1.18

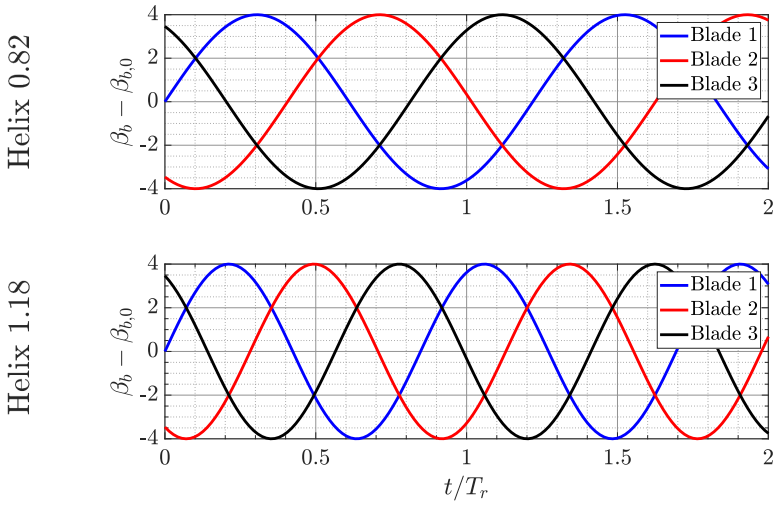

(a) Blade pitch for all three blades for both actuated cases

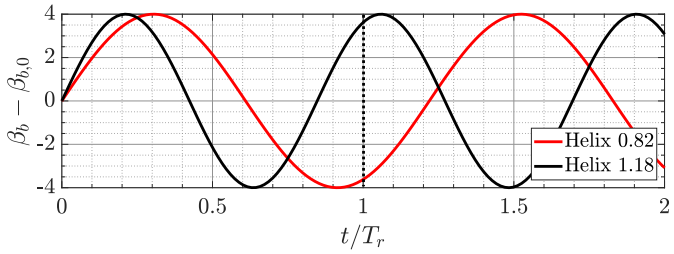

(b) Comparison of the actuated cases for blade 1

Figure 6.22: Blade pitch for all three blades for the two cases, Helix 0.82 and Helix 1.18, with $\beta_{b,0} = 0.4°$ and $\hat{\beta} = 4°$ as a function of the normalized time t/T_r

The blade pitch signals for the two cases, Helix 0.82 and Helix 1.18, are visualized in Figure 6.22 for a fixed blade pitch offset $\beta_{b,0} = 0.4°$. Since, the *G1 model* is three-bladed, the azimuthal blade positions are $\theta_{1,0} = 0°$, $\theta_{2,0} = -120°$ and $\theta_{2,0} = -240°$.

6.2.4 Wake measurements: Time-averaged velocity field

The following section covers the main results of the time-averaged measurements conducted with the FRAP in the wind turbine wake. Hence, the downstream turbine is removed from the W/T (2. stage setup) and the probe is traversed according to the measurement grid depicted in Figure 6.23. All measurement are conducted at hub height $z/D = 0$.

In Figure 6.24, contour plots of the normalized time-averaged streamwise velocity component $\bar{u}/U_\infty$ for the baseline, Helix 0.82 and Helix 1.18 cases are shown. In accordance with the findings in the extracted power observations, the wake velocity has recovered earlier for the actuated cases. However, differences in the wake shape can be seen between the Helix 0.82 and Helix 1.18 case. While the baseline case wake boarder

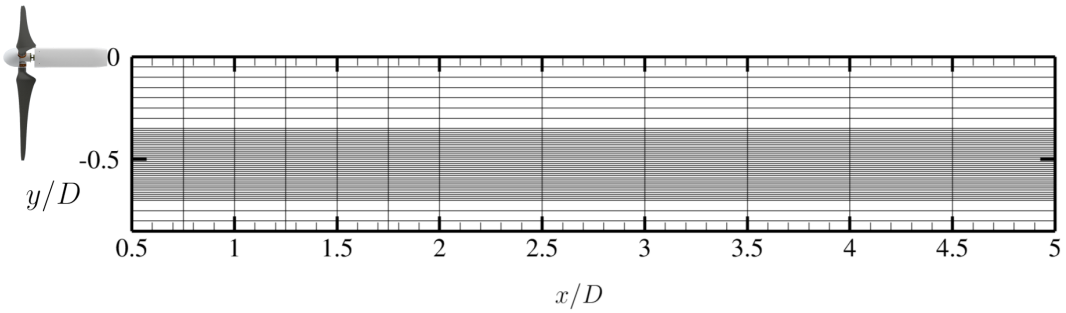

Figure 6.23: Major measurement grid for the wind turbine wake investigations at hub height $z/D = 0$

starts to show entrainment somewhere around $x/D = 2$, a clear separation between low and high energetic flow fields is still present at $x/D = 5$. In the actuated cases, already at the most upstream measurement location $x/D = 0.5$, no distinct wake boarder can be identified. In order to see which instability mechanisms are dominant and where they occur, Figure 6.25 shows contour plots of the normalized time-averaged RMS-values of the streamwise fluctuations u_{rms}/U_∞ for the three cases. For the baseline case, most fluctuations can be seen where the the tip vortices move downstream and separate the wake. Between $x/D = (1.0,\ 2.0)$, the onset of a mixing process can be detected, and hence, leapfrogging is expected. The transient/phase-locked discussion in Section 6.2.5 will provide information about this region for the baseline case. In contrast to the flow patterns in the baseline case, in the actuated cases way higher fluctuation contents are already detectable in the wake. The fluctuations enable an entrainment of the energy-containing flow from outside into the wake. Thereby, mixing is promoted and a recovery of the wake is visible.

In addition to the presented contour plots, the following two figures 6.26 and 6.27 give an insight into the normalized time-averaged streamwise velocity component $\bar{u}/U_\infty$, the velocity component $\bar{w}/U_\infty$, the RMS-values of the streamwise fluctuations u_{rms}/U_∞ and Reynolds stresses $u'v'/U_\infty^2$ at distinct downstream positions $x/D = \{0.5,\ 1.0,\ 2.0,\ 5.0\}$. As already seen in the contour plots, in contrast to the baseline case, a comparably weak wake boarder is present for the actuated scenarios in the very near wake $x/D < 1$ (see Figure 6.26 a) and c)). Both actuated cases show a stronger wake recovery already at $x/D = 2.0$. Furthermore, it can be seen that the Helix 1.18 streamwise velocities at lateral positions close to the centerline recover earlier. Both actuated cases show streamwise velocities above $\bar{u}/U_\infty > 0.7$ at the former location of the downstream turbine (sensor G1 in 1. stage tests) at $x/D = 5.0$. As already mentioned in the theoretical part in Section 6.2.1, the actuation of the out of sync blade pitch provokes a clockwise or counter clockwise additional rotation of the wake. This can be seen in the $\bar{w}/U_\infty$ velocity component plots as well. In stark contrast to the baseline case, where a relatively large upwards velocity in the wake is present, especially the Helix 1.18 with its counter clockwise rotation counteracts this upwards velocity resulting in very small up- or downward velocities in the farther wake. When discussing the velocity

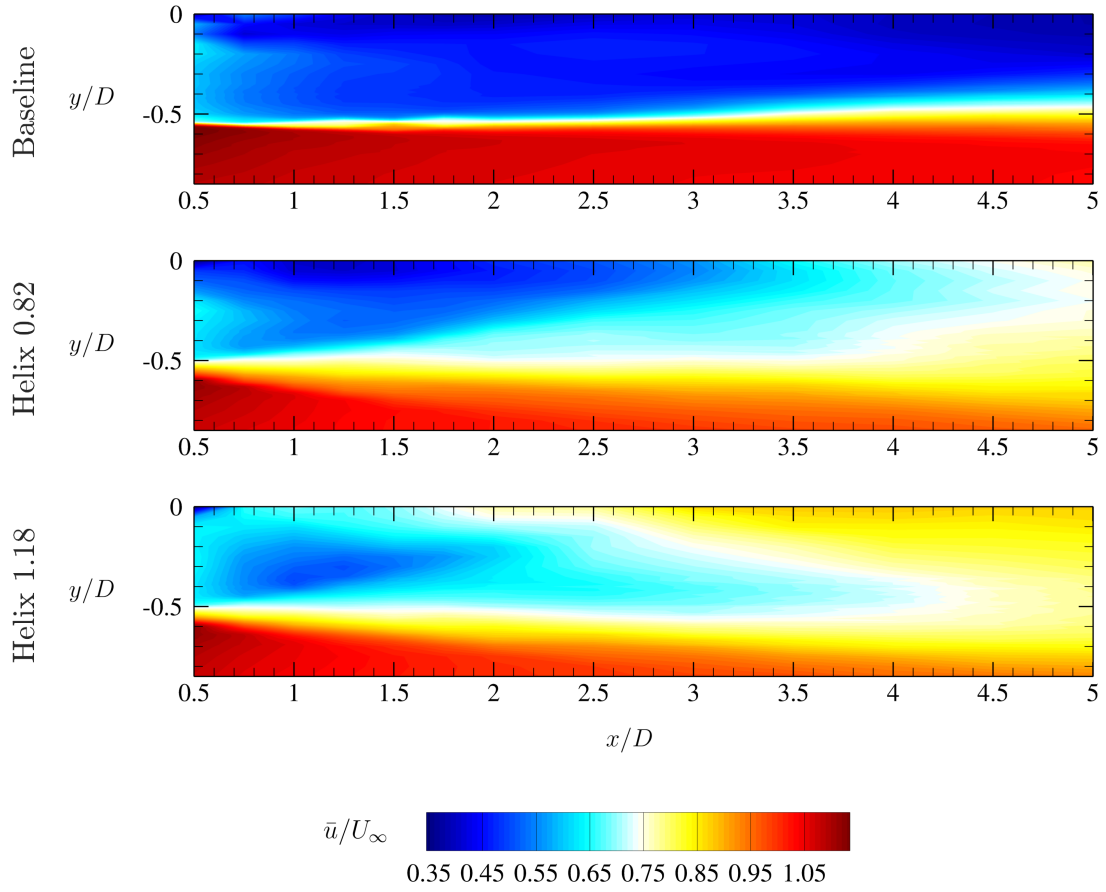

Figure 6.24: Contour plot of the normalized time-averaged streamwise velocity component $\bar{u}/U_\infty$

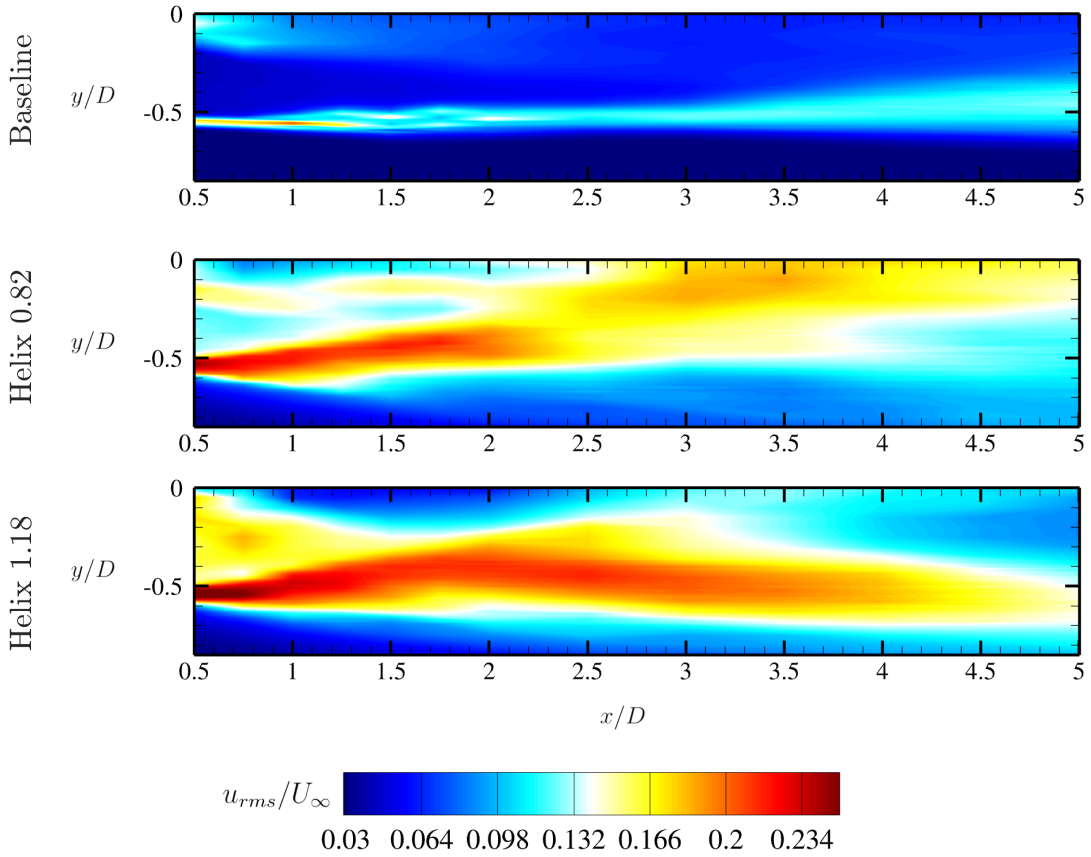

Figure 6.25: Contour plot of the normalized time-averaged RMS-values of the streamwise fluctuations u_{rms}/U_∞

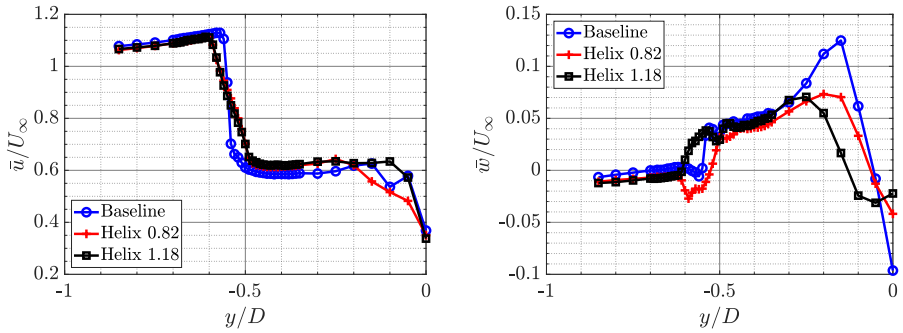

(a) $\bar{u}/U_\infty$ at $x/D = 0.5$

(b) $\bar{w}/U_\infty$ at $x/D = 0.5$

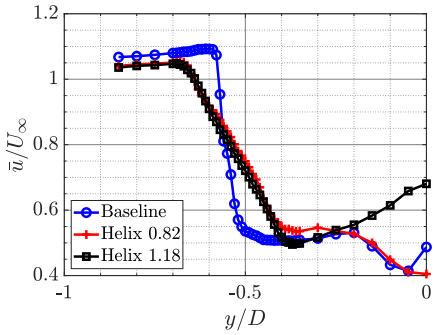

(c) $\bar{u}/U_\infty$ at $x/D = 1.0$

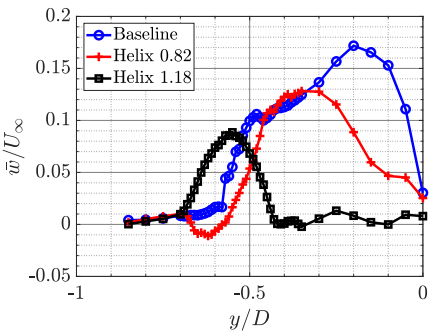

(d) $\bar{w}/U_\infty$ at $x/D = 1.0$

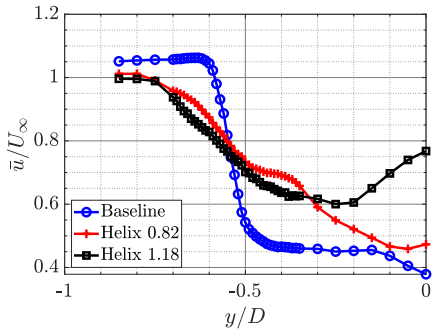

(e) $\bar{u}/U_\infty$ at $x/D = 2.0$

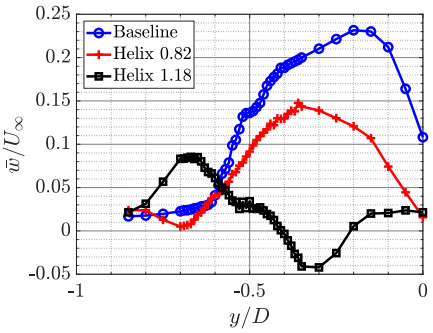

(f) $\bar{w}/U_\infty$ at $x/D = 2.0$

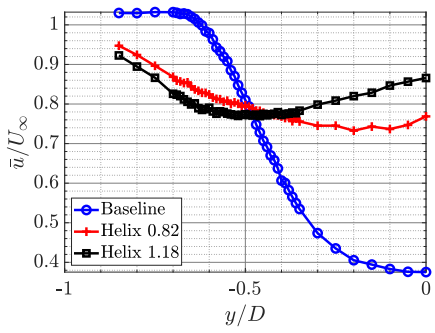

(g) $\bar{u}/U_\infty$ at $x/D = 5.0$

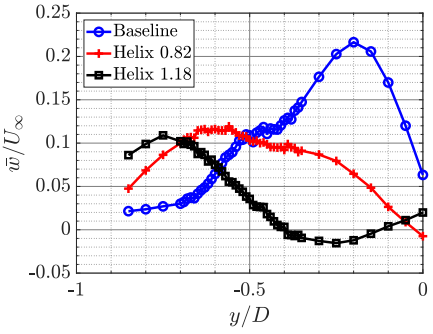

(h) $\bar{w}/U_\infty$ at $x/D = 5.0$

Figure 6.26: a), c), e), g) Normalized time-averaged streamwise velocity component $\bar{u}/U_\infty$ and b), d), f), h) velocity component $\bar{w}/U_\infty$ at multiple downstream positions $x/D = \{0.5,\ 1.0,\ 2.0,\ 5.0\}$

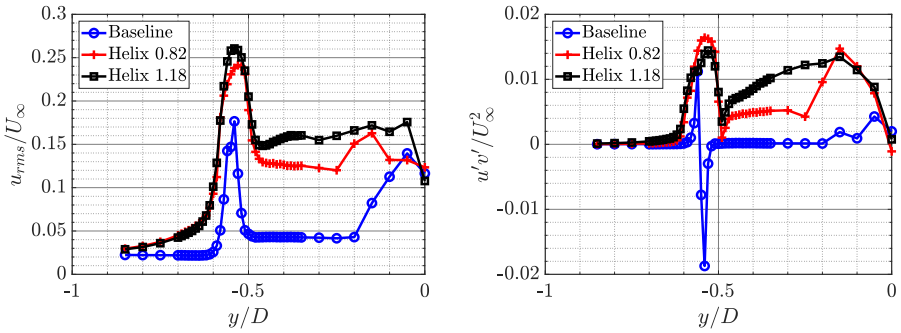

(a) u_{rms}/U_∞ at $x/D = 0.5$ **(b)** $u'v'/U_\infty^2$ at $x/D = 0.5$

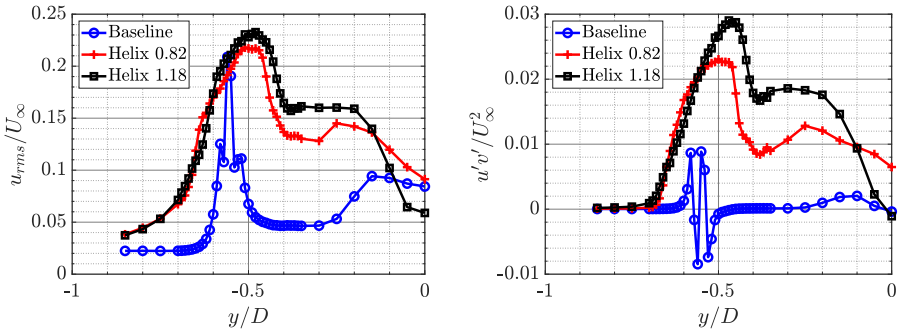

(c) u_{rms}/U_∞ at $x/D = 1.0$ **(d)** $u'v'/U_\infty^2$ at $x/D = 1.0$

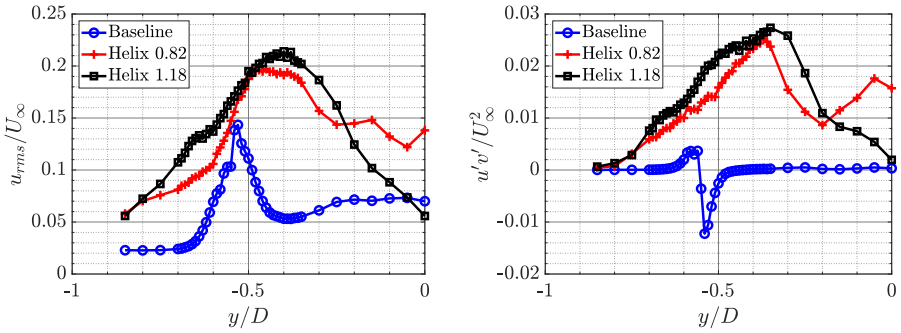

(e) u_{rms}/U_∞ at $x/D = 2.0$ **(f)** $u'v'/U_\infty^2$ at $x/D = 2.0$

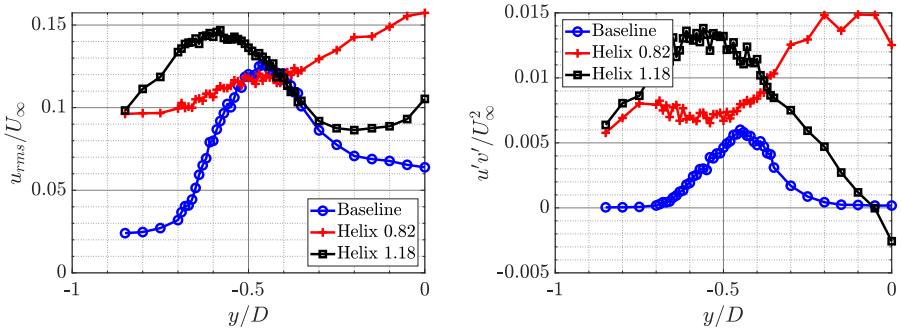

(g) u_{rms}/U_∞ at $x/D = 5.0$ **(h)** $u'v'/U_\infty^2$ at $x/D = 5.0$

Figure 6.27: a), c), e), g) Normalized time-averaged RMS-values of the streamwise fluctuations u_{rms}/U_∞ and b), d), f), h) Reynolds stresses $u'v'/U_\infty^2$ at multiple downstream positions $x/D = \{0.5,\ 1.0,\ 2.0,\ 5.0\}$

fluctuations in Figure 6.27, higher levels of perturbations can be seen throughout all lateral positions y/D for the Helix cases for all investigated downstream distances x/D. Thus, more mixing is already present in the very near wake for the actuated cases. It is therefore assumed that no conventional instability mechanism can be accounted for the wake recovery, like the leapfrogging mechanism. For the baseline case, solely at the locations of the blade tip vortex $y/D \approx -0.55$ and the root vortex $y/D \approx -0.05$ higher fluctuations are detectable. In the farther downstream location at $x/D = 5.0$, the Helix 1.18 streamwise fluctuations are very similar to the baseline case in the region $|y/D| < 0.5$, while the Helix 0.82 case shows higher values at the centerline. The Reynolds stresses $u'v'/U_\infty^2$ show no distinct vortex system for the actuated cases, whereas for the baseline case a change of sign quantifies a pronounced vortex shedding at around $y/D \approx -0.55$. Furthermore for the baseline case, the onset of a instability mechanism – leapfrogging – can be seen by two very close changes in the sign of the Reynolds stresses (see Figure 6.27 d)).

As a next step, in order to discover the governing mechanisms in the actuated cases, kinetic energy spectra are calculated for various locations in the wake of the turbine. Figure 6.28 shows the spectra at four locations $P1 = (x/D, y/D)_1 = (0.5, -0.55)$, $P2 = (2.0, -0.55)$, $P3 = (0.5, -0.15)$ and $P4 = (2.0, -0.15)$. As expected, the baseline spectra solely experience peaks at the rotational frequency $f_r = 14\ Hz$ and its higher harmonics. The peak magnitudes decrease with increasing distance from the turbine. In the more inward locations inside the wake $y/D = -0.15$, these peaks are barely detectable. Looking at the spectra of the actuated cases, the system is governed by multiple higher harmonic peaks, based on the first harmonic of the excitation frequency $f_e = 2.5\ Hz$. As already seen in the turbine hub moments, the system is governed by the excitation frequency f_e instead of the rotational frequency f_r as seen in the baseline flow. Especially in the low bandwidth, additional energy is added for the actuated cases. Together with the already shown plots in Figure 6.27, it can now be concluded that low bandwidth content due to the additional out of sync actuation is introduced in the entire wake $|y/D| < 0.5$ leading to earlier entrainment and faster wake recovery. However, the question how the aerodynamics on the turbine blades in the actuated cases look like can only be evaluated when looking at transient flow data. This will be done in the next section, discussing the phase-locked FRAP measurements.

6.2.5 Wake measurements: Phase-locked/transient observations

In this section, a more detailed analysis of the transient wind turbine wake is conducted using phase-locked post-processed data obtained from the FRAP measurements and the azimuthal blade position signal. Figure 6.29 schematically depicts the principle of the phase-locking process. Each rotation with a rotational period T_r is equally divided into N segments. In this schematic figure, the full rotation is exemplary divided into $N = 12$ segments $\Delta\theta = 360°/N = 30°$. All data points inside a segment and in corresponding segments of same phase (same color) in the upcoming rotational periods are gathered and averaged to a single value, the phase-locked value for this segment. In the wake measurements, the azimuthal position is processed in form of a saw tooth analog signal,

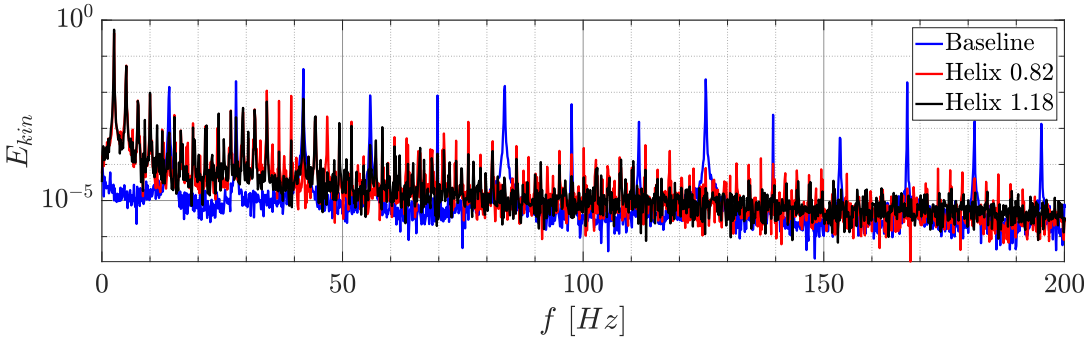

(a) $x/D = 0.5$ and $y/D = -0.55$

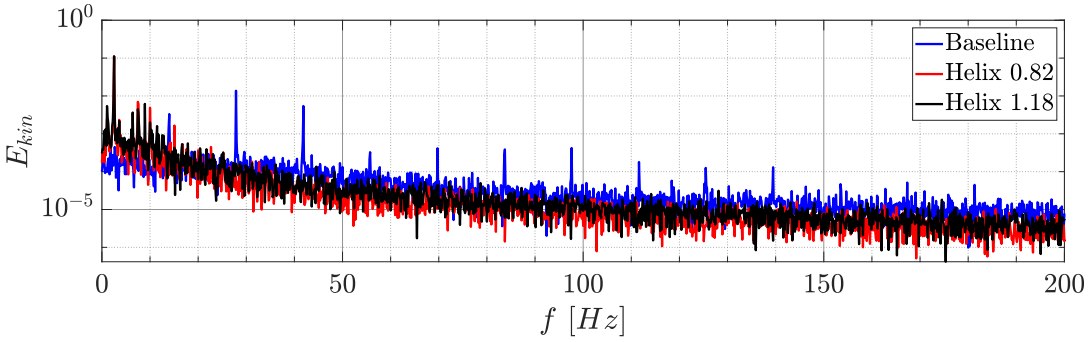

(b) $x/D = 2.0$ and $y/D = -0.55$

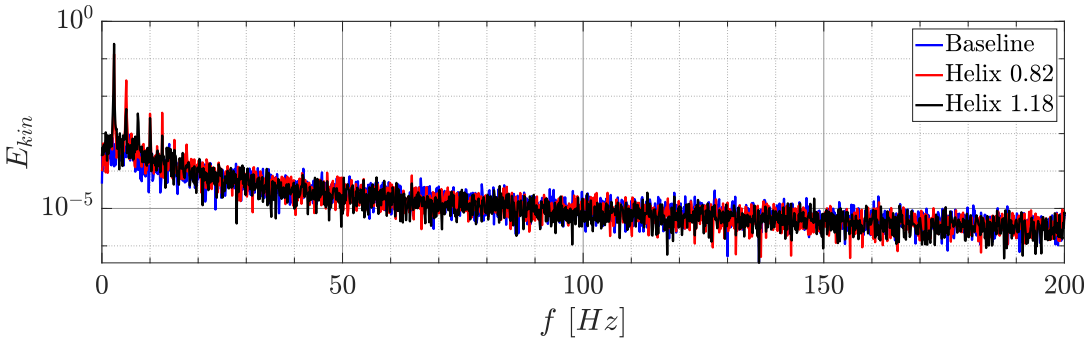

(c) $x/D = 0.5$ and $y/D = -0.15$

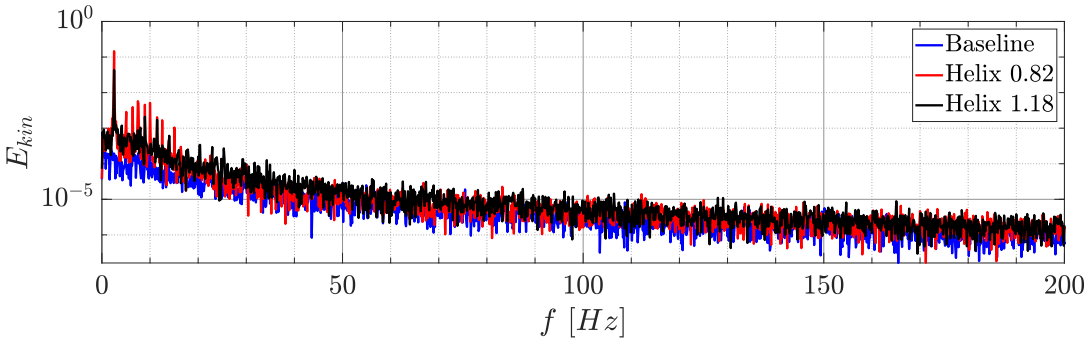

(d) $x/D = 2.0$ and $y/D = -0.15$

Figure 6.28: Kinetic energy spectra E_{kin} at various measurement locations in the turbine wake at $x/D = \{0.5,\ 2.0\}$ and $y/D = \{-0.15, -0.55\}$

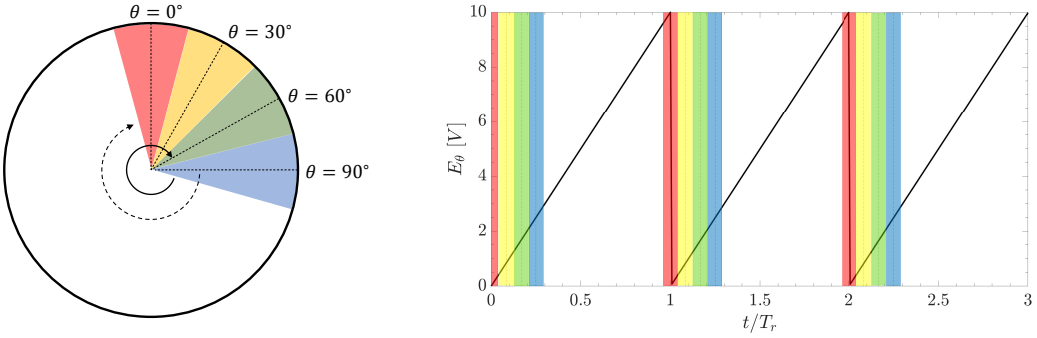

Figure 6.29: Phase-locking principle visualized by the rotational location of the blade θ and the acquired analog output signal voltage E_θ

where $E_\theta = 0\ V$ and $E_\theta = 10\ V$ correspond to $\theta = 0°$ and $\theta = 360°$, respectively. So the FRAP measurements can be conducted without any trigger mechanism and are fully synchronized in the post-processing via the shown phase-locking procedure. In the following analysis, one rotational period was divided into 120 segments. Thus, each phase-locked value maps data of a segment of $\Delta\theta = 3°$.

Here, it has to be noted and must not be forgotten throughout the following discussion, that the results present the phase-locking with the rotational period T_r. Since the actuation of the blade pitch is slightly out of sync, the results cannot fully show a transient behavior as it really occurs at the blade! Solely, a phase-locked averaged investigation is possible. For the baseline case, since no blade pitch actuation is active, the phase-locked results represent a realistic visualization of the flow over one rotor revolution.

Therefore, in Figure 6.30 the instability mechanism – leapfrogging – for the baseline case, which occurs between $x/D = (1.0,\ 2.0)$ is shown by a representation of the normalized phase-locked RMS-values of the streamwise fluctuations $u_{rms,\theta}/U_\infty$. At $x/D = 1.0$, a clear separation of three distinct vortices per revolution can be detected. The index $()_\theta$ indicates the phase-averaged property. The phase difference between the occurrence of the vortices is still approximately $\Delta\theta = 120°$, as expected for a three-bladed turbine. However, a first inward movement is seen, and hence, the instability and interaction between the helical vortices is introduced. In more downstream positions, the roll up process of multiple vortices starts and results in a almost complete merging of the three vortices to a single structure at $x/D = 2.0$.

The figures in the following section represent the data basis for the discussion of the phase-averaged results of the turbine wake. Data was gathered at four downstream line locations $x/D = \{0.5,\ 1.0,\ 2.0,\ 5.0\}$ and are shown for the phase-averaged rotational period T_r. Furthermore, in order to link to the time-averaged results from Section 6.2.4, the time-averaged plots are also shown in the figures. For the sake of consistency, the axes are switched to have a matching y-axis with the phase-locked contour plots.

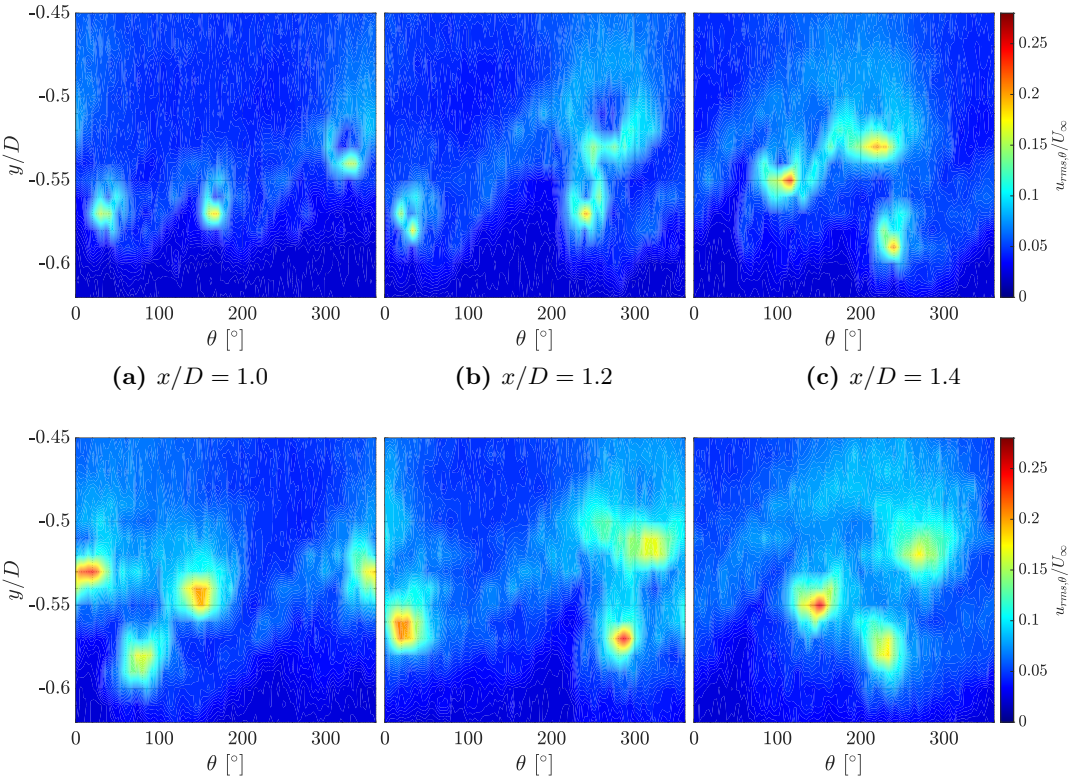

(a) $x/D = 1.0$ **(b)** $x/D = 1.2$ **(c)** $x/D = 1.4$

(d) $x/D = 1.6$ **(e)** $x/D = 1.8$ **(f)** $x/D = 2.0$

Figure 6.30: Leapfrogging in the baseline case: Normalized phase-locked RMS-values of the streamwise fluctuations $u_{rms,\theta}/U_\infty$ at multiple downstream positions $x/D = (1.0 : 0.2 : 2.0)$

In Figure 6.31, the normalized phase-locked streamwise velocity component $\bar{u}_\theta/U_\infty$ in the turbine wake is visualized. In comparison to the baseline case, where the shedding blade tip vortices are still detectable up to $x/D = 2.0$, the velocity field in streamwise directions looks more uniform over one rotor revolution already at downstream distances at around $x/D = 1.0$. Largest gradients occur at the lateral location $y/D = -0.55$ for the baseline case. As stated in the time-averaged results, the shedding region is laterally larger for the Helix cases, around $y/D = (-0.5, -0.6)$ for a downstream distance of $x/D = 1.0$.

A comparison between the tested cases of the normalized phase-locked out-of-plane velocity component $\bar{w}_\theta/U_\infty$ is depicted in Figure 6.32. At $x/D = 1.0$, three periodic coherent structures are visible for all three cases corresponding to the three blades per revolution. At $x/D = 2.0$, things have changed: for the baseline case, very high upwind velocity components are measured and can be accounted to the induction of the root vortex system on the wake flow. A counter rotation of the wake compared to the blade movement direction is seen. Moreover, a clear separation between the three blade vortex structures is still present. However, for the Helix cases, the intended influencing of the wake by introducing out of sync phenomena results in a changed distribution of the out-of-plane velocities. In the Helix 0.82 case, the upwards component is increased in the inner section $|y/D| < 0.5$. Three coherent structures with stronger negative velocities are displaced to farther lateral locations at $x/D = 1.0$. For the Helix 1.18 case, an antagonistic behavior is detectable at $x/D = 1.0$. Inside the wake region $|y/D| <= 0.5$, an almost constant or downward velocity is measured. The coherent structures are displaced to more central positions. At $x/D = 2.0$, only one coherent structure is seen for both actuated cases. The shown results demonstrate that the Helix 1.18 actuation works against the initial wake rotation (CCW movement), whereas the Helix 0.82 works with the wake rotation (CW movement).

Next, in Figure 6.33, the normalized phase-locked RMS-values of the streamwise fluctuations $u_{rms,\theta}/U_\infty$ are presented. Similar to the already mentioned results in the discussion before, the baseline case experiences three distinct, separated peaks due to the three tip vortices per revolution. Furthermore, the fluctuation level resulting from the root vortex system near the centerline is increased. A totally different situation can be identified for the Helix cases. Really high fluctuation contents are additionally introduced by the actuation. At the nearest downstream line location at $x/D = 0.5$, a band of really high fluctuations with separated peaks ($\Delta\theta \approx 120°$) is detected for both Helix cases. However, the Helix 1.18 case shows a more uniform and higher fluctuation level throughout the full revolution. As can be seen in the more downstream contour figure, the additional fluctuations provoke an earlier mixing and entrainment of higher velocity flow from the outer area with faster velocities, leading to a more uniform fluctuation level at $x/D = 5.0$.

In order to understand the flow physics for the actuated cases better, a further refinement at locations closer to the turbine is performed. A refined measurement grid in the region between $y/D = (-0.45, -0.62)$ and $x/D = (0.35, 0.64)$ for both actuated cases is defined and additional measurements are conducted. The spatial distance between the points is fixed to $\Delta(y/D) = \Delta(x/D) = 0.01$ in each direction. The contour plots

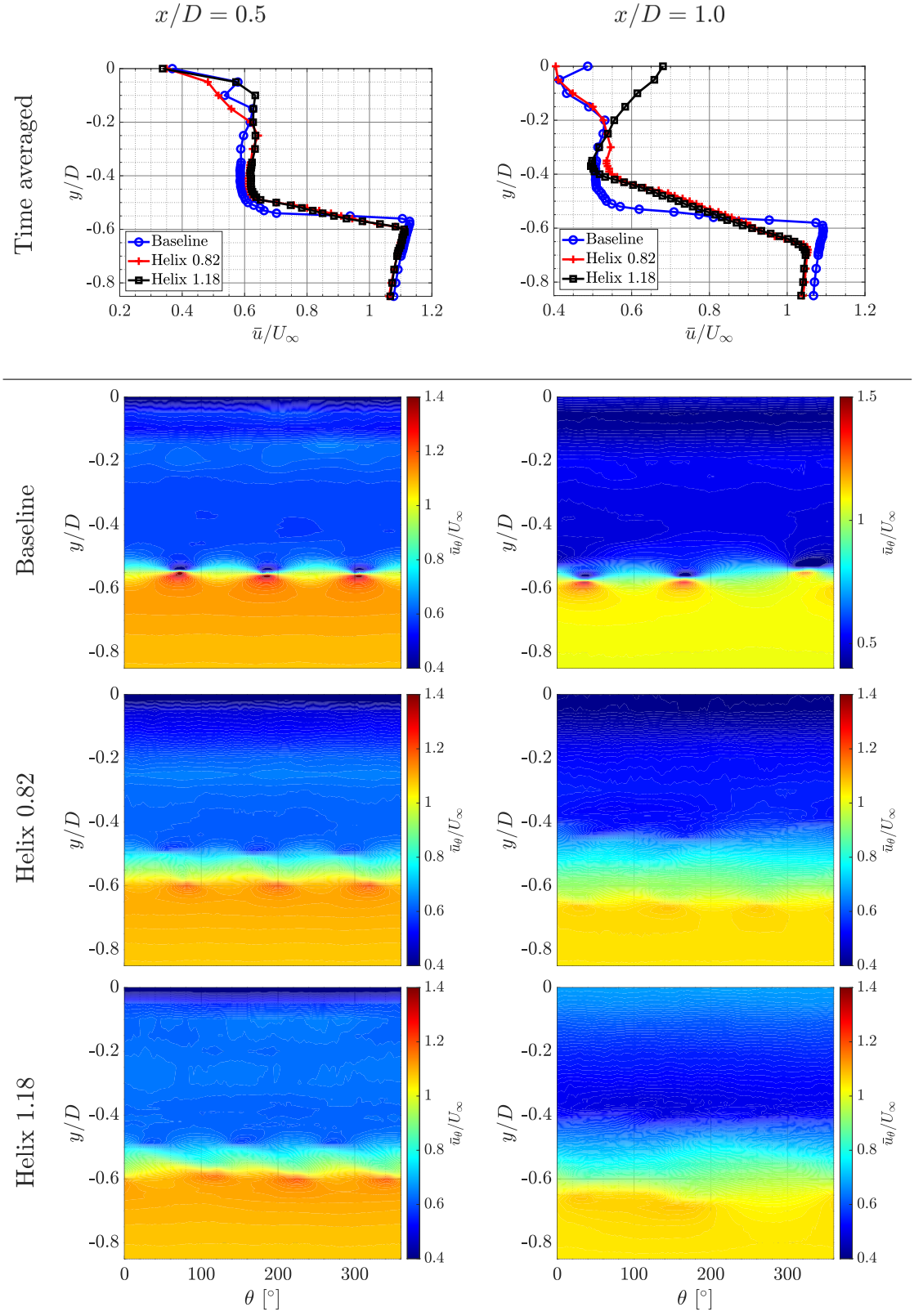

Figure 6.31: Normalized phase-locked streamwise velocity component $\bar{u}_\theta/U_\infty$ at multiple downstream positions $x/D = \{0.5,\ 1.0,\ 2.0,\ 5.0\}$

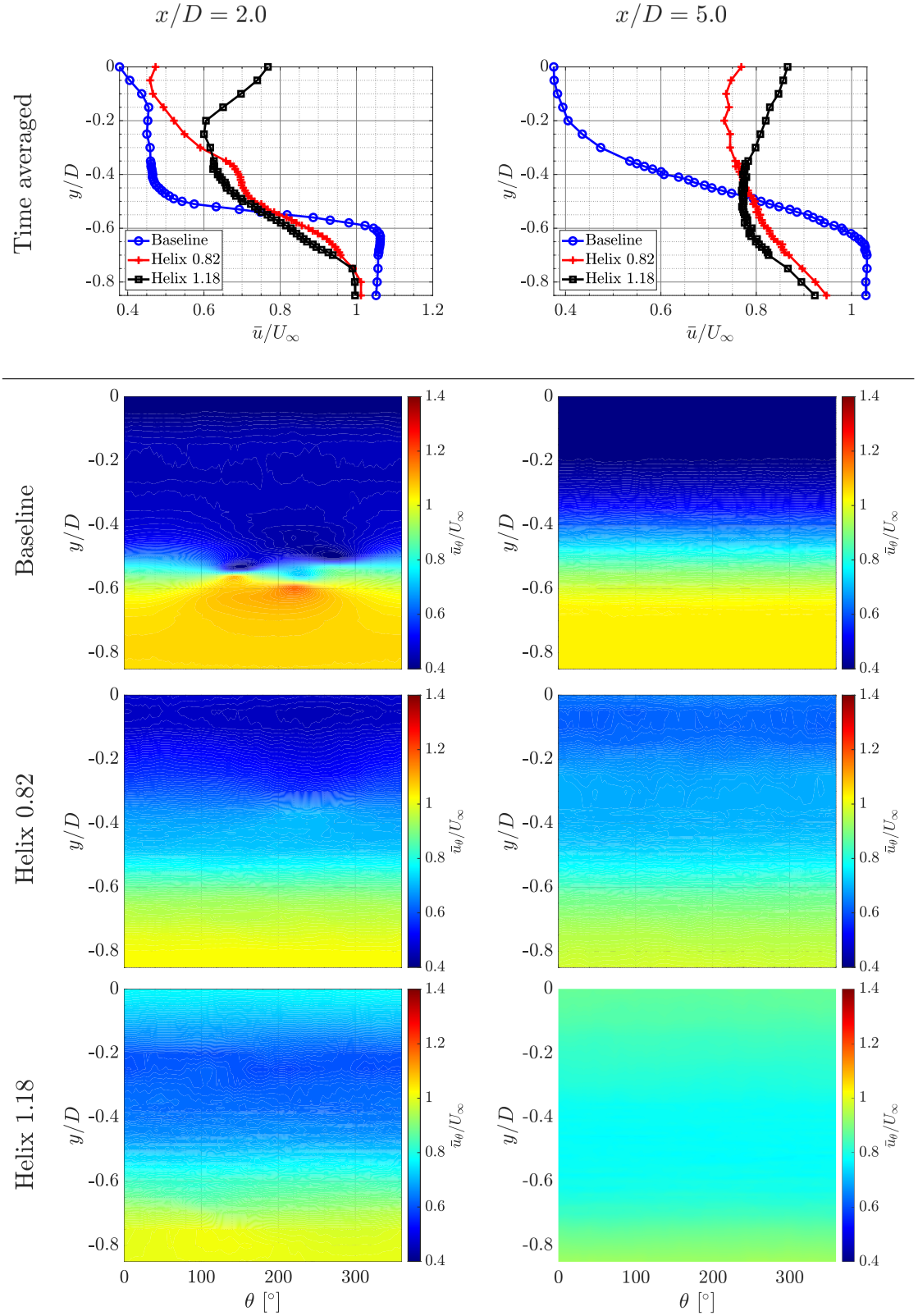

Figure 6.31: Normalized phase-locked streamwise velocity component $\bar{u}_\theta/U_\infty$ at multiple downstream positions $x/D = \{0.5,\ 1.0,\ 2.0,\ 5.0\}$ (cont.)

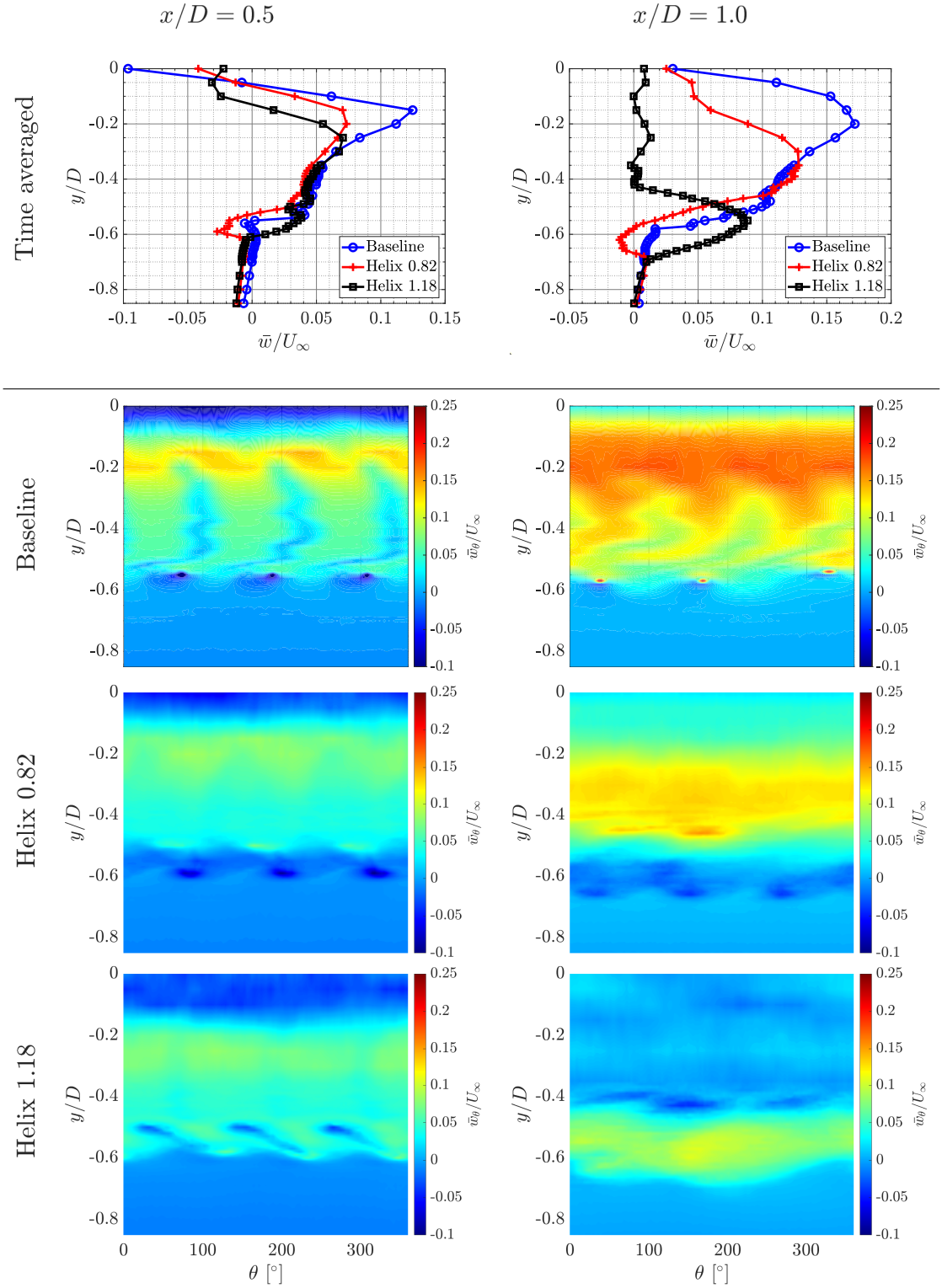

Figure 6.32: Normalized phase-locked velocity component $\bar{w}_\theta/U_\infty$ at multiple downstream positions $x/D = \{0.5,\ 1.0,\ 2.0,\ 5.0\}$

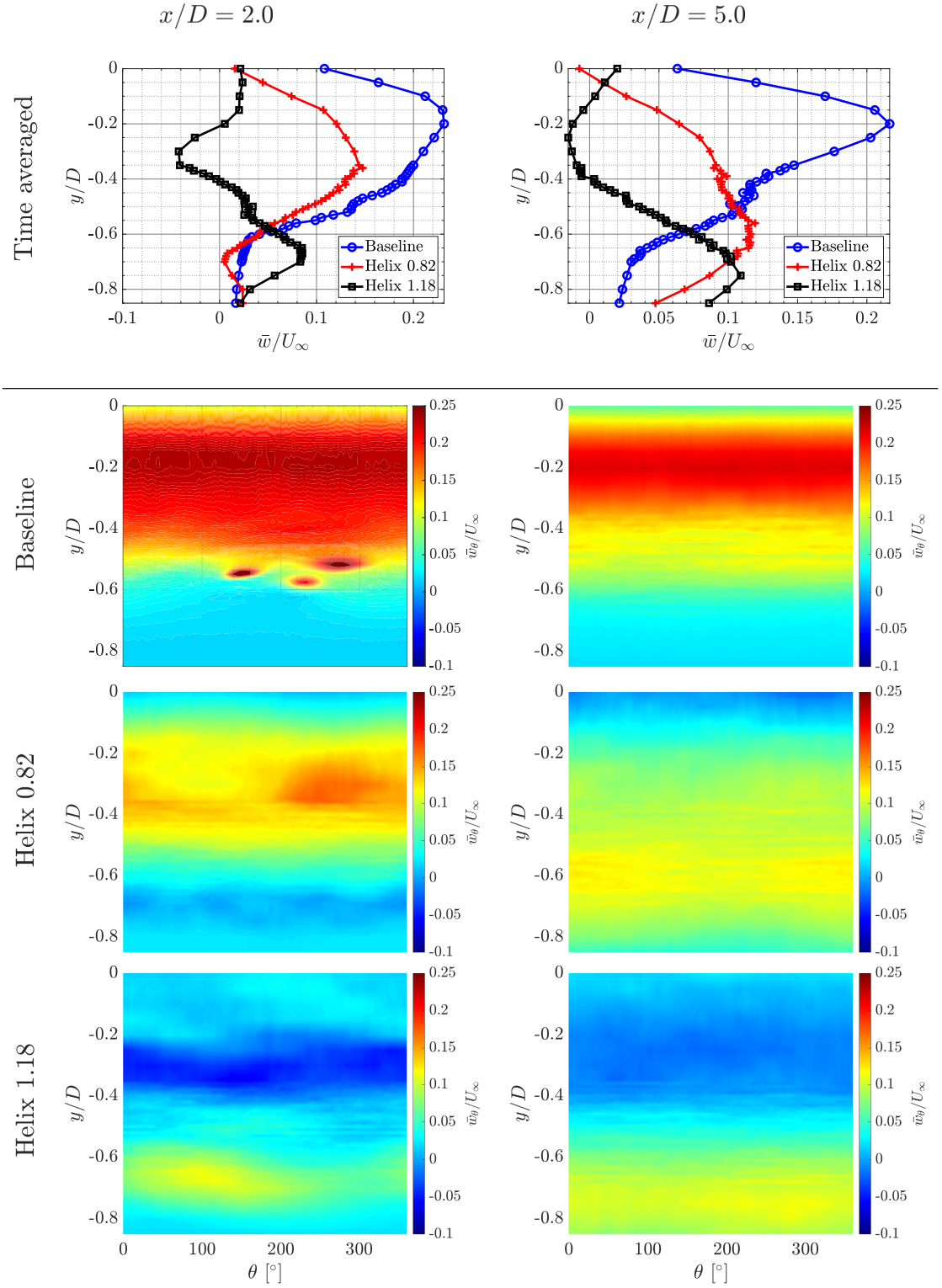

Figure 6.32: Normalized phase-locked velocity component $\bar{w}_\theta/U_\infty$ at multiple downstream positions $x/D = \{0.5,\ 1.0,\ 2.0,\ 5.0\}$ (cont.)

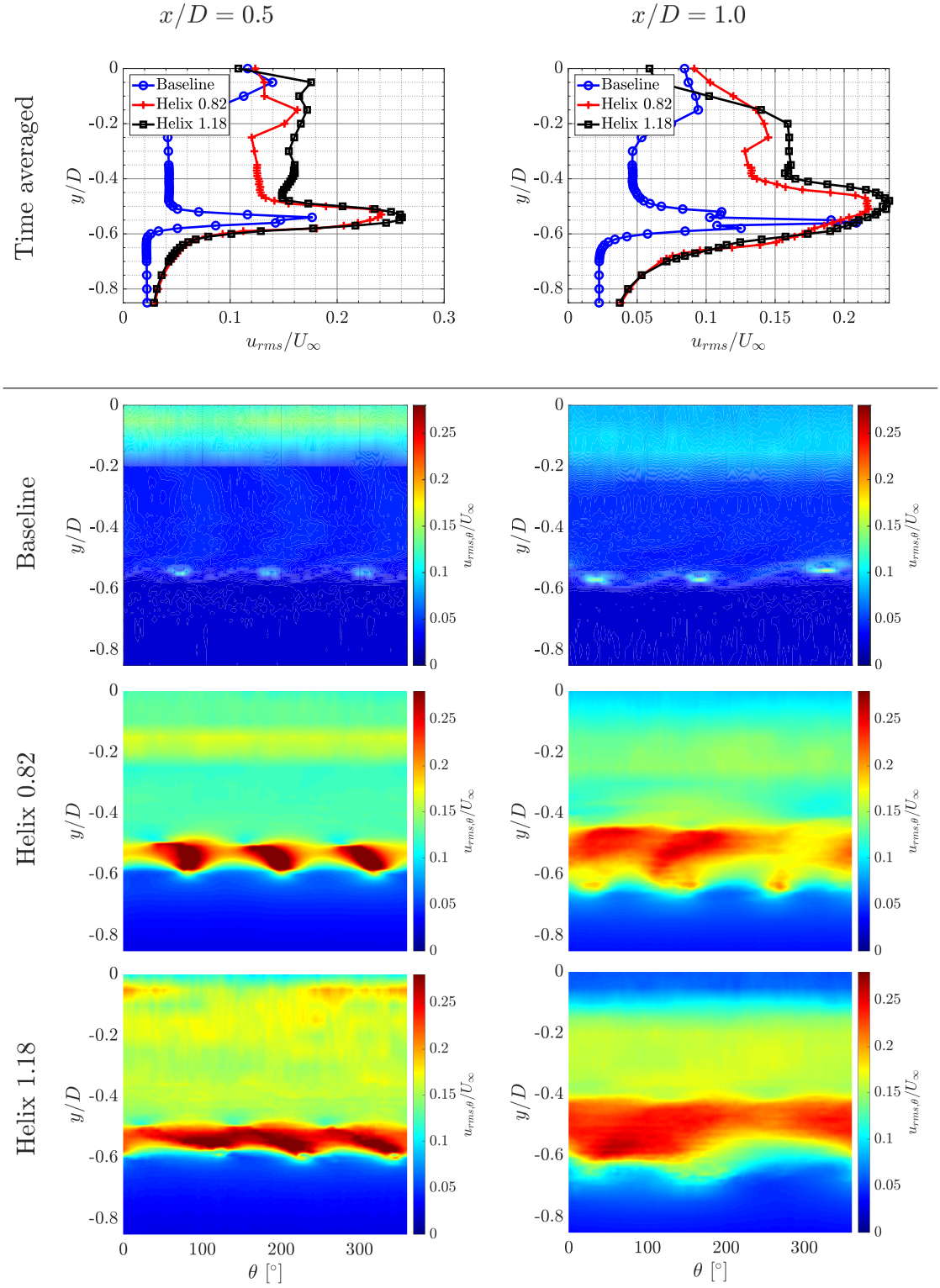

Figure 6.33: Normalized phase-locked RMS-values of the streamwise fluctuations $u_{rms,\theta}/U_\infty$ at multiple downstream positions $x/D = \{0.5,\ 1.0,\ 2.0,\ 5.0\}$

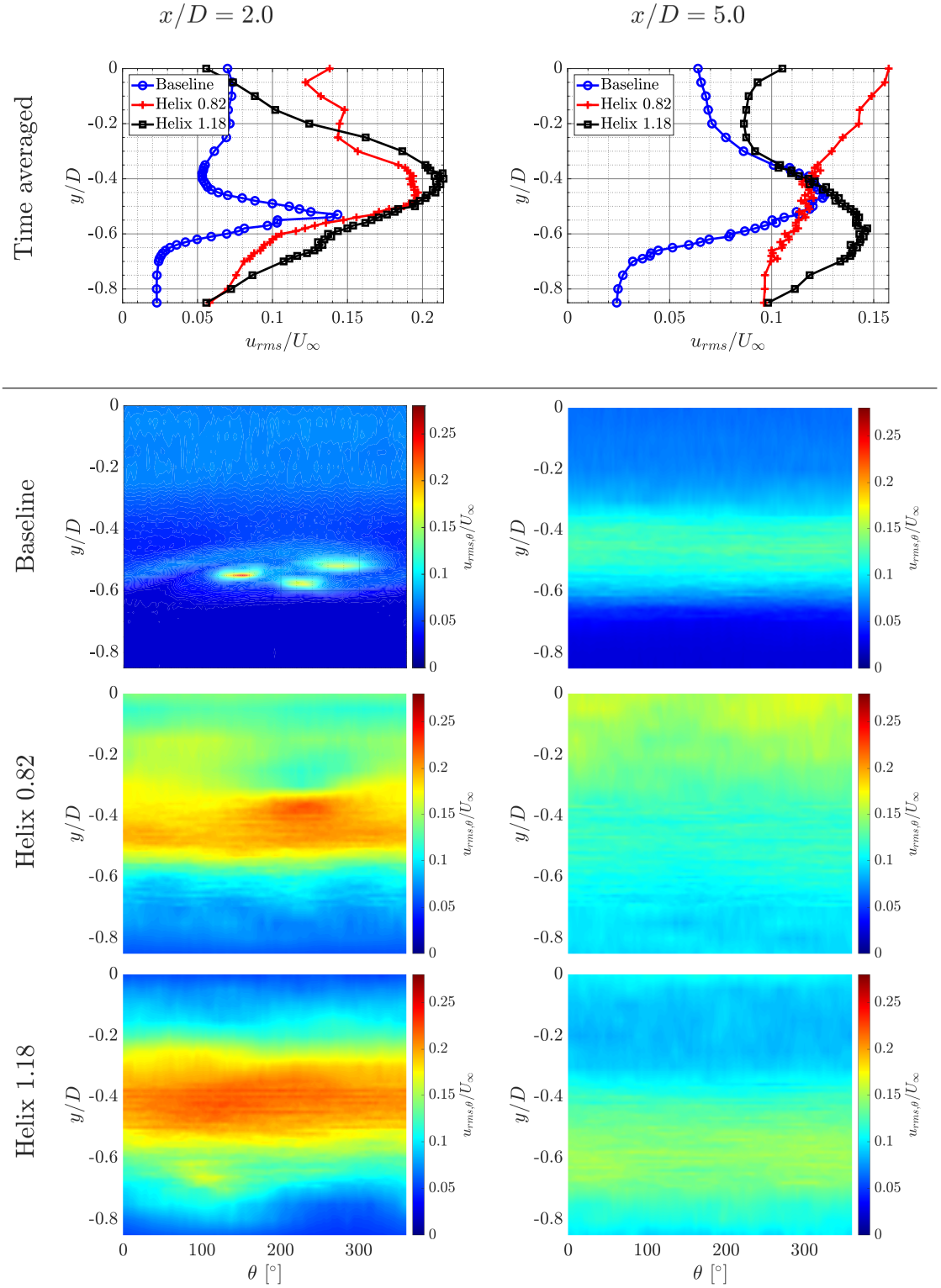

Figure 6.33: Normalized phase-locked RMS-values of the streamwise fluctuations $u_{rms,\theta}/U_\infty$ at multiple downstream positions $x/D = \{0.5,\ 1.0,\ 2.0,\ 5.0\}$ (cont.)

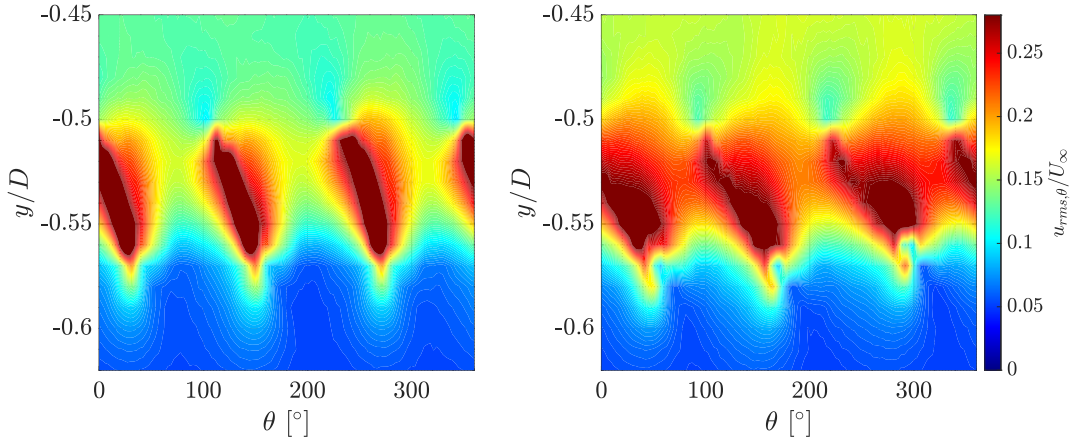

(a) Helix 0.82 **(b)** Helix 1.18

Figure 6.34: Normalized phase-locked RMS-values of the streamwise fluctuations $u_{rms,\theta}/U_\infty$ at a downstream position of $x/D = 0.35$

in Figure 6.34 show the normalized phase-locked RMS-values of the streamwise fluctuations $u_{rms,\theta}/U_\infty$ over one rotation at the closest distance $x/D = 0.35$ for both actuation cases. As already mentioned before, both cases experience high fluctuation levels of around $u_{rms,\theta}/U_\infty \approx 0.25$ between lateral locations $y/D = (-0.5, -0.57)$. However, the Helix 1.18 contours are more smeary, and hence, a more constant input of fluctuation is seen over one rotor revolution. It must not be forgotten that, as already mentioned, this representation does not show the realistic vortex shedding since the actuation is out of sync to the rotational frequency, which is the basis for the phase-locking procedure. The phenomena shown here describe multiple flow situation that occur throughout the actuation time.

For this reason, two additional constant-pitch experiments are conducted. Within the measurements, the additional blade pitch is changed to a constant value matching either the minimum or the maximum of the dynamic blade pitch motion of the actuated cases $\Delta\beta = const. = \pm 4°$. Figure 6.35 shows the vortex shedding (visualized by $u_{rms,\theta}/U_\infty$) over one rotor revolution for the extreme fixed pitch cases. For the $\Delta\beta = -4°$ case, the turbine extracts more power and the blades experience higher loading. Thus, a stronger vortex forms at the blade tips. The stronger the vortex is, the larger the distance it moves to more radially positions. The opposite happens for the $\Delta\beta = +4°$ case, where the high pitch angle leads to an unloaded turbine blade, where more air passes the rotor surface. Weaker tip vortices form and the wake is not widening up as for lower blade pitch angles. The lateral position of the detectable vortices for the fixed-pitch cases match the maximum values measured for the dynamically pitched Helix cases in Figure 6.34.

As the last step of the wind turbine wake investigations, phase-locked contour plots of the entire refined measurement x-y-plane are shown in Figure 6.36. There, the normal-

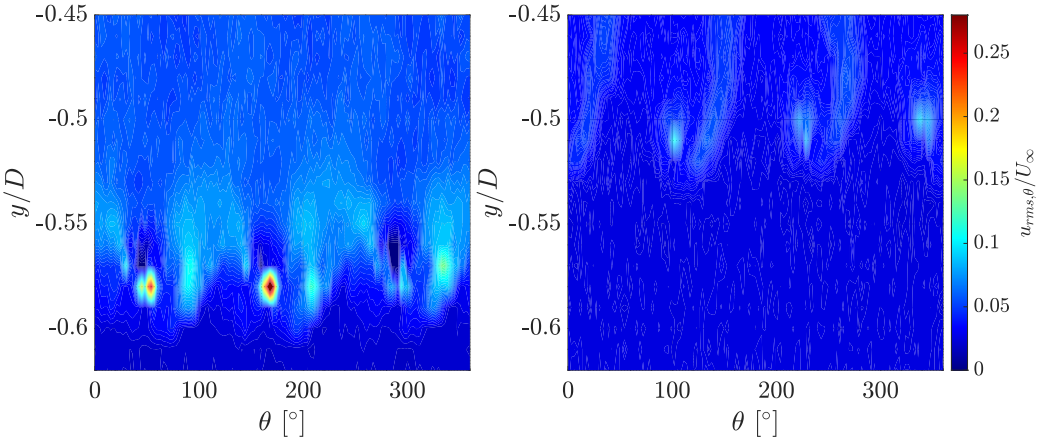

(a) $\Delta\beta = -4°$ **(b)** $\Delta\beta = 4°$

Figure 6.35: Normalized phase-locked RMS-values of the streamwise fluctuations $u_{rms,\theta}/U_\infty$ for fixed pitch $\Delta\beta = -4°$ and $\Delta\beta = 4°$ at a downstream position of $x/D = 0.35$

ized phase-locked vorticity in z-direction (out of plane) ξ_z is shown for multiple phase locked positions corresponding to azimuthal blade positions $\theta = \{0,\ 30,\ 60,\ 90\}°$. The normalized vorticity in z-direction is calculated as follows:

$$\xi_z = \frac{D}{U_\infty}\omega_z = \frac{D}{U_\infty}\left(\frac{\partial v}{\partial x} - \frac{\partial u}{\partial y}\right) \tag{6.4}$$

Once again, both actuated cases are directly compared in the figure. Here, vortex-sheet-shaped structures travel downstream and broaden. Nevertheless, since solely phase-locked results are shown, which were locked with the rotational frequency f_r and not with the actuation frequency $f_\beta = f_r \pm f_e$, the "vortex sheets" visualize an averaged representation of the flow structures travelling downstream. It is noteworthy that for the Helix 0.82 case, the two vortices at the extreme y/D-positions travel downstream almost identically, at the same phase-locked time. A C-shaped structure corresponding to the sinusoidal vortex shedding with different vortex strengths forms. In contrast to that, the Helix 1.18 case shows an additional delay in the shedding of the two extreme positions. A diagonal-shaped structure travels downstream in the phase-locked flow field.

Further analysis can and must be conducted to get the full transient flow behavior in the wake of the dynamically actuated wind turbine. Phase-locking the data with the actuation frequency f_β or the underlying, FFT-identified beat frequency f_e could enhance the interpretability of the measured data. Further details can be found in the publication under review by Mühle et al. [172].

6.2.6 Concluding remarks

To sum up, in this application scenario, the wake of a wind turbine is measured by fast-response pressure probe measurements in the W/T-C of TUM-AER. An isolated wind

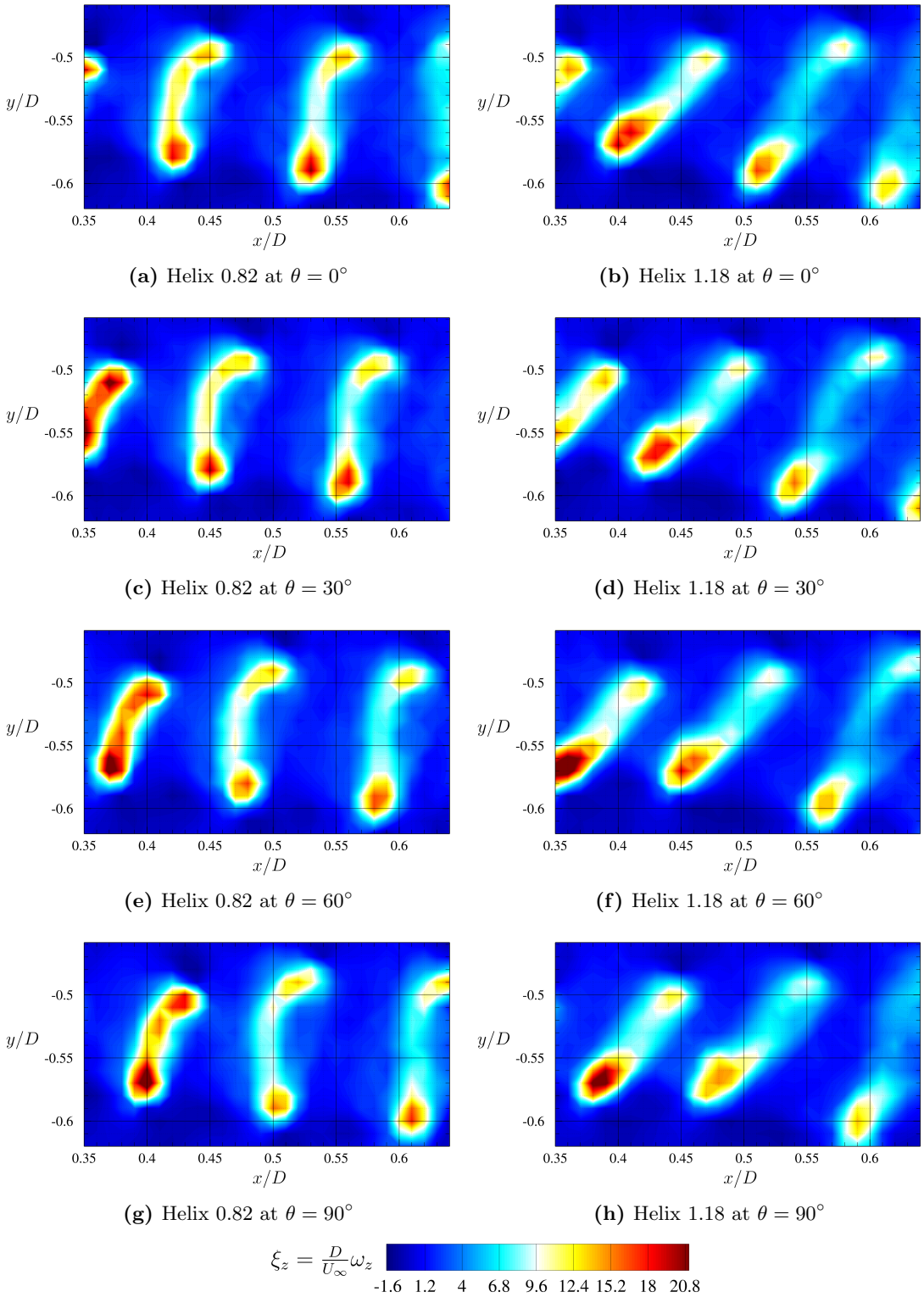

(a) Helix 0.82 at $\theta = 0°$

(b) Helix 1.18 at $\theta = 0°$

(c) Helix 0.82 at $\theta = 30°$

(d) Helix 1.18 at $\theta = 30°$

(e) Helix 0.82 at $\theta = 60°$

(f) Helix 1.18 at $\theta = 60°$

(g) Helix 0.82 at $\theta = 90°$

(h) Helix 1.18 at $\theta = 90°$

Figure 6.36: Normalized phase-locked vorticity in z-direction ξ_z at multiple azimuthal positions $\theta = \{0,\ 30,\ 60,\ 90\}°$

farm scenario with two turbines is investigated in a two stage setup. Besides a baseline case without any actuation, two actuated individual pitch control cases (Helix 0.82 and Helix 1.18) are tested. The *Helix* control strategy induces earlier wake mixing and thus wake recovery. Thereby, another turbine located downstream would experience higher velocities and more uniform inflow conditions and thus, results in higher power output. The FRAP measurements allow for a thorough description of the flow field in the wake. The investigation is also backed by an analysis in the frequency domain, identifying frequency bandwidth content of special interest. In addition to a time-averaged description of the wake, a phase-locked investigation can be conducted. By additionally acquiring a synchronization signal, independent FRAP measurements are synchronized in the post-processing procedure. A quasi transient analysis of the data in the 3D wake is possible. The two actuated cases both show an earlier mixing and entrainment of high energetic fluid already near the rotor plane. A classical instability mechanism (see leapfrogging in the baseline case) is not present in the actuated cases. The actuated *Helix 1.18* case shows even better results than the *Helix 0.82* case. Here, in addition to the fluctuation being inserted into the flow by the pitch controls, the additional frequency of the pitch actuation works against the detaching vortex system, thus reduces the momentum in the flow, and leads to a more uniform flow also in the velocity components perpendicular to the axial velocity. The Helix approach is a promising approach that can contribute to a synergistic interaction of multiple wind turbines, as found in wind farms.

7 Conclusions and outlook

This final chapter pursues two main goals: On the one hand, it should give an overview of the obtained findings, which should serve as an essential input to answer the research question stated in the introduction. On the other hand, it gives an outlook on some potential future enhancements of the probe and the sensor technology employed in it.

As already motivated in the introduction, the central questions of this thesis are whether multi-hole probes can be used for certain unsteady aerodynamics measurement scenarios and to what extent they can compete with other measurement systems. In order to ensure these requirements, especially the spatial and temporal resolution of fast-response aerodynamic probes (FRAP) have to be investigated. The FRAP is carefully assessed in comparison to optical measurement techniques, such as particle-image velocimetry (PIV) and laser-Doppler anemometry (LDA), and the main competitive probe-based technique, hot-wire (HW) anemometry. Accordingly, it is to be investigated a) whether the positive characteristics of these various measurement techniques can be combined in an additively manufactured multi-hole pressure probe and b) whether a highly robust, very performant probe for unsteady measurement tasks in subsonic wind tunnels is available by using novel sensor technology.

The following work description presents the main steps of the performed efforts for the characterization of a multi-hole pressure probe for unsteady aerodynamics analysis. The most important steps in design, manufacturing/assembly, calibration and measurement have been identified and analyzed separately, in order to finally identify the suitability of the probe for specific applications and to compare it with other measurement systems.

The chapter on multi-hole probes and pressure sensor theory, Chapter 2, takes an introductional position. Basic relationships in the functioning of multi-hole probes are given. In addition, FRAPs are categorized with respect to other measurement techniques for their use in subsonic wind tunnels. In addition, the necessity of using and functional principle of small differential pressure sensors is shown. The main emphasis is put on fiber-optic pressure sensors, which could replace conventional piezo-resistive sensors in the future. Beyond that, the prototypes of both fast-response probes and sensors used in this thesis are presented, and the advances that have been achieved are outlined.

Chapter 3 builds the theoretical foundation of the applied calibration and reconstruction methods. An interpolation based method is primarily used for the spatial calibration where the time-averaged pressures measured at the pressure ports are correlated with the time-averaged flow properties. Since the aerodynamic probe calibration can

be characterized as a regression problem, besides a standard polynomial interpolation approach Bayesian statistics, in form of the Gaussian process regression, can be used to exploit the similarities of the calibration data of geometrically similar probes. Moreover, two approaches for the determination of the temporal calibration dataset are presented and discussed. The standard frequency test rig approach results in a stepwise transfer function in the frequency domain. In addition, the characterization of the acoustic line-cavity-system can also be carried out in a shock tube, in which the pressure rise due to the shock is used in a system identification step.

The quantification and characterization of the fiber-optic sensors and the probe behavior takes place in Chapter 4. The fiber-optic sensors are tested on their sensitivity towards pressure and temperature change. Thereby, current limitations but also great potential for further improvements are discussed. Furthermore, the sensors are applied in two temporal calibration cases where the transfer function of tubings of various geometric sizes are acquired. The benefits and the application of the two temporal calibration setup options are explained in more detail and a comparison is made to standard piezo-resistive sensors. Furthermore, a generic probe is investigated with CFD simulations, which has a similar geometry to the additively manufactured probe used in the experimental wind tunnel tests. The main focus of the numerical investigations of the flow around the probe and the determination of the transfer function of a line-cavity system lies on the assessment of the applicability of numeric simulations and their similarity to experimental and analytical solutions (potential theory and transfer function solution of Bergh and Tijdeman [113]).

While the preceding chapters do not cover tests of a fully assembled FRAP, Chapter 5 examines the quantification and discussion of the measurement resolution and uncertainty when conducting measurements with the probe. Essential definitions of metrology and uncertainty quantification are introduced and several important factors regarding the uncertainty in probe measurement are discussed, e.g. in the sensor technology or in the data acquisition. However, the main part of the chapter comprises the measurements in grid-generated turbulence to quantify the spatial and temporal resolution of the FRAP. In addition to results available from the literature at comparable conditions, reference measurements are carried out with different hot-wire probes. Turbulent time and length scales are analysed and the limitations, advantages and disadvantages of the probes are explained.

In the chapter on application fields, Chapter 6, the measurement capabilities of the fast-response aerodynamic probe are demonstrated in two bigger measurement campaigns. While the investigation of the near wake of a circular cylinder in the sub-critical Reynolds number range takes the role of a rather academic validation case, the analysis of the wake of a wind turbine experiencing highly dynamic blade actuation is a very industry-oriented test case. In both cases, the flow field is first considered on a time-averaged basis. In addition, velocity spectra are examined to identify dominant flow phenomena and to better characterize their dependencies on other parameters. Further-

more, in the analysis of the wind turbine wake, a phase-averaged quasi-transient flow field is considered additionally, allowing a more detailed description of the underlying unsteady flow phenomena.

Finally, an evaluation of the research objectives is performed on the basis of the key results and findings in this thesis.

Research Objective 1 With which means is it possible to develop a robust measurement device for transient flow phenomena for subsonic wind tunnels?

The additive manufacturing process and the robust probe design ensures an easy to use setup for wind tunnel applications. Arbitrary shaped probe heads can be manufactured by the use of selective-laser melting. The packaging of the sensors inside the probe was improved throughout the thesis (see Section 2.1.2). The use of optimized spatial calibration and data reduction algorithms allows a high accuracy of reconstruction in both velocity and flow angles, as seen in Chapter 3. The development and characterization of novel fiber-optic sensors in Chapter 4 present a competitive alternative to state-of-the-art piezo-resistive sensors, which are needed to adequately detect the pressures inside the probe. Sensors were characterized with respect to pressure and temperature changes. With the help of the reliable determination of the acoustic behavior in the line-cavity system inside the probe (temporal calibration), the distorted amplitudes and the phase shift can be reconstructed. The comparison of measured data with simulation data and analytical descriptions in Section 4.2 shows, that a precise experimental determination of the spatial and temporal characteristics of the probe is absolutely crucial. Thus, a precise determination of the 3D velocity vector with contents in the higher-frequency band can be realized.

Research Objective 2 What are the limiting specifications and components related to spatial and temporal resolution and how can these limitations be addressed?

This research objective was mainly addressed with the study on grid-generated turbulence in Chapter 5. Measurements showed an overall good agreement to reference data. Minor deviations in regions with small velocity fluctuations, and hence very small pressure fluctuations, were observed in the FRAP data. This behavior was backed with spectral investigations, which showed the limits of the FRAP: the minimal resolution of the FRAP sensors/DAQ system and the bandwidth limit of the experimentally acquired temporal calibration limited the data quality at higher bandwidth. To quantify the comparability of probe-based measurement solutions with respect to spatial filtering, an equivalent length scale was introduced for the FRAP to allow comparison with the wire length of hot-wire probes. For the FRAP, an equivalent wire length of $l_{w,equi.} = 2.0\ mm$ was calculated and lies below the outer dimension of the probe tip $d_{tip} = 3\ mm$. In order to address the limitations, an even smaller probe could be designed and manufactured to reduce spatial filtering. Moreover, temporal filtering could be overcome with improved sensor technology, as described in the outlook at the end of this chapter.

Research Objective 3 How can elaborate software solutions in data reduction or analysis facilitate the use of the probe or expand the range of possible applications?

In the course of the thesis, several algorithms for data processing have been newly developed, used or adapted on the basis of already existing algorithms. The continued improvements on the calibration/reconstruction algorithm resulted in an increased accuracy of the reconstruction, see Section 4.2.2.1. Moreover, Sections 3.1.2 and 4.2.2.2 discussed the application of Gaussian Process regression for the spatial calibration of probes. For future probes with similar geometric properties, the number of actually measured calibration points needed to generate a calibration surface can be decreased over one order of magnitude by applying the $\mathcal{GP}$ regression. The reconstruction accuracy slightly decreases thereby, but stays in an acceptable range. In the course of wake investigations on a generic aircraft configuration [158] and on a wind turbine in Section 6.2, an efficient phase-averaged analysis for the visualization of a quasi-transient flow field was developed. With the aid of characteristic periodic synchronization signals, the time-independent FRAP measurements could be correlated. The interpretation thus goes beyond a simple evaluation of the individual time signals (e.g. in form of velocity spectra) and expands the range of possible applications and test setups.

Research Objective 4 Will the probe show appropriate performance and be able to replace or outperform other measurement techniques?

The assessment of the fourth research objective is a holistic task and therefore also includes the assessment of the first three research objectives. A competitive probe for unsteady aerodynamics analyses has been developed based on the results of the investigations and the improvements of the probe characteristics. In multiple tests and measurements in Chapters 4, 5 and 6, the FRAP measurement results were validated and compared to different other measurement techniques. In the application scenarios in Chapter 6, the capabilities of the FRAP were demonstrated in detail. Measurements with the FRAP showed a very robust and easy to use handling and a fast and cost-efficient setup. The incorporation of advanced (post-) processing routines, allows time-averaged, phase-locked and transient analyses of the flow field patterns. As intended and questioned in the introduction, the FRAP design integrates the positive features of other measurement techniques with the existing properties of conventional pressure probes. Pressure probes for unsteady aerodynamics analyses extend the range of measurement instrumentation for the use in subsonic wind tunnels. They are arguably the first choice in probe-based systems for many measurement applications. FRAPs can also compete with optical, non-invasive measurement methods, since the acquisition and maintenance costs are considerably lower. In addition, as described above, thanks to the advanced and easy to use post-processing procedures, FRAPs can also be used to detect unsteady flow phenomena.

The numerous investigations and tests in this thesis have shown the potential but also the limitations of the current probe design. For this reason, it is evident that future

developments could be initiated in the long term. The following outlook presents only some vague ideas and should show possibilities to increase the measurement potential.

As seen in the quantification of the spatial and temporal resolution of the current probe assembly, additional miniaturization of the probe dimensions could further reduce spatial and temporal filtering. While additive manufacturing processes could already realize smaller probe heads, the major improvement potential lies within the applied sensor technology. As seen, the limits of the piezo-resistive sensor could be avoided by the application of newly developed fiber-optic pressure sensors in the future. By further improving the fiber-optic sensor characteristics while also decreasing the sensor size, FRAP designs could be improved: either the probe in general could get smaller and have less intrusive effects on the flow, or the sensors could be placed closer to the probe tip and thus reduce the attenuation effects of the line-cavity-system inside the probe. Furthermore, the fiber-optic sensor should be further developed regarding its robustness, stability and sensitivity against mechanical deformation and temperature. Thereby, the risk of damaging the sensor when assembling the probe could be avoided. Moreover, by eliminating the use of adhesives in the sensor assembly, the sensor would be entirely composed out of fused silica and would not differ in the thermal expansion coefficients of the material. Therefore, the sensor would only be limited by the maximum tolerable temperature for fused silica regarding thermal stability.

Besides the possible advances in design and manufacturing, the probe's capabilities could also be enhanced by further advances in the post-processing software for calibration and reconstruction, as well as in the further processing of the probe data in various applications for the interpretation of the flow field. As already shown by the application of Gaussian process regression for the spatial calibration of probes in this thesis, machine learning methods have great potential to reduce the computational effort and to process large datasets in an efficient way. As part of these efforts, it is also worth considering the potential of developing a virtual surrogate model for the probe. Thereby, predictive models for future probe configurations could be derived based on experimental, numerical and analytical data sets and models. Parameter studies for the probe design and the optimal use in different scenarios could be carried out virtually on the computer and thus an optimal configuration could be found for each application prior to the manufacturing. In addition, the smart use of the connected sensor systems of the already highly instrumented measurement models could be of great interest. In the application chapter, the use of specific sensor data from the wind turbine for synchronization tasks for the separately measured probe data showed that a phase-averaged flow field could be reconstructed. Through further sensor fusion methods, more complicated flow phenomena and measurement setups could be realized and a greater explanatory capability of the measurement data could be gained.

Bibliography

[1] R. W. Ainsworth, R. J. Miller, R. W. Moss, and S. J. Thorpe. Unsteady pressure measurement. *Measurement Science and Technology*, 11(7):1055–1076, 2000.

[2] H. Babinsky, U. Kuschel, and H. Hodson. The aerodynamic design and use of multi-sensor pressure probes for MEMS applications. In *XVth Bi-Annual Symposium on Measuring Techniques in Transonic and Supersonic Flows in Cascades and Turbomachines*, Florence, Italy, 2000.

[3] D. Lengani, B. Paradiso, and A. Marn. A method for the determination of turbulence intensity by means of a fast response pressure probe and its application in a LP turbine. *Journal of Thermal Science*, 21(1):21–31, 2012.

[4] C. R. Gossweiler. Sonden und Messsystem für schnelle aerodynamische Strömungsmessung mit piezoresistiven Druckgebern. Dissertation, ETH Zurich, 1993.

[5] H. J. Humm. Optimierung der Sondengestalt für aerodynamische Messungen in hochgradig fluktuierenden Strömungen. Dissertation, ETH Zurich, 1996.

[6] P. Kupferschmied. On the methodology of time-resolved measurements with aerodynamic probes in compressors and turbines. Dissertation, ETH Zurich, 1998.

[7] W. P. Gizzi. Dynamische Korrekturen für schnelle Strömungssonden in hochfrequent fluktuierenden Strömungen. Dissertation, ETH Zurich, 2000.

[8] C. R. Gossweiler, P. Kupferschmied, and G. Gyarmathy. On Fast-Response Probes: Part 1 - Technology, Calibration, and Application to Turbomachinery. *Journal of Turbomachinery*, 117(4):611, 1995.

[9] H. J. Humm, C. R. Gossweiler, and G. Gyarmathy. On Fast-Response Probes: Part 2 - Aerodynamic Probe Design Studies. *Journal of Turbomachinery*, 117(4):618, 1995.

[10] P. Kupferschmied, P. Köppel, C. Roduner, and G. Gyarmathy. On the development and application of the Fast-Response Aerodynamic Probe system in turbomachines - Part 1: The measurement system. *Journal of Turbomachinery*, 122(July 2000):505, 2000.

[11] C. Roduner, P. Kupferschmied, P. Köppel, and G. Gyarmathy. On the development and application of the Fast-Response Aerodynamic Probe system in turbomachines - Part 2: Flow, Surge, and Stall in a Centrifugal Compressor. *Journal of Turbomachinery*, 122(July 2000):517, 2000.

[12] P. Köppel, C. Roduner, P. Kupferschmied, and G. Gyarmathy. On the development and application of the Fast-Response Aerodynamic Probe system in turbomachines - Part 3: Comparison of Averaging Methods Applied to Centrifugal Compressor Measurements. *Journal of Turbomachinery*, 122(July 2000):527, 2000.

[13] O. Rediniotis, E. Johansen, T. Tsao, A. Seifert, and L. Pack. MEMS-based probes for velocity and pressure measurements in unsteady and turbulent flowfields. In *37th Aerospace Sciences Meeting and Exhibit*, Reston, Virigina, Jan 1999. American Institute of Aeronautics and Astronautics.

[14] M. Zeiger and O. Rediniotis. Embedded-sensor air-data systems for uav's. In *1st UAV Conference*, 2002.

[15] O. Rediniotis, R. Allen, M. Zeiger, and E. Johansen. Embedded-Sensor, Fast-Response Multi-Hole Probes. In *41st Aerospace Sciences Meeting and Exhibit*, Reno, Nevada, Jan 2003. American Institute of Aeronautics and Astronautics.

[16] E. S. Johansen. Development of a fast-response multi-hole probe for unsteady and turbulent flowfields. Dissertation, Texas A&M University, 2001.

[17] E. S. Johansen and O. K. Rediniotis. Unsteady calibration of fast-response pressure probes, part 1: Theoretical studies. *AIAA Journal*, 43:816–826, 2005.

[18] E. S. Johansen and O. K. Rediniotis. Unsteady calibration of fast-response pressure probes, part 2: Water-tunnel experiments. *AIAA Journal*, 43:827–834, 2005.

[19] E. S. Johansen and O. K. Rediniotis. Unsteady calibration of fast-response pressure probes, part 3: Air-jet experiments. *AIAA Journal*, 43:835–845, 2005.

[20] G. Persico, P. Gaetani, and A. Guardone. Design and analysis of new concept fast-response pressure probes. *Measurement Science and Technology*, 16(9):1741, 2005.

[21] C. H. Sieverding, T. Arts, R. Dénos, and J. F. Brouckaert. Measurement techniques for unsteady flows in turbomachines. *Experiments in Fluids*, 28(4):285–321, 2000.

[22] J. F. Brouckaert. Fast response aerodynamic probes for measurements in turbomachines. *Proceedings of the Institution of Mechanical Engineers, Part A: Journal of Power and Energy*, 221(6):811–813, 2007.

[23] A. Fioravanti, G. Lenzi, G. Ferrara, and L. Ferrari. Development of a Fast-Response Aerodynamic Pressure Probe Based on a Waveguide Approach. *Journal of Engineering for Gas Turbines and Power*, 139(3):031902, 2016.

[24] Z. Liu and G. Paniagua. Design of Directional Probes for High-Frequency Turbine Measurements. *Journal of Engineering for Gas Turbines and Power*, 140(1):011601, 2017.

[25] S. D. Grimshaw and J. V. Taylor. Fast Settling Millimetre-Scale Five-Hole Probes. In *ASME Turbo Expo 2016*, 2017.

[26] A. Hövelmann. Analysis and control of partly-developed leading-edge vortices. Dissertation, Technical University of Munich, 2016.

[27] C. Tropea, A. Yarin, and J. Foss. *Springer Handbook of Experimental Fluid Mechanics*. Springer Handbooks. Springer, 2007.

[28] C. Breitsamter. Nachlaufwirbelsysteme großer Transportflugzeuge. Habilitation, Technical University of Munich, 2007.

[29] D. Telionis, Y. Yang, and O. Rediniotis. Recent developments in multi-hole probe (mhp) technology. *Proceedings of COBEM*, 2009.

[30] R. G. Dominy and H. P. Hodson. An Investigation of Factors Influencing the Calibration of Five-Hole Probes for Three-Dimensional Flow Measurements. *Journal of Turbomachinery*, 115(3):513, 1993.

[31] J. Crawford and A. Michael Birk. Influence of Tip Shape on Reynolds Number Sensitivity for a Seven Hole Pressure Probe. *Journal of Engineering for Gas Turbines and Power*, 135(9), 2013.

[32] I. Gibson, D. Rosen, and B. Stucker. *Additive Manufacturing Technologies*. Springer New York, New York, NY, 2015.

[33] F. M. Heckmeier, D. Iglesias, S. Kreft, S. Kienitz, and C. Breitsamter. Development of unsteady multi-hole pressure probes based on fiber-optic pressure sensors. *Engineering Research Express*, 1(2), 2019.

[34] Vectoflow GmbH. Products & services, 2019. https://www.vectoflow.de/en/products/, accessed on 2019-01-07.

[35] M. Börner and R. Niehuis. Development of the Additive Manufactured Miniaturized Wedge Probe Optimized for 2D Transonic Wake Flow Measurements. In *XXIV Biannual Symposium on Measuring Techniques in Turbomachinery*, Prague, Czech Republic, 2018.

[36] E. Bach, M. Bohon, C. O. Paschereit, and P. Stathopoulos. Development of an instrumented guide vane set for rdc exhaust flow characterization. In *2018 Joint Propulsion Conference*, 2018.

[37] T. Decker. Entwicklung und Konstruktion einer Sonde für instationäre aerodynamische Messungen. Diploma thesis, Technical University of Munich, 2015.

[38] P. Regtien and E. Dertien. *Sensors for Mechatronics: Second Edition*. Elsevier, 2018.

[39] K. Meusel. Entwicklung, Aufbau und Optimierung eines differentiellen, faseroptischen Drucksensors basierend auf dem Fabry-Pérot-Interferometer und dessen Einsatz in einer instationären Mehrlochsonde. Master's thesis, Chair of Aerodynamics and Fluid Mechanics, Technical University of Munich, April 2019. Supervisor: F.M. Heckmeier, C. Breitsamter.

[40] M. J. Schmid, M. S. Müller, B. A. Kuhnle, M. W. Bauer, R. Pongratz, and A. Altmikus. Fiber optic acoustic pressure sensor with high dynamic range and low noise. In *Proceedings of the ETC 2016 - 36th European Telemetry and Test Conference*, Nürnberg, 2016.

[41] M. J. Schmid, B. A. Kuhnle, S. U. Kienitz, C. F. Napierala, C. Scheit, A. Altmikus, M. S. Müller, and A. W. Koch. A fiber-optic sensor for measuring quasi-static and unsteady pressure on wind energy converters. In *4SMARTS-Symposium*, Braunschweig, 2017.

[42] S. U. Kienitz, L. Lohr, M. J. Schmid, and A. W. Koch. Static and dynamic pressure measurement in flight test application with optical fabry–pérot sensors. *IEEE Transactions on Instrumentation and Measurement*, 70:1–11, 2021.

[43] F. Mitschke. *Fiber optics: Physics and technology: Second Edition.* Springer Berlin Heidelberg, 8 2016.

[44] H. Hashemian, C. L. Black, and J. P. Farmer. Assessment of fiber optic pressure sensors. In *U.S. Nuclear Regulatory Commission, NUREG/CR-6312*, 1995.

[45] M. Gander, W. MacPherson, J. Barton, R. Reuben, J. Jones, R. Stevens, K. Chana, S. Anderson, and T. Jones. Embedded micromachined fiber-optic fabry-perot pressure sensors in aerodynamics applications. *IEEE Sensors Journal*, 3(1):102–107, 2003.

[46] G. Hill, R. Melamud, F. Declercq, A. Davenport, I. Chan, P. Hartwell, and B. Pruitt. Su-8 mems fabry-perot pressure sensor. *Sensors and Actuators A: Physical*, 138(1):52–62, 2007.

[47] H. S. Yalcin, A. Arikoglu, and I. Ozkol. Free vibration analysis of circular plates by differential transformation method. *Applied Mathematics and Computation*, 212(2):377–386, 2009.

[48] S. Yin, P. B. Ruffin, and F. T. Yu. *Fiber Optic Sensors (2nd edition).* CRC Press Boca Raton FL, New York, NY, 2019.

[49] W.-C. Zhang, Q.-C. Chen, L.-Y. Zhang, and H. Zhao. Fiber optic fabry-perot sensor with stabilization technology for acoustic emission detection of partial discharge. In *2018 IEEE International Conference on High Voltage Engineering and Application (ICHVE)*, pages 1–4, 2018.

[50] Q. Yu and X. Zhou. Pressure sensor based on the fiber-optic extrinsic fabry-perot interferometer. *Photonic Sensors*, 1(1):72–83, 2011.

[51] J. Yin, T. Liu, J. Jiang, K. Liu, S. Wang, Z. Qin, and S. Zou. Batch-producible fiber-optic fabry-pérot sensor for simultaneous pressure and temperature sensing. *IEEE Photonics Technology Letters*, 26(20):2070–2073, 2014.

[52] A. Wang, H. Xiao, J. Wang, Z. Wang, W. Zhao, and R. G. May. Self-calibrated interferometric-intensity-based optical fiber sensors. *Journal of Lightwave Technology*, 19(10):1495, 2001.

[53] LightFab GmbH. Products & technology, 2019. https://www.lightfab.de/, accessed on 2019-06-04.

[54] J. Gottmann, M. Hermans, N. Repiev, and J. Ortmann. Selective Laser-Induced Etching of 3D Precision Quartz Glass Components for Microfluidic Applications - Up-Scaling of Complexity and Speed. *Micromachines*, 8(110), 2017.

[55] S. Kienitz, S. Kreft, M. Schmid, M. Staats, and A. Koch. Miniature Airworthy Fiber-Optic Pressure Sensors for Measuring Static Pressure and Acoustics. In *Aerospace Europe Conference 2020, Bordeaux, 25.-28.2.2020*, 2020.

[56] D. Bohn and H. Simon. Mehrparametrige Approximation der Eichräume und Eichflächen von Unterschall- bzw. Überschall-5-Loch-Sonden. *tm - Technisches Messen*, 468-479(JG):81–89, Jan 1975.

[57] C. Ostowari and W. H. Wentz. Modified calibration technique of a five-hole probe for high flow angles. *Experiments in Fluids*, 1(3):166, 1983.

[58] K. N. Everett, A. A. Gerner, and D. A. Durston. Seven-hole cone probes for high angle flow measurement: Theory and calibration. *AIAA Journal*, 21(7):992–998, 1983.

[59] C. S. Lee and N. J. Wood. Calibration and data reduction for a five-hole probe. NASA STI/Recon Technical Report N, 1986.

[60] M. C. Gameiro Silva, C. A. Pereira, and J. M. Cruz. On the use of a linear interpolation method in the measurement procedure of a seven-hole pressure probe. *Experimental Thermal and Fluid Science*, 28(1):1–8, 2003.

[61] R. Benay. A global method of data reduction applied to seven-hole probes. *Experiments in Fluids*, 54(6), 2013.

[62] E. Houtman and W. Bannink. The calibration and measuring procedure of a five-hole hemispherical head probe in compressible flow, 1989.

[63] S. O. Kjelgaard. Theoretical derivation and calibration technique of a hemispherical-tipped, five-hole probe. NASA Technical Memorandum 4047, NASA, 1988.

[64] A. J. Pisasale and N. A. Ahmed. Examining the Effect of Flow Reversal on Seven-Hole Probe Measurements. *AIAA Journal*, 41(12):2460–2467, 2003.

[65] A. J. Pisasale and N. A. Ahmed. Development of a functional relationship between port pressures and flow properties for the calibration and application of multihole probes to highly three-dimensional flows. *Experiments in Fluids*, 36(3):422–436, 2004.

[66] G. Zilliac and M. Field. Calibration of Seven-Hole Pressure Probes for Use in Fluid Flows with Large Angularity. NASA Technical Memorandum 102200, NASA, 1989.

[67] G. G. Zilliac. Modelling, calibration, and error analysis of seven-hole pressure probes. *Experiments in Fluids*, 14:104–120, 12 1993.

[68] H. Akima. A Method of Bivariate Interpolation and Smooth Surface Fitting for Irregularly Distributed Data Points. *ACM Transactions on Mathematical Software (TOMS)*, 4(2):148–159, 1978.

[69] C. Venkateswara Babu, M. Govardhan, and N. Sitaram. A method of calibration of a seven-hole pressure probe for measuring highly three-dimensional flows. *Measurement Science and Technology*, 9(3):468–476, 1998.

[70] K. M. Argüelles Díaz, J. M. Fernández Oro, and E. Blanco Marigorta. Direct calibration framework of triple-hole pressure probes for incompressible flow. *Measurement Science and Technology*, 19:75401, 2008.

[71] A. Paul, R. Upadhyay, and a. Jain. A novel calibration algorithm for five-hole pressure probe. *International Journal of Engineering, Science and Technology*, 3(2):89–95, 2011.

[72] A. L. Treaster and A. M. Yocum. Calibration and Application of Five-Hole Probes. *ISA Transactions*, 18(3):23–34, 1979.

[73] L. A. Smith and J. B. Adcock. Effect of Reynolds number and mach number on flow angularity probe sensitivity. NASA Technical Memorandum 87750, NASA, 1986.

[74] E. Clark, J. Henfling, and D. Aeschliman. Calibration of hemispherical-head flow angularity probes. In *17th Aerospace Ground Testing Conference*, 1992.

[75] A. L. Ericksen, R. W. Gallington, and B. M. Rao. Rapid Calibration of Seven-Hole Probes. NASA Technical Memorandum 107040, NASA, 1995.

[76] C. W. Wenger and W. J. Devenport. Seven-hole pressure probe calibration method utilizing look-up error tables. *AIAA Journal*, 37(6):675–679, 1999.

[77] T. Yasa and G. Paniagua. Robust Post-Processing Procedure for Multi-Hole Pressure Probes. In *Proceedings of ASME Turbo Expo 2011: Volume 3*, pages 457–463, 2011.

[78] T. Yasa and G. Paniagua. Robust procedure for multi-hole probe data processing. *Flow Measurement and Instrumentation*, 26:46–54, 2012.

[79] S. Shaw-Ward, S. C. McParlin, P. Nathan, and D. M. Birch. Optimal Calibration of Directional Velocity Probes. *AIAA Journal*, 56(7):2594–2603, 2018.

[80] E. S. Johansen, O. Rediniotis, and G. Jones. The Compressible Calibration of Miniature Multi-Hole Probes. *Transactions of the ASME*, 123(March 2001):128–138, 2001.

[81] C. M. Bishop. *Pattern Recognition and Machine Learning*. Springer-Verlag, Berlin, Heidelberg, 2006.

[82] A. R. C. Franken and P. C. Ivey. Accelerating the Calibration of Multi-Hole Pressure Probes by Applying Advanced Computational Methods. In *Proceedings of ASME Turbo Expo 2004: Volume 2*, 2004.

[83] R. Vijayagopal, M. Pathak, and O. Rediniotis. Miniature multi-hole pressure probes - Their neural network calibration and frequency response enhancement. *36th AIAA Aerospace Sciences Meeting and Exhibit*, 1998.

[84] O. K. Rediniotis and G. Chrysanthakopoulos. Application of neural networks and fuzzy logic to the calibration of the seven-hole probe. *Journal of Fluids Engineering, Transactions of the ASME*, 120(1):95–101, 1998.

[85] O. K. Rediniotis and R. Vijayagopal. Miniature multihole pressure probes and their neural-network-based calibration. *AIAA Journal*, 37(6):666–674, 1999.

[86] H.-Y. Fan, W.-Z. Lu, G. Xi, and S.-J. Wang. An Improved Neural-Network-Based Calibration Method for Aerodynamic Pressure Probes. *Journal of Fluids Engineering*, 125(1):113–120, 2003.

[87] H. Nikpey Somehsaraei, M. Hölle, H. Hönen, and M. Assadi. A novel approach based on artificial neural network for calibration of multi-hole pressure probes. *Flow Measurement and Instrumentation*, 73(February), 2020.

[88] H. H. Lee, I. I. Shinder, J. D. Wright, and M. R. Moldover. Application of ANFIS method to the non-nulling calibration of multi-hole pitot tube. *Procedia Engineering*, 79(1st ICM):125–132, 2014.

[89] H. H. Lee. A Novel Calibration Method for Multi-Hole Pitot Tubes. *Applied Mechanics and Materials*, 764-765:1329–1333, 2015.

[90] M. H. Beale, M. T. Hagan, and H. B. Demuth. Deep Learning Toolbox - User's Guide, R2019a. Technical report, MathWorks, Inc., 2019.

[91] M. T. Hagan and M. B. Menhaj. Training feedforward networks with the marquardt algorithm. *IEEE transactions on neural networks / a publication of the IEEE Neural Networks Council*, 5:989–93, 02 1994.

[92] F. M. Heckmeier and C. Breitsamter. Aerodynamic probe calibration using Gaussian process regression. *Measurement Science and Technology*, 31, 2020.

[93] A. Gelman, J. B. Carlin, H. S. Stern, and D. B. Rubin. *Bayesian Data Analysis*. Chapman and Hall/CRC, 3rd edition, 2014.

[94] C. E. Rasmussen and C. K. I. Williams. *Gaussian Processes for Machine Learning*. The MIT Press, 2006.

[95] J. Chilés and P. Delfiner. *Geostatistics: Modeling Spatial Uncertainty*. Wiley Series in Probability and Statistics. John Wiley & Sons, Ltd, 2012.

[96] A. Krause, A. Singh, and C. Guestrin. Near-optimal sensor placements in gaussian processes: Theory, efficient algorithms and empirical studies. *Journal of Machine Learning Research*, 9, Feb. 2008.

[97] R. K. Pandit, D. Infield, and J. Carroll. Incorporating air density into a gaussian process wind turbine power curve model for improving fitting accuracy. *Wind Energy*, 22(2):302–315, 2019.

[98] T. Chen. Calibration of spectroscopic sensors with gaussian process and variable selection. *IFAC Proceedings Volumes*, 40(5):137–142, 06 2007.

[99] R. A. García-Ruiz, J. L. Blanco-Claraco, J. López-Martínez, and J. Callejón-Ferre. Uncertainty-aware calibration of a hot-wire anemometer with gaussian process regression. *IEEE Sensors Journal*, 19(17):7515–7524, 2019.

[100] R. Agrawal, R. D. Whalley, H. C.-H. Ng, D. J. C. Dennis, and R. J. Poole. Minimizing recalibration using a non-linear regression technique for thermal anemometry. *Experiments in Fluids*, 60(116), 2019.

[101] C. E. Rasmussen. *Gaussian Processes in Machine Learning*, pages 63–71. Springer Berlin Heidelberg, Berlin, Heidelberg, 2004.

[102] J. Nocedal and S. J. Wright. *Numerical Optimization*. Springer, New York, NY, USA, 2nd edition, 2006.

[103] J. Quinonero Candela and C. Rasmussen. A unifying view of sparse approximate gaussian process regression. *Journal of Machine Learning Research*, 6:1935–1959, 2005.

[104] E. Snelson and Z. Ghahramani. Sparse gaussian processes using pseudo-inputs. In Y. Weiss, B. Schölkopf, and J. C. Platt, editors, *Advances in Neural Information Processing Systems 18*, pages 1257–1264. MIT Press, 2006.

[105] C. E. Rasmussen and H. Nickisch. The GPML Toolbox version 4.2. Technical report, August 22, 2018.

[106] C. E. Rasmussen and H. Nickisch. Gaussian processes for machine learning (gpml) toolbox. *Journal of machine learning research*, 11(Nov):3011–3015, 2010.

[107] G. Kirchhoff. Ueber den Einfluss der Wärmeleitung in einem Gase auf sie Schallbewegung. *Annalen der Physik und Chemie*, 134, 1868.

[108] J. W. S. Rayleigh. *The theory of sound*, volume 2 of *Cambridge Library Collection - Physical Sciences*. Cambridge University Press, 1878.

[109] A. S. Iberall. Attenuation of oscillatory pressures in instrument lines. *Journal of Research of the National Bureau of Standards: Research Paper RP2115*, 45, 1950.

[110] D. R. Raichel. *The Science and Applications of Acoustics*. Springer, New York, NY, 2006.

[111] S. A. Whitmore and C. T. Leondest. Pneumatic Distortion Compensation for Aircraft Surface Pressure Sensing Devices. *Journal of Aircraft*, 28(12):828–836, 1991.

[112] O. K. Rediniotis and M. M. Pathak. Simple technique for frequency-response enhancement of miniature pressure probes. *AIAA Journal*, 37(7):897–899, 1999.

[113] H. Bergh and H. Tijdeman. Theoretical and experimental results for the dynamic response of pressure measuring systems. *NLR-TR F.238*, page 21, 1965.

[114] P. L. Blackshear, W. D. Rayle, and L. K. Tower. Study of screeching combustion in a 6-inch simulated afterburner. *National Advisory Committee for Aeronautics*, Technical Note 3567, 1955.

[115] T. W. Nyland, D. R. Englund, and R. C. Anderson. On the dynamics of short pressure probes: Some design factors affecting frequency response. *NASA Technical Note*, TN D-6151, 1971.

[116] R. Semaan and P. Scholz. Pressure correction schemes and the use of the Wiener deconvolution method in pneumatic systems with short tubes. *Experiments in Fluids*, 53(3):829–837, 2012.

[117] H. Tijdeman. On the propagation of sound waves in cylindrical tubes. *Journal of Sound and Vibration*, 39:1–33, 3 1975.

[118] W. B. Richards. Propagation of sound waves in tubes of noncircular cross section. *NASA Technical Paper*, 2601, 1986.

[119] H. Irwin, K. Cooper, and R. Girard. Correction of distortion effects caused by tubing systems in measurements of fluctuating pressures. *Journal of Wind Engineering and Industrial Aerodynamics*, 5:93–107, 1979.

[120] J. D. Holmes and R. E. Lewis. The dynamic response of pressure-measurement systems. In *9th Australian Fluid Mechanics Conference*, pages 537 – 540, 1986.

[121] H. Kobayashi, T. Leger, and J. M. Wolff. Experimental and Theoretical Frequency Response of Pressure Transducers for High Speed Turbomachinery. *International Journal of Turbo and Jet Engines*, 17(2):153–160, 2000.

[122] D. R. Englund and W. B. Richards. The infinite line pressure probe. NASA Technical Memorandum 83582, NASA, 1984.

[123] N. V. de Wyer, J.-F. Brouckaert, and R. L. Miorini. On the determination of the transfer function of infinite line pressure probes for turbomachinery applications. In *Proceedings of ASME Turbo Expo 2012: Volume 1: Aircraft Engine; Ceramics; Coal, Biomass and Alternative Fuels; Controls, Diagnostics and Instrumentation*, page 883. ASME, 6 2012.

[124] S. A. Whitmore and B. Fox. Improved accuracy, second-order response model for pressure sensing systems. *Journal of Aircraft*, 46:491–500, 2009.

[125] B. F. Hall and T. Povey. A practical model for pressure probe system response estimation (with review of existing models). *Measurement Science and Technology*, 29:aaa58f, 2018.

[126] J. Kutin and A. Svete. On the theory of the frequency response of gas and liquid pressure measurement systems with connecting tubes. *Measurement Science and Technology*, 29:125108, 2018.

[127] Z. Wang, M. Giglmaier, T. Hopfes, L. Köglmeier, and N. A. Adams. Impact of sensor housing geometries on transient stagnation pressure measurements in impulse facilities. *Experimental Thermal and Fluid Science*, 109(June):109851, 2019.

[128] F. M. Heckmeier, N. Mooshofer, T. Hopfes, C. Breitsamter, and N. A. Adams. Experimental investigation of a line-cavity system equipped with fiber-optic differential pressure sensors in a shock tube. In A. Dillmann, G. Heller, E. Krämer, and C. Wagner, editors, *New Results in Numerical and Experimental Fluid Mechanics XIII*, pages 709–718, Cham, 2021. Springer International Publishing.

[129] G. Paniagua and R. Dénos. Digital compensation of pressure sensors in the time domain. *Experiments in Fluids*, 32(4):417–424, 2002.

[130] L. Ljung. System Identification Toolbox - User's Guide. Technical report, MathWorks, Inc., 2020.

[131] N. Mooshofer. Charakterisierung eines faser-optischen, differentiellen Drucksensors in einem Stoßrohr. Semester thesis, Chair of Aerodynamics and Fluid Mechanics, Technical University of Munich, March 2020. Supervisor: F.M. Heckmeier, C. Breitsamter.

[132] A. Molz. Numerische Strömungssimulation für verschiedene Sondenkopfformen von Mehrlochsonden. Semester thesis, Chair of Aerodynamics and Fluid Mechanics,

Technical University of Munich, September 2020. Supervisor: F.M. Heckmeier, C. Breitsamter.

[133] F. M. Heckmeier, S. Hayböck, and C. Breitsamter. Spatial and temporal resolution of a fast-response aerodynamic pressure probe in grid-generated turbulence. *Experiments in Fluids*, 62(44), 2021.

[134] R. B. Abernethy, R. P. Benedict, and R. B. Dowdell. Asme measurement uncertainty. *Journal of Fluids Engineering, Transactions of the ASME*, 107:161–164, 6 1985.

[135] Joint Committee for Guides in Metrology. JCGM 100: Evaluation of measurement data – Guide to the expression of uncertainty in measurement. Technical report, JCGM, 2008.

[136] Joint Committee for Guides in Metrology. JCGM 104: Evaluation of measurement data – An introduction to the "Guide to the expression of uncertainty in measurement" and related documents. Technical report, JCGM, 2009.

[137] Joint Committee for Guides in Metrology. JCGM GUM-6: Guide to the expression of uncertainty in measurement – Part 6: Developing and using measurement models. Technical report, JCGM, 2009.

[138] J. Bauer. Evaluation of Uncertainty and Error in Multi-Hole Pressure Probe Measurements. Master's thesis, Chair of Aerodynamics and Fluid Mechanics, Technical University of Munich, March 2020. Supervisor: F.M. Heckmeier, C. Breitsamter.

[139] R. J. Moffat. Contributions to the theory of single-sample uncertainty analysis. *Journal of Fluids Engineering*, 104:250, 1982.

[140] B. A. Reichert and B. J. Wendt. A new algorithm for five-hole probe calibration, data reduction, and uncertainty analysis. NASA Technical Memorandum 106458, NASA, 1994.

[141] D. Sumner. A comparison of data-reduction methods for a seven-hole probe. *Journal of Fluids Engineering*, 124:523–527, 2002.

[142] G. Dell'Era, M. Mersinligil, and J.-F. Brouckaert. Assessment of unsteady pressure measurement uncertainty—part i: Single sensor probe. *Journal of Engineering for Gas Turbines and Power*, 138:041601, 2015.

[143] G. Dell'Era, M. Mersinligil, and J.-F. Brouckaert. Assessment of unsteady pressure measurement uncertainty—part ii: Virtual three-hole probe. *Journal of Engineering for Gas Turbines and Power*, 138:041602, 2015.

[144] M. Hölle, C. Bartsch, and P. Jeschke. Evaluation of measurement uncertainties for pneumatic multihole probes using a monte carlo method. *Journal of Engineering for Gas Turbines and Power*, 139:072605, 2017.

[145] S. Yavuzkurt. A guide to uncertainty analysis of hot-wire data. *Journal of Fluids Engineering, Transactions of the ASME*, 106:181–186, 6 1984.

[146] S. Rezaeiravesh, R. Vinuesa, M. Liefvendahl, and P. Schlatter. Assessment of uncertainties in hot-wire anemometry and oil-film interferometry measurements for wall-bounded turbulent flows. *European Journal of Mechanics, B/Fluids*, 72:57–73, 11 2018.

[147] A. Ashok, S. C. Bailey, M. Hultmark, and A. J. Smits. Hot-wire spatial resolution effects in measurements of grid-generated turbulence. *Experiments in Fluids*, 53(6):1713–1722, 2012.

[148] S. C. Bailey, G. J. Kunkel, M. Hultmark, M. Vallikivi, J. P. Hill, K. A. Meyer, C. Tsay, C. B. Arnold, and A. J. Smits. Turbulence measurements using a nanoscale thermal anemometry probe. *Journal of Fluid Mechanics*, 663:160–179, 2010.

[149] O. Reynolds. IV. On the dynamical theory of incompressible viscous fluids and the determination of the criterion. *Philosophical Transactions of the Royal Society of London*, 186:123–164, 1895.

[150] G. I. Taylor. Statistical theory of turbulence. *Proceedings of the Royal Society A: Mathematical, Physical and Engineering Sciences*, 151(873):421–444, 1935.

[151] D. Ting. *Basics of Engineering Turbulence*. Academic Press, 2016.

[152] S. B. Pope. *Turbulent flows*. Cambridge University Press, Cambridge, 2011.

[153] A. N. Kolmogorov, V. Levin, J. C. R. Hunt, O. M. Phillips, and D. Williams. The local structure of turbulence in incompressible viscous fluid for very large reynolds numbers. *Proceedings of the Royal Society of London. Series A: Mathematical and Physical Sciences*, 434(1890):9–13, 1991.

[154] MathWorks, Inc. MATLAB Signal Processing Toolbox - User's Guide, R2020b. Technical report, MathWorks, Inc., 2020.

[155] P. Bearman. *Corrections for the Effect of Ambient Temperature Drift on Hot-wire Measurements in Incompressible Flow*. National Physical Laboratory (Aero report). NPL, 1969.

[156] P. M. Ligrani and P. Bradshaw. Spatial resolution and measurement of turbulence in the viscous sublayer using subminiature hot-wire probes. *Experiments in Fluids*, 5(6):407–417, 1987.

[157] L. Mydlarski and Z. Warhaft. Passive scalar statistics in high-Péclet-number grid turbulence. *Journal of Fluid Mechanics*, 358:135–175, 1998.

[158] J. Ruhland, F. M. Heckmeier, and C. Breitsamter. Wake vortex analysis on transport aircraft wing featuring oscillating flaps by means of experimental and numerical approach. *Aerospace Science and Technology*, XXX:XXX, 2021.

[159] D. Sedlacek, F. M. Heckmeier, A. Usbek, and C. Breitsamter. Analysis of vortex burst phenomena on generic hybrid delta wing planforms at subsonic speeds. In A. Dillmann, G. Heller, E. Krämer, and C. Wagner, editors, *New Results in Numerical and Experimental Fluid Mechanics XIII*, pages 282–291, Cham, 2021. Springer International Publishing.

[160] M. Zdravkovich and P. Bearman. *Flow Around Circular Cylinders Volume 1: Fundamentals*. Oxford University Press, Oxford, 1997.

[161] L. Ong and J. Wallace. The velocity field of the turbulent very near wake of a circular cylinder. *Experiments in Fluids*, 20:441–453, 1996.

[162] C. Norberg. Ldv-measurements in the near wake of a circular cylinder. *Advances in understanding of bluff body wakes and vortex-induced vibration*, pages 1–12, 1998.

[163] P. Parnaudeau, J. Carlier, D. Heitz, and E. Lamballais. Experimental and numerical studies of the flow over a circular cylinder at reynolds number 3900. *Physics of Fluids*, 20:085101, 8 2008.

[164] A. A. Hetz, M. N. Dhaubhadel, and D. P. Telionis. Vortex shedding over five in-line cylinders cylinders. *Journal of Fluids and Structures*, 5:243–257, 1991.

[165] F. M. Heckmeier, D. Iglesias, and C. Breitsamter. Unsteady multi-hole probe measurements of the near wake of a circular cylinder at sub-critical reynolds numbers. In A. Dillmann, G. Heller, E. Krämer, C. Wagner, C. Tropea, and S. Jakirlić, editors, *New Results in Numerical and Experimental Fluid Mechanics XII*, pages 643–652, Cham, 2020. Springer International Publishing.

[166] L. Lourenco and C. Shih. Characteristics of the plane turbulent near wake of a circular cylinder, a particle image velocimetry study. published in ref. [168], 1994.

[167] Y. Zhou and R. A. Antonia. A study of turbulent vortices in the near wake of a cylinder. *Journal of Fluid Mechanics*, 253:643, 8 1993.

[168] P. Beaudan and P. Moin. Numerical experiments on the flow past a circular cylinder at sub-critical reynolds number. Technical report, Stanford University, 1994.

[169] C. Norberg. An experimental investigation of the flow around a circular cylinder: influence of aspect ratio. *Journal of Fluid Mechanics*, 258:287, 1994.

[170] A. Prasad and C. H. Williamson. Three-dimensional effects in turbulent bluff-body wakes. *Journal of Fluid Mechanics*, 343:235–265, 1997.

[171] J. A. Frederik, B. M. Doekemeijer, S. P. Mulders, and J.-W. van Wingerden. The helix approach: Using dynamic individual pitch control to enhance wake mixing in wind farms. *Wind Energy*, 23(8):1739–1751, 2020.

[172] F. Mühle, F. M. Heckmeier, F. Campagnolo, C. Breitsamter, and C. Bottasso. Wind tunnel investigations of an individual pitch control strategy for wind farm power optimization. *XXX*, XXX(XXX):XXX, 2021.

[173] L. Lignarolo, D. Ragni, F. Scarano, C. Simão Ferreira, and G. van Bussel. Tip-vortex instability and turbulent mixing in wind-turbine wakes. *Journal of Fluid Mechanics*, 781:467–493, 2015.

[174] S. Sarmast, R. Dadfar, R. F. Mikkelsen, P. Schlatter, S. Ivanell, J. Sørensen, and D. Henningson. Mutual inductance instability of the tip vortices behind a wind turbine. *Journal of Fluid Mechanics*, 755:705–731, 2014.

[175] J. N. Sørensen. Instability of helical tip vortices in rotor wakes. *Journal of Fluid Mechanics*, 682:1–4, 2011.

[176] W. Munters and J. Meyers. An optimal control framework for dynamic induction control of wind farms and their interaction with the atmospheric boundary layer. *Philosophical Transactions of the Royal Society A: Mathematical, Physical and Engineering Sciences*, 375(2091):20160100, 2017.

[177] J. A. Frederik, R. Weber, S. Cacciola, F. Campagnolo, A. Croce, C. Bottasso, and J.-W. van Wingerden. Periodic dynamic induction control of wind farms: proving the potential in simulations and wind tunnel experiments. *Wind Energy Science*, 5(1):245–257, 2020.

[178] F. Campagnolo, V. Petrović, J. Schreiber, E. M. Nanos, A. Croce, and C. L. Bottasso. Wind tunnel testing of a closed-loop wake deflection controller for wind farm power maximization. *Journal of Physics: Conference Series*, 753:032006, 2016.

[179] F. Campagnolo, V. Petrović, C. L. Bottasso, and A. Croce. Wind tunnel testing of wake control strategies. In *2016 American Control Conference (ACC)*, 2016.

[180] F. Mühle, J. Bartl, T. Hansen, M. S. Adaramola, and L. Sætran. An experimental study on the effects of winglets on the tip vortex interaction in the near wake of a model wind turbine. *Wind Energy*, 23(5):1286–1300, 2020.

A List of Publications

Peer-Reviewed Publications

- M. Winter, **F. M. Heckmeier**, and C. Breitsamter. CFD-Based Aeroelastic Reduced-Order Modeling Robust to Structural Parameter Variations, *Aerospace Science and Technology*, Vol. 67, pp. 13–30, 2017. DOI: 10.1016/j.ast.2017.03.030
- **F. M. Heckmeier**, D. Iglesias, S. Kienitz, and C. Breitsamter. An Innovative Development of a Five-Hole Pressure Probe for Highly Unsteady Flow Phenomena, *Proceedings of the ASME Turbo Expo 2019: Turbomachinery Technical Conference and Exposition. Volume 6: Ceramics; Controls, Diagnostics, and Instrumentation; Education; Manufacturing Materials and Metallurgy*, Phoenix, Arizona, USA, June 17–21, 2019. DOI: 10.1115/GT2019-90079
- **F. M. Heckmeier**, D. Iglesias, S. Kreft, S. Kienitz, and C. Breitsamter. Development of unsteady multi-hole pressure probes based on fiber-optic pressure sensors, *Engineering Research Express*, Vol. 1, pp. 025023, 2019. DOI: 10.1088/2631-8695/ab4f0d
- **F. M. Heckmeier**, D. Iglesias, and C. Breitsamter. Unsteady Multi-hole Probe Measurements of the Near Wake of a Circular Cylinder at Sub-critical Reynolds Numbers, *Notes on Numerical Fluid Mechanics and Multidisciplinary Design*, *New Results in Numerical and Experimental Fluid Mechanics XII*, pp. 643–652, 2020. DOI: 10.1007/978-3-030-25253-3_61
- **F. M. Heckmeier**, and C. Breitsamter. Aerodynamic probe calibration using Gaussian process regression, *Measurement Science and Technology*, Vol. 31, pp. 125301, 2020. DOI: 10.1088/1361-6501/aba37d
- **F. M. Heckmeier**, S. Hayböck, and C. Breitsamter. Spatial and temporal resolution of a fast-response aerodynamic pressure probe in grid-generated turbulence, *Experiments in Fluids*, Vol. 62, 44, 2021. DOI: 10.1007/s00348-021-03141-7
- **F. M. Heckmeier**, N. Mooshofer, T. Hopfes, C. Breitsamter, and N. A. Adams. Experimental investigation of a line-cavity system equipped with fiber-optic differential pressure sensors in a shock tube, *Notes on Numerical Fluid Mechanics and Multidisciplinary Design*, *New Results in Numerical and Experimental Fluid Mechanics XIII*, pp. 709–718, 2021. DOI: 10.1007/978-3-030-79561-0_67
- D. Sedlacek, **F. M. Heckmeier**, A. Usbek, and C. Breitsamter. Analysis of Vortex Burst Phenomena on Generic Hybrid Delta Wing Planforms at Subsonic Speeds, *Notes on Numerical Fluid Mechanics and Multidisciplinary Design*, *New Results*

in Numerical and Experimental Fluid Mechanics XIII, pp. 282–291, 2021. DOI: 10.1007/978-3-030-79561-0_27

- P. Nieto Muro, **F. M. Heckmeier**, S. Jenkins, and C. Breitsamter. Development of an Analytic Convection Model for a Heated Multi-Hole Probe, *Sensors*, Vol. 21, 18, 6218, 2021. DOI: 10.3390/s21186218

Conference Contributions w/o Peer-Review Process

- **F. M. Heckmeier**, K. Meusel, S. Kienitz, D. Iglesias, and C. Breitsamter. Development of Fiber-Optic Pressure Sensors for the Usage in Unsteady Multi- Hole Probes, *Proceedings der 27. GALA-Fachtagung "Experimentelle Strömungsmechanik"*, Erlangen, Germany, September 3-5, 2019. ISBN: 978-3-9816764-6-4
- E. Nanos, J. Robke, **F. M. Heckmeier**, K. Jones, M. Cerny, G. V. Iungo, and C. L. Bottasso. Wake Characterization of a Multipurpose Scaled Wind Turbine Model, *AIAA Scitech 2019 Forum* San Diego, California, USA, January 7-11, 2019. DOI: 10.2514/6.2019-2082

Conference Presentations w/o Publication

- M. Winter, **F. M. Heckmeier**, and C. Breitsamter. Effiziente instationäre Luftkraftberechnung für veränderliche Struktureigenmoden mittels CFD-basierten Modellen reduzierter Ordnung, *17. STAB-Workshop*, Göttingen, Germany, 2015.
- **F. M. Heckmeier**, D. Iglesias, and C. Breitsamter. Entwicklung einer Mehrlockdrucksonde zur Erfassung instationärer Phänomene, *18. STAB-Workshop*, Göttingen, Germany, 2017.
- **F. M. Heckmeier**, and C. Breitsamter. Gaußprozesse zur Kalibrierung von aerodynamischen Sonden, *19. STAB-Workshop*, Göttingen, Germany, 2019.
- F. Mühle, **F. M. Heckmeier**, C. Breitsamter, and C. L. Bottasso. Wind tunnel investigations of an individual pitch control strategy for wind farm power optimization, *Wind Energy Science Conference 2021*, Hannover, Germany, 2021.

B List of Supervised Student Theses

Bachelor Theses

- P. Varillas Iglesias: Implementierung und Bewertung von verschiedenen Ansätzen zur Kalibrierung von Mehrlochsonden, 2017.
- J. Prummer: Qualifizierung der Düsenströmung im Mehrzweckwindkanal, 2018.
- N. Mooshofer: Implementierung und Aufbau eines Kalibrierstands zur statischen Kalibrierung von Mehrlochsonden, 2018.
- E. Boughanmi: Konstruktion, experimenteller Aufbau und Durchführung von Validierungsversuchen instationärer Anströmung bei Mehrlochsonden, 2018.
- M. Mrvelj: Druckmessungen mit Mehrlochsonden in Strömungen mit Geschwindigkeitsgradienten, 2019.

Semester Theses

- N. Mooshofer: Charakterisierung eines faser-optischen, differentiellen Drucksensors in einem Stoßrohr, 2020.
- A. Molz: Numerische Strömungssimulation für verschiedene Sondenkopfformen von Mehrlochsonden, 2020.
- S. Hayböck: Charakterisierung der räumlichen und zeitlichen Auflösung einer instationären Mehrlochsonde, 2020.
- A. Garcia-Risco: Calibration of aerodynamic probes: Development of a GUI and improvement of data reduction algorithms, 2020.

Master Theses

- K. Meusel: Entwicklung, Aufbau und Optimierung eines differentiellen, faseroptischen Drucksensors basierend auf dem Fabry-Pérot-Interferometer und dessen Einsatz in einer instationären Mehrlochsonde, 2019.
- J. Bauer: Evaluation of Uncertainty and Error in Multi-Hole Pressure Probe Measurements, 2020.
- P. Nieto Muro: Development of a heated 5-hole probe for aircraft applications, 2020.